Comparative analysis of metallated phthalocyanines for photodynamic therapy of solid tumors

Lionel Mendes Dias

Tese para obtenção do Grau de Doutor em
Biomedicina
(3º ciclo de estudos)

Orientador: Prof. Doutor Michal Heger
Co-orientador: Prof. Doutor José Eduardo Brites Cavaco
Co-orientador: Prof. Doutora Baoyue Ding

Júri:
Prof. Doutor Ilídio Joaquim Sobreira Correia
Prof. Doutora Cecília Reis Alves dos Santos
Prof. Doutora Maria do Amparo Ferreira Faustino
Prof. Doutora Maria Filomena Rabaça Roque Botelho
Prof. Doutor José Ruiz-López
Prof. Doutor Michal Heger

Covilhã, 29 de Maio de 2023

Declaração de Integridade

Eu, Lionel Mendes Dias, que abaixo assino, estudante com o número de inscrição D1570 do curso de 3° grau em Biomedicina da Faculdade de Ciências da Saúde, declaro ter desenvolvido o presente trabalho e elaborado o presente texto em total consonância com o **Código de Integridades da Universidade da Beira Interior**.

Mais concretamente afirmo não ter incorrido em qualquer das variedades de Fraude Académica, e que aqui declaro conhecer, que em particular atendi à exigida referenciação de frases, extratos, imagens e outras formas de trabalho intelectual, e assumindo assim na íntegra as responsabilidades da autoria.

Universidade da Beira Interior, Covilhã 16/06/2023

Lionel Mendes Dias

Dedicatory

I would like to dedicate this thesis to my family, my friends, my colleagues and my promotor/supervisors. Without their support, it would never have been possible.

Acknowledgements

I could not initiate my acknowledgements without first thanking my family for the unconditional support they have given me in this very long journey, and I will do it so in Portuguese: Aos meus pais, Agostinho e Alexandrina Dias, muito obrigado por tudo o que fizeram e fazem por mim! Vocês tem sido mais do que um apoio na minha vida, vocês são o meu pilar. Sem a vossa força eu não teria conseguido chegar ao final desta jornada. O mesmo digo à minha irmã Corinne, ao meu cunhado António Manuel, e ao meu sobrinho Duarte, que sempre me apoiaram em tudo! E apesar da distância, estiveram sempre do meu lado. Também não poderia esquecer-me dos meus primos e tios que igualmente contribuíram para formar uma corrente de apoio que me deu garras para continuar. Agora em Espanhol: A mi compañero Iván González, un enorme agradecimiento por toda la paciencia que ha tenido conmigo y por toda la motivación que me ha dado en mis días más bajos. Fuiste tú quien me dio fuerza y me mantuvo en calma cuando más lo necesitaba. Por eso y mucho más, muchas gracias de corazón!

To all my friends that so often have heard me complaining throughout these years, and still were there to listen and give me strength, I simply cannot thank you enough! While the list is slightly bigger, I would like to personally thank a few: Patrick Waller, thank you for all the encouragement and friendship given since the beginning of my PhD. You have been supporting me throughout this bumpy road and I cannot thank you enough for always being there for me; To Urtelinda Ramos, for always being by my side and supporting me, beside the distance. Our conversations have lifted me up so many times when I was feeling down, that I simply cannot thank you enough for all your friendship; To Silvia Teixeira and family (her partner Rui and her son Rodrigo), for feeding me with Portuguese food whenever I was feeling homesick and giving me all of the energy to continue this journey; A special thank you to Andrea De Leeuw and Coen van Heycop, for all the friendship and support throughout this journey and not only! You received me in Amsterdam with open arms and always treated me as a member of your family. To Dominique Miranda, Paulo Fonseca and Reza, a very big thank you for making sure that I would not get a burnout and reminding me that there is a life out there, outside of studies and work; And to Jerónimo Martín, for always being there when no one could. To all of you and to other friends not here listed, a big thank you for all the support.

Although I am an integral part of this research project, the mind and soul belongs to my promotor Prof. Doctor Michal Heger. I am deeply grateful for everything you have done for me throughout these years. Without you this PhD would have never happen. To my co-promotors Prof. Doctor Eduardo Cavaco and Prof. Doctor Baoyue Ding, thank you very much for your supervision and guidance. You were always prompt to help me at any time, and I really appreciate all your availability and support. A very big thank you to Ruud Weijer for all the teachings and supervision on my first year in Amsterdam. Your work in the field was my main reference and inspiration to continue.

With equal importance, I would like to take this opportunity to also thank the entire PDT family (as well as the curcumin and the mushroom team too), that have changed members throughout the years but without each and single of your contributions, this project wouldn't have continued as successfully. So thank you to Mark de Keijzer, Daniel de Klerk, Daniël Ernst, Tony Kleijn, Lianne de Haan, Leonardo Franchi, Farangis Sharifi, Rozemarie Spekman, Els Boon, Eveline Hoebe, Timothy Kombrink, Robert van Kooten, Karisma Nanda and Pelin Karsili. Wishing you all lots of success in your careers. Of course I have to thank also all of the members of the old department of Experimental Surgery at the Academisch Medisch Centrum (Universiteit van Amsterdam). Your direct and/or indirect contributions have made this PhD possible, even in the hardest times. While I am sorry that I am not able to include all the names, I still would like to give a big thank you to Albert van Wijk, Kenneth chin, Belle van Rosmalen, Lindy Alles, Ruurdtje Hoekstra, Amaran Suntharan, Zühre Uz, Przemek Krawczyk and Thomas van Gulik.

I could not forget to thank as well the entire team at the Department of Pharmaceutics of the Jiaxing University Medical College (China) for allowing such a life changing experience to happen, and for receiving me as one of their own at the Jiaxing university. I have learned a lot during my time in Jiaxing and it had a major contribution to this project. So thank you to Xuan Huang, Baoyue Ding, Mingjuan Li, Kaikai Wu, Yu Liu and all the other team members for your contributions and friendship.

Since there is no present nor future without a past, I could not forget to include in the list my former professors and friends from my bachelor's degree in Pharmacy (Polytechnic Institute of Guarda - School of Health). A big thank you to Prof. Dr. Fátima Roque, Prof. Dr. Sandra Ventura, Prof. Dr. Maximiano Ribeiro and Prof. Dr. André Araújo Pereira for all the teachings during my time at Guarda. Your patience with me did pay off at the end. A very special thank you to Prof. Dr. Paula Coutinho, for always believing in me and my capabilities, and for helping me initiating my PhD journey. Also to my dear friend Inês Neves Ribeiro and her husband Luís Ribeiro, for all the support giving during my student life at Guarda and now in the Netherlands.

Last but not least, a huge thank you to all my colleagues at uniQure, but specially for my team members at DPD (past and present members), who have continuously supported me in the last few years of my PhD. So Thank you to Edina Ljubovic Couteau, Mihaela Apetri, Simi Mathew, Feilong Sun, Marcello Morales, Jeroen Heuts, Zahra Balasi (Sanaz), Harutai Niramis, Latika Singh, Rose Babu, Ngan Tran, Fionnuala Moody, Liang Qin, Dylan Power and Katarina Bukara.

Resumo Alargado

A terapia fotodinâmica (do inglês PDT) baseia-se essencialmente na administração de um fotossensibilizador e da sua acumulação no local do tumor, seguido de irradiação com luz de comprimento de onda específico. Consequentemente, o oxigénio singleto e outras espécies reativas de oxigénio/nitrogénio (ROS/RNS) são produzidos a partir de oxigénio biodisponível no microambiente do tumor, e são os principais responsáveis pela erradicação do tumor por meio de três mecanismos distintos: 1) morte celular por apoptose/necrose/autofagia; 2) rutura microvascular do tumor mediado por trombose; e 3) uma resposta anti-tumoral do sistema imunitário.

PDT funciona de forma eficaz em certos tipos de cancro, mas menos eficaz em tumores que se alojam em órgãos internos e estruturas de órgãos, como por exemplo: o pâncreas e a árvore biliar. Além disso, efeitos adversos como a fototoxicidade da pele, são um grande obstáculo para uma ampla aplicabilidade no setor clínico. Os pacientes precisam de residir em ambientes escuros durante semanas após a terapia, para se protegerem da luz solar, o que é anti-ético nos casos em que os pacientes têm apenas alguns meses de vida. Nesse sentido, o objetivo da presente tese consiste na investigação de fotonanomedicamentos mais adequados para estes pacientes. Para esse fim, foram encapsulados fotossensibilizadores de segunda geração em transportadores lipossomais que são direcionados ao interstício do tumor após administração intravenosa. Os ftalocianine metalados, como o ftalocianine de zinco lipofílico (ZnPC) e o ftalocianine de alumínio (AlPC), bem como seus derivados tetrassulfonados hidrofílicos (ZnPCS4 e AlPCS4), atestam todos os requisitos clínicos para uso em PDT. No entanto, até o momento não houve comparação direta para determinar qual desses fotossensibilizadores é o mais fototóxico para as células tumorais e, portanto, merece mais desenvolvimento pré-clínico e clínico. Esses estudos serão conduzidos de forma a que permita a seleção do fotossensibilizador ideal para o desenvolvimento de uma terceira e quarta geração de fotossensibilizadores (por exemplo, co-encapsulamento de inibidores de vias de sobrevivência de células tumorais com fotossensibilizadores de segunda geração).

A presente tese descreve a avaliação e a comparação entre os ftalocianines metalados (ZnPC e AlPC) encapsulados em lipossomas com alvo para o interstício tumoral (ITLs), e os seus equivalentes hidrofílicos (ZnPCS4 e AlPCS4). Para isso, iniciamos a investigação através de uma avaliação *in vitro* usando células A431 como modelo para células tumorais, com uma disfunção no gene supressor tumoral P53 e superexpressão do receptor de factor de crescimento epidermal (EGFR). Como metodologia numa primeira abordagem foi avaliada a toxicidade no escuro (sem luz de ativação para a PDT) em função da concentração de fotossensibilizadores, utilizando os corantes WST-1 e sulforrodamina B como indicação da viabilidade celular. Seguiu-se o registo da captura celular em detrimento do tempo de exposição com os fotossensibilizadores, e também da sua distribuição a nível intracelular. Ambos os parâmetros foram determinados através da técnica de citometria de fluxo e de microscopia confocal, usando a fluorescência intrínseca dos fotossensibilizadores. Os valores de LC_{50} foram então estabelecidos para cada PS a um cumprimento de onda de 671 nm e uma exposição radiante de 15 J/cm^2, após 1 hora de exposição com os fotossensibilizadores. Finalizamos o nosso primeiro estudo com a avaliação da morte celular em função do tempo pós-PDT, e também com a análise do ciclo celular 24 horas após a PDT.

Através desta investigação observamos que, na ausência de iluminação, AlPC e ZnPC em ITLs não foram tóxicos para as células até uma concentração de 1,5 µM (exposição por até 72 h). No entanto, AlPCS4 e ZnPCS4 demonstraram toxicidade no escuro na ordem dos 5 µM e dos 2,5 µM, respetivamente. A absorção de todos os fotossensibilizadores foi observada tão cedo quanto 1 min após a adição de fotossensibilizadores às células, e aumentou em amplitude durante um período de incubação de 2 h. Porém, após 60 min de incubação com os fotossensibilizadores, todo o espaço não nuclear da célula foi fotossensibilizado, com a acumulação dos fotossensibilizadores em múltiplas estruturas subcelulares, especialmente no caso de AlPC e AlPCS4. A PDT de células fotossensibilizadas com ZnPC, AlPC e AlPCS4 foi capaz de produzir valores de LC_{50} na ordem dos 0,13 µM, 0,04 µM e 0,81 µM, respetivamente (24 horas após PDT, com base no ensaios com sulforrodamina B). O ZnPCS4 não foi capaz de induzir fototoxicidade, o que foi igualmente observado nos resultados obtidos na análise da morte celular e também do ciclo celular. Nas 4 h após PDT, a morte celular resumiu-se principalmente à apoptose para ZnPC e AlPC, que foi gradualmente aumentada em células fotossensibilizadas com AlPC durante 8 h. Por sua vez, as células tratadas com ZnPC recuperaram nas 8 h após PDT em comparação com 4 h pós-PDT. O AlPCS4 foi capaz de induzir a morte celular de forma significativa por necrose para além da apoptose, sendo que a maior parte da morte celular já se havia manifestado 2 h após a PDT. Durante o período de 8 h, a morte celular por via necrótica que era inicialmente a mais predominante, mas foi perdendo para a morte celular apoptótica tardia. A sinalização de morte celular coincidiu com redução de células na fase G0/G1 (ZnPC, AlPC, AlPCS4) e com a redução da atividade celular na

fase S (ZnPC, AlPC, AlPCS4) e fase G2 (ZnPC e AlPC) do ciclo celular. A interrupção do ciclo celular foi mais profunda em células que foram incubadas com AlPC e submetidas a PDT.

Com a intenção de validar resultados prévios, foram delineadas experiências utilizando o nosso modelo comparativo com os quatro ftalocianines metalados numa linhagem representativa da população celular num tumor (células endoteliais, fibroblastos e macrófagos), e também utilizando células de colangiocarcinoma humano como representante de células cancerígenas. Para além de todos os parâmetros avaliados no estudo anterior, optou-se por dar um passo em frente na investigação, e foi avaliada também a toxicidade sistémica de cada fotossensibilizador em embriões de peixe-zebra (Danio rerio) e galinha (Gallus gallus domesticus). Além disso, determinou-se o risco de fototoxicidade da pele usando murganhos (Mus musculus) BALB/c nude como modelo *in vivo*. Um estudo piloto sobre a eficácia da PDT também foi realizado em murganhos nude BALB/c portadores de xenoenxertos humanos de cancro de mama triplo negativo (MDA-MB-231).

Como principais resultados observou-se que todos os fotossensibilizadores ativos (exceto ZnPCS4) foram capazes de fotossensibilizar efetivamente células cancerígenas e células não cancerosas. Além disso, os fotossensibilizadores em estudo não induziram nenhuma toxicidade sistémica significativa em embriões de peixe-zebra e galinha. No entanto, ZnPCS4 e ZnPC em ITLs foram associados à fototoxicidade da pele, enquanto os fotossensibilizadores contendo alumínio não exerceram nenhuma fototoxicidade detetável no tecido cutâneo. Por último, ZnPC e AlPC encapsulados em ITLs são igualmente eficazes em reduzir o volume tumoral de xenoenxertos de cancro da mama humano em murganhos nude BALB/c, e foram superiores a outros fotossensibilizadores fora do grupo dos ftalocianines quando avaliados em detrimento da dose administrada por mol.

Em resumo, as investigações envolvendo o ZnPCS4 para terapia fotodinâmica oncológica serão descontinuadas no nosso grupo, já que ZnPCS4 demonstrou-se menos eficaz comparativamente aos restantes fotossensibilizadores em estudo. Por outro lado, ZnPCS4 revelou também sinais alarmantes de fototoxicidade cutânea. Deste modo, através das investigações incluídas na presente tese de doutoramento concluímos que AlPC e o seu derivativo hidrofílico AlPCS4 são os fotossensibilizadores menos tóxicos e mais eficazes. Assim sendo, pretendem-se continuar com estes dois fotossensibilizadores em futuros estudos rumo ao desenvolvimento de uma plataforma

integrando os ITLs juntamente com outro agente quimioterápico para o tratamento eficaz de tumores sólidos através da PDT.

Palavras-chave

Terapia fotodinâmica; Zinco-ftalocianine; Alumínio-ftalocianine; Lipossomas; Toxicidade; Fototoxicidade cutânea; Eficácia terapêutica

Abstract

Photodynamic therapy (PDT) comprises the administration of a photosensitizer (PS) and its accumulation within the tumor site, followed by irradiation with light of a specific wavelength. Consequently, singlet oxygen and other reactive oxygen/nitrogen species (ROS/RNS) are produced from bioavailable oxygen at the tumor's microenvironment and are responsible for the tumor's eradication. PDT works effectively in certain types of cancer, but poorly in tumors that reside in internal organs and organ structures such as the pancreas and biliary tree. Moreover, adverse effect such as skin phototoxicity is a major obstacle to more widespread clinical applicability. To that end, we encapsulated a second-generation of PS into liposomal carriers that are targeted to the tumor interstitium after intravenous administration. Therefore, this doctoral thesis describes essentially the evaluation and comparison between lipophilic metallated-phthalocyanines (ZnPC and AlPC) encapsulated in interstitially-targeted liposomes (ITLs), and their corresponding hydrophilic derivatives (ZnPCS4 and AlPCS4). To do so, we initiated the doctoral research through our first study by performing an attritional assessment *in vitro* using A431 cells as a template for tumor cells with a dysfunctional P53 tumor suppressor gene and epidermal growth factor receptor (EGFR) overexpression. As a methodology for our investigations, we have first assessed the dark toxicity as a function of PS concentration using the water-soluble tetrazolium salt (WST-1) and sulforhodamine B dyes as an indication of the cell viability. Using the same principle, we then drew the LC_{50} values for each PS through PDT at 671 nm and a light exposure of 15 J/cm^2 following 1 hour of PS exposure. We continued our research looking into a time-dependent uptake and intracellular distribution of the PS, and we finalized our first study with the assessment of the mode of cell death as well as the cell cycle arrest at 24 hours after PDT. Through this research we observed that, in the absence of illumination, AlPC and ZnPC in ITLs were not toxic to cells up to a 1.5 μM PS concentration and exposure for up to 72 h, but for AlPCS4 and ZnPCS4, the dark toxicity was at 5 μM and at 2.5 μM, respectively. However, PDT of cells photosensitized with ZnPC, AlPC, and AlPCS4 yielded LC_{50} values of 0.13 μM, 0.04 μM, and 0.81 μM, respectively (24 hours post-PDT based on sulforhodamine B assay). The uptake of all PSs was observed as early as 1 min after PS addition to cells and increased in amplitude during a 2-h incubation period. ZnPCS4 did not induce notable phototoxicity, which was echoed in the mode of cell death and cell cycle arrest data. However, AlPCS4 induced considerable necrosis in addition to apoptosis, whereby most of the cell death had already manifested as early as 2 h after PDT. Cell death signaling coincided with a reduction in cells in the G0/G1 phase (ZnPC, AlPC, AlPCS4) and cell cycle arrest in the S-phase (ZnPC, AlPC, AlPCS4) and G2 phase (ZnPC and AlPC). With the intention of validating our previous research, we have moved forward with the investigations through a second study by using our comparative model with the four metallated-phthalocyanines in a human cholangiocarcinoma cell line and tumor-comprising cells (endothelial cells, fibroblasts, and macrophages), as a representation of the tumor's microenvironment. In addition to all parameters assessed in the previous study, we went one step further and evaluated the systemic toxicity of each PS in zebrafish and in chicken embryos, and while using BALB/c nude mice as our *in vivo* model, we researched for signs of skin phototoxicity. A pilot study on PDT efficacy was also performed in BALB/c nude mice bearing human triple-negative breast cancer (MDA-MB-231) xenografts. The key findings were that photodynamically active PSs (all except ZnPCS4) were able to effectively photosensitize cancer cells and non-cancerous cells. In addition, PSs in study did not induced any notable systemic toxicity in zebrafish and chicken embryos. However, ITL-delivered ZnPC and ZnPCS4 were associated with skin phototoxicity, while the aluminum containing PSs did not exert any detectable sign of cutaneous phototoxicity. Last but not least, ITL-delivered ZnPC and AlPC are equally effective in their tumor-killing capacity in human tumor breast cancer xenografts, and superior to other non-phthalocyanine PSs when appraised on a per mole administered dose basis. In summary, the research on the applications of ZnPCS4 for oncological PDT will be discontinued in our group as it failed the attrition step regarding phototoxicity and it showed alarming signs of cutaneous phototoxicity. It is therefore concluded that AlPC and its derivative AlPCS4 are the least toxic and most effective PSs to employ with respect to ITLs as part of the comprehensive tumor targeting and PS delivery platform.

Keywords

Photodynamic therapy; Zinc-phthalocyanine; Aluminum-phthalocyanine; Liposomes; Toxicity; Skin phototoxicity; Therapeutic efficacy.

Table of Contents

List of Figures

List of Tables

List of Acronyms and Abbreviations

•OH	-	hydroxyl radical
O_2	-	molecular oxygen
$^1O_2$	-	singlet oxygen
O_2•-	-	superoxide anion radical
1PS*	-	excited singlet state photosensitizer
3PS*	-	excited triplet state photosensitizer
ALA	-	5aminolevulinic acid
AlPC	-	aluminum (III) phthalocyanine chloride
AlPCS4	-	tetrasulfonated aluminum (III) phthalocyanine chloride
AP	-	activator protein
ATP	-	adenosine triphosphate
AV	-	annexin V
BC	-	before-Christ
BID	-	BH3 interacting-domain
BPD-MA	-	benzoporphyrin derivative monoacid ring A
BSA	-	bovine serum albumin
Ca^{2+}	-	calcium ions
CRT	-	calreticulin
d	-	day(s)
DAMP	-	damage-associated molecular patterns
DC	-	dendritic cells
$DCFH_2$	-	20,70-dichlorodihydrofluorescein
DLI	-	drug-light interval
DMEM	-	Dulbecco’s modified Eagle medium
DMSO	-	dimethyl sulfoxide
DNA	-	deoxyribonucleic acid
dpf	-	days post-fertilization
DPPC	-	1,2-dipalmitoyl-*sn*-glycero-3-phosphocholine
DR	-	death receptor
DSPE-PEG	-	L-α-phosphatidylethanolamine, distearoyl methoxypolyethylene glycol conjugate
EDD	-	embryonic development day
EGFR	-	epidermal growth factor receptor
EHCC	-	extrahepatic cholangiocarcinoma
EMA	-	european medicines agency
EPR	-	enhanced permeability and retention
ER	-	endoplasmic reticulum
ETL	-	endothelium-targeting liposome
F	-	fluorescence
FBS	-	fetal bovine serum
FDA	-	food and drug administration
GMP	-	good manufacturing practice
GSH	-	glutathione
h	-	hour(s)
H_2O_2	-	hydrogen peroxide
H&E	-	hematoxylin & eosin

HEPES - 2-[4-(2-hydroxyethyl)piperazin-1-yl]ethanesulfonic acid
HIF - hypoxia-inducible factor
HMGB - high mobility group box
HO - haeme oxygenase
HpD - hematoporphyrin derivative
Hpf - hours post fertilization
HPPH - 2-(1-hexyloxyethyl)-2-devinyl pyropheophorbide
HSP - heat shock proteins
HUVECs - human umbilical vein endothelial cells
IL - interleukin
iPDT - interstitial-PDT
IR - infrared
ISC - intersystem crossing
ITL - interstitially targeted liposomes
iv - intravenous
L - length
LC$_{50}$ - median lethal dose (*in vitro*)
LC$_{90}$ - lethal dose at 90 percent (*in vitro*)
LD$_{50}$ - mediam lethal dose (*in vivo*)
LDL - low density lipoprotein
LED - light-emitting diode
logP - octanol:water partition coefficient
MDR - multi-drug resistance
min - minute(s)
MIP - macrophage inflammatory proteins
mTHPC - 5,10,15,20-tetrakis(3-hydroxyphenyl)chlorin (*Temoporfin*)
m-THPP - 5,10,15,20-tetrakis(3-hydroxyphenyl)porphyrin
NaCl - sodium chloride
NADPH - nicotinamide adenine dinucleotide phosphate
NF-κB - nuclear factor κB
NPe6 - mono-L-aspartyl chlorin e6
NRF - nuclear E2-related factor
OOPS - 1,2-dioleoylphosphatidylserine
P - phosphorescence
PBS - phosphate-buffered saline
PC - phthalocyanine
PDI - polydispersity index
PDT - photodynamic therapy
PEG - polyethylene glycol
PFA - paraformaldehyde
PI - propidium iodide
POPC - [(2R)-3-hexadecanoyloxy-2-[(*Z*)-octadec-9-enoyl]oxypropyl]2-(trimethylazaniumyl)ethyl phosphate
PS - photosensitizer
RAGE - receptor for advanced glycation end products
RNAse - ribonuclease
ROS - reactive oxygen species
RT - room temperature
S$_0$ - ground singlet state
S$_1$ - excited singlet state
SD - standard deviation

SI	-	selectivity index
SRB	-	sulforhodamine B
T_0	-	ground triplet state
T_1	-	excited triplet state
TF	-	transcription factors
TLR	-	toll-like receptor
TNF	-	tumor necrosis factor
$TPPS_4$	-	5,10,15,20-tetrakis(4-sulfonatophenyl)porphyrin
TRAIL	-	tumor necrosis factor-related apoptosis-inducing ligand
Tpr	-	tryptophan
TRIS	-	tris(hydroxymethyl)aminomethane
TTL	-	tumor cell-targeting liposome
USA	-	United States of America
V	-	volume
W	-	width
WST-1	-	water-soluble tetrazolium 1
ZnPC	-	zinc (II) phthalocyanine
ZnPCS4	-	tetrasulfonated zinc (II) phthalocyanine

Chapter 1

Introduction

1. Chapter 1 - Introduction

1.1. Brief history of photodynamic therapy

The use of light as a potential source of treatment, either alone (also known as phototherapy) or in combination with chemical compounds (equally referred as photochemotherapy), was already acknowledged by certain ancient civilizations throughout the world, dating back to thousands of years before-Christ (BC). Although light therapy became well known after the term "heliotherapy" was brought by the ancient Greek Herodotus, back in 525 BC (1,2), the contents mentioned in the earlier Papyrus Ebers referred about an ancient practice by Egyptians for treatment of vitiligo, with the ingestion of a boiled extract derived from a type of weed, *Ammi majus L*, followed by sun exposure (1,3). A similar practice was reported around 1100 after-Christ by an Arab physician called Ibn al-Bitar, in his book named "Mofradat El-Adwiya" (1). In China and India, healers would perform similar practices but using seeds of *Psoralea corylifolia* for treatment of skin conditions, such as psoriasis (1,4). Despite the earlier events in history, progress in the field have only begun after the work developed by Niels Ryberg Finsen, who won in 1903 the only Nobel prize so far awarded in the field of photomedicine, in recognition of his contributions for treatment of *lupus vulgaris* using concentrated light radiation (1,5).

The current clinical concept of Photodynamic Therapy (PDT) was, however, first described by Oscar Raab, a medical student working under the supervision of Professor Herman von Tappeiner, in Munich (Germany) (6). During his studies, Oscar Raab wisely observed that low concentrations of acridine red could be lethal to *protozoan paramecium* when exposed to light (6,7). In the following years, Professor Tappeiner in collaboration with Jesionek and other scientists, have demonstrated that topical application of eosin in combination with light could treat human skin cancers through a process mainly mediated by bioavailable oxygen (8,9). Since then, the interests in the field have risen throughout the scientific community.

Hematoporphyrin, first isolated in 1841 by Scherer while performing experiments in blood (6,10), became famous as the first photosensitizing agent administered in humans when in 1913, the German Friedrich Meyer-Betz, decided to injected himself with 200 mg to determine whether or not the same effects observed in mice could be replicate in humans (11,12). Although Meyer-Betz was not successful with his attempt, and instead suffered with prolonged pain and swelling in light-exposed areas (11,12), it led to the development of hematoporphyrin derivative (HpD) from hematoporphyrin by Schwartz in 1955 (6,11,13). This important achievement allowed other scientists, such as Lipson, Baldes, Kelly and Snell, to demonstrate further the therapeutic capacities of HpD as a photosensitizer (PS)(6,11,14).

However, it was not until the extensive work from Dougherty (between 1975 and 1978), that complete cure of malignant cutaneous tumors was achieved by combining the administration of HpD with red light exposure (14–16). These promising results were confirmed through several clinical trials with improved versions of HpD in patients with mainly skin and bladder cancers (14–16). Finally, a milestone for PDT was achieved in 1993 when porfimer sodium (a semi-purified version of HpD and commercially known as Photofrin), received regulatory approval from Canada for treatment of bladder cancer (11,14). Since this important landmark was accomplished, research have continued to prove the applicability of porfimer sodium in treating cancers of multiple sites, such as bladder; lungs; esophagus; head and neck; eye and brain (11,14). In addition, new PSs and other innovations have been developed throughout the time, giving continuation to a promising field, which is PDT.

1.2. Clinical applications of Photodynamic Therapy

The medical and biomedical applications of PDT procedures are broad and have interested several industries in managing various human diseases with the successes of PDT. From photodynamic inactivation of microorganisms for averting antimicrobial resistance, to dermatological treatment of several skin conditions (*e.g.*, Acne, port-wine stains, psoriasis), the promising applications are numerous and continuously growing (17–21). Nonetheless, PDT appliance in oncology is one of the most explored and studied field of PDT application, that brought innovation and successful developments in the prevention and treatment of different type of cancers.

1.2.1. Photodynamic therapy in clinical oncology

Compared with surgery, chemotherapy or radiotherapy, PDT is a clinically approved and minimally/non-invasive therapeutic procedure that harnesses important benefits, such as: reduced damage to healthy tissues (22), cost-effectiveness with associated life expectancy increase, and it can be combined with other therapies without requiring therapeutic follow-ups but repeatable when needed (23).

PDT essentially encompasses two main phases throughout its clinical application: first, PS pharmacokinetics, and second, PS pharmacodynamics. In PS pharmacokinetics, PS is initially administered systemically or locally (*e.g.*, intravenous, intraperitoneal, or topical administration), determining if its biodistribution occurs throughout the entire body or solo within the location of administration (24,25). When PS is administrated intravenously, the extend of time between PS administration and light exposure is designated as drug-light interval (DLI). DLI is an important element to be considered in PDT clinical protocols as the length of DLI is correlated to the accumulation and concentration of PS in tumor, which will also help determine the light dosage necessary for an efficient treatment (24,26). PS biodistribution and accumulation in tumor is often favored by the fenestrated vasculature and reduced lymphatic drainage of tumor's microenvironment, characteristic of most solid tumors (26). This phenomenon known as enhanced permeability and retention (EPR) effect, allows the extravasation and passive accumulation of PS in the tumor tissue (27). The biodistributive behavior of a PS depends essentially on: PS ability to refrain from aggregation and avoid its removal through cells of the mononuclear phagocyte system (immune system) (28,29) or simply undergo pinocytosis and/or phagocytosis by tumor-associated macrophages (28,30); PS ability to bind to macromolecules, such as low-density lipoprotein (LDL) and albumin (28,31,32); and PS ability to undergo an increase in its lipophilicity (octanol/water partition coefficient or log P) in the more acidic tumor milieu (28,33). Depending on the via of administration, PS metabolization may occur or not prior accumulation in the tumor, and PS excretion is typically occurring alongside the first and second phase of the clinical process, at a rate depending mostly on the PS's chemical and pharmacological properties (27). The second and last phase of clinical PDT concerns PS pharmacodynamics, where PS activation occurs through light exposure at the tumor site, and together with bioavailable oxygen, PDT can follow its natural chain of reactions that leads ultimately to tumor ablation/destruction (see figure 1.1 A) (28).

For the process of photoactivation, irradiation must be performed with light of a specific wavelength, corresponding to the optimal absorption band of the PS, and at predetermined fluence rates. Once the above-mentioned two-steps are accomplished, PS in cancer cells will undergo a series of photochemical and photophysical reactions, that will lead to the formation of reactive biomolecular species, responsible for the consequential effects causing tumor cells' death, vasculature shutdown and an anti-tumor immune response (22) (see figure 1.1 B). To optimize a therapeutic protocol in order to achieve a desired outcome in clinical settings, the following variables must be considered: the type of PS (physicochemical and pharmacological properties) and dose administrated; the via of administration and DLI period necessary; the type of light source (wavelength) and dose applied (fluence rate); the tumor's characteristics and local bioavailable oxygen levels (22). In PDT, the pharmacotherapeutic profile of a PS can be judged based on its phototherapeutic index, which is defined through the ratio between its toxicity after photoactivation with light of specific wavelength, and its toxicity in the dark (also called inert toxicity)(34).

The treatment modality of PDT has proven efficient against a variety of benignant and malignant tumors, where responsive rates higher than 70% were achieved for treatment of skin cancers and esophageal malignancies (35–38). Relatively poor responsive rates (lower than 50%) were still observed in the treatment of nasopharyngeal carcinomas (39), bladder tumors (40), and extrahepatic cholangiocarcinomas (41). In fact, PDT still poses many challenges in the treatment of solid tumors, mainly due to the geometrical complexity and non-homogeneous nature of the tumors, limiting the optical penetration depth and light scattering (42). However, interstitial and intra-operative approaches for treatment of bulky solid tumors located in the head and neck (43), brain (44), prostate (45), lung (46), and breast (47), have been investigated using multiple light-emitting fibers to deliver the desired light dose. Nevertheless, PDT is considered an advantageous therapeutic adjuvant when surgical resection of solid tumors might leave residual microscopic cancerous tissue behind (48).

Once PDT treatment is performed, patients are normally recommended to follow certain preventive measures to avoid possible phototoxic reactions. For instances, patients are usually indicated to avoid direct exposure to outdoor/indoor sunlight and bright indoor light, for a period that can go up to 90 days after therapy (49). Sunglasses, sunscreen, gloves, hats and any light protective materials should be considered if exposure to light may occur in the following days after PDT (49).

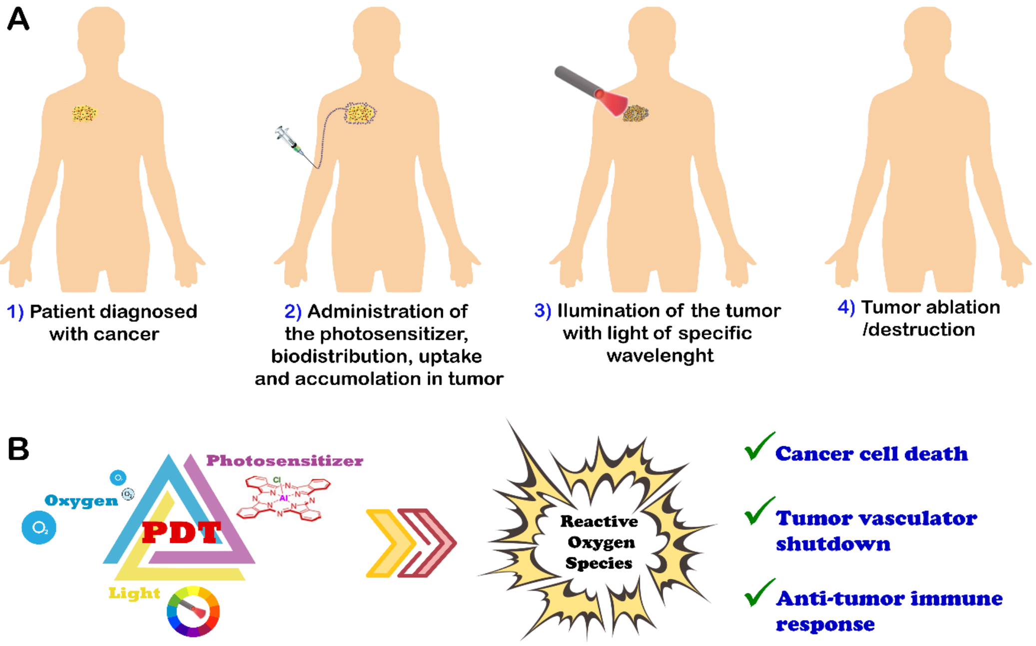

Figure 1.1 - The principles of clinical photodynamic therapy (PDT) for oncological treatment. (A) Illustration of the four main steps applied in clinical PDT, from the diagnose and the administration of the photosensitizer (PS) until the local illumination, and consequentially, the ablation/destruction of the tumor. (B) Representative schema illustrating the PDT process initiated by PDT's essential elements (photosensitizer + light + oxygen) to generate reactive oxygen species responsible for tumor cells death, vasculature occlusion and anti-tumor immune response. Figure made by the author.

1.3. Photodynamic therapy: general mechanisms and essential components

PDT refers to any modality in which the dynamic of a light is exploited in combination to a light-sensitive chemical substance (normally called photosensitizing agent or photosensitizer) and under the presence of bioavailable oxygen *in situ*, to generate a treatment against a pathological condition or disease. The photochemical mechanism behind PDT include three main components, which by themselves are not toxic or almost not toxic from any toxicity, but their mutual interaction altogether leads to desired effects in pathological tissue. These three main components are: light of a specific and adequate wavelength for photoactivation; the PS; and bioavailable oxygen in targeted cells (50).

1.3.1. Photochemical and photophysical mechanisms

The photodynamic reaction is initiated when the light of adequate wavelength is absorbed by PS located in specific *situ*, generating reactive species through the transfer of energy/electrons from excited PS to bioavailable molecules (*e.g.*, oxygen and nitrogen), which are therefore responsible for the photokilling capacities of this modality (28). In detail, when irradiation starts and light reaches PS at original ground singlet state (two electrons with opposite spins at low orbital energy), the photonic energy absorbed by PS promotes the excitation of these electrons to another high energy orbital level called excited singlet state (with electrons still at opposite spins) (51–54). The relatively short-time and unstable PS in excited singlet state, allow it to lose its energy by emitting light (fluorescence) or heat (known as internal conversion or non-radiative decay), or alternatively undergo a process named "Intersystem crossing", in which the spin of the excited electron inverts (spinning in parallel conformation) to form a relatively long-lived triplet-state (51–54). Consequentially, PS in triplet state may undergo one of the following processes: decay back to ground state energy level by emitting phosphorescence; transfer an electron (Type I photochemical reaction); or transfer energy (type II photochemical reaction) (28, 51–55). In type I reactions, interactions may occur directly with organic molecules and molecular oxygen (O_2) in microenvironment, forming radicals such as superoxide anion radical ($O_2{\bullet}-$), responsible to produce Reactive Oxygen Species (ROS) (28, 51–55). Direct energy transfer to O_2 as per type II reactions lead to the formation of singlet oxygen ($^1O_2$), which typically occurs when triplet-state PS energy is higher than singlet-state $^1O_2$ (~94.5 kJ/mol) (28, 51–55). As type II reactions are considered simpler and thermodynamically in favor of red-absorbing PS, they are more predominant comparatively to type I reactions (28, 51–55). Therefore, singlet oxygen quantum yield is considered one indicator of PS efficiency, as it determines if PS can use photonic energy to convert ground-state dioxygen into the excited singlet-state $^1O_2$ (51–55). However, the lifetime of $^1O_2$ is very short (~10-320 ns) and limits its diffusion to very short distances (~220 or less) (28, 51–55). The process of photosensitization above described is illustrated in figure 1.2. Both type of reactions can occur competitively, and the preferential path is mostly determined by PS characteristics, the light and light-dosage applied, and by the concentration of locally available oxygen (28, 51–55). ROS and other bio-reactive species generated through these mechanisms are, therefore, responsible for the downstream biological effects occurring *in vitro*, *in vivo* and in clinical PDT.

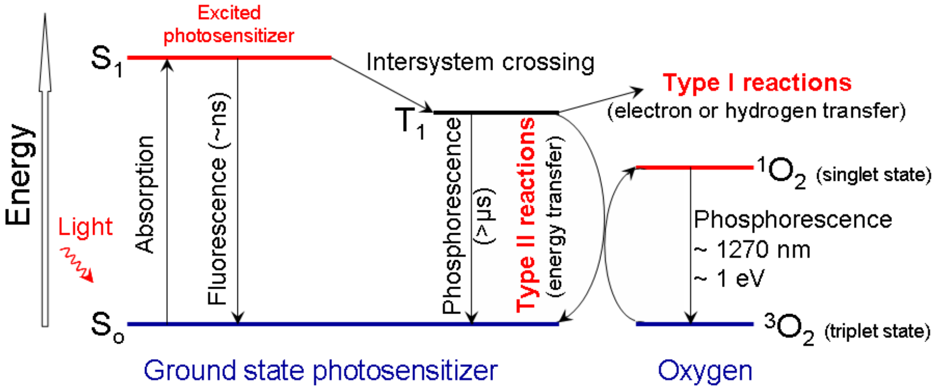

Figure 1.2 - Illustration of the process of photosensitization through a modified Jablonski diagram. The process of photosensitization is initiated through the light exposure of the PS and its consequent moving from a ground singlet state (S_0) to an excited singlet state (S_1). PS in S_1 state may undergo intersystem crossing to an excited triplet state (T_1) that can lead to either type I reactions (via electron/hydrogen transfer) or type II reactions, via transfer of energy to molecular oxygen and form the singlet oxygen ($^1O_2$). This figure was copied from (54) with the consent of the corresponding author.

1.3.2. Light

In PDT, for a photochemical reaction to happen, the wavelength of light responsible for photoactivation must match the electron absorption spectrum of the PS. In addition, the total light dose (J/cm^2) administrated, calculated as the product of the fluence rate (W/cm^2) and treatment time (sec), has to be sufficient to promote the maximum of the therapy at a given PS. Therefore, the selection of the light system is an important step to take into account while creating a PDT protocol. However, the wavelength of the emission light is far more relevant than just exciting PS for therapy. Typically, short-wavelength light (300 – 600 nm) has lower tissue penetration depth compared with near infrared (IR) wavelength light (600 – 800 nm) (54,56), as explained in figure 1.3. That has to do with competitive light absorption by endogenous chromophores, such as hemoglobin (λmax at 420 nm) and bilirubin (λmax at

460 nm) (28). Besides, sunlight is more intense at shorter wavelength compared to near IR wavelengths (28). Longer wavelength light (> 850 nm) however, does not provide sufficient energy for PS to transit to its triplet state and generate ROS (56). Consequently, for PDT clinical purposes, the therapeutic window of light emission wavelength is between 650 and 850 nm (54,56). In addition, physicians have to consider the optical properties of the illuminated tissue, since light is prune to different effects that can compromise its diffusion through the tissue, such as light reflection, scattering and absorption (54,56–58).

The use of lamps (halogen, fluorescent, tungsten or xenon lamps) combined with short-/long-pass filters to reduce ultra-violet and infra-red emissions, was considered standard and are still in use for suitable dermatological treatments (58,59). They provide a wide emission spectral output with low maintenance and affordable prices, that can be used to simultaneously photoactivate multiple PSs with different excitation wavelength (58,59). More recently, lamps have been gradually replaced by light-emitting diode systems (LED), which does not require optical filters due to their narrow-banded light emission (59–61), and when built in arrays, LEDs can irradiate large surface areas at equally low price compared to other sources. Lasers have been widely used as coherent light sources for PDT. They are characterized as monochromatic light sources and their wavelength can be paired exactly with the absorption wavelength of the PS, avoiding hyperthermia caused by emitted light outside of the desired band (59,61). Laser systems are considered highly convenient and accurate for the delivery of light into internal tumors, either interstitially or endoscopically, as they can be coupled to optical fibers with diffusing tips (59,61). Initially, dye lasers (*e.g.*, argon-ion, or coper/gold -vapor lasers) were predominantly used in the industry and science, but their size, cost and complexity were considered major drawbacks. The appearance of diode lasers in the market with total output around 2 W of continuous wave, emitting light at 633 nm, and convenient size/weight, have brought significant improvements in the PDT field (59,61,62).

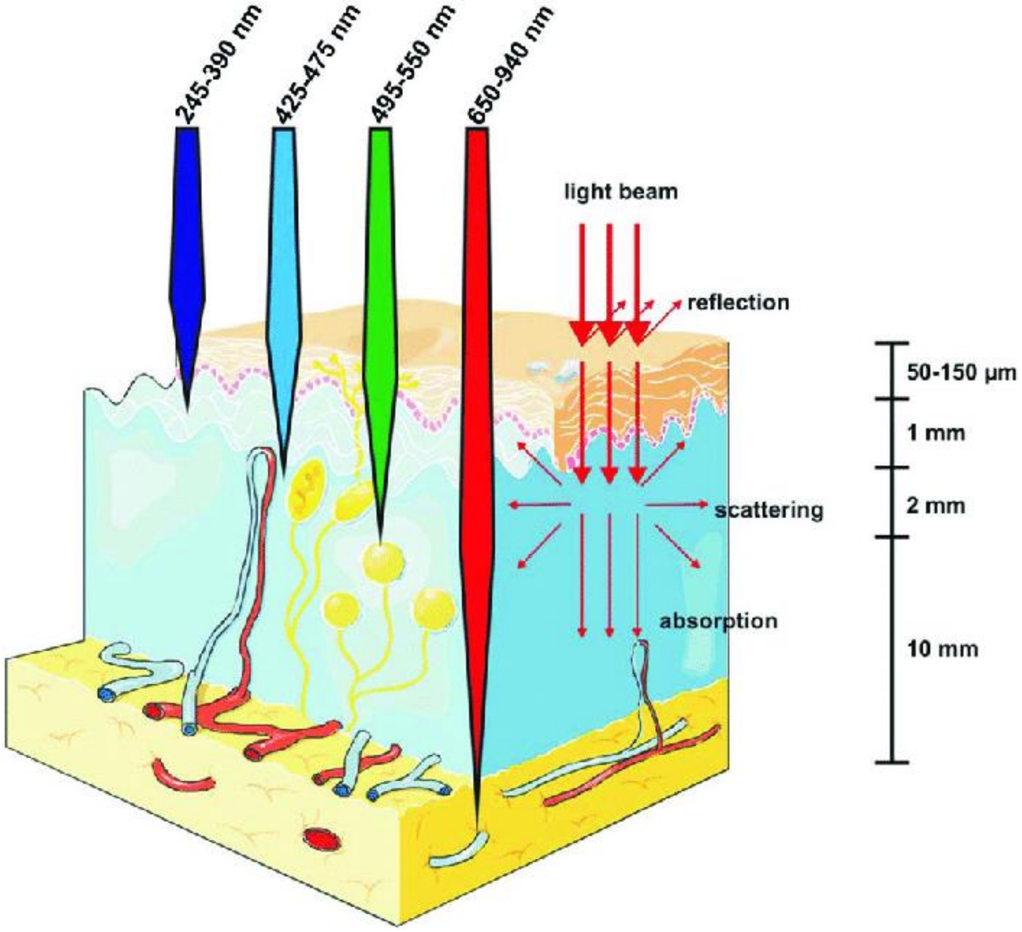

Figure 1.3 - Light properties in interaction with tissue. Light-tissue penetration depth per wavelength range, and the different effects occurring in tissue (reflection, scattering and absorption). This figure was copied from (56) with the consent from the corresponding author, which was adapted from the version in (54).

There are five main light-application modes used in *in vivo*/clinical PDT that are prior divided into two groups: external and internal illumination. One of the most common application mode is the superficial irradiation, widely used in skin-cancer PDT derived treatments but also for internal localized/spot treatment (*e.g.*, stomach tumors), and consists of front/cavity surface irradiation. For internal cavities/organs, light-delivery can vary into cylindrical superficial irradiation, when a cylindrical diffuser is used (*e.g.,* esophageal tumor); spherical superficial irradiation, when a microsphere is used at the end of the fiber (*e.g.*, bladder cancer); and interstitial irradiation, when the diffuser source is embedded inside the tumor (*e.g.,* solid tumors) (63). When it comes about deciding between pulsed or continuous light, the conclusions are not unanimous. While most findings, either *in vitro* or *in vivo*, refer that no significant changes in PDT efficacy are seen between pulsed and continuous wave (63,64), other investigations have shown differences in tumor's response and type of cell death (65,66).

1.3.3. Photosensitizers

The main purpose of a PS is to generate a triplet excited state of energy through the exposure of light, that is sufficiently reactive enough to trigger PDT's mechanisms. Theoretically, an ideal PS should be photochemically efficient, biologically stable, and selectively accumulated in the targeted tissue comparatively to its surrounding (67,68). In other words, PS should meet a set of requirements, such as: be highly chemically pure; stable at room temperature; activated only in presence of light with a specific wavelength within the therapeutic window (between 650 and 800nm) and with a high extinction coefficient (εmax >50,000 M^{-1} cm^{-1}); have minimum absorption between 400 and 600 nm to prevent from sunlight derived photosensitivity; have high quantum yields of ROS formation and resistance to photodecomposition; have minimal to non-existent dark toxicity and do not exhibit any mutagenicity or carcinogenicity; have improved pharmacokinetics with high selectivity for neoplastic tissues; last but not least, be affordable and simple to synthesize (53,67–70). Several PSs in cancer therapy can be categorized by their basic chemical structures into porphyrins, chlorins, bacteriochlorins, phthalocyanines, phenothiazines, anthraquinones, xanthenes, cyanines, curcuminoids and BODIPY (69). Additionally, PSs can be classified according to their chronological developments as belonging to the first- or second-generation of PS (71).

1.3.3.1. The 1st generation of photosensitizers

Belonging to the first-generation of photosensitizers is Hematoporphyrin, a complex mixture of porphyrinic compounds isolated from hemoglobin of red blood cells that became the first generation called PS (69,72). Through its purification and chemical modification it was discovered the HpD, a more selective type of PS towards neoplastic tissues (69,72). Finally, the first marketed PS ever in PDT was Porfimer Sodium, or also known as Photofrin (commercial name), developed by a mixture of porphyrin dimers and oligomers isolated from HpD (72,73). Porphyrins are compounds based on a ring of four interconnected and modifiable pyrrole subunits, known for absorbing visible light (70). Photofrin was first approved in Canada at 1993 for treatment of bladder cancer, and in December 1995 by the Food and Drug Administration (FDA) for treatment of obstructive esophageal cancer. Currently, it can be used additionally for treatment of endobronchial cancer and High-grade Dysplasia in Barrett's Esophagus (68,69). Photofrin is typically administrated intravenously and irradiated at a wavelength of 630 nm, with a laser light dose varying between 130 - 300

J/cm^2 using a fiber optic diffuser and lasting between 40 – 50 hours following injection (74). An analogue of Photofrin was created and is commercialized in Russia under the name of Photogem, which consist of a mixture of monomers, dimers, and oligomers of HpD (69). This generation of PS have been widely explored for PDT oncological treatment, especially Photofrin. However, inconveniences due to poor chemical purity and pharmacological properties were found during their application in clinical, originating serious side effects such as skin photosensitivity. In the example of Photofrin, patients should prevent sunlight or bright indoor light exposure for a period between 30 to 90 days to avoid any phototoxicity (49). The need for alternatives that would cease with the drawbacks and limitations observed with the first-generation have led to the development of the second-generation of PS.

1.3.3.2. The 2nd generation of photosensitizers

While the drawbacks associated with the first generation of photosensitizes did not prevent from clinical approval and treatment of certain cancers, it certainly reduced significantly its medical applicability and recommendation. Starting from the 1980s, the development of a second-generation of PS aiming for improved purity, long wavelength absorption, low photosensitivity, and high tissue selectivity, had just begun (68–70,75) Through decades, a large number of potential PS candidates with improved properties have been proposed, and few of them have reached clinical trials with much fewer having succeeded (see table in 1.1 a list of clinically approved PS and other relevant PSs that are/have been in clinical trials).

Going deeper into this generation of PS, we can encounter two major groups: the porphyrins family and the non-porphyrins PSs. Modifications in the structure of the porphyrins have led to changes in the absorbance spectrum leaning towards longer wavelengths and within the therapeutic window of PDT (69). 5,10,15,20-tetrakis(3-hydroxyphenyl)porphyrin (m-THPP) and 5,10,15,20-tetrakis(4-sulfonatophenyl)porphyrin ($TPPS_4$) are porphyrin derivatives (75). Despite their longest wavelength absorption band being around ≈650 nm, they have low absorption coefficients but still showing signs of skin phototoxicity. An interesting discovery was 5aminolevulinic acid (ALA), which by itself is not having any photochemical activity but function as a prodrug by taking profit of the overwhelmed heme biosynthesis pathway to enzymatically get converted into a highly photoreactive protoporphyrin IX (69,75,76). ALA was first commercially introduced as Levulan for treatment of actinic keratosis by DUSA Pharmaceuticals at the United States of America (USA) in 1999, and together with other protoporphyrin IX precursors (such as Metvix), they are currently being exploited for PDT application in basal cell carcinoma, amongst other diseases (69).

Chlorins are a subgroup of compounds deriving from porphyrins, and diverging essentially by two extra hydrogens in one pyrrole ring (69). This rather simple structural change have led to a shift in the absorption band (from 640 to 700 nm) and an increase in the εmax (40,000 M^{-1} cm^{-1}), that ultimately promoted the creation of several other PSs (69). One of the PSs is the 5,10,15,20-tetrakis(3-hydroxyphenyl)chlorin (mTHPC), with the generic name Temoporfin and by the commercial name Foscan (68,75). Temoporfin was approved in 2001 by the European Medicines Agency (EMA) for treatment of advanced head and neck squamous cell carcinoma, however, its clinical application have been studied for a variety of cancers, such as bile duct cancers, non-resectable non-small-cell lung cancers, and nasopharyngeal carcinomas (14). If the powerful photochemical characteristics of Foscan are in one hand considerate an advantage, its suboptimal properties can be seen as a disadvantage for inducing damage to normal tissues surrounding the tumor. Nevertheless, the risk of skin phototoxicity is considerate moderate when compared with Photofrin, and lasts for approximately two weeks after therapy (69). Also included in the chlorins subgroup are the benzoporphyrin derivatives, such as the FDA approved PS named Visudyne, also known as Verteporfin, which consists of a liposomal formulation containing Benzoporphyrin derivative monoacid ring A (BPD-MA) (69,77). Amongst the list of PS derived from the chlorin's family you can find Rostaporfin (Purlytin, Photrex), researched for treatment of Kaposi's sarcoma and age-related macular degeneration (69,71,78), and also the mono-L-aspartyl chlorin e6 (NPe6 or Talaporfin), also known as Laserphyrin, approved in Japan in 2003 to treat lung cancer, and most recently completed the phase 3 clinical trials for liver and colon cancers (69,71,79).

Pheophorbides and bacterioheophorbides are another subgroup from the porphyrins big family, and they are well known by their high εmax (100,000 M^{-1} cm^{-1} or higher) in the near-IR region (700 - 850 nm) and also high quantum yields of triplet state, increasing the ROS production (69). An example of two PS that made their way into clinical trials is Padoporfin (WST09 – Tookad) and its water-soluble derivative padeliporfin (WST11– Stakel Soluble), developed for prostate and urothelial cancer treatment, respectively (69,71,80). Belonging also in the pheophorbides subgroup is the 2-(1-hexyloxyethyl)-2-devinyl pyropheophorbide (HPPH, marketed as Photochlor), researched for clinical treatment of esophageal cancer, basal cell carcinoma, lung cancer and Barrett's esophagus (69,71,80). Other subgroups within the porphyrins big family to be considerate are the Texaphyrins, with motexafin lutetium (Lu-Tex, and its marketed names Lutrin, Optrin and Antrin) (69,80,81); and phthalocyanines, which it is going to be addressed separately in section 1.3.3.2.1 .

Although the majority of PSs are coming from porphyrins family, there are other molecular structures non-porphyrin like capable of exhibit PDT activity. From the anthraquinones we have Hypericin, which absorbs at 590 nm with εmax of approximately 44,000 M^{-1} cm^{-1} and have been studied for treatment of squamous cell carcinoma and basal cell carcinoma (69,80,82). From the phenothiazinium family we can find Methylene blue that absorbs at 666 nm with εmax of 82,000 M^{-1} cm^{-1}, and Toluidine blue with absorption at 596 nm and 630 nm for a εmax (630 nm) of around 51,000 M^{-1} cm^{-1} (69,80,83). Within the Xanthenes group there is the Rose Bengal and the 4,5-Dibromorhodamine methyl ester (TH 9409), and from the Cyanines group there is Merocyanine 540 (69). Last but not least, from the Curcuminoids family we have, a natural colorant isolated from rhizomas of *Curcuma longa L* exhibiting absorption at 420 nm and a εmax at around 55,000 M^{-1} cm^{-1} (69,84).

Table 1.1 - List of clinically approved photosensitizers and in clinical trials for oncological PDT.

Photosensitizer	Brand name	λmax (nm)	Approved country	Cancer type
Porfimer sodium	Photofrin	630	Worldwide	Esophageal, lung, gastric, endobronchial, bladder, bile duct and cervical cancer
Mixture of monomers, dimers, and oligomers of HpD	Photogem	660	Russia	Respiratory and digestive tracts, urogenital
5-Aminolevulinic acid (ALA)	Levulan	635	Worldwide	Skin (Actinic keratosis)
Methyl aminolevulinate (MAL)	Metvix	635	Canada, USA and Europe	Skin (Actinic keratosis) and basal cell carcinoma
Benzoporphyrin derivative monoacid ring A (BPD-MA, Verteporfin)	Visudyne	690	Norway, China	Age-related macular degeneration
Meta-tetra (hydroxyphenyl)chlorin (m-THPC, temoporfin)	Foscan	652	Europe	Advanced Head and neck cancer
Mixture of sodium salts of chlorine e6, chlorine p6, and purpurine	Radachlorin	662	Russia	Skin cancer
N-aspartyl chlorin e6 (NPe6, Talaporfin)	Laserphyrin, Litx	664	Japan	Lung, Liver and colon cancer
Palladium bacteriopheophorbide monolysine taurine (WST11, Padeliporfin)	TOOKAD Soluble, Stakel	753	Europe	Prostate cancer
Mixture of sulfonated aluminum phthalocyanine	Photosens	675	Russia	Skin, breast, oropharyngeal, lung, bladder and cervical cancers

Photosensitizer	Brand name	λmax (nm)	*Clinical phase	Cancer type
Redaporfin	LUZ11	749	Phase 2	Head and Neck Cancer
Rostaporfin	Purlytin, Photrex	664	Phase 3	Kaposi's sarcoma and age-related macular degeneration
Palladium bacteriopheophorbide (WST09 or Padoporfin)	TOOKAD	763	Terminated	Prostate cancer
Motexafin lutetium (Lu-Tex)	Lutrin, Optrin, Antrin	732	Terminated	Prostate cancer, age-related macular degeneration, breast cancer, cervical cancer

2-(1-Hexyloxyethyl)-2-devinyl pyropheophorbide (HPPH)	Photochlor	665	Phase 2	Esophageal cancer, basal cell carcinoma, lung cancer, Barrett's esophagus
Liposomal zinc phthalocyanine (Zn-PC)	CGP55847	670	Terminated	Squamous cell carcinomas of the upper aerodigestive tract
Di-sulfonic-di-phthalimidomethyl phthalocyanine zinc di-potassium salt	Photocyanine	670	Phase 1	Skin cancer and esophageal cancer
Silicon phthalocyanine 4	Pc4	675	Phase 1	Non-melanoma skin cancer and cutaneous T-cell Non-Hodgkin Lymphoma

*Listed only the most advanced and completed clinical phase.
This search was made in March 2022, and it utilized the following references:(7,14,68,69,75,77–79,85–87)

1.3.3.2.1. Phthalocyanines

One of the most promising group of PS belonging to the second-generation are the phthalocyanines (PCs). Structurally, PCs are planar aromatic macrocycles formed by four isoindoline type units linked through nitrogen atoms (see figure 1.4) (86,88). The most common PSs of the PC family are the metallated-PC, which during the synthesis, a metal cation is introduced in the central cavity and closes the ring that forms the tetra macrocycle, and stabilizes the PC's chemical structure (79,86,88). In fact, the type of metal/metalloid cation can dictate PS's photophysical properties. Diamagnetic metal-containing PCs (Al^{3+}, Ga^{2+}, Zn^{2+}) exhibits higher and longer-lived triplet state- and singlet oxygen- quantum yields compared with paramagnetic metal-containing PCs (Co^{2+}, Cu^{2+}, Fe^{2+}) (28,86,88). In addition, PCs are highly chemically versatile compounds that allows the addition of functional groups to each isoindole structures, conferring desired solubilizing properties without entirely compromising their photodynamic capacities (28,86,88).

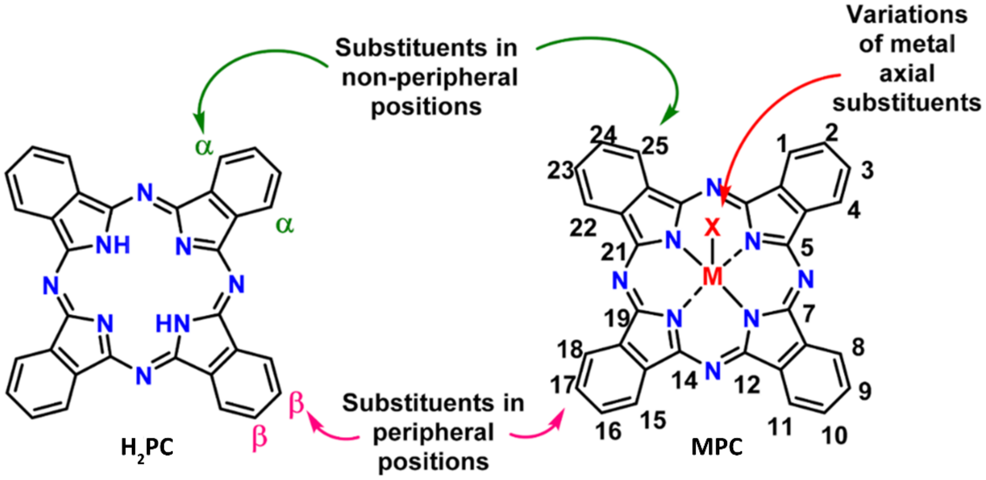

Figure 1.4 - General structure of metal-free phthalocyanine (left) and metallated phthalocyanine (right). Schematic representation of metallated and non-metallated phthalocyanines, with reference on their structural modulation sites (non-peripheral and peripheral positions), as well as the central cavity for metal insertion in metallated phthalocyanines. This figure was copied from (86) with the consent from the corresponding author.

Metallated-PCs have been highly studied for PDT oncological applications as they possess numerous advantages comparatively to other PSs of first and second generation. First, they are chemically versatile and stable, also relatively simple to synthesize and economically cheap to produce (28,86,88); Second, their near-IR Q-band maximum and superior molar absorptivity allows for higher light absorption at deeper tissue levels (28,89); Third, their lower absorption between 400 and 600 nm prevents from unfavorable spectral overlap with the sunlight, and therefore, lower the risk of skin phototoxicity (28,90) ; Fourth, their higher εmax in combination with greater triplet state- and singlet oxygen- quantum yields allows for lower PS administered concentrations necessary for equal or higher therapeutic responses (28,90); And fifth, metallated-PCs do not exhibit significant dark toxicity nor genotoxicity/mutagenicity (28,90,91). Although phthalocyanines and the majority of the second-generation of PS are generally activated at higher wavelengths (650–800 nm), and demonstrate fewer side effects comparatively with the prior generation of PS, their poor solubility in water makes them vulnerable candidates to intravenous administrations (28). Therefore, advances are being made to tackle their poor pharmacokinetic properties.

For the same reasons highlighted above, there have been so far four PCs derivatives in clinical trial for PDT application. CGP55847 is a liposomal formulation (palmitoyl-oleoyl-phosphatidylcholine and di-oleoyl phosphatidylserine) encapsulating ZnPC and investigated for use on squamous cell carcinoma of the upper aerodigestive tract (78,79,92). However, due to non-medical reasons, its clinical trials were discontinued (79). Photocyanine (trade name of Di-sulfonic-di-phthalimidomethyl phthalocyanine zinc di-potassium salt) is a PS candidate from China indicated for skin cancer and esophageal cancer (93). Pc4 is a silicon based PC in study for topical and intravenous administration, with great potential for breast, colon and ovarian cancers, and indicated in clinical trials for treatment of Non-melanoma skin cancer and cutaneous T-cell Non-Hodgkin Lymphoma (14,85). Last but not least, the only commercially approved PC so far is Photosens, a solution containing a mixture of sulfonated aluminum phthalocyanine varying between 1 to 4 sulfonated groups (14,94). It was approved in Russia in 2001 and commercialized by NIOPIK for treatment of a variety of cancers, including skin cancers, breast cancer, oropharyngeal cancer, lung cancer, bladder and cervical cancers (14,94).

1.3.3.2.1.1. Zinc- and aluminum- phthalocyanines

Zinc phthalocyanine (ZnPC) and aluminum phthalocyanine (AlPC) are typically excited at 674 and 680 nm, respectively, which is within the therapeutic range of light for clinical use allowing for deeper tissue penetration (28). Their molar extinction coefficients are substantially higher ($>10^5$ M^{-1} cm^{-1}) comparatively to other PS of first and second generation, meaning a more efficient photon absorption (28). Dimerization and aggregation of metallated-PCs such as ZnPC and AlPC was found to compromise their photophysical and photodynamic properties by reducing the ability of electron transfer reductions and singlet oxygen production (95). Hence, two main strategies aiming to enhance metallated-PCs hydrophilicity were mostly explored by researchers, which included: the introduction of strongly hydrophilic groups (sulfonic, carboxyl and phosphoric groups) in the peripheral and/or non-peripheral position of the isoindole rings ; and the utilization of drug delivery systems (addressed further in section 1.6.1).

A hydrophilic version of ZnPC and AlPC was studied by *Chan et al.* through the addition of sulfonated molecules to the isoindole groups, resulting in a variety of sulfonated Zn- and Al-PC (96). Despite the contradictory findings of *Chan et al* between the two different models using AlPC (*in vitro* and *in vivo*), the results obtained in BALB/c mice inoculated with Colo-26 tumors have shown a greater effect on tumor regression with higher degree of sulfonated groups, mainly due to the differences in hydrophilicity (AlPcS4 > AlPcS3 > AlPcS2 > AlPcS1) (97). Therefore, tetrasulfonated ZnPC and AlPC (ZnPCS4 and AlPCS4, respectively) remained fairly popular amongst all of the sulfonated versions mainly due to their high hydrophilicity. The lipo/hydrophilicity of a PS is not only crucial to determine its sub-cellular localization after uptake (*e.g.,* cell membrane, cytoplasm, organelles), but also to define the most predominant mode of cell death applied in post-PDT (*e.g.,* necrosis, apoptosis, autophagy). The difference in log P values (ZnPC = 8.50; AlPC = 8.91; ZnPCS4 = -1.70 and AlPCS4 = -

0.74) also dictates their pharmacokinetic profile (see Figure 2.1 for more details about these PS's photophysical and photochemical properties found in literature). Hydrophilic PSs have an increased bioavailability and distribution but lower cellular uptake and faster excretion rates. On the other hand, lipophilic PSs exhibits an higher affinity to cellular membranes, but they also tend to aggregate in aqueous solvents if not conjugated to a molecular vehicle (*e.g.*, albumin) or encapsulated in a water soluble drug carriers, for parenteral administration (96,97). An overview of the chemical structures and photophysical properties of ZnPC, AlPC, ZnPCS4, and AlPCS4 is shown in Figure 1.5.

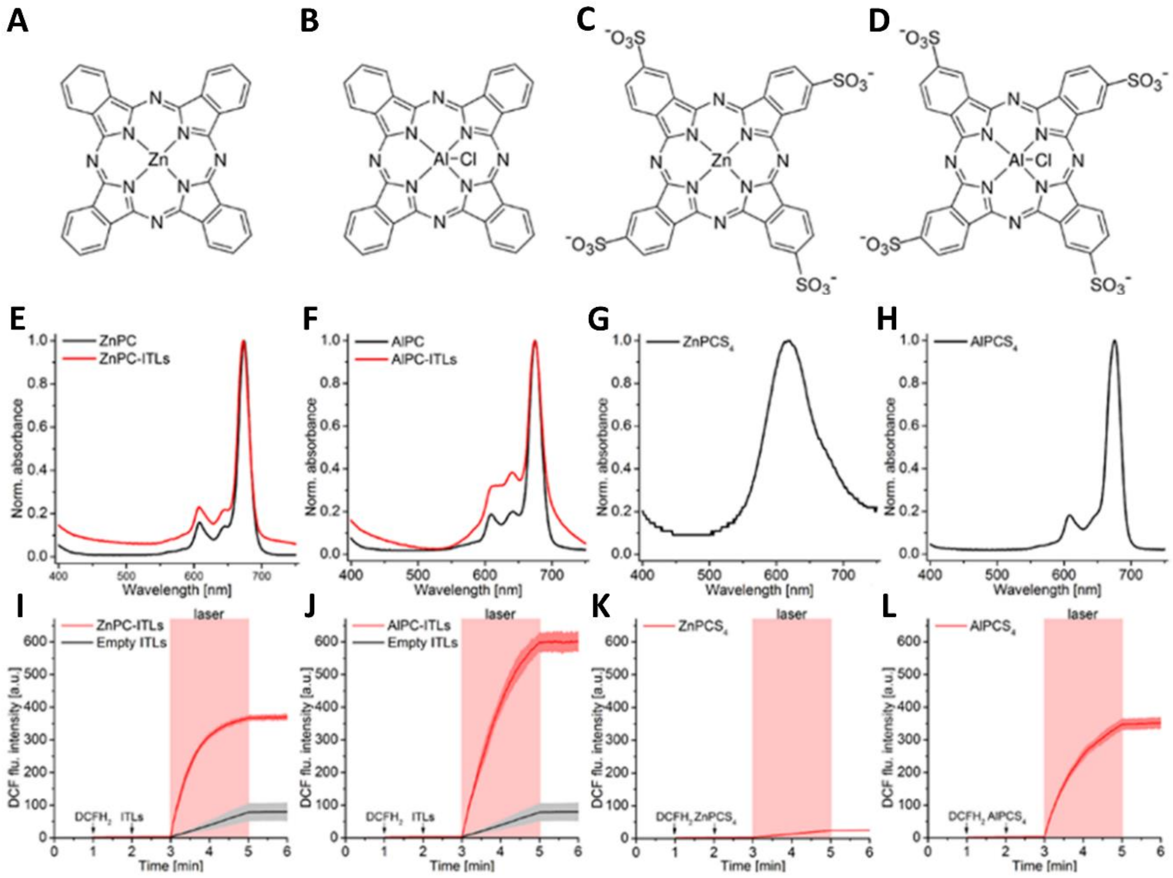

Figure 1.5 - Overview of the structural and photophysical properties of Zinc- and Aluminum-Phthalocyanine in comparison to their tetrasulfonated versions. The Chemical structures of ZnPC (**A**), AlPC (**B**), one of the possible isomers of tetrasulfonated ZnPC (ZnPCS4) and tetrasulfonated AlPC (AlPCS4) (**C** and **D**). The normalized absorption spectra are provided for: ZnPC/AlPC dissolved in pyridine and encapsulated in liposomes (ITLs) composed of DPPC:DSPE-PEG (96:4, molar ratio) at a ZnPC or AlPC:lipid ratio of 0.003 (**E and F**, respectively), and tetrasulfonated ZnPC (ZnPCS4)/ AlPC (AlPCS4) in MilliQ, both at a 1.5-mM final PS concentration (**G and H**, respectively). The ROS-generating capacity of ZnPC-ITLs (**I**), AlPC-ITLs (**J**), ZnPCS4 in physiological buffer (**K**), and AlPCS4 in physiological buffer (**L**) during PDT (pink area) was determined using the oxidation-sensitive fluorogenic probe 20,70-dichlorodihydrofluorescein ($DCFH_2$). This figure was adapted from (28) with the consent from the corresponding author.

1.3.4. Oxygen

Despite being sometimes neglected in the equation, O_2 plays an important role in the efficacy of PDT for cancer treatment. It is a crucial element in the formation of singlet oxygen and ROS upon PS photoactivation, from which most of the downstream disruptive events and PDT's biological effects would be reduced to minimum if O_2 would be missing (98). In addition, tumor's hypoxia resulting from insufficient vasculature translates in poor PS bioavailability in cancer cells, and therefore, an unsuccessful treatment (99). Since different type of tumors or even different regions within the tumor have various concentrations of O_2, PDT should be carefully considered, and its application adjusted to each clinical case.

To overcome the limitations of hypoxia in PDT, strategies to control O_2 levels shall be considered during the design of the protocol. For instances, to optimize the rate of generated ROS per bioavailable O_2, it is possible to monitor O_2 consumption by PDT relatively to its diffusion in targeted tissues (99,100). This can be accomplished by increasing the light exposure time for the same light dose, or through intermittent irradiation of the tumor (99,101). Another reported method was to increase tumor's oxygenation through hyperbaric oxygen therapy (99,102). However, the damage in tumor's vasculature occurring through the process of PDT reinforces the existing hypoxia environment, limiting the success of the therapy. Other methods are currently under investigation and predominantly involves the co-administration of a self-generating O_2 agent (*e.g.*, Manganese dioxide, H_2O_2-activatable catalase, perfluorocarbon) responsible to decompose and catalyse hydrogen peroxide (H_2O_2) in tumor's microenvironment into O_2 (100,103).

1.3.5. PDT dosimetry

PDT dosimetry takes part in the planning, monitorization and verification of the treatment, and describes the measurement of quantifiable parameters with the goal of improving the outcome of the therapy. There are currently three different approaches/methodologies considered in PDT dosimetry: direct dosimetry, explicit dosimetry and implicit dosimetry (104,105). Direct dosimetry measures the end product and principal responsible for PDT's outcome, which is meanly the generated singlet oxygen (106,107). Singlet oxygen can be detected through a technique called singlet oxygen luminescence, that relies on the transition of oxygen from the S1 to T0 states to detect its phosphorescence emission at 1270 nm (106). Despite of its importance in clinical PDT, singlet oxygen luminescence requires complex instrumentation and the signal-to-noise ratio often mislead the final results (104). The concept of implicit and explicit PDT dosimetry was first introduced by *Wilson et al.* in the 90s (108). In sum, explicit dosimetry refers to the individual measurement of well-defined quantifiable attributes that has direct influence/input in the therapy (*e.g.*, light fluence, PS concentration, and tissue oxygenation), whereas implicit dosimetry refers to the measurement of quantifiable parameters that are indirectly or implicitly correlated with the therapy (105,108). One of the most common examples of implicit dosimetry is the measurement of fluorescence photobleaching. Ground state PS molecules can be depleted during PDT via photobleaching through light treatment or oxidized by singlet oxygen. If we assume that PS depletion is due to oxidation by $^1O_2$, then the PDT dose can be measured implicitly by quantifying the PS depletion (107,109).

Explicit dosimetry is the most common PDT dosimetric approach used in clinical. It relies essentially on light, PS and oxygen dosimetry to create a PDT model/protocol. In conventional clinical settings, PDT dose was based on the administered PS dose, light fluence rate (mW/cm^2), the incident light dose (J/cm^2), and the DLI. Hence, the American Association of Physicists in Medicine have created the most commonly used guideline for clinical implementation of a photodynamic dose, defined as the number of photons (ph) absorbed by the PDT drug per gram (g) of tissue (ph/g) (110). However, this photodynamic dose does not consider the quantum yield (Φ) of oxidative radicals, the effect of oxygen on quantum yield, nor the fraction of radicals that oxidize critical sites (110). Under the scope of light dosimetry (explicit dosimetry), isotropic detectors are often used to measure light fluence directly, as it captures both incident and scattered light (105,111). Diffuse optical tomography has also shown promising results for determining 3-dimension distribution of optical properties, however, it has a limited tissue penetration depth of approximately 10 cm (105,112,113). In PS dosimetry (explicit dosimetry), PS concentration is often determined through biopsy sampling of the tissue and PS extraction for quantification using spectrophotometric assays. However, newer methods use fluorescence-based assays to directly measure the fluorescence or absorption of PS *in situ*, through optical fibres (105,114,115). Last but not least, oxygen dosimetry (explicit dosimetry) uses the polarographic Clark-type needle electrode as the standard tool for measuring partial oxygen pressure in tissue (114,116). This method is based on the electrochemical reduction of $^3O_2$ to generate a measurable electric current proportional to the concentration of $^3O_2$ around the probe (114). However, it is an invasive method, it consumes oxygen, and multiple punctures are needed to spatially map the partial oxygen pressure across the tumor (114). Optical measurement of $^3O_2$ is seen as the most attractive and less invasive alternative, and are often based on time-resolved measurement of the phosphor lifetime or ratiometric intensity (117). Another alternative is the tomographic assessment of oxygen by magnetic resonance imaging and positron emission tomography, but spatial resolution is limited for such a large and expensive imaging tool (104,105,107,118).

Biophysical/biological tissue response monitoring can also be used as a dosimetric method to monitor vascular shut-down, treatment-induced necrosis, and blood flow monitoring through laser Doppler or diffuse correlation spectroscopy (107). Guided ultrasound photoacoustic imaging and non-invasive tumor blood flow monitoring during treatment have also been reported to predict PDT's outcome in *in vivo* settings (107,119). Nevertheless, two or more of the above mentioned methodologies can be incorporated simultaneously in a PDT protocol, and PDT dosimetry should ideally be based on a plurality of methodologies rather than a single approach.

1.4. Biological effects of PDT

The therapeutic outcome of PDT is mainly determined by cellular and biochemical mechanisms originated from the oxidative damage produced by PS photoactivation. Crucial key initial factors for PDT's outcome are PS biodistribution at tumor's microenvironment, intracellular uptake, and subcellular localization (28). Since ROS produced by PDT have relatively short lifetime and limited diffusion, the extent of damage and consequential biological effects will depend largely on PS localization, in the moment of light activation (28,120). PS localized at tumor's vascular endothelial cells will therefore cause damage at tumor's vasculature, while PS at cancer cells will be directly responsible for tumor's cells death. Hence, a local inflammation is produced by PS activity in tumor and local oxidative stress, which leads to a PDT-mediated immunologic response pledged to reinforce and enhance the primary attack against cancer cells (see Figure 1.6 for an illustrative overview of the photophysical and biological mechanisms participating in PDT) (28,121).

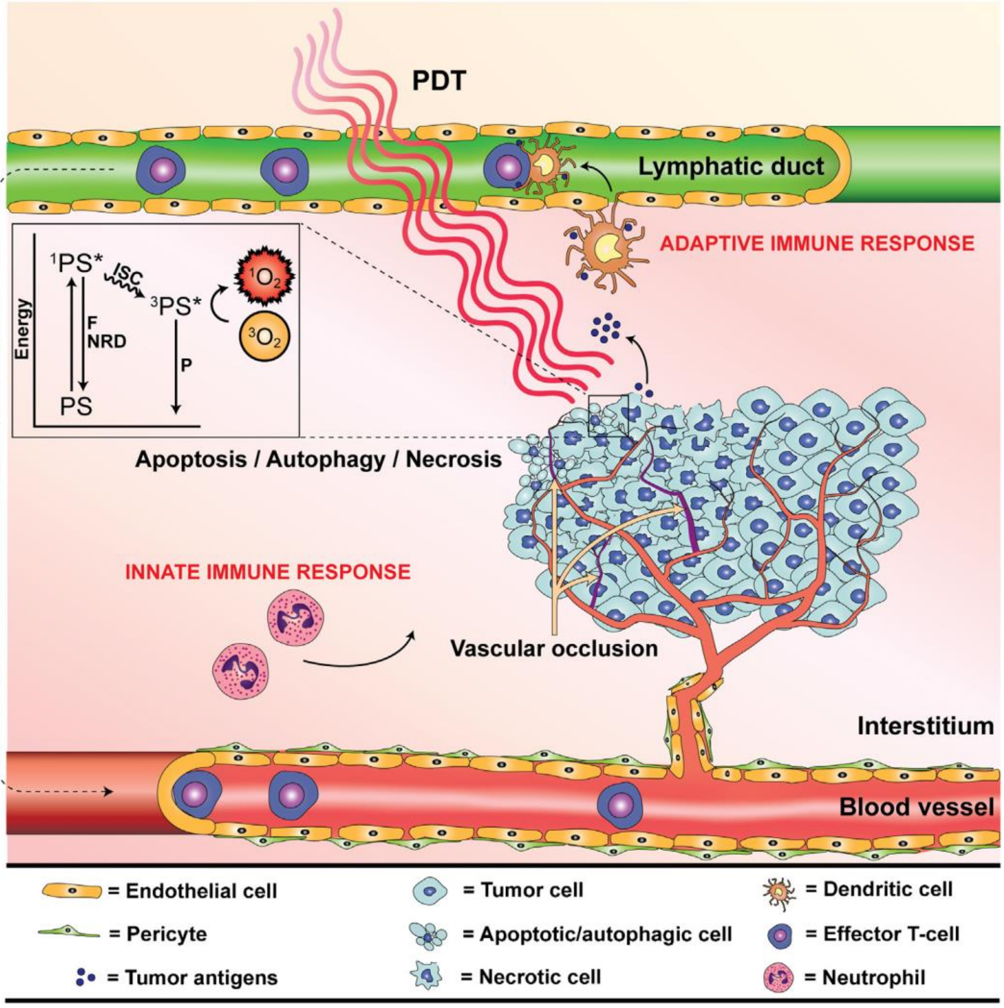

Figure 1.6 - Representation of the photophysical and biological mechanisms in photodynamic therapy (PDT). After the accumulation of the photosensitizer (PS) in tumor, PS molecules are activated by light (laser) of a specific wavelength that consequentially triggers the process of photosensitization. The generation of singlet oxygen and its ROS derivatives leads to tumor cell death (via apoptosis, autophagy and/or necrosis), to intratumoral vascular occlusion, and an anti-tumor immune response (via the innate as well as the adaptive immune system). Abbreviations: ground state photosensitizer (PS), excited singlet state photosensitizer (1PS*), fluorescence (F), intersystem crossing (ISC), excited triplet state photosensitizer (3PS*), and phosphorescence (P). This figure was copied from (28) with the consent from the corresponding author.

1.4.1. Cellular uptake and intracellular distribution of PS

Cellular uptake and subcellular localization of PS dependents on several parameters: 1) the degree of lipophilicity (122); 2) the chemical structure, type and number of neutral/charged interactive groups, and degree of molecular asymmetry (123); 3) the binding with macromolecules, including low-density lipoproteins and albumin (28,31,32); 4) the extent of aggregates formed in aqueous solvents (28,29); and 5) the capability of undergoing endocytosis (*e.g.,* pinocytocis and phagocytosis) by cancer cells or tumor-associated macrophages, either through caveolae and/or clathrin-dependent mechanisms (30,124).

Upon cellular internalization, either by diffusion or via endocytic pathways, PS is translocated to distinct intracellular loci according to its ionic charge, log P value and amphiphilicity (122). Its intracellular localization can be temporary though, since PS is in constant dynamic after the initial entry (28). Anionic PSs typically end up in lysosomes, whereas cationic PSs are driven towards the mitochondria (28,125). While hydrophilic PSs tend to localize in lysosomes, lipophilic PSs are preferentially retained in the plasma membrane and intracellular membranes (*e.g.*, mitochondrial and endoplasmic reticulum membrane)(28,126–128). It is not commonly reported to find PS localized in the cell nucleus, which conveniently reduces the risk of deoxyribonucleic acid (DNA) mutations induced by PDT, and that are often associated with chemo- or radio- therapy (129). In PDT, it is of great importance to investigate the spatiotemporal dynamics of PSs following cellular uptake, as it gives a comprehensive understanding of the cell death mode and pathways undertaken by cancer cells upon photoactivation. However, it is natural that PS often targets more than one cellular location, resulting in concomitant activation of different cell death pathways, and consequentially, limiting the efficacy of activated cell survival mechanisms and stress responses after PDT (28).

1.4.2. PDT mediated cell death

Intracellular PS concentration, fluence rate, extent of ROS generation and the degree of oxidative damage, are some of the most important factors dictating cell's response to PDT. However, PSs subcellular location upon PDT is one of the most utilized parameters to distinguish the different cell death pathways triggered after treatment (130). In addition to intracellular PS localization, PDT-mediated cytotoxicity can vary between different cell lines, intracellular PS concentration, light dose, bioavailable oxygen, and residual energy status governing the eventual mode of cell death (28).

In PDT, there are three predominant main mode of cell death that can be distinguished: apoptosis, necrosis, and autophagy. Irradiation of plasma membrane-localized PS may induce necrosis-like cell death that is preceded by loss of plasma membrane integrity due to peroxidation of unsaturated phospholipids (131). In contrast, irradiation of PS localized in cytoplasm may lead to cell death characterized by cell shrinkage with intact plasma membrane and cytoplasmic vacuole formation (132). Lysosome-targeted PSs may induce ROS-triggered cell death via leakage of cathepsins from lysosomes, in result of lipid peroxidation-mediated lysosome rupture (133–135). The released cathepsins from lysosomes will exhibit proteolytic activity in the intracellular matrix and cleave BH3 interacting-domain death agonist (BID) to form truncated-BID (t-BID), which ultimately culminates in apoptosis (133–135). Similarly, PS localized in the endoplasmic reticulum (ER) is believed to be responsible for the release of Ca^{2+} as well as unfolded/misfolded proteins into the cytosol, culminating in the activation of caspase-mediated apoptosis (136–138). In this case, apoptosis is initiated by the translocation of the released Ca^{2+} from ER to the mitochondria, leading to the formation of the apoptogen and to the loss of mitochondrial membrane potential (136–138). PDT-induced mitochondrial lipid peroxidation has been demonstrated to release pro-apoptotic factors responsible for apoptosis when residual ATP levels are high enough to facilitate this energy-dependent mode of cell death (139–141). Lastly, PDT-mediated cell death by PS localized in the Golgi apparatus can lead to organelle fragmentation as a sign of early apoptotic events (142,143), and is also capable of inducing apoptosis via a calcium-dependent pathway that did not involve mitochondria (144).

For all the different responses to PDT with PS in various subcellular compartments, an oxidative damage threshold is what generally governs the fate of a cell. When the oxidative damage threshold is crossed and the level of damage exceeds the restorative capacity by survival mechanisms, cells will typically undergo a cell death program (28). Autophagy generally constitutes a cytoprotective mechanism through which cells recycle damaged and degraded organelles. Under lower PS dosages, PDT is able to induce pro-survival autophagy, whereas both autophagic cell death and apoptosis are induced at higher dosages of either PS at equal radiant exposure (145–147). Despite being responsible for a much lower number of cell death reported after PDT treatment compared with apoptosis or necrosis, autophagy can still occur with PS in different intracellular locations.

1.4.3. Intratumoral vascular damage

Intratumoral vasculature plays an important role in tumor sustenance and progression, by providing cancer's cells with oxygen and nutrients. For PDT, tumor's vasculature can be the primary delivery route for PS to reach the cancer cells. Therefore, the application of PDT not only leads to cancer's cells death, but also to the destruction of tumor's microvasculature, culminating in a local anoxic/hypoxic and malnourished environment for tumor's growth (28,148).

Blood vessels constitute an ideal target for PDT since physiological abundance of the radical nitric oxide and oxygen corresponds to exacerbated ROS production upon PS excitation (28). Depending on PS, the effects of PDT in tumor's vasculature are associated with an increase in platelet activation, thromboxane release, leukocyte adhesion, platelet aggregation and thrombus formation (28,149–151). Furthermore, thrombus are efficient chemo attractants for cells belonging to the innate immune systems (*e.g.*, neutrophils and macrophages) (28,150,151) . Once activated by local thrombus, immune cells can release cytokines and chemokines to attract additional immune cells to the thrombostatic situ, triggering a pro-inflammatory signaling that leads to an anti-tumor immune response and removal of PDT-afflicted tissue (28,150,151).

In practical terms however, PDT protocols in favor of tumor's vasculature photodamage require an iv administration of PS with a short DLI, to guarantee that tumor's irradiation is performed when highest PS concentration is still in the intratumoral vascular cells. This means that the optimal destruction of tumor's vasculature is at the expenses of direct PDT-induced cancer's cells death.

1.4.4. Immunogenic response

The effects of PDT were once considered straight forward and localized, being mostly determined by the photoactivation of PS in tumor. However, a deeper understanding of the field and about post-PDT events, have revealed a secondary and equally important mechanism for cancer treatment, the intervention of an anti-tumor immune response. PDT-induced anti-tumor immune response is essentially initiated by a sterile inflammatory response promoted by the release/exposure of damage-associated molecular patterns (DAMPs) (28,152). There are different types of DAMPs, depending on their original intracellular structures or chosen mode of cell death, and it can include heat shock proteins (HSP), calreticulin (CRT), adenosine triphosphate (ATP) or other molecules such as tumor necrosis factor-α (TNF-α), interleukin-1β (IL-1β) or interleukin-6 (IL-6), macrophage inflammatory proteins 1 and 2 (MIP-1 and MIP-2), amongst others (28). DAMPs are therefore responsible for initiating and augmenting the pro-inflammatory response, and attract the host innate immune cells, such as neutrophils, mast cells, macrophages, and dendritic cells (DC), to restore homeostasis in the affected region (152–154). They promote the phagocytosis of damaged cells and cell debris in the targeted tissue, and are responsible for the subsequent activation of the adaptive immune system (152–154).

The maturation of DCs by DAMPs, and their ability to present tumor's associated antigens on their extracellular membrane, initiates the process of specific antitumor immunity (28,152–154). Once DCs in lymph nodes exposes tumor's antigens to CD4+ T cells, the chain of reaction is initiated for the stimulation of CD8+ cytotoxic T lymphocytes (28,152–154). The CD8+ cytotoxic T lymphocytes instead, will acquire the ability to recognize and specifically destroy cancer cells in tumor and circulation throughout the body, ensuring a systemic anti-tumor immune response (28,152–154). Since PDT may not affect equally all cancer cells in tumor, this systemic anti-tumor immunity acquired from post-PDT events is crucial to guarantee long-term PDT efficacy, complementing the damaging effects from ROS alone in tumor cells (28). A more detailed representation of the main mechanisms involved in the activation of the immune system after PDT is illustrated in Figure 1.7.

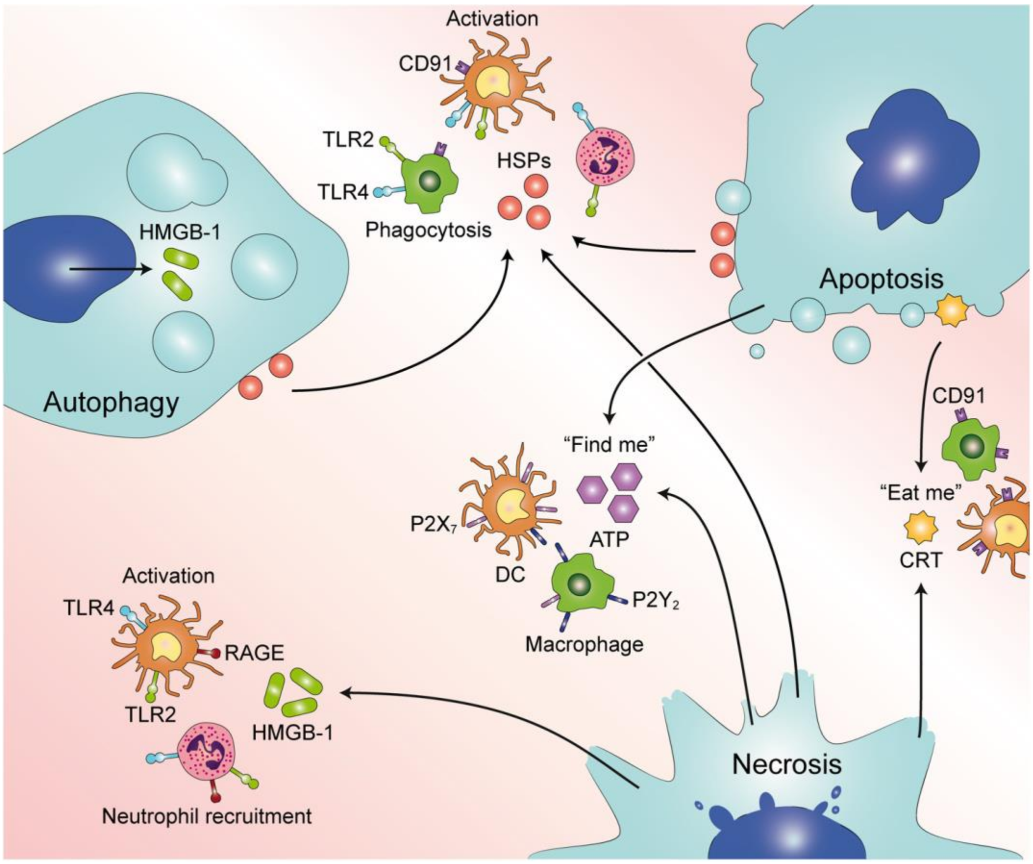

Figure 1.7 - Representation of the main mechanisms involved in the activation of the immune system after photodynamic therapy (PDT). After PDT, apoptotic cells, necrotic and autophagic cells expose and/or release heat shock protein 60 (HSP60) and HSP70 to the extracellular matrix. HSPs instead, interacts with immune cells via Toll-like receptor 2 (TLR2), TLR4, and CD91, which leads to immune cell activation. In addition, apoptotic and necrotic cells express and/or release calreticulin (CRT) and adenosine triphosphate (ATP), resulting in dendritic cells (DC) and macrophage cells activation via CD91 (for CRT) and/or via interaction with the P2Y2 and P2X7 receptor (for ATP). Necrosis is accompanied by the release of high mobility group box-1 (HMGB-1), culminating in DC activation and neutrophil recruitment via TLR2, TLR4, and receptor for advanced glycation end products (RAGE). In addition, HMGB-1 may act as an important regulator of autophagic cell death when in response to oxidative stresses. This figure was copied from (28) with the consent from the corresponding author.

1.5. PDT main drawbacks

Despite the numerous advantages of PDT application in oncology, there are still some pitfalls to consider before choosing PDT as the main treatment option. In fact, the significant burden on patients has led several treatment centers to abandon PDT as a treatment option for terminal cancer patients due to ethical considerations (28,155). PDT is mostly applicable for light-reachable cancer's in non-metastatic phases, that meet a certain criteria in terms of location and cell density, so that light can travel uniformly through all the tumor cells for PS's activation and PDT's downstream effects occurring (54). However, most of PDT's drawbacks do not come from the technique/methodology itself but from PS or tumor's biology, and are mainly related to PS's suboptimal spectral properties, route of administration associated with unfavorable pharmacokinetics, and triggered survival pathways in cancer cells after PDT (156–159). Although the second-generation of photosensitizers have brought a major improvement in the field, their high lipophilicity and impaired pharmacokinetic properties are still a concern (28). Same happens with the survival mechanisms that cancer cells undergo once experiencing oxidative stress (156–159).

1.5.1. Skin phototoxicity

Skin photosensitivity and other light-sensitivity reactions have been identified as the most significant adverse effects from PDT. Essentially, it has to do with the accumulation and retention of some PS in the skin of PDT's patients after treatment (91,160). Their exposure to sunlight or strong artificial light can trigger photodynamic reactions to PS remained in skin or other light exposed areas (*e.g.,* eyes), causing skin lesions (burns, erythema, crusting) or visual disturbances (91,160). Therefore, patients must avoid direct sunlight exposure for several weeks after treatment, until PS levels in skin are reduced and the risk of skin phototoxicity is minimized (49,74). A test to verify skin sensitivity is performed generally 30 days after treatment, with a 10 min exposure of the hand in direct sunlight/strong indoor light. If symptoms such as red marks, swelling or blisters are found after test, patients should remain in dark conditions for at least 2 additional weeks (49,74). It has been reported that PDT treatments using porfimer sodium (Photofrin) might induce to skin photosensitivity for a period that can last between 4 and 12 weeks (49,74,91). Despite the benefits of the therapy, it is believed that the risks for photosensitivity were responsible for the redrawing of therapy, either by patients or by doctors (28,155).

1.5.2. Mechanisms of resistance

Drug resistance is a major obstacle found in cancer therapy that is common to many types of treatment, such as chemotherapy, radiotherapy and it also includes PDT. It is often seen tumor cells that are less vulnerable to cytotoxic drugs, either due to reduced uptake or increased drug efflux, but also derived from the activation of cell survival mechanisms. As previously stated, the mechanism of autophagy is either a controlled mode of cell death or a repairing mechanism that allows cancer cells to recycle oxidative-damaged organelles and survive from the PDT-mediated cell damages (145,147).

One of the mechanisms generally associated with multi-drug resistance (MDR) is the active transport of a large class of hydrophobic PS from the cytoplasm to the extracellular medium (efflux), mediated by membrane transporters known as ATP-binding cassettes (159,161,162). Intracellular antioxidants such as glutathione (GSH) and haeme oxygenase-1 (HO-1), also play an important role against the oxidative stress originated from PDT, and often represent a primary line of defense (159,163,164). Basically, GSH reduces free radicals by being oxidized to glutathione dissulfide, and is reduced back do GSH by glutathione reductase, using nicotinamide adenine dinucleotide phosphate (NADPH) as the electron donor (159,164). HO-1 is an enzyme that under stress conditions can scavenge ROS, reducing PDT efficacy and promoting cell death recovery (159,163). The therapeutic failure may vary between PS and tumor's cells phenotype/genotype, with different abilities to manage and survive from oxidative challenges. The most known survival pathways are mediated by transcription factors such as activator protein-1 (AP-1), nuclear E2-related factor 2 (NRF2), hypoxia-inducible factor 1 (HIF-1), and nuclear factor κB (NF-κB) (156–159). These transcription factors and kinases facilitate the survival of cancer cells from various circumstances, such as a disrupted redox balance, low oxygen availability, apoptotic/autophagic signaling, and oxidative damage to proteins (156–159). Illustrated in Figure 1.8 are the main survival pathways involved in tumor cells after PDT, as well as the main responses triggered after each signaling pathways.

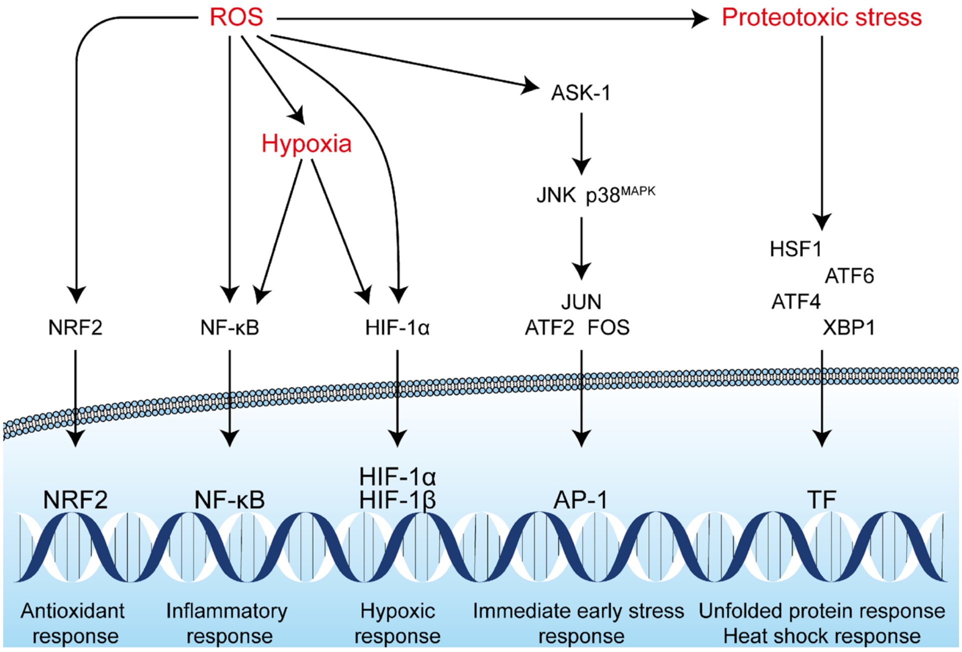

Figure 1.8 - Representation of the main survival pathways involved in tumor cells after photodynamic therapy (PDT). The activation of cell survival pathways in cancer cells is mainly initiated by reactive oxygen species (ROS), originated from post-PDT. ROS directly can trigger the NRF2-mediated antioxidant response and the ASK1-induced immediate early stress response. The hypoxia and proteotoxic stresses originated from the vascular shutdown and the oxidation of proteins, are both involved in the activation of the NF-κB inflammatory response and the HIF-1 hypoxic response. In addition, proteotoxic stresses may lead to the activation of several transcription factors (TF), including HSF1, ATF4, ATF6, and XBP1, that are responsible for the unfolded protein response and heat shock responses. This figure was copied from (159) with the consent from the corresponding author.

1.6. Recent developments

The use of PDT for oncological treatment has advanced slowly into clinical practice, and it might be due to lack of ideally attributes from PS (*e.g.*, first generation of PS), the complexity in treatment protocol optimization, and the technological resources required for clinical application (156–159). However, progress have been made in the field through the time being, and researchers are bringing more innovation, aiming to make PDT a more attractive and safe therapy (165,166).

Advances have been made in different elements involved in the PDT process throughout the time. For instances, efforts to circumvent the difficulties of light delivery have been challenged by using optical fibers through endoscopy or vascular catheterization, and deliver light to previously inaccessible regions of the body (167–169). Interstitial-PDT (iPDT) is also a major improvement in PDT's light delivery, which consists in the image-guided insertion of one or more optical fibers into the tumor's bulk, to deliver the appropriate light dose to cancer cells (167–169). Two-photon PDT is also an active research strategy aiming to increase the effective depth of PDT treatment through the absorption of two photons simultaneously by single PS (170–172). The two-photon absorption by PS would allow the use of light with wavelength above 800 nm, and still overcome the energy threshold necessary for photodynamic reaction (170–172).

Progresses were not only made towards technical improvements of light delivery, but concerning the overall knowledge of the therapy as well, such as involved mechanisms and responses concerning PDT and PDT's resistance (158,159). However, most of the research lines have been focused on strategies to overcome poor pharmacokinetics or photochemical properties, with the solo aim of improving PDT's efficacy. Some of these strategies were able to combine PDT with drug delivery systems of improved selectivity towards cancer cells or other targets in tumor's microenvironment (24,28,173,174).

1.6.1. Drug delivery systems for PDT

Target-delivered therapy have always been a desired and distinguished feature of treatments applied in oncology. Unspecific uptake of chemotherapeutics can lead to undesired secondary effects that threaten patient's life-quality and wellbeing (166). Consequently, drug delivery systems encapsulating chemotherapeutics offers a better solution compared with their non-encapsulated versions, showing improved solubility and delivery to the tumor, at enhanced therapeutic efficacy and reduced side effects (28,175). In PDT, the use of delivery systems to vehicle PS towards cancer cells was considerate a major development that nowadays it is identified as third generation of PS (28).

A suitable carrier for PDT use should always consider the following essential prerequisite: First, ROS generation must not be suppressed by the carrier (176,177). Second, dark toxicity shall be reduced or maintained when compared with PS alone (176,177). Third, the nanocarrier must improve PS's bioavailability and biodistribution upon administration, which can include targeting of cancer cells and/or controlled release of PS (178,179).

Delivery systems are primary organized into two different categories, according to their main composition: inorganic or organic nanoparticles. Inorganic nanoparticles are structurally described as spheres, shells or nanotubes of different types (ceramic/silica, quantum dots, magnetic, metallic and carbon based nanoparticles), while organic nanocarriers can be further distinguished between lipid-based (such as liposomes, micelles) and non-lipid-based delivery systems (28,173,174). Both types of delivery systems have distinguished physico-chemical attributes that makes them more or less suitable for PS delivery. In addition, nanocarriers are also categorized between active or passive tumor targeting, if includes or not specific targeting moieties (such as antibodies, peptides or aptamers) (176,177).

Lipid-based delivery systems are water-compatible vehicles for the encapsulation of hydrophobic PSs, and it typically includes low-density lipoproteins (LDL), micelles, liposomes and solid lipid nanoparticles (28). LDLs are endogenous particles meant to transport lipophilic biomolecules (*e.g.*, cholesterol) through the bloodstream until reaching the cells, and are mainly composed of cholesterol, phospholipids, triglycerides, and apolipoproteins (180,181). Micelles are described as small-diameter particles composed of a phospholipid monolayer, with the hydrophilic head groups positioned at the water interface (182–184). Solid lipid nanoparticles are mostly defined by their solid lipid core stabilized by a surfactant (185). Apart from LDLs, lipid-based delivery systems are versatile, have enhance circulation half-life (through PEGylation), and can conjugate with target-specific ligands (28). The liposomes are going to be further discussed in section 1.6.1.1.

In contrast, non-lipid-based nanoparticles refers mostly to proteins/peptides (albumin, lactoferrin, gelatin, collagen) or polymers (glycerol, dendrimers, cyclodextrins) (28,176,177). Dendrimers are supramolecular assemblies composed of branched polyaminoamides that can be synthesized in a controlled manner with a high monodispersity, but very laborious when compared to other delivery systems (186,187). Polymeric micelles are nanoparticles composed of amphiphilic polymers, including PEG-based phospholipid conjugates and poloxamers (188,189). Despite their high structural stability and low toxicity, the development of polymeric micelles is often associated with technical difficulties linked with their synthesis and inefficient drug incorporation methods (188,189). In contrast, gold nanoparticles and quantum dots are nano- particles with unique physico-chemical and optical properties, respectively (190–193). Gold nanoparticles have adjustable excitation wavelength to wavelengths in the far red, while Quantum dots are semiconductor nanocrystals that function as light acceptors for subsequent PS activation (188,189). Despite gold nanoparticles and quantum dots are considered appealing for PDT use, their potential toxicity can limit clinical application (188,189). In Table 1.2 is displayed an overview of lipid- and non-lipid-based nanoparticles that have been used for the delivery of PSs as well as the most relevant advantages and disadvantages per each type of carrier.

Table 1.2 - List of lipid-based and non-lipid-based nanoparticles used in photodynamic therapy for the delivery of photosensitizers.

Type	Size	Advantages	Disadvantages
Lipid-based delivery systems			
Liposomes	15-1000 nm	-Versatility (hydrophilic and hydrophobic carrier) -Non-toxic and similar to the cell membrane -High payload	-Stability -Short shelf-life
Low-density lipoprotein	18-25 nm	-Endogenous carrier -Protects the drugs -Circulation time	-Specificity -Requires over expression of low-density lipoprotein receptors
Micelles	2-20 nm	-Synthesis -Shelf-life -Low viscosity	-Low solubilization -Potential surfactant toxicity
Solid lipid nanoparticles	50-1000 nm	-Easy to scale-up -Water-based technology -Biocompatibility	-Particle growth/aggregation -Drug loading capacity
Non lipid-based delivery systems			
Dendrimers	1-100 nm	-Versatility (hydrophilic and hydrophobic carrier) -Monodispersity -High payload	-Lack of *in vivo* data -Laborious preparation
Gold nanoparticles	1-100 nm	-Versatility (hydrophilic and hydrophobic carrier) -Physico-chemical properties of gold -Synthesis	-Potential toxicity -Costs
Polymeric micelles	10-100 nm	-Versatility (hydrophilic and hydrophobic carrier) -Structural stability -Low toxicity	-Synthesis -No universal incorporation method
Polymeric nanoparticles	10-1000 nm	-Versatility (hydrophilic and hydrophobic carrier) -Biocompatibility -Synthesis	-Stability -encapsulation efficiency
Quantum dots	2-100 nm	-Versatility (hydrophilic and hydrophobic carrier) -Unique optical properties -Tunable surface properties	-Potential toxicity -Reduced biocompatibility

This table was copied from (28) with the consent from the corresponding author, and it utilized the following references: (173,178–194)

1.6.1.1. Liposomes

Liposomes are sphere-shaped artificial vesicles made essentially of cholesterol and other natural and nontoxic phospholipids, positioned structurally into one or more phospholipid bilayers (92,195–197). The classification of liposomes can be based on different criteria, such as: size (small liposomes are usually between 30–70 nm diameter and large liposomes have a diameter >100 µm); lamellarity (unilamellar and multilamellar); method of preparation (reversed-phase evaporation, extrusion method, and by dehydration-rehydration method); and surface composition/modification strategies (conventional liposomes, PEGylated liposomes, cationic/anionic liposomes, ligand-targeted liposomes and multifunctional liposomes)(28,195,196).

For PDT oncological applications, liposomes can also be classified based on their tumor's targeting strategies into: interstitially-targeted liposomes (ITLs), endothelial-targeted liposomes (ETLs) and tumor-targeted liposomes (TTLs) (see Figure 1.9) (28). Actively targeted liposomes, such as TTLs, are typically antibody- or ligand- modified liposomes aiming to enhance the accumulation and retention in tumor through target binding, resulting in increased PDT effects and minimized side-effects related to non-specific PS accumulation (28,198). Since intratumoral vasculature plays an important role in tumor's sustenance and progression, tumor's blood vessels also constitute an ideal target for PDT (199,200). Cationic liposomes, otherwise known as ETLs, are partly composed of phospholipids with positively charged head groups that electrostatically associate with the negatively charged glycocalyx of inflamed or angiogenic endothelial cells (28,199,200). The role and principles of ITLs are going to be further discussed in section 1.6.1.1.1. In addition, liposomes for PDT application were designed with triggered release mechanisms that prevents PS release at immediate environment, guaranteeing its release at site upon specific stimulus (28,201,202). Thus, PS can adequately migrate to specific intracellular targets or to associate with cells, ensuring maximum killing effects of short-lived generated ROS. The most reported strategies include thermo-sensitive liposomes (temperature) (203,204), Fusogenic liposomes (fusogenic viral proteins coupled to their membrane surface) (195,205); and pH-sensitive (206,207).

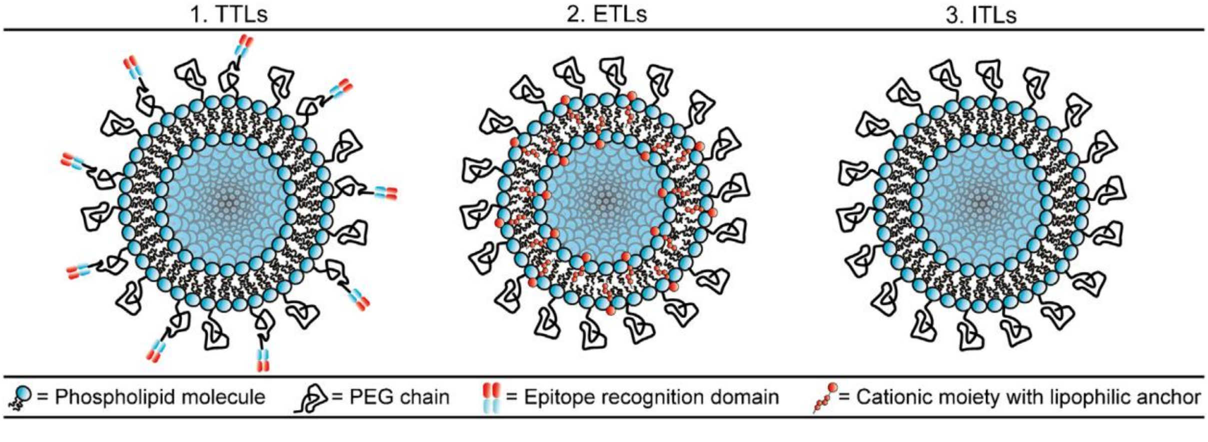

Figure 1.9 - Illustration of the three main type of liposomes classified based on tumor targeting strategies. In 1) it is represented the Tumor cell-targeting liposomes (TTLs), containing specific epitope recognition domains (for example antibodies, nanobodies, or peptides) that are conjugated to an anchor molecule such as a modified polyethylene glycol (PEG) chain. In 2) are Endothelial cell-targeting liposomes (ETLs), cationic liposomes with strong affinity for the negatively charged tumor endothelium. Last but not least, in 3) are the Interstitially-targeted liposomes (ITLs), which are passively accumulate in the tumor interstitium due to the enhanced permeability and retention (EPR) effect and poor lymphatic drainage in solid tumors. This figure was copied from (28), with the consent from the corresponding author.

In regards to PDT, liposomal encapsulation of PS is beneficial when considering several aspects: 1) liposomes can encapsulate both hydrophilic and lipophilic molecules in aqueous media, and therefore, capable of transport highly lipophilic PS through the bloodstream (208,209); 2) the risk of PS aggregation in biological fluids, which impacts ROS formation, is reduced by means of liposomal encapsulation (208,209); 3) considering their high payload, a single liposome delivers much higher concentration of PS, achieving in theory a lethal oxidative stress at very low liposomal concentrations (28,195,196). For this same reason, liposomal encapsulation is deemed to minimize PS accumulation in the skin, which not only reduces phototoxicity but also improves PS bioavailability in tumor (28,196,210); 4) liposomes are capable of co-encapsulating additional pharmacological compounds in a single delivery system, thus improving the therapeutic efficacy with no additional toxicity when composed of neutral phospholipids (28,211,212); And 5), their versatility in terms of membrane composition allows for the functionalization of liposomes and further implementation into different targeting strategies (213–215).

1.6.1.1.1. Interstitially-targeted liposomes

Tumor's interstitium is essentially rich of tumor-associated fibroblasts and immune cells (macrophages) that continuously remodels the stroma (extracellular matrix), promoting neovascularization and cancer cells invasion/migration (216–218). Hence, tumor's interstitium constitutes an important target for PDT as its considerable damage may include two important mechanisms: the oxidation of cell membranes (specially cancer cells) in the tumor's microenvironment, and the activation of immune cells through cellular constituents or oxidized extracellular biomolecules that are taken up by the immune cells following PDT (28,216–219).

The targeting abilities of ITLs are mainly attributed to its composition. ITLs are liposomes generally composed of neutral (zwitterionic) phospholipids (such as phosphatidylcholines) and polyethylene glycol (PEG) lipids (4–6%), for steric stabilization and to impart stealth properties (210,213,220). The inclusion of lipids with PEG-headgroups is known to prolong the half-life circulation time of liposomes, due to repulsive interactions between PEG-grafted membranes and blood constituents (210,213,220). Therefore, the retention of ITLs in the tumor's interstitium can proceed passively via the EPR effect (27,28). The size of the ITLs plays an important role to contemplate the EPR effect *in vivo*, as liposomes with diameter greater than 200 nm will not easily extravasate the tumor's vasculature, but on the other end ITLs smaller than 160 nm would be heavily taken up by the liver (28,195,221). According to *Wu et al.* (222), sterically stabilized liposomes were more rapidly accumulated (3–4 fold more) in the interstitial compartment of xenografted rats with breast adenocarcinomas

(R3230Ac), compared to non-PEGylated versions. Alternatively, LDL can serve as an additional vehicle for the transfer of lipophilic PSs from the ITLs to the tumor cells, leading to tumor-specific accumulation (28,223).

With respect to PDT studies using ITLs, our PDT group led by Prof. Dr. Michal Heger has successfully demonstrated that ITLs composed of DPPC:cholesterol:DSPE-PEG and a ZnPC:lipid ratio of 0.003 exhibited no dark toxicity, but became cytotoxic upon irradiation of extrahepatic cholangiocarcinoma (Sk-Cha-1) cells in a lipid concentration-dependent manner (28,129,158,197). Our group also demonstrated that neither the photophysical properties of PS nor their ROS generating capabilities were compromised through the encapsulation in ITLs, and ZnPC-ITLs with ZnPC:lipid ratios higher than 0.003 did not produce ROS more extensively nor induced more protein oxidation (as demonstrated in **I-L** from Figure 1.5, and in Figure 1.10) (28,197). It was observed as well that PDT with ZnPC-ITLs was able to induce both, apoptosis and necrosis in PDT treated Sk-Cha-1 cells, with necrosis being the most predominant mode of cell death (28,197). Furthermore, the use of PEGylated liposomes such as ITLs has been associated with enhanced therapeutic efficacy in the PDT field when compared to non-PEGylated equivalents (28,197).

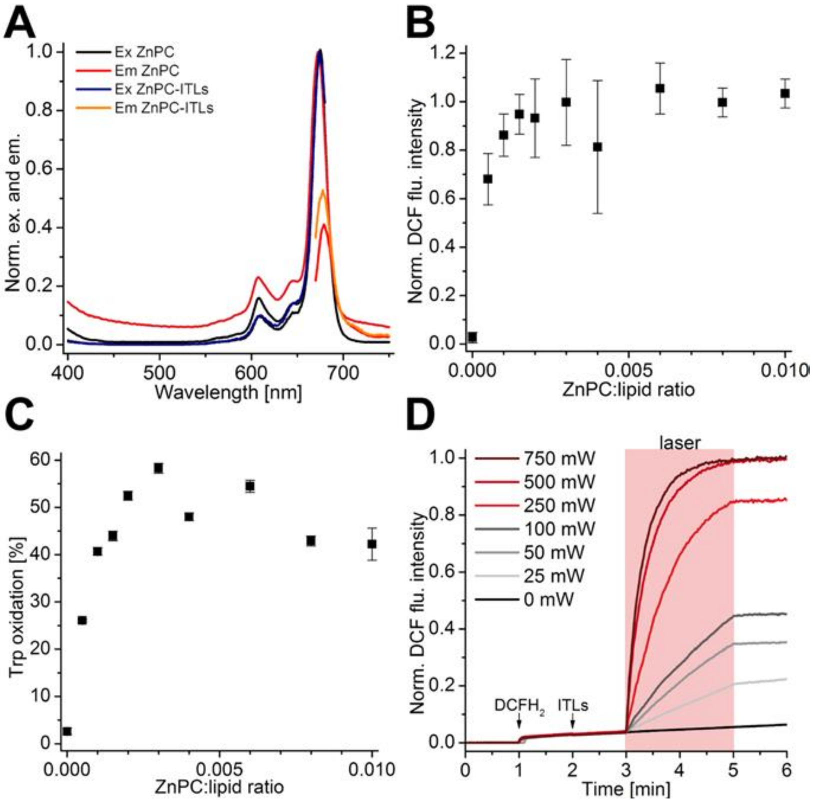

Figure 1.10 - Characterization of Zinc-Phthalocyanine (ZnPC) encapsulated in interstitially-targeted liposomes (ITLs). In (A) it is shown the normalized fluorescence emission (Em) and excitation (Ex) spectra of unencapsulated ZnPC and ZnPC-containing liposomes (ZnPC–ITLs). In (B) the ZnPC:lipid ratio in correlation with the ROS generation capacities of ZnPC-ITLs following PDT. The ROS production was assessed

using the probe 20,70-dichlorodihydrofluorescein ($DCFH_2$). In (C), the ZnPC:lipid ratio-dependent oxidation of tryptophan (Trp) residues presents in bovine serum albumin after PDT with ZnPC–ITLs. Finally, in (D) is shown the Laser power-dependent oxidation kinetics of $DCFH_2$ during PDT with ZnPC–ITLs. The ITLs are composed of DPPC:cholesterol:DSPE-PEG (66:30:4 molar ratio) in physiological buffer. The protocol is described in (197) and the figure was copied from (28).

1.7. Thesis overview and aim

This doctoral thesis focuses essentially in the evaluation and comparison between lipophilic metallated-phthalocyanines (ZnPC and AlPC) encapsulated in ITLs, and their equivalent hydrophilic derivatives (ZnPCS4 and AlPCS4). To organize the different aspects, the present thesis was divided into four chapters. In chapter 1 it is given an introduction containing general and relevant knowledge in the field. In chapter 2, we initiated our investigations through an attritional assessment performed *in vitro* using all four PSs in a single cell line. The analyses were performed in cultured A431 cells as a template for tumor cells with a dysfunctional P53 tumor suppressor gene and epidermal growth factor receptor (EGFR) overexpression. First, dark toxicity was assessed as a function of PS concentration using the WST-1 and sulforhodamine B assays. Second, time-dependent uptake and intracellular distribution were determined by flow cytometry and confocal microscopy, respectively, using the intrinsic fluorescence of the PSs. Third, the LC_{50} values were established for each PS using a 671 nm diode laser at a radiant exposure of 15 J/cm^2, after 1-h PS exposure. Finally, the mode of cell death as a function of post-PDT time and cell cycle arrest at 24 h after PDT were analyzed. Chapter 3 entails a follow-up of the previous chapter, where the abovementioned PSs were compared in a human cholangiocarcinoma cell line (Sk-Cha-1) and in tumor-comprising cells (endothelial cells, fibroblasts, and macrophages) as a representation of the tumor's microenvironment. Moreover, the systemic toxicity, skin phototoxicity, and *in vivo* photodynamic efficacy were determined in this chapter in addition to the same parameters assessed in chapter 2. Last but not least, chapter 4 focuses on the overall conclusions of the thesis as well as a brief look on the future trends reserved for the field of PDT.

The aim of this doctoral thesis encompasses two main goals: 1) to compare multiple photosensitizers of one family in a systematic manner that could help deciding between which PS should continue forward for the development of a third and fourth-generation of PSs. The ultimate goal of this research project was to explore and create a liposomal formulation that can incorporate one or more PS, in combination or not with other co-adjuvant drugs that may help eliminating some of the PDT's drawbacks, such as cell survival/resistance mechanisms after PDT. And 2), to establish a minimalistic research framework for translational science colleagues who aim to develop and test novel PSs and bring it at warp speed to clinical trials. Hence, novel photosensitizers can be quickly and facilely tested and benchmarked against clinically approved photosensitizers by following our attritional approach.

1.8. References

1. Hönigsmann H. History of phototherapy in dermatology. *Photochem Photobiol Sci*. 2013;12(1):16-21.
2. Pathak MA, Fitzpatrick TB. The evolution of photochemotherapy with psoralens and UVA (PUVA): 2000 BC to 1992 AD. *J Photochem Photobiol B*. 1992;14(1-2):3-22.
3. Da Silva Veiga P. Health and Medicine in Ancient Egypt: Magic and science. *BAR Int. Ser. 1967*. 2009;2–82.
4. Khushboo PS, Jadhav VM, Kadam VJ, Sathe NS. Psoralea corylifolia Linn.- "Kushtanashini". *Pharmacogn Rev*. 2010;4(7):69-76.
5. The nobel prize in physiology or medicine 1903. NobelPrize.org. Accessed January 6, 2022. https://www.nobelprize.org/prizes/medicine/1903/summary/.
6. Ackroyd R, Kelty C, Brown N, Reed M. The history of photodetection and photodynamic therapy. *Photochem Photobiol*. 2001;74(5):656.
7. Cengel KA, Simone CB 2nd, Glatstein E. PDT: What's Past Is Prologue. *Cancer Res*. 2016;76(9):2497-2499.
8. Gold MH, Goldman MP. 5-aminolevulinic acid photodynamic therapy: where we have been and where we are going. *Dermatol Surg*. 2004;30(8):1077-1084.
9. Jesionek A, von Tappeiner H. Zur behandlung der hautcarcinome mit fluorescierenden stoffen. *Dtsch Arch Klin Med*. 1905;85:223–39.
10. Kou J, Dou D, Yang L. Porphyrin photosensitizers in photodynamic therapy and its applications. *Oncotarget*. 2017;8(46):81591-81603.
11. Allison RR, Mota HC, Sibata CH. Clinical PD/PDT in North America: An historical review. *Photodiagnosis Photodyn Ther*. 2004;1(4):263-277.
12. Abdel-Kader MH. History of photodynamic therapy. *Photodynamic Therapy*. 2014; 3-22.
13. Schwartz, S., Absolon, K., and Vermund, H. Some relationships of porphyrins, x-rays and tumors. *Univ. Minnesota Med. Bull.* 1955;27: 7–13.
14. Hamblin MR. Photodynamic Therapy for Cancer: What's Past is Prologue. *Photochem Photobiol*. 2020;96(3):506-516.
15. Dougherty TJ, Kaufman JE, Goldfarb A, Weishaupt KR, Boyle D, Mittleman A. Photoradiation therapy for the treatment of malignant tumors. *Cancer Res*. 1978;38(8):2628–35.
16. Kessel D. Photodynamic Therapy: A Brief History. *Journal of Clinical Medicine*. 2019;8(10):1581.
17. Boen M, Brownell J, Patel P, Tsoukas MM. The Role of Photodynamic Therapy in Acne: An Evidence-Based Review. *Am J Clin Dermatol*. 2017;18(3):311–21.
18. Chun-Hua T, Li-Qiang G, Hua W, et al. Efficacy and safety of hemoporfin photodynamic therapy for port-wine stains in paediatric patients: A retrospective study of 439 cases at a single centre. *Photodiagnosis Photodyn Ther*. 2021;36:102568.
19. Choi YM, Adelzadeh L, Wu JJ. Photodynamic therapy for psoriasis. *J Dermatolog Treat*. 2015;26(3):202-207.
20. Sperandio FF, Huang YY, Hamblin MR. Antimicrobial Photodynamic Therapy to Kill Gram-negative Bacteria. *Recent Pat Antiinfect Drug Discov*. 2013;8(2):108.
21. Plaetzer K, Berneburg M, Kiesslich T, Maisch T. New applications of photodynamic therapy in biomedicine and biotechnology. *Biomed Res Int*. 2013;2013:161362.

22. Triesscheijn M, Baas P, Schellens JH, Stewart FA. Photodynamic therapy in oncology. *Oncologist*. 2006;11(9):1034-1044.
23. Hopper C, Niziol C, Sidhu M. The cost-effectiveness of Foscan mediated photodynamic therapy (Foscan-PDT) compared with extensive palliative surgery and palliative chemotherapy for patients with advanced head and neck cancer in the UK. *Oral Oncol*. 2004;40(4):372-382.
24. Saavedra R, Rocha LB, Dąbrowski JM, Arnaut LG. Modulation of biodistribution, pharmacokinetics, and photosensitivity with the delivery vehicle of a bacteriochlorin photosensitizer for photodynamic therapy. *ChemMedChem*. 2014;9(2):390-398.
25. Jori G. In vivo transport and pharmacokinetic behavior of tumour photosensitizers. *Ciba Found Symp*. 1989;146:78–94.
26. Huang Z, Xu H, Meyers AD, et al. Photodynamic therapy for treatment of solid tumors--potential and technical challenges. *Technol Cancer Res Treat*. 2008;7(4):309-320.
27. Maeda H. The enhanced permeability and retention (EPR) effect in tumor vasculature: the key role of tumor-selective macromolecular drug targeting. *Adv Enzyme Regul*. 2001;41:189-207.
28. Weijer R, Broekgaarden M, Kos M, van Vught R, Rauws EA, Breukink EJ, van Gulik TM, Storm G, and Heger M. Enhancing photodynamic therapy of refractory solid cancers: Combining second-generation photosensitizers with multi-targeted liposomal delivery. *J Photochem Photobiol C*. 2015;23(103-31.
29. Van De Putte M, Roskams T, Bormans G, Verbruggen A, De Witte PA. The impact of aggregation on the biodistribution of hypericin. *Int J Oncol*. 2006;28(3):655-660.
30. Korbelik M, Krosl G, Olive PL, Chaplin DJ. Distribution of Photofrin between tumour cells and tumour associated macrophages. *Br J Cancer*. 1991;64(3):508-512.
31. Barel A, Jori G, Perin A, Romandini P, Pagnan A, Biffanti S. Role of high-, low- and very low-density lipoproteins in the transport and tumor-delivery of hematoporphyrin in vivo. *Cancer Lett*. 1986;32(2):145-150.
32. El-Far MA, Pimstone NR. Tumour localization of uroporphyrin isomers I and III and their correlation to albumin and serum protein binding. *Cell Biochem Funct*. 1983;1(3):156-160.
33. Peng Q, Moan J, Cheng LS. The effect of glucose administration on the uptake of photofrin II in a human tumor xenograft. *Cancer Lett*. 1991;58(1–2):29–35.
34. Mccain J, Colón KL, Barrett PC, Monro SMA, Sainuddin T, Roque Iii J, et al. Photophysical Properties and Photobiological Activities of Ruthenium(II) Complexes Bearing π-Expansive Cyclometalating Ligands with Thienyl Groups HHS Public Access. *Inorg Chem*. 2019;58(16):10778–90.
35. de Visscher SAHJ, Dijkstra PU, Tan IB, Roodenburg JLN, Witjes MJH. mTHPC mediated photodynamic therapy (PDT) of squamous cell carcinoma in the head and neck: a systematic review. *Oral Oncol*. 2013;49(3):192–210.
36. Foley P, Freeman M, Menter A, Siller G, El-Azhary RA, Gebauer K, et al. Photodynamic therapy with methyl aminolevulinate for primary nodular basal cell carcinoma: results of two randomized studies. *Int J Dermatol*. 2009;48(11):1236–45.
37. Mackenzie GD, Dunn JM, Selvasekar CR, Mosse CA, Thorpe SM, Novelli MR, et al. Optimal conditions for successful ablation of high-grade dysplasia in Barrett's oesophagus using aminolaevulinic acid photodynamic therapy. *Lasers Med Sci*. 2009;24(5):729–34.
38. Sibille A, Lambert R, Souquet JC, Sabben G, Descos F. Long-term survival after photodynamic therapy for esophageal cancer. Gastroenterology. 1995;108(2):337–44.
39. Zq S. [Photodynamic therapy of nasopharyngeal carcinoma by argon or dye laser--an analysis of 137 cases]. *Chinese journal of oncology*. 1992;14:290–2.

40. Nseyo UO, DeHaven J, Dougherty TJ, Potter WR, Merrill DL, Lundahl SL, et al. Photodynamic therapy (PDT) in the treatment of patients with resistant superficial bladder cancer: a long-term experience. *J Clin Laser Med Surg*. 1998;16(1):61–8.
41. Wiedmann M, Berr F, Schiefke I, Witzigmann H, Kohlhaw K, Mössner J, et al. Photodynamic therapy in patients with non-resectable hilar cholangiocarcinoma: 5-year follow-up of a prospective phase II study. *Gastrointest Endosc.* 2004;60(1):68–75.
42. Huang Z, Xu H, Meyers AD, Musani AI, Wang L, Tagg R, et al. Photodynamic therapy for treatment of solid tumors--potential and technical challenges. *Technol Cancer Res Treat.* 2008;7(4):309–20.
43. Biel M. Advances in photodynamic therapy for the treatment of head and neck cancers. *Lasers Surg Med.* 2006;38(5):349–55.
44. Muller PJ, Wilson BC. Photodynamic therapy of brain tumors--a work in progress. *Lasers Surg Med.* 2006;38(5):384–9.
45. Selman SH. Photodynamic therapy for prostate cancer: One urologist's perspective. *Photodiagnosis Photodyn Ther.* 2007;4(1):26–30.
46. Shafirstein G, Battoo A, Harris K, Baumann H, Gollnick SO, Lindenmann J, et al. Photodynamic Therapy of Non-Small Cell Lung Cancer. Narrative Review and Future Directions. *Ann Am Thorac Soc.* 2016;13(2):265–75.
47. Banerjee SM, El-Sheikh S, Malhotra A, et al. Photodynamic therapy in primary breast cancer. *Journal of Clinical Medicine.* 2020;9(2):483.
48. Hopper C. Photodynamic therapy: a clinical reality in the treatment of cancer. *Lancet Oncol.* 2000;1:212-219.
49. What is PDT with Photofrin® (Porfimer Sodium) for injection? Photofrin®. April 11, 2022. Accessed January 6, 2022. https://photofrin.com/patient-information/.
50. Abdel-Kader MH. History of photodynamic therapy. Photodynamic Therapy: From Theory to Application. *Springer.* 2014;61(5):3–22.
51. Plaetzer K, Krammer B, Berlanda J, Berr F, Kiesslich T. Photophysics and photochemistry of photodynamic therapy: fundamental aspects. *Lasers Med Sci.* 2009;24(2):259–68.
52. Castano AP, Demidova TN, Hamblin MR. Mechanisms in photodynamic therapy: part one-photosensitizers, photochemistry and cellular localization. *Photodiagnosis Photodyn Ther.* 2004;1(4):279-293.
53. Abrahamse H, Hamblin MR. New photosensitizers for photodynamic therapy. *Biochem J.* 2016;473(4):347-364.
54. Agostinis P, Berg K, Cengel KA, et al. Photodynamic therapy of cancer: an update. *CA Cancer J Clin.* 2011;61(4):250-281.
55. Juarranz A, Jaén P, Sanz-Rodríguez F, Cuevas J, González S. Photodynamic therapy of cancer. Basic principles and applications. *Clin Transl Oncol.* 2008;10(3):148-154.
56. Zhou Z, Song J, Nie L, Chen X. Reactive oxygen species generating systems meeting challenges of photodynamic cancer therapy. *Chem Soc Rev.* 2016;45(23):6597-6626.
57. Ochsner M. Photophysical and photobiological processes in the photodynamic therapy of tumours. *J Photochem Photobiol B.* 1997;39(1):1–18.
58. Dominika Nowis, Marcin Makowski, Tomasz Stokłosa, Magdalena Legat, Tadeusz Issat JG. Direct tumor damage mechanisms of photodynamic therapy. *Acta Biochim Pol.* 2005;52(2):339–52.
59. Brancaleon L, Moseley H. Laser and non-laser light sources for photodynamic therapy. *Lasers Med Sci.* 2002;17(3):173–86.
60. Nair GB, Dhoble SJ. A perspective perception on the applications of light-emitting diodes. *Luminescence.* 2015;30(8):1167–75.

61. Kim MM, Darafsheh A. Light sources and dosimetry techniques for photodynamic therapy. *Photochemistry and Photobiology*. 2020;96(2):280-294.
62. Barr, H., Boulos, P.B., Macrobert, A.J. et al. Comparison of lasers for photodynamic therapy with a phthalocyanine photosensitizer. *Laser Med Sci*. 1989;4: 7–12.
63. Wang I. Photodynamic Therapy and Laser-Based Diagnostic Studies of Malignant Tumours. Lund University Medical Laser Centre, Department of Oncology, Lund University Hospital (Thesis); 1999.
64. Cowled PA, Grace JR, Forbes IJ. Comparison of the efficacy of pulsed and continuous-wave red laser light in induction of photocytotoxicity by haematoporphyrin derivative. *Photochem Photobiol*. 1984;39(1):115-117.
65. Mallidi S, Anbil S, Bulin AL, Obaid G, Ichikawa M, Hasan T. Beyond the Barriers of Light Penetration: Strategies, Perspectives and Possibilities for Photodynamic Therapy. *Theranostics*. 2016;6(13):2458-2487.
66. Miyamoto Y, Umebayashi Y, Nishisaka T. Comparison of phototoxicity mechanism between pulsed and continuous wave irradiation in photodynamic therapy. *J Photochem Photobiol B*. 1999;53(1–3):53–9.
67. Kataoka H, Nishie H, Hayashi N, et al. New photodynamic therapy with next-generation photosensitizers. Ann Transl Med. 2017;5(8):183.
68. Allison RR, Downie GH, Cuenca R, Hu XH, Childs CJ, Sibata CH. Photosensitizers in clinical PDT. *Photodiagnosis Photodyn Ther*. 2004;1(1):27-42.
69. Ormond AB, Freeman HS. Dye Sensitizers for Photodynamic Therapy. *Materials (Basel)*. 2013;6(3):817-840.
70. Pushpan SK, Venkatraman S, Anand VG, Sankar J, Parmeswaran D, Ganesan S, et al. Porphyrins in photodynamic therapy - a search for ideal photosensitizers. *Curr Med Chem Anticancer Agents*. 2002;2(2):187–207.
71. Baskaran R, Lee J, Yang SG. Clinical development of photodynamic agents and therapeutic applications. *Biomaterials Research*. 2018;22(1):1–8.
72. Moan J, Peng Q. An outline of the hundred-year history of PDT. *Anticancer Res*. 2003;23(5A):3591–600.
73. Kessel D, Thompson P, Musselman B, Chang CK. Probing the structure and stability of the tumor-localizing derivative of hematoporphyrin by reductive cleavage with LiAlH4. *Cancer Res*. 1987 Sep;47(17):4642–5.
74. Photofrin® (Porfimer sodium) for Injection. U.S. National Library of Medicine. Accessed January 22, 2022. https://dailymed.nlm.nih.gov/dailymed/ lookup.cfm?setid=f5fdda24-da7d-4e61-936e-9d1a55056b82.
75. Bonnett R. Photosensitizers of the Porphyrin and Phthalocyanine Series for Photodynamic Therapy. *Chemical Society Reviews*. 1987;13(3):1–12.
76. Peng Q, Berg K, Moan J, Kongshaug M, Nesland JM. 5-Aminolevulinic acid-based photodynamic therapy: principles and experimental research. *Photochem Photobiol*. 1997;65(2):235–51.
77. Panjehpour M, DeNovo RC, Petersen MG, et al. Photodynamic therapy using Verteporfin (benzoporphyrin derivative monoacid ring A, BPD-MA) and 630 nm laser light in canine esophagus. *Lasers Surg Med*. 2002;30(1):26-30.
78. McFarland SA, Mandel A, Dumoulin-White R, Gasser G. Metal-based photosensitizers for photodynamic therapy: the future of multimodal oncology?. *Curr Opin Chem Biol*. 2020;56:23-27.
79. Sekkat N, van den Bergh H, Nyokong T, Lange N. Like a bolt from the blue: phthalocyanines in biomedical optics. *Molecules*. 2011;17(1):98-144.
80. O'Connor AE, Gallagher WM, Byrne AT. Porphyrin and nonporphyrin photosensitizers in oncology: preclinical and clinical advances in photodynamic therapy. *Photochem Photobiol*. 2009;85(5):1053-1074.

81. Josefsen LB, Boyle RW. Photodynamic therapy and the development of metal-based photosensitisers. *Met Based Drugs*. 2008;2008:276109.
82. Garg AD, Krysko DV, Vandenabeele P, Agostinis P. Hypericin-based photodynamic therapy induces surface exposure of damage-associated molecular patterns like HSP70 and calreticulin. *Cancer Immunol Immunother*. 2012;61(2):215-221.
83. Tardivo JP, Del Giglio A, de Oliveira CS, et al. Methylene blue in photodynamic therapy: From basic mechanisms to clinical applications. *Photodiagnosis Photodyn Ther*. 2005;2(3):175-191.
84. Kazantzis KT, Koutsonikoli K, Mavroidi B, Zachariadis M, Alexiou P, Pelecanou M, et al. Curcumin derivatives as photosensitizers in photodynamic therapy: photophysical properties and in vitro studies with prostate cancer cells. Cite this: *Photochem Photobiol Sci*. 2020;19:193.
85. ClinicalTrials.gov. Accessed April 19, 2022. https://clinicaltrials.gov/.
86. Schmidt AM, Calvete MJF. Phthalocyanines: An old dog can still have new (photo)tricks! *Molecules*. 2021;26(9):1–22.
87. Chilakamarthi U, Giribabu L. Photodynamic therapy: Past, present and future. *The Chemical Record*. 2017;17(8):775-802.
88. Nemykina VN, Lukyanets EA. Synthesis of substituted phthalocyanines. *Arkivoc*. 2010;2010(1):136–208.
89. Brasseur N. Sensitizers for PDT: phthalocyanines (book chapter). The Royal Society of Chemistry. 2003; vol. 2, pp. 105-118.
90. van Lier JE, Spikes JD. The chemistry, photophysics and photosensitizing properties of phthalocyanines. *Ciba Found Symp*. 1989;146:17-32.
91. Weijer, R. Enhancing photodynamic therapy of refractory solid cancers. 2017; [Thesis, fully internal, Universiteit van Amsterdam]
92. Ghosh S, Carter KA, Lovell JF. Liposomal formulations of photosensitizers. *Biomaterials*. 2019;218:119341.
93. Huang K, Yan M, Zhang H, Xue J, Chen J. A phthalocyanine-based photosensitizer for effectively combating triple negative breast cancer with enhanced photodynamic anticancer activity and immune response. *Eur J Med Chem*. 2022;241:114644.
94. Brilkina AA, Dubasova LV, Sergeeva EA, et al. Photobiological properties of phthalocyanine photosensitizers Photosens, Holosens and Phthalosens: A comparative in vitro analysis. *Journal of Photochemistry and Photobiology B: Biology*. 2019;191:128-134.
95. Ghani F, Kristen J, Hans R. Solubility Properties of Unsubstituted Metal Phthalocyanines in Different Types of Solvents. *Journal of Chemical & Engineering Data*. 2012;57:439–449.
96. Chan WS, Marshall JF, Svensen R, Bedwell J, Hart IR. Effect of sulfonation on the cell and tissue distribution of the photosensitizer aluminum phthalocyanine. *Cancer Res*. 1990;50(15):4533–8.
97. Chan WS, West CM, Moore JV, Hart IR. Photocytotoxic efficacy of sulphonated species of aluminium phthalocyanine against cell monolayers, multicellular spheroids and in vivo tumours. *Br J Cancer*. 1991;64(5):827-832.
98. Henderson BW, Fingar VH. Relationship of tumor hypoxia and response to photodynamic treatment in an experimental mouse tumor. *Cancer Res*. 1987;47(12):3110–4.
99. Larue L, Myrzakhmetov B, Ben-Mihoub A, Moussaron A, Thomas N, Arnoux P, et al. Fighting Hypoxia to Improve PDT. *Pharmaceuticals (Basel)*. 2019;12(4):163.
100. Shen Z, Ma Q, Zhou X, et al. Strategies to improve photodynamic therapy efficacy by relieving the tumor hypoxia environment. *NPG Asia Materials*. 2021;13(1).

101. Kawauchi S, Morimoto Y, Sato S, Arai T, Seguchi K, Asanuma H, et al. Differences between cytotoxicity in photodynamic therapy using a pulsed laser and a continuous wave laser: study of oxygen consumption and photobleaching. *Lasers in Medical Science*. 2004;18(4):179–83.
102. Mei LH, Yang G, Fang F. Hyperbaric Oxygen Combined with 5-Aminolevulinic Acid Photodynamic Therapy Inhibited Human Squamous Cell Proliferation. *Biol Pharm Bull*. 2019;42(3):394-400.
103. Lin T, Zhao X, Zhao S, et al. O2-generating MnO2 nanoparticles for enhanced photodynamic therapy of bladder cancer by ameliorating hypoxia. *Theranostics*. 2018;8(4):990-1004.
104. Jarvi MT, Patterson MS, Wilson BC. Insights into photodynamic therapy dosimetry: Simultaneous singlet oxygen luminescence and photosensitizer photobleaching measurements. *Biophysical Journal*. 2012;102(3):661–71.
105. Zhu TC, Finlay JC, Wilson B. Photodynamic Therapy: Fundamentals and Dosimetry. *Medical Physics*. 2005;32(6):2150.
106. Jarvi MT, Niedre MJ, Patterson MS, Wilson BC. Singlet oxygen luminescence dosimetry (SOLD) for photodynamic therapy: current status, challenges and future prospects. *Photochem Photobiol*. 2006;82(5):1198–210.
107. Kim MM, Darafsheh A. Light Sources and Dosimetry Techniques for Photodynamic Therapy. *Photochem Photobiol*. 2020;96(2):280-294.
108. Wilson BC, Patterson MS, Lilge L. Implicit and explicit dosimetry in photodynamic therapy: a New paradigm. *Lasers Med Sci*. 1997;12(3):182–99.
109. Sterenborg H, de Wolf J, Koning M, Kruijt B, van den Heuvel A, Robinson D. Phosphorescence-Fluorescence ratio imaging for monitoring the oxygen status during photodynamic therapy. *Opt Express*. 2004;12(9):1873-1878.
110. Patterson MS. Photodynamic therapy dosimetry: A TO Z. In: Handbook of Photodynamic Therapy: Updates on Recent Applications of Porphyrin-Based Compounds. *Medical Physics Publishing*; 2016. p. 295–316.
111. van Staveren HJ, Marijnissen HPA, Aalders MCG, Star WM. Construction, quality assurance and calibration of spherical isotropic fibre optic light diffusers. *Lasers in Medical Science* ;. 1995;10(2):137–47.
112. Zhu TC, Finlay JC. The role of photodynamic therapy (PDT) physics Vol. 35. *Medical Physics. John Wiley and Sons Ltd*; 2008. p. 3127–36.
113. Holboke MJ, Tromberg BJ, Li X, et al. Three-dimensional diffuse optical mammography with ultrasound localization in a human subject. *J Biomed Opt*. 2000;5(2):237-247.
114. Lai B (Master Thesis). Implementation of a spatially-resolved explicit photodynamic therapy dosimetry system utilizing multi-sensor fiber optic probes. *Department of Medical Biophysics - University of Toronto*. 2009.
115. Diamond KR, Patterson MS, Farrell TJ. Quantification of fluorophore concentration in tissue-simulating media by fluorescence measurements with a single optical fiber. *Appl Opt*. 2003;42(13):2436-2442.
116. Clark LC, Wolf R, Granger D, Taylor Z. Continuous Recording of Blood Oxygen Tensions by Polarography. *Journal of Applied Physiology*. 1953;6(3):189–93.
117. Foster TH, Nichols MG, Georgakoudi I, Hull EL. Microelectrode and optical measurements of oxygen in biological systems in vitro and in vivo. *SPIE Proceedings*. Published online 1996. doi:10.1117/12.239567
118. J P. Celli, B Q. Spring, I. Rizvi, C L. Evan, K S. Samkoe, S. Verma, B W. Pogue and TH. Imaging and Photodynamic Therapy: Mechanisms, Monitoring and Optimization. *Chemical Reviews*. 2010;110(5):2795–838.

119. Mallidi S, Watanabe K, Timerman D, Schoenfeld D, Hasan T. Prediction of tumor recurrence and therapy monitoring using ultrasound-guided photoacoustic imaging. *Theranostics*. 2015;5(3):289–301.

120. Redmond RW, Kochevar IE. Spatially resolved cellular responses to singlet oxygen. *Photochem Photobiol*. 2006;82(5):1178–86.

121. Henderson BW, Dougherty TJ. How does photodynamic therapy work?. *Photochem Photobiol*. 1992;55(1):145-157.

122. Pucelik B, Sułek A, Drozd A, et al. Enhanced Cellular Uptake and Photodynamic Effect with Amphiphilic Fluorinated Porphyrins: The Role of Sulfoester Groups and the Nature of Reactive Oxygen Species. *Int J Mol Sci*. 2020;21(8):2786. Published 2020 Apr 16.

123. Mroz P, Bhaumik J, Dogutan DK, Aly Z, Kamal Z, Khalid L, et al. Imidazole metalloporphyrins as photosensitizers for photodynamic therapy: role of molecular charge, central metal and hydroxyl radical production. *Cancer Lett*. 2009; 282(1):63–76.

124. Mohammadpour R, Safarian S, Buckway B, Ghandehari H. Comparative Endocytosis Mechanisms and Anticancer Effect of HPMA Copolymer- and PAMAM Dendrimer-MTCP Conjugates for Photodynamic Therapy. *Macromolecular Bioscience*. 2017; 17(4):1600333.

125. Woodburn KW, Vardaxis NJ, Hill JS, Kaye AH, Phillips DR. Subcellular localization of porphyrins using confocal laser scanning microscopy. *Photochem Photobiol*. 1991; 54(5):725–32.

126. Castano AP, Demidova TN, Hamblin MR. Mechanisms in photodynamic therapy: part two-cellular signaling, cell metabolism and modes of cell death. *Photodiagnosis Photodyn Ther*. 2005;2(1):1-23.

127. Wessels JM, Strauss W, Seidlitz HK, Rück A, Schneckenburger H. Intracellular localization of meso-tetraphenylporphine tetrasulphonate probed by time-resolved and microscopic fluorescence spectroscopy. *J Photochem Photobiol B*. 1992; 12(3):275–84.

128. Lin CW, Shulok JR, Kirley SD, Cincotta L, Foley JW. Lysosomal localization and mechanism of uptake of Nile blue photosensitizers in tumor cells. *Cancer Res*. 1991; 51(10):2710–9.

129. Broekgaarden M, Weijer R, van Wijk AC, Cox RC, Egmond MR, Hoebe R, et al. Photodynamic therapy with liposomal zinc phthalocyanine and tirapazamine increases tumor cell death via DNA damage. *Journal of Biomedical Nanotechnology*. 2017; 13(2):204–20.

130. Oliveira CS, Turchiello R, Kowaltowski AJ, Indig GL, Baptista MS. Major determinants of photoinduced cell death: Subcellular localization versus photosensitization efficiency. *Free Radical Biology and Medicine*. 2011;51(4):824–33.

131. Girotti AW. Photodynamic lipid peroxidation in Biological Systems. *Photochemistry and Photobiology*. 1990;51(4):497-509.

132. Hsieh YJ, Wu CC, Chang CJ, Yu JS. Subcellular localization of Photofrin determines the death phenotype of human epidermoid carcinoma A431 cells triggered by photodynamic therapy: when plasma membranes are the main targets. *J Cell Physiol*. 2003; 194(3):363–75.

133. Moan J, Berg K, Anholt H, Madslien K. Sulfonated aluminium phthalocyanines as sensitizers for photochemotherapy. Effects of small light doses on localization, dye fluorescence and photosensitivity in V79 cells. *International Journal of Cancer*. 1994 ;58(6):865–70.

134. Berg K, Madslien K, Bommer JC, Oftebro R, Winkelman JW, Moan J. Light induced relocalization of sulfonated meso-tetraphenylporphines in NHIK 3025 cells and effects of dose fractionation. *Photochem Photobiol.* 1991;53(2):203-210.

135. Wilson PD, Firestone RA, Lenard J. The role of lysosomal enzymes in killing of mammalian cells by the lysosomotropic detergent N-dodecylimidazole. *J Cell Biol.* 1987;104(5):1223-1229.

136. Moserova I, Kralova J. Role of ER stress response in photodynamic therapy: ROS generated in different subcellular compartments trigger diverse cell death pathways. *PLoS One*. 2012;7(3):e32972.

137. Buytaert E, Callewaert G, Hendrickx N, Scorrano L, Hartmann D, Missiaen L, et al. Role of endoplasmic reticulum depletion and multidomain proapoptotic BAX and BAK proteins in shaping cell death after hypericin-mediated photodynamic therapy. *The FASEB Journal*. 2006;20(6):756–8.

138. Kessel D, Conley M, Vicente MGH, Reiners JJ. Studies on the Subcellular Localization of the Porphycene CPO. *Photochemistry and Photobiology*. 2005;81(3):569.

139. Kessel D, Luo Y, Deng Y, Chang CK. The Role of Subcellular Localization in Initiation of Apoptosis by Photodynamic Therapy. *Photochemistry and Photobiology*. 1997; 65(3):422–6.

140. Kessel D, Luo Y. Mitochondrial photodamage and PDT-induced apoptosis. *Journal of Photochemistry and Photobiology B: Biology*. 1998;42(2):89–95.

141. Plaetzer K, Kiesslich T, Krammer B, Hammerl P. Characterization of the cell death modes and the associated changes in cellular energy supply in response to AlPcS4-PDT. *Photochem Photobiol Sci.* 2002;1(3):172-177.

142. Mukherjee S, Chiu R, Leung SM, Shields D. Fragmentation of the Golgi apparatus: an early apoptotic event independent of the cytoskeleton. *Traffic*. 2007;8(4):369-378.

143. Soldani C, Bottone MG, Croce AC, Fraschini A, Bottiroli G, Pellicciari C. The Golgi apparatus is a primary site of intracellular damage after photosensitization with Rose Bengal acetate. *Eur J Histochem*. 2004;48(4):443–8.

144. Ogata M, Inanami O, Nakajima M, Nakajima T, Hiraoka W, Kuwabara M. Ca(2+)-dependent and caspase-3-independent apoptosis caused by damage in Golgi apparatus due to 2,4,5,7-tetrabromorhodamine 123 bromide-induced photodynamic effects. *Photochem Photobiol.* 2003;78(3):241-247.

145. Valli F, García Vior MC, Roguin LP, Marino J. Crosstalk between oxidative stress-induced apoptotic and autophagic signaling pathways in Zn(II) phthalocyanine photodynamic therapy of melanoma. *Free Radical Biology and Medicine*. 2020;152:743–54.

146. Berlanda J, Kiesslich T, Engelhardt V, Krammer B, Plaetzer K. Comparative in vitro study on the characteristics of different photosensitizers employed in PDT. *Journal of Photochemistry and Photobiology B: Biology*. 2010;100(3):173–80.

147. Pattingre S, Tassa A, Qu X, et al. Bcl-2 antiapoptotic proteins inhibit Beclin 1-dependent autophagy. *Cell.* 2005;122(6):927-939.

148. Dolmans DEJGJ, Kadambi A, Hill JS, Waters CA, Robinson BC, Walker JP, et al. Vascular accumulation of a novel photosensitizer, MV6401, causes selective thrombosis in tumor vessels after photodynamic therapy. *Cancer Res*. 2002;62(7):2151–6.

149. Fingar VH, Kik PK, Haydon PS, et al. Analysis of acute vascular damage after photodynamic therapy using benzoporphyrin derivative (BPD). *Br J Cancer*. 1999;79(11-12):1702-1708.

150. Heger M, van Golen RF, Broekgaarden M, van den Bos RR, Neumann HAM, van Gulik TM, et al. Endovascular laser–tissue interactions and biological responses in relation to endogenous laser therapy. *Lasers Med Sci.* 2014;29(2):405–22.

151. Heger M, Beek JF, Moldovan NI, van der Horst CMAM, van Gemert MJC. Towards optimization of selective photothermolysis: prothrombotic pharmaceutical agents as potential adjuvants in laser treatment of port wine stains. A theoretical study. *Thromb Haemost*. 2005;93(2):242–56.
152. Castano AP, Mroz P, Hamblin MR. Photodynamic therapy and anti-tumour immunity. *Nat Rev Cancer*. 2006;6(7):535-545.
153. Gallo PM, Gallucci S. The dendritic cell response to classic, emerging, and homeostatic danger signals. Implications for autoimmunity. *Front Immunol*. 2013;4:138.
154. Chen GY, Nuñez G. Sterile inflammation: sensing and reacting to damage. *Nat Rev Immunol*. 2010;10(12):826-837.
155. Rauws EAJ. Photodynamic therapy and Klatskin tumour: An overview. *Scandinavian Journal of Gastroenterology*. 2006;41:135–8.
156. Weijer R, Broekgaarden M, van Golen RF, Bulle E, Nieuwenhuis E, Jongejan A, et al. Low-power photodynamic therapy induces survival signaling in perihilar cholangiocarcinoma cells. *BMC Cancer*. 2015;15(1):1014.
157. Moor AC. Signaling pathways in cell death and survival after photodynamic therapy. *J Photochem Photobiol B*. 2000;57(1):1-13.
158. Weijer R, Clavier S, Zaal EA, Pijls MME, van Kooten RT, Vermaas K, et al. Multi-OMIC profiling of survival and metabolic signaling networks in cells subjected to photodynamic therapy. *Cellular and Molecular Life Sciences*. 2017; 74(6):1133–51.
159. Broekgaarden M, Weijer R, van Gulik TM, Hamblin MR, Heger M. Tumor cell survival pathways activated by photodynamic therapy: a molecular basis for pharmacological inhibition strategies. *Cancer and Metastasis Reviews*. 2015;34(4):643–90.
160. Bellnier DA, Greco WR, Loewen GM, Nava H, Oseroff AB, Dougherty TJ. Clinical pharmacokinetics of the PDT photosensitizers porfimer sodium (Photofrin), 2-[1-hexyloxyethyl]-2-devinyl pyropheophorbide-a (Photochlor) and 5-ALA-induced protoporphyrin IX. *Lasers in Surgery and Medicine*. 2006; 38(5):439–44.
161. Hamblin MR. Drug efflux pumps in photodynamic therapy. *Drug Efflux Pumps in Cancer Resistance Pathways: From Molecular Recognition and Characterization to Possible Inhibition Strategies in Chemotherapy*. 2020; p. 251-276.
162. Klaassen CD, Reisman SA. Nrf2 the Rescue: Effects of the Antioxidative/Electrophilic Response on the Liver. *Liver*. 2011;244(1):57–65.
163. Gozzelino R, Jeney V, Soares MP. Mechanisms of cell protection by heme oxygenase-1. *Annu Rev Pharmacol Toxicol*. 2010;50:323–54.
164. Kimani SG, Phillips JB, Bruce JI, MacRobert AJ, Golding JP. Antioxidant inhibitors potentiate the cytotoxicity of photodynamic therapy. *Photochem Photobiol*. 2012;88(1):175–87.
165. Hu T, Wang Z, Shen W, Liang R, Yan D, Wei M. Recent advances in innovative strategies for enhanced cancer photodynamic therapy. *Theranostics*. 2021; 11(7):3278–300.
166. Park J, Lee YK, Park IK, Hwang SR. Current limitations and recent progress in nanomedicine for clinically available photodynamic therapy. *Biomedicines*. 2021; 9(1):1–17.
167. Ismael FS, Amasha H, Bachir W. Optimized Cylindrical Diffuser Powers for Interstitial PDT Breast Cancer Treatment Planning: A Simulation Study. *Biomed Res Int*. 2020; 2020:2061509.
168. Shafirstein G, Bellnier DA, Oakley E, Hamilton S, Habitzruther M, Tworek L, et al. Irradiance controls photodynamic efficacy and tissue heating in experimental tumours: implication for interstitial PDT of locally advanced cancer. *British Journal of Cancer*. 2018; 119(10):1191–9.

169. Vermandel M, Quidet M, Vignion-Dewalle AS, Leroy HA, Leroux B, Mordon S, et al. Comparison of different treatment schemes in 5-ALA interstitial photodynamic therapy for high-grade glioma in a preclinical model: An MRI study. *Photodiagnosis Photodyn Ther*. 2019;25:166–76.
170. Juzeniene A, Peng Q, Moan J. Milestones in the development of photodynamic therapy and fluorescence diagnosis. *Photochemical and Photobiological Sciences*. 2007; p. 1234–45.
171. Bhawalkar JD, Kumar ND, Zhao CF, Prasad PN. Two-photon photodynamic therapy. *J Clin Laser Med Surg*. 1997;15(5):201–4.
172. Zhuang W, Yang L, Ma B, Kong Q, Li G, Wang Y, et al. Multifunctional Two-Photon AIE Luminogens for Highly Mitochondria-Specific Bioimaging and Efficient Photodynamic Therapy. *ACS Appl Mater Interfaces*. 2019; 11(23):20715–24.
173. Calixto GM, Bernegossi J, de Freitas LM, Fontana CR, Chorilli M. Nanotechnology-Based Drug Delivery Systems for Photodynamic Therapy of Cancer: A Review. *Molecules*. 2016;21(3):342.
174. Mokwena MG, Kruger CA, Ivan MT, Heidi A. A review of nanoparticle photosensitizer drug delivery uptake systems for photodynamic treatment of lung cancer. *Photodiagnosis Photodyn Ther*. 2018;22:147-154.
175. Hong EJ, Choi DG, Shim MS. Targeted and effective photodynamic therapy for cancer using functionalized nanomaterials. *Acta Pharm Sin B*. 2016;6(4):297-307.
176. Lamch Ł, Pucek A, Kulbacka J, Chudy M, Jastrzębska E, Tokarska K, et al. Recent progress in the engineering of multifunctional colloidal nanoparticles for enhanced photodynamic therapy and bioimaging. *Adv Colloid Interface Sci*. 2018;261:62–81.
177. Kruger CA, Abrahamse H. Utilisation of targeted nanoparticle photosensitiser drug delivery systems for the enhancement of photodynamic therapy. *Molecules*. 2018;23(10).
178. Rak J, Pouckova P, Benes J, Vetvicka D. Drug Delivery Systems for Phthalocyanines for Photodynamic Therapy. *Anticancer Res*. 2019;39(7):3323-3339.
179. Mesquita MQ, Dias CJ, Gamelas S, Fardilha M, Neves MGPMS, Faustino MAF. An insight on the role of photosensitizer nanocarriers for photodynamic therapy. *Anais da Academia Brasileira de Ciencias*. 2018;90(1):1101–30.
180. Reddi E, Zhou C, Biolo R, Menegaldo E, Jori G. Liposome- or LDL-administered Zn (II)-phthalocyanine as a photodynamic agent for tumours. I. Pharmacokinetic properties and phototherapeutic efficiency. *British Journal of Cancer*. 1990; 61(3):407–11.
181. Harisa GI, Alanazi FK. Low density lipoprotein bionanoparticles: From cholesterol transport to delivery of anti-cancer drugs. *Saudi Pharmaceutical Journal*. 2014;22(6):504–15.
182. Bagwe RP, Kanicky JR, Palla BJ, Patanjali PK, Shah DO. Improved drug delivery using microemulsions: rationale, recent progress, and new horizons. *Crit Rev Ther Drug Carrier Syst*. 2001;18(1):77–140.
183. Decreau R, Richard MJ, Verrando P, Chanon M, Julliard M. Photodynamic activities of silicon phthalocyanines against achromic M6 melanoma cells and healthy human melanocytes and keratinocytes. J Photochem Photobiol B. 1999;48(1):48-56.
184. Shao J, Dai Y, Zhao W, Xie J, Xue J, Ye J, et al. Intracellular distribution and mechanisms of actions of photosensitizer Zinc(II)-phthalocyanine solubilized in Cremophor EL against human hepatocellular carcinoma HepG2 cells. *Cancer Letters*. 2013;330(1):49–56.
185. Pardeshi C, Rajput P, Belgamwar V, Tekade A, Patil G, Chaudhary K, et al. Solid lipid based nanocarriers: an overview. *Acta Pharm*. 2012;62(4):433–72.

186. Battah SH, Chee CE, Nakanishi H, Gerscher S, MacRobert AJ, Edwards C. Synthesis and Biological Studies of 5-Aminolevulinic Acid-Containing Dendrimers for Photodynamic Therapy. *Bioconjugate Chemistry*. 2001;12(6):980–8.
187. Svenson S, Tomalia DA. Dendrimers in biomedical applications—reflections on the field. *Advanced Drug Delivery Reviews*. 2012;64:102–15.
188. Lamch Ł, Bazylińska U, Kulbacka J, Pietkiewicz J, Bieżuńska-Kusiak K, Wilk KA. Polymeric micelles for enhanced Photofrin II® delivery, cytotoxicity and pro-apoptotic activity in human breast and ovarian cancer cells. *Photodiagnosis and Photodynamic Therapy*. 2014;11(4):570–85.
189. Sibata MN, Tedesco AC, Marchetti JM. Photophysicals and photochemicals studies of zinc(II) phthalocyanine in long time circulation micelles for Photodynamic Therapy use. *European Journal of Pharmaceutical Sciences*. 2004;23(2):131–8.
190. Arvizo R, Bhattacharya R, Mukherjee P. Gold nanoparticles: Opportunities and challenges in nanomedicine. *Expert Opinion on Drug Delivery*. 2010;7(6):753–63.
191. Drbohlavova J, Adam V, Kizek R, Hubalek J. Quantum dots - characterization, preparation and usage in biological systems. *International Journal of Molecular Sciences*. 2009;10(2):656–73.
192. Stuchinskaya T, Moreno M, Cook MJ, Edwards DR, Russell DA. Targeted photodynamic therapy of breast cancer cells using antibody–phthalocyanine–gold nanoparticle conjugates. *Photochemical & Photobiological Sciences*. 2011;10(5):822–31.
193. Fowley C, Nomikou N, McHale AP, McCaughan B, Callan JF. Extending the tissue penetration capability of conventional photosensitisers: a carbon quantum dot–protoporphyrin IX conjugate for use in two-photon excited photodynamic therapy. *Chemical Communications*. 2013;49(79):8934–6.
194. Yokoyama M. Polymeric micelles as a new drug carrier system and their required considerations for clinical trials. *Expert Opinion on Drug Delivery*. 2010;7(2):145–58.
195. Akbarzadeh A, Rezaei-Sadabady R, Davaran S, Joo SW, Zarghami N, Hanifehpour Y, et al. Liposome: Classification, preparation, and applications. *Nanoscale Research Letters*. 2013;8(1):1.
196. Derycke AS, de Witte PA. Liposomes for photodynamic therapy. *Adv Drug Deliv Rev*. 2004;56(1):17-30.
197. Broekgaarden M, Kroon A, Gulik T, Heger M. Development and In Vitro Proof-of-Concept of Interstitially Targeted Zinc- Phthalocyanine Liposomes for Photodynamic Therapy. *Current Medicinal Chemistry*. 2013;21(3):377–91.
198. Broekgaarden M, van Vught R, Oliveira S, Roovers RC, van Bergen En Henegouwen PMP, Pieters RJ, et al. Site-specific conjugation of single domain antibodies to liposomes enhances photosensitizer uptake and photodynamic therapy efficacy. *Nanoscale*. 2016;8(12):6490–4.
199. Thurston G, McLean JW, Rizen M, Baluk P, Haskell A, Murphy TJ, et al. Cationic liposomes target angiogenic endothelial cells in tumors and chronic inflammation in mice. *Journal of Clinical Investigation*. 1998;101(7):1401–13.
200. Longo JPF, Leal SC, Simioni AR, de Fátima Menezes Almeida-Santos M, Tedesco AC, Azevedo RB. Photodynamic therapy disinfection of carious tissue mediated by aluminum-chloride-phthalocyanine entrapped in cationic liposomes: An in vitro and clinical study. *Lasers in Medical Science* ;. 2012;27(3):575–84.
201. Shum P, Kim JM, Thompson DH. Phototriggering of liposomal drug delivery systems. *Advanced Drug Delivery Reviews*. 2001;53(3):273–84.

202. Fomina N, Sankaranarayanan J, Almutairi A. Photochemical mechanisms of light-triggered release from nanocarriers. *Advanced Drug Delivery Reviews*. 2012;64(11):1005–20.
203. Amin M, Huang W, Seynhaeve ALB, ten Hagen TLM. Hyperthermia and temperature-sensitive nanomaterials for spatiotemporal drug delivery to solid tumors. *Pharmaceutics*. 2020;12(11):1–23.
204. Abu Dayyih A, Alawak M, Ayoub AM, Amin MU, Abu Dayyih W, Engelhardt K, et al. Thermosensitive liposomes encapsulating hypericin: Characterization and photodynamic efficiency. *International Journal of Pharmaceutics* . 2021;609:121195.
205. Kunisawa J, Masuda T, Katayama K, Yoshikawa T, Tsutsumi Y, Akashi M, et al. Fusogenic liposome delivers encapsulated nanoparticles for cytosolic controlled gene release. *journal of the Controlled Release Society*. 2005;105(3):344–53.
206. Ma J, Wu H, Li Y, Liu Z, Liu G, Guo Y, et al. Novel Core-Interlayer-Shell DOX/ZnPc Co-loaded MSNs@ pH-Sensitive CaP@PEGylated Liposome for Enhanced Synergetic Chemo-Photodynamic Therapy. *Pharm Res*. 2018;35(3):57.
207. Karanth H, Murthy RSR. pH-sensitive liposomes--principle and application in cancer therapy. *J Pharm Pharmacol*. 2007;59(4):469–83.
208. Garcia AM, Alarcon E, Muñoz M, Scaiano JC, Edwards AM, Lissi E. Photophysical behaviour and photodynamic activity of zinc phthalocyanines associated to liposomes. *Photochemical & Photobiological Sciences*. 2011;10(4):507–14.
209. Damoiseau X, Schuitmaker HJ, Lagerberg JWM, Hoebeke M. Increase of the photosensitizing efficiency of the Bacteriochlorin a by liposome-incorporation. *Journal of Photochemistry and Photobiology B: Biology*. 2001;60(1):50–60.
210. Jori G. Factors controlling the selectivity and efficiency of tumour damage in photodynamic therapy. *Lasers in Medical Science*. 1990;5(2):115–20.
211. Mayhew E, Ito M, Lazo R. Toxicity of non-drug-containing liposomes for cultured human cells. *Exp Cell Res*. 1987;171(1):195–202.
212. Campbell PI. Toxicity of some charged lipids used in liposome preparations. *Cytobios*. 1983;37(145):21–6.
213. Senior J, Delgado C, Fisher D, Tilcock C, Gregoriadis G. Influence of surface hydrophilicity of liposomes on their interaction with plasma protein and clearance from the circulation: Studies with poly(ethylene glycol)-coated vesicles. *BBA - Biomembranes*. 1991;1062(1):77–82.
214. Hansen CB, Kao GY, Moase EH, Zalipsky S, Allen TM. Attachment of antibodies to sterically stabilized liposomes: evaluation, comparison and optimization of coupling procedures. *BBA - Biomembranes*. 1995;1239(2):133–44.
215. Gabizon A, Papahadjopoulos D. The role of surface charge and hydrophilic groups on liposome clearance in vivo. *BBA - Biomembranes*. 1992;1103(1):94–100.
216. Mueller MM, Fusenig NE. Friends or foes - Bipolar effects of the tumour stroma in cancer. *Nature Reviews Cancer*. 2004;4(11):839–49.
217. Gomer CJ, Ferrario A, Luna M, Rucker N, Wong S. Photodynamic therapy: Combined modality approaches targeting the tumor microenvironment. *Lasers in Surgery and Medicine*. 2006;38(5):516–21.
218. Misra S, Hascall VC, Markwald RR, O'Brien PE, Ghatak S. Inflammation and cancer. *Wound Healing*. 2017; p. 239-274.
219. Jeffrey W. Pollard. Tumour-educated macrophages promote tumour progression and metastasis. *Nature Reviews Cancer*. 2004;4:71–78.
220. Papahadjopoulos D, Allen TM, Gabizon A, Mayhew E, Matthay K, Huang SK, et al. Sterically stabilized liposomes: Improvements in pharmacokinetics and antitumor therapeutic efficacy. *Proc Natl Acad Sci U S A*. 1991;88(24):11460–4.

221. Isele U, Schieweck K, Kessler R, van Hoogevest P, Capraro H. Pharmacokinetics and Body Distribution of Liposomal Zinc Phthalocyanine in Tumor-Bearing Mice: Influence of Aggregation State, Particle Size, and Composition. *Journal of Pharmaceutical Sciences*. 1995;84(2):166–73.
222. Wu NZ, Da D, Rudoll TL, Needham D, Whorton AR, Dewhirst MW. Increased microvascular permeability contributes to preferential accumulation of Stealth liposomes in tumor tissue. *Cancer Res*. 1993;53(16):3765–70.
223. Polo L, Bianco G, Reddi E, Jori G. The effect of different liposomal formulations on the interaction of Zn(II)-phthalocyanine with isolated low and high density lipoproteins. *The International Journal of Biochemistry & Cell Biology*. 1995;27(12):1249–55.

Chapter 2

Paper I

Journal of Photochemistry & Photobiology, B: Biology 216 (2021) 112146

Contents lists available at ScienceDirect

Journal of Photochemistry & Photobiology, B: Biology

journal homepage: www.elsevier.com/locate/jphotobiol

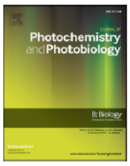

Attritional evaluation of lipophilic and hydrophilic metallated phthalocyanines for oncological photodynamic therapy

Lionel Mendes Dias [a,b,c], Farangis Sharifi [c,d,1], Mark J. de Keijzer [a,e,1], Barbara Mesquita [e], Emilie Desclos [c,d], Jakub A. Kochan [c,d], Daniel J. de Klerk [a], Dani¨el Ernst [a], Lianne R. de Haan [a], Leonardo P. Franchi [f,g], Albert C. van Wijk [c], Enzo M. Scutigliani [c,d], José E.B. Cavaco[b], Antonio C. Tedesco [g], Xuan Huang [a], Weiwei Pan [h], Baoyue Ding [a,2], Przemek M. Krawczyk [c,d,2], Michal Heger [a,e,*,2], on behalf of the Photodynamic Therapy Study Group

[a] Department of Pharmaceutics, Jiaxing Key Laboratory for Photonanomedicine and Experimental Therapeutics, College of Medicine, Jiaxing University, Jiaxing, Zhejiang, PR China

[b] CICS-UBI, Health Sciences Research Centre, University of Beira Interior, Covilhã, Portugal

[c] Department of Medical Biology, Cancer Center Amsterdam, Amsterdam UMC, Amsterdam, The Netherlands

[d] Laboratory of Experimental Oncology and Radiobiology (LEXOR), Cancer Center Amsterdam, Academic Medical Center, Amsterdam, The Netherlands

[e] Department of Pharmaceutics, Utrecht Institute for Pharmaceutical Sciences, Utrecht University, Utrecht, The Netherlands

[f] Departamento de Bioquímica e Biologia Molecular, Instituto de Ciências Biológicas (ICB) 2, Campus Samambaia, Universidade Federal de Goiás (UFG), Goiânia, GO, Brazil

[g] Department of Chemistry, Center of Nanotechnology and Tissue Engineering - Photobiology and Photomedicine Research Group, Faculty of Philosophy, Sciences, and Letters of Ribeirão Preto, University of São Paulo, São Paulo, Brazil

[h] Department of Cell Biology, College of Medicine, Jiaxing University, Jiaxing, PR China

[*] Corresponding author at: Jiaxing Key Laboratory for Photonanomedicine and Experimental Therapeutics, Department of Pharmaceutics, College of Medicine, Jiaxing University, Jiaxing, Zhejiang, PR China.

[1] Shared first authorship.

[2] Shared senior authorship.

2. Chapter 2 - Paper I: Attritional evaluation of lipophilic and hydrophilic metallated phthalocyanines for oncological photodynamic therapy

2.1. Abstract

Background and aim: Oncological photodynamic therapy (PDT) relies on photosensitizers (PSs) to photo-oxidatively destroy tumor cells. Currently approved PSs yield satisfactory results in superficial and easy-to-access tumors but are less suited for solid cancers in internal organs such as the biliary system and the pancreas. For these malignancies, second-generation PSs such as metallated phthalocyanines are more appropriate. Presently it is not known which of the commonly employed metallated phtahlocyanines, namely aluminum phthalocyanine (AlPC) and zinc phthalocyanine (ZnPC) as well as their tetrasulfonated derivatives AlPCS4 and ZnPCS4, is most cytotoxic to tumor cells. This study therefore employed an attritional approach to ascertain the best metallated phthalocyanine for oncological PDT in a head-to-head comparative analysis and standardized experimental design.

Methods: ZnPC and AlPC were encapsulated in PEGylated liposomes. Analyses were performed in cultured A431 cells as a template for tumor cells with a dysfunctional P53 tumor suppressor gene and EGFR overexpression. First, dark toxicity was assessed as a function of PS concentration using the water-soluble tetrazolium-1 (WST-1) and sulforhodamine B (SRB) assays. Second, time-dependent uptake and intracellular distribution were determined by flow cytometry and confocal microscopy, respectively, using the intrinsic fluorescence of the PSs. Third, the LC_{50} values were established for each PS at 671 nm and a radiant exposure of 15 J/cm^2 following 1-h PS exposure. Finally, the mode of cell death as a function of post-PDT time and cell cycle arrest at 24 h after PDT were analyzed.

Results: In the absence of illumination, AlPC and ZnPC were not toxic to cells up to a 1.5-μM PS concentration and exposure for up to 72 h. Dark toxicity was noted for AlPCS4 at 5 μM and ZnPCS4 at 2.5 μM. Uptake of all PSs was observed as early as 1 min after PS addition to cells and increased in amplitude during a 2-h incubation period. After 60 min, the entire non-nuclear space of the cell was photosensitized, with PS accumulation in multiple subcellular structures, especially in case of AlPC and AlPCS4. PDT of cells photosensitized with ZnPC, AlPC, and AlPCS4 yielded LC_{50} values of 0.13 μM, 0.04 μM, and 0.81 μM, respectively, 24 h post-PDT (based on sulforhodamine B assay). ZnPCS4 did not induce notable phototoxicity, which was echoed in the mode of cell death and cell cycle arrest data. At 4 h post-PDT, the mode of cell death comprised mainly apoptosis for ZnPC and AlPC, the extent of which was gradually exacerbated in AlPC-photosensitized cells during 8 h. ZnPC-treated cells seemed to recover at 8 h post-PDT compared to 4 h post-PDT, which had been observed before in another cell line. AlPCS4 induced considerable necrosis in addition to apoptosis, whereby most of the cell death had already manifested at 2 h after PDT. During the course of 8 h, necrotic cell death transitioned into mainly late apoptotic cell death. Cell death signaling coincided with a reduction in cells in the G0/G1 phase (ZnPC, AlPC, AlPCS4) and cell cycle arrest in the S-phase (ZnPC, AlPC, AlPCS4) and G2 phase (ZnPC and AlPC). Cell cycle arrest was most profound in cells that had been photosensitized with AlPC and subjected to PDT.

Conclusions: Liposomal AlPC is the most potent PS for oncological PDT, whereas ZnPCS4 was photodynamically inert in A431 cells. AlPC did not induce dark toxicity at PS concentrations of up to 1.5 µM, *e.g.*, > 37 times the LC_{50} value, which is favorable in terms of clinical phototoxicity issues. AlPC photosensitized multiple intracellular loci, which was associated with extensive, irreversible cell death signaling that is expected to benefit treatment efficacy and possibly immunological long-term tumor control, granted that sufficient AlPC will reach the tumor *in vivo*. Given the differential pharmacokinetics, intracellular distribution, and cell death dynamics, liposomal AlPC may be combined with AlPCS4 in a PS cocktail to further improve PDT efficacy.

Keywords: photosensitizers, cell death; cell survival; phototoxicity; dark toxicity; zinc phthalocyanine; aluminum phthalocyanine

2.2. Introduction

Photodynamic therapy (PDT) using the photosensitizers (PSs) porfimer sodium, 5-aminolevulinic acid (ALA) and its ester derivative, and 5,10,15,20-tetrakis(3-hydroxyphenyl)chlorin (mTHPC, Temoporfin) has been clinically approved for the treatment of various types of benign and (pre-)malignant lesions (1). Porfimer sodium is indicated for esophageal cancer, lung adenocarcinoma, and endobronchial cancer (2). ALA and ALA-ester are employed to treat actinic keratosis, basal cell carcinoma, and squamous cell carcinoma (3). mTHPC is used to treat advanced head and neck squamous cell carcinoma (4). Most PSs are associated with clinical drawbacks, which mainly entail skin phototoxicity (1) due to PS accumulation and retention in the skin as a result of the PS's lipophilicity (5). Consequently, patients are advised to remain shielded from ambient light for 4 to 12 weeks for porfimer sodium ($\log P \approx 8.5$) and 2 to 6 weeks for mTHPC ($\log P \approx 7.4$) (6).

For non-terminal cancer, post-therapeutic dark periods in the order of weeks are not problematic. However, experimental PDT modalities are also being developed for incurable cancer types that are associated with a median life expectancy of less than 1 year, including pancreatic cancer (7, 8) and extrahepatic cholangiocarcinoma (9-12). Clinical studies on PDT of extrahepatic cholangiocarcinoma have yielded superior results compared to palliative chemotherapy (13, 14), underscoring the need for continued translational and clinical PDT research for cholangiocarcinomas. Nevertheless, post-therapeutic dark periods of several weeks are ethically objectionable for patients diagnosed with either of these malignancies. In fact, our treatment center (Amsterdam UMC) ceased PDT of extrahepatic cholangiocarcinoma on such ethical grounds. PDT modalities for highly lethal malignancies should therefore be optimized to safely reduce the post-therapeutic dark period while preserving PDT efficacy and allow patients to have a more dignified end stage of their life.

Several research groups, including ours, have resorted to targeted photonanomedicines using liposomal encapsulation for intratumoral delivery of PSs (6). The fundamental premise for packaging PSs into sterically stabilized liposomes is to increase the size of the pharmacological entity, such that PS passage through endothelial fenestrations in the cutaneous microcirculation is limited and dermal accumulation deterred. Endothelial fenestrations in the dermal microcirculation are approximately 15 nm (15, 16), while lipophilic PS-encapsulating liposomes composed of dipalmitoyl phosphocholine typically have a mean diameter of 130-190 nm (9, 17, 18). Secondary reasons are that liposomes can be (immuno)targeted to tumor cells (18) and tumor vascular endothelium (19), or designed to passively accumulate in the tumor stroma and disrupt the tumor microenvironment (20). Differential targeting enables the development of liposomal PS cocktails for a more comprehensive approach to photochemical tumor destruction (6). Moreover, concentrating the drug molecules into a liposome allows for greater pharmacodynamic action compared to the unencapsulated drug (21). The uptake of a few liposomes loads the tumor cell with ample PS molecules to induce photokilling upon PDT. Metaphorically, this is best described by a 'Trojan Horse' (PS-loaded liposome) being transported into the cell as opposed to individual 'soldiers' (PSs) having to pass across a fortified cell wall. As a result, targeted photonanomedicines exact lower PS dosages for tumor destruction and are therefore well-suited to ameliorate skin phototoxicity. Another strategy to reduce skin phototoxicity is to select PSs that are rapidly cleared from the circulation, yet abundantly accumulate in the tumor during their relatively short circulation time (5, 22). Hydrophilic PSs generally meet these pharmacokinetics and disposition criteria, as exemplified by the comparison between the hydrophilic PS sulfonated aluminum phthalocyanine (AlPCS) versus the fat-soluble porfimer sodium. AlPCS produced considerably less skin phototoxicity than porfimer sodium upon light exposure of photosensitized skin following equal dark periods, while also significantly outperforming porfimer sodium with respect to PDT efficacy in mouse mammary (CaD2) carcinoma (23). A third approach to reduce skin phototoxicity is to employ PSs that have absorption bands deeper in the red spectrum (5), given the lower intensity of far-red wavelengths in sunlight (*e.g.*, 670 nm for metallated phthalocyanines (PCs)) than shorter-red wavelengths (*e.g.*, 630 nm for porfimer sodium) (6). Finally, selecting PSs with high extinction coefficients lowers the dose required to induce tumor cell death (24).

Metallated PCs (Figure 2.1) are PSs that structurally, photochemically, and pharmacokinetically comply with the requirements stipulated above to reduce skin phototoxicity. Metallated PCs have relatively high extinction coefficients (Figure 2.1) (6) and are chemically versatile in that the octanol:water partition coefficient (logP) - and hence the degree of hydrophilicity - can be downmodulated by the conjugation of charged/polar functional groups (23, 25). Our primary focus has been on ZnPC encapsulated into PEGylated liposomes that collectively exhibit no dark (geno)toxicity *in vitro* and *in vivo* but become toxic to tumor cells upon illumination (9, 11, 26, 27). Inasmuch as sulfonation of the isoindole benzo moieties of ZnPC to yield tetrasulfonated ZnPC (ZnPCS4) impairs the photoproduction of reactive oxygen species (ROS) in an aqueous environment (6), ZnPCS4 is not expected to be as toxic to tumor cells as ZnPC upon PDT. Irrespectively, some studies reported therapeutic efficacy achieved with ZnPCS4 (28-30), possibly due to the formation of oxygen-free radicals (31). Alternatively, the lipophilic AlPC packaged into nanoparticles composed of stearic acid/oleic acid (32), stearic acid/glyceryl behenate (33), lecithin/poloxamer 188/soybean oil/poly(D,L-lactide-co-glycolide) (34), and liposomes (35, 36) as well as its hydrophilic counterpart tetrasulfonated AlPC (AlPCS4) have been used for oncological PDT with encouraging outcomes *in vitro* and *in vivo* (23, 37).

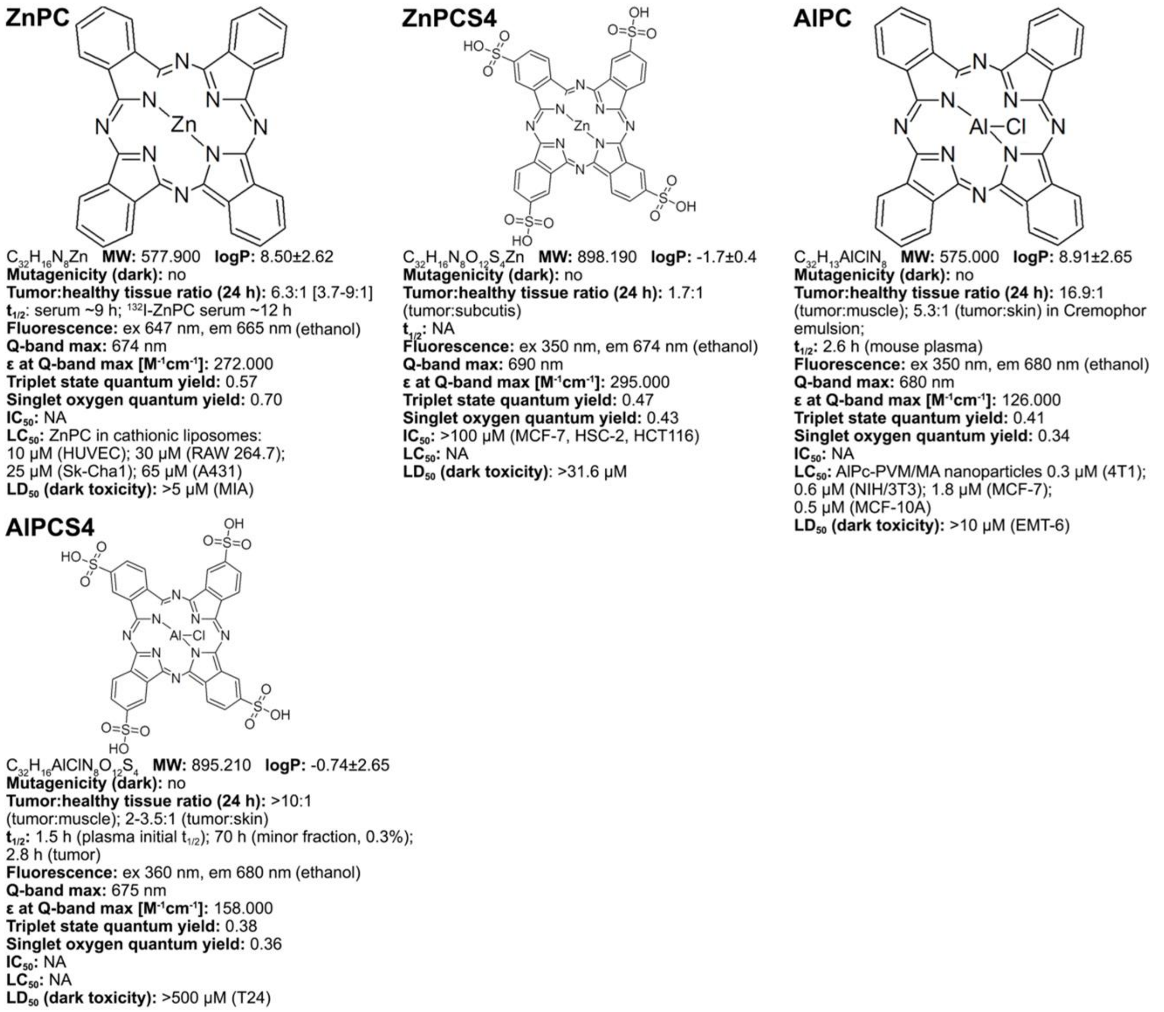

ZnPC

$C_{32}H_{16}N_8Zn$ **MW:** 577.900 **logP:** 8.50±2.62
Mutagenicity (dark): no
Tumor:healthy tissue ratio (24 h): 6.3:1 [3.7-9:1]
$t_{1/2}$: serum ~9 h; ^{132}I-ZnPC serum ~12 h
Fluorescence: ex 647 nm, em 665 nm (ethanol)
Q-band max: 674 nm
ε at Q-band max [$M^{-1}cm^{-1}$]: 272.000
Triplet state quantum yield: 0.57
Singlet oxygen quantum yield: 0.70
IC_{50}: NA
LC_{50}: ZnPC in cathionic liposomes:
10 µM (HUVEC); 30 µM (RAW 264.7);
25 µM (Sk-Cha1); 65 µM (A431)
LD_{50} (dark toxicity): >5 µM (MIA)

ZnPCS4

$C_{32}H_{16}N_8O_{12}S_4Zn$ **MW:** 898.190 **logP:** -1.7±0.4
Mutagenicity (dark): no
Tumor:healthy tissue ratio (24 h): 1.7:1
(tumor:subcutis)
$t_{1/2}$: NA
Fluorescence: ex 350 nm, em 674 nm (ethanol)
Q-band max: 690 nm
ε at Q-band max [$M^{-1}cm^{-1}$]: 295.000
Triplet state quantum yield: 0.47
Singlet oxygen quantum yield: 0.43
IC_{50}: >100 µM (MCF-7, HSC-2, HCT116)
LC_{50}: NA
LD_{50} (dark toxicity): >31.6 µM

AlPC

$C_{32}H_{13}AlClN_8$ **MW:** 575.000 **logP:** 8.91±2.65
Mutagenicity (dark): no
Tumor:healthy tissue ratio (24 h): 16.9:1
(tumor:muscle); 5.3:1 (tumor:skin) in Cremophor
emulsion;
$t_{1/2}$: 2.6 h (mouse plasma)
Fluorescence: ex 350 nm, em 680 nm (ethanol)
Q-band max: 680 nm
ε at Q-band max [$M^{-1}cm^{-1}$]: 126.000
Triplet state quantum yield: 0.41
Singlet oxygen quantum yield: 0.34
IC_{50}: NA
LC_{50}: AlPc-PVM/MA nanoparticles 0.3 µM (4T1);
0.6 µM (NIH/3T3); 1.8 µM (MCF-7);
0.5 µM (MCF-10A)
LD_{50} (dark toxicity): >10 µM (EMT-6)

AlPCS4

$C_{32}H_{16}AlClN_8O_{12}S_4$ **MW:** 895.210 **logP:** -0.74±2.65
Mutagenicity (dark): no
Tumor:healthy tissue ratio (24 h): >10:1
(tumor:muscle); 2-3.5:1 (tumor:skin)
$t_{1/2}$: 1.5 h (plasma initial $t_{1/2}$); 70 h (minor fraction, 0.3%);
2.8 h (tumor)
Fluorescence: ex 360 nm, em 680 nm (ethanol)
Q-band max: 675 nm
ε at Q-band max [$M^{-1}cm^{-1}$]: 158.000
Triplet state quantum yield: 0.38
Singlet oxygen quantum yield: 0.36
IC_{50}: NA
LC_{50}: NA
LD_{50} (dark toxicity): >500 µM (T24)

Figure 2.1 - Molecular structure of zinc phthalocyanine (ZnPC), tetrasulfonated ZnPC (ZnPCS4), aluminum phthalocyanine (AlPC), and tetrasulfonated AlPC (AlPCS4). Photodynamic therapy-pertinent photophysical and photochemical properties as well as dark toxicity and phototoxicity are provided. The molecular structures of ZnPCS4 and AlPCS4 are a representation of one of the possible isomers. Abbreviations: ε, molar extinction coefficient; em, fluorescence emission maximum; ex, excitation wavelength; IC_{50}, half-maximal inhibitory concentration; LC_{50}, median lethal dose (*in vitro*); LD_{50}, median lethal dose (*in vivo*); logP, octanol:water partition coefficient; MW, molecular weight; max, maximum; $t_{1/2}$, circulation half-time. Values in brackets indicate range. Acronyms in parentheses refer to cell lines. Data assembled from literature (6, 22, 25, 26, 38-51).

To date, no study has undertaken a head-to-head comparative analysis of PDT efficacy between water-soluble liposomal ZnPC, ZnPCS4, liposomal AlPC, and AlPCS4 to ascertain the most potent PC-based PS for PDT of difficult-to-treat cancer types at minimal skin phototoxicity. In this study, we therefore encapsulated AlPC into our interstitially targeted liposomes (ITLs). The PS-ITLs have proven anti-tumor efficacy and safety in regard to ZnPC (9, 11, 26) and the formulation is known to passively accumulate in the tumor (52, 53). The ITLs further meet the low skin phototoxicity criteria by (1) being too large to extravasate through endothelial fenestrations and (2) encapsulating a PS with a Q-band absorption maximum that resides favorably in the therapeutic window and solar spectrum (*e.g.*, greater optical penetration depth). The ZnPC-ITLs were compared to AlPC-ITLs and subsequently to their tetrasulfonated variants using an attritional approach in terms of dark toxicity, *in vitro* uptake and intracellular localization, and PDT efficacy, further zooming in on mode of cell death and cell cycle arrest. The main conclusion of the study is that AlPC-ITLs were the most effective PS for PDT of tumor cells.

2.3. Materials and methods

Supplemental material is designated with prefix ‘S.’ A list of abbreviations is provided in the supplemental material. The chemicals and reagents are summarized in Table S2.1. Equipment and disposables are listed in Table S2.2. Sample sizes are indicated per experiment in the results section and/or the figure legends. The concentrations listed are final unless specified otherwise. All procedures involving PSs were performed under dim light.

2.3.1. Materials

ZnPC and AlPC were dissolved in pyridine at a 178 µM and 150 µM stock concentration, respectively. ZnPCS4 and AlPCS4 were dissolved in phosphate-buffered saline (PBS) at a 1-mM stock concentration. All PS stock solutions were stored under a nitrogen atmosphere at room temperature (RT) (ZnPC and AlPC) or at 4 °C (ZnPCS4 and AlPCS4) in the dark. Phospholipids were dissolved in chloroform and stored under a nitrogen atmosphere at -20 °C. The phospholipid concentration of stock solutions was determined spectrophotometrically by an inorganic phosphate quantification method modified from Rouser et al. (9, 54). Physiological buffer was composed of 10 mM HEPES, 0.88% (w/v) NaCl, pH = 7.4, 0.293 osmol/kg (9).

2.3.2. Cell culture

Human epidermoid carcinoma (A431) cells were cultured in T75 flasks in phenol red-containing DMEM medium supplemented with 10% fetal bovine serum (FBS), 100 U/mL penicillin, 100 µg/mL streptomycin, and 2 mM L-glutamine and grown under standard culture conditions (dark, 37 °C, humidified atmosphere composed of 5 % CO2 and 95 % air).

Cells were sub-cultured twice per week at a ratio of 1:14 to maintain a logarithmic growth phase at all stages. The cells were washed with PBS (RT, 10 mL/T75 flask) prior to detachment by incubation with Accutase (1 mL/T75 flask) for 10 min under standard culture conditions. Cells were harvested by the addition of fully supplemented DMEM and transferred to a new T75 flask.

Cells, detached as described above, were seeded into 24-well plates 24 h prior to an experiment unless stated otherwise. A seeding density of 1.5×10^5 cells/well was used to achieve ~90% confluence at the time of the experiment. Cell counting was performed with an aliquot of 10 µL using a hemocytometer and a brightfield microscope.

During the experiments, DMEM without FBS and phenol red (DMEM-/-) was used when cells were incubated with PSs or reagents.

2.3.3. Preparation and characterization of ITLs

ITLs composed of DPPC and DSPE-PEG (96:4) molar ratio were prepared by the lipid film hydration technique as described previously (9). Briefly, the phospholipids and ZnPC or AlPC were premixed at the desired ratios and the organic phase was evaporated under a stream of nitrogen gas at 40 °C in a water bath. The lipid films were vacuum exsiccated for 30 min to remove residual organic solvent and hydrated with physiological buffer. The suspension was tip sonicated and the liposomes were stored at 4 °C under a nitrogen atmosphere in the dark. The PS:phospholipid molar ratio was 0.003 (9). The liposomes were characterized for size and polydispersity as well as zeta-potential by dynamic light scattering and electrophoretic mobility analysis, respectively, as described in (9).

2.3.4. Dark toxicity

The toxicity of each PS was assessed in A431 cells in absence of illumination. Cells seeded in 24-wells plates were washed with PBS at RT, and PS in DMEM-/- was added at concentrations ranging from 0-10 µM for AlPCS4 and ZnPCS4, or from 0-1.5 µM for AlPC-ITLs and ZnPC-ITLs (0-500 µM phospholipid concentration). Medium containing 20% DMSO was used as positive control for complete cell death and DMEM-/- as negative control. After 24, 48, and 72 h incubation with the PS at standard culture conditions, WST-1 and SRB assays were performed as described in sections 2.3.8 and 2.3.9, respectively. Each group (PS concentration and incubation time) was measured in triplicate.

2.3.5. Spectral properties of photosensitizers

The absorption, fluorescence emission, and fluorescence excitation spectra of liposomal ZnPC and AlPC as well as ZnPCS4 and AlPCS4 were determined so that flow cytometry and confocal microscopy could be performed at the proper settings. ZnPC-ITLs and AlPC-ITLs were prepared as described in section 2.3.3 and diluted in physiological buffer to a 1.5 µM PS concentration. ZnPCS4 and AlPCS4 were dissolved in physiological buffer at a 1.5 µM concentration. For fluorescence measurements, the concentration of ZnPCS4 had to be increased to 15 µM for optimal read-out.

Absorption was measured and corrected for physiological buffer (blank sample). Based on the absorption spectrum, the fluorescence excitation wavelength was determined: λex = 650 ± 5 nm for ZnPC, ZnPCS4, and AlPC and 590 ± 5 nm for AlPCS4. Next, based on the fluorescence emission spectrum, the emission wavelength for the excitation spectrum was determined: λem = 707 ± 5 nm for ZnPC, ZnPCS4, and AlPC and 757 ± 5 nm for AlPCS4. Fluorescence emission and excitation spectra were read at a detector gain of 750 V and at a scan rate of 120 nm/min. Fluorescence data were corrected to 0 for the wavelength with the lowest intensity. All data were normalized to the Q band maximum. Normalized spectra were plotted in Origin software (MicroCal, Northampton, MA).

2.3.6. Photosensitizer-cell association analysis by flow cytometry

The interaction between PSs and A431 cells was studied by flow cytometry. All four PS were diluted in DMEM-/- to a PS concentration of 375 nM, corresponding to a final phospholipid concentration of 125 µM for AlPC-ITLs and ZnPC-ITLs.

PSs were added to cells seeded in 12 wells-plates for 1, 30, 60, and 120 min and incubated under standard culture conditions. After harvesting with 100 µL of Accutase for 10 min at standard culture conditions, cells were collected in 500 µL of DMEM-/- at RT, transferred from each well to a 2 mL centrifuge tube (Safe-lock), and centrifuged for 5 min at 500 × g and 4 °C. The supernatant was discarded, cells were resuspended in 500 µL of DMEM-/- at RT, and the samples were analyzed by flow cytometry.

Viable cells were gated based on their preset forward-scatter and side-scatter properties. PS autofluorescence was measured at λex = 633 nm and λem = 661 ± 20 nm and a fixed detector voltage (625 V). The excitation wavelength coincides with the blue Q-band absorption shoulder of the photosensitizers (6), and causes autofluorescence as a result of radiative S1 -> S0 state decay of a small fraction of the excited state electrons. Ten thousand events were collected in the gated region. Association was calculated from the difference between the mean fluorescence intensity of photosensitized cells relative to the mean fluorescence intensity of non-photosensitized cells (N = 3 independent experiments per incubation time). Data were processed in FlowJo software.

2.3.7. Analysis of photosensitizer uptake and intracellular distribution by confocal microscopy

PS uptake and intracellular distribution were assessed by confocal laser scanning microscopy. Cells seeded in 6-wells plates containing a circular sterile 25-mm coverslip were incubated with the PS (1 mL/well) in DMEM-/- for 15, 30, and 60 min at standard culture conditions. The final PS concentrations were 10 μM for AlPCS4 and ZnPCS4 and 3 μM for AlPC-ITLs and ZnPC-ITLs (1 mM phospholipid concentration). Next, cells were washed with PBS (RT, 1 mL/well) prior to fixation with 2% paraformaldehyde (PFA, 1 mL/well) in PBS (RT) for 15 min in the dark. The 2% PFA in PBS was decanted, and wells were washed once with PBS at RT and immersed in 1 mL of ice-cold PBS for storage at 4 °C until confocal microscopy imaging (typically within 24 h).

Directly before imaging, 10 μL of Hoechst 33342 (0.5 mg/mL in water) was added to each sample and incubated for 3 min at RT to stain nuclear DNA of fixed cells. Subsequently, the cover slip was secured in the steel ring of the microscope stage, 1 mL of PBS (RT) was added, and imaging was performed at the following settings: Hoechst (λex = 405 nm; λem = 479 nm), ZnPC-ITLs (λex = 660 nm; λem = 790 nm), AlPC-ITLs (λex = 660 nm; λem = 790 nm), ZnPCS4 (λex = 633 nm; λem = 790 nm), and AlPCS4 (λex = 650 nm; λem = 790 nm). A 63× oil immersion objective was used.

2.3.8. Mitochondrial redox (WST-1) assay

The WST-1 colorimetric assay was performed to determine mitochondrial redox state (55) as part of *in vitro* PS toxicovigilance. The ZnPC and AlPC have a logP of > 8 and hence localize to cell and organelle membranes, including mitochondria (6). Inasmuch as mitochondria play a key role in cell death, particularly when the electron transport chain is dysregulated (56), a mitochondrial redox function assay was selected to gauge dark toxicity of the PSs. The WST-1 assay is ideal because it does not notably interfere in cell physiology, allowing subsequent cell viability analysis by other methods.

Briefly, cells were washed once with PBS (37 °C). WST-1 reagent was added to DMEM-/- at a 1:25 volume ratio. A 300 µL aliquot was transferred to each well (for 24 wells plates) and cells were incubated for 20 min under standard culture conditions. After incubation, 100 µL of the medium containing WST-1 was transferred in duplicate to a 96 wells plate. The absorption was read using a plate reader at 450 nm and a reference wavelength of 620 nm for background subtraction. The background-corrected mean ± SD absorption at 450 nm was calculated per concentration and incubation time ($N = 3$) and normalized to the mean WST-1 absorbance of untreated cells ($N = 3$). Finally, the remainder of the WST-1-containing medium was removed by washing once with PBS (37 °C) using a squirt bottle and processed further for total protein content as described in the next section.

2.3.9. Cell viability (SRB) assay

The sulforhodamine B (SRB) colorimetric assay was used to measure total protein content as a more definitive parameter of cytotoxicity. This assay is based on the premise that dead and late-stage dying cells detach from the well plate bottom, leaving only viable cells that are stained and semi-quantified (57).

Following the single wash, cells were tapped dry and fixed with 300 µL of 10% ice-cold trichloroacetic acid in Milli-Q for at least 1 h at 4 °C. Next, the cells were washed 5 × with Milli-Q (RT) using a squirt bottle and stained with 0.4% SRB dissolved in 1% acetic acid in Milli-Q for at least 15 min (300 µL/well for a 24-well plate). The SRB solution was decanted, and the cells were washed 4 × with 1% acetic acid in a squirt bottle (RT) to remove unbound SRB. The well plate was left to dry at 37 °C for at least 15 min. Once dried, 500 µL of 10 mM unbuffered TRIS base in Milli-Q (RT) was added to each well and the plate was gently rocked for at least 1 min to completely dissolve the SRB. Absorption was measured in a microplate reader at 564 nm and 600 nm and a reference wavelength of 690 nm for background correction. The corrected mean ± SD absorption at 564 nm was calculated per concentration and incubation time and normalized to the corrected mean SRB absorbance of untreated cells (N = 3/group). Absorbance data at 600 nm were used to determine cell viability when the optical density of the 564 nm read was > 1.3.

2.3.10. PDT of cultured cells

To compare photodynamic efficacy between the PSs, mitochondrial redox state and total protein content were measured after PDT. Cells seeded in 24 wells plates were incubated for 1 h with PS in DMEM-/- as described in section 2.3.2. Next, cells were washed once with PBS (RT, 500 µL/well) and received fresh DMEM-/- (37 °C, 500 µL/well). The cells were illuminated with a 671 nm solid state diode laser at 500 mW for 57 s/well (the diameter of the beam was equal to the diameter of each well; 15.6 mm, 1.9 cm^2), equating to a cumulative radiant exposure of 15 J/cm^2 per well. The laser output power was confirmed with a power meter before every illumination. A black surface was placed below the 24 wells plate to absorb stray light during illumination. Following illumination, the cells were incubated in DMEM-/- for 4 h or 24 h at standard culture conditions to emulate PDT-induced malnutrition due to vascular shutdown (58, 59). Lastly, the WST-1 assay followed by the SRB assay were performed as described in sections 2.3.8 and 2.3.9, respectively. The results were normalized to the mean of the control group containing only medium (N = 3/group). Graphs and LC_{50} values were obtained using the non-linear fit data analysis in Prism (GraphPad Software, San Diego, CA, USA).

2.3.11. Analysis of mode of cell death

Cell death was characterized according to phosphatidylserine externalization (indicative of apoptosis) and plasma membrane disruption (indicative of necrosis), which were analyzed by flow cytometry. Cells seeded in 12 well plates were treated by PDT as described in section 2.3.10. Illumination was performed at 500 mW for 1 min and 54 s, accounting for a cumulative radiant exposure of 15 J/cm^2 per well. The plate was kept at 37 °C using a plate heater during PDT. After 2 h, 4 h, and 8 h of incubation at standard culture conditions (N = 3 per time point), the medium was transferred into 15 mL sterile centrifuge tubes, along with the attached cells that were harvested following trypsinization (100 µL of Accutase for 10 min at standard culture conditions). Cells were then centrifuged at 500 × g for 5 min and 4 °C. The supernatant was decanted, and the cell pellet was resuspended in 100 µL of 1 × annexin V binding buffer (RT) containing 5 µL of Alexa Fluor 488-conjugated annexin V. The annexin V binding buffer was diluted 5 × with Milli-Q. After 15-min incubation at RT, 399 µL of diluted annexin V binding buffer was added, and the cell suspension was transferred to 5-mL round-bottom flow cytometry tubes. Subsequently, 1 µL of propidium iodide (PI, 0.1 mg/mL diluted annexin V binding buffer) was added 5 min prior to flow cytometry. Cells were gated based on forward scatter and sideways scatter properties. Cell remnants and cell-derived microparticles were gated out. Annexin V and PI fluorescence was measured at λex = 488 nm, λem = 530 ± 30 nm and λex = 488 nm, λem = 670 nm long pass filter, respectively. Ten thousand events were collected in the gated region. The scatterplots were analyzed in FlowJo software (BD Biosciences, Franklin Lakes, NJ, USA), where quadrants were positioned based on the green and red fluorescence of untreated cells. Viable cells were quantified as annexin V-negative / PI-negative, while cells that were in early apoptosis were quantified as annexin V-positive / PI-negative. Cells in late apoptosis and necrosis were clustered and quantified as annexin V-positive / PI-positive and annexin V-negative / PI-positive, respectively (modified from (60)). Data were plotted in Prism.

2.3.12. Cell cycle analysis

To determine the effects of PDT on cell cycle phases (DNA content; G0/G1, S and G2/M), PDT-treated cells were stained with PI and analyzed by flow cytometry (10, 12, 17). Cells seeded in 12-well plates were incubated for 60 min with PS (ZnPC-ITLs and AlPC-ITLs, 31.25 µM PS concentration; ZnPCS4 and AlPCS4, 0.31 µM) in DMEM-/- (37 °C, 1000 µL/well). After washing with PBS (37 °C), fresh DMEM-/- was added and cells were illuminated as described in section 2.3.10 (N = 3 per PS) or kept in the dark (control cells). Cells were harvested 24 h after PDT (or incubation in the dark) with Accutase (100 µL/well, 10 min at standard culture conditions) in 1 mL of PBS (RT). The cells were transferred to 15-mL sterile centrifuge tubes and washed twice by centrifugation at 500 × g for 5 min and 4 °C. Following the second centrifugation step, the supernatant was decanted and the pellet was resuspended in 300 µL of PBS (RT). Cells were fixed by dropwise addition of 700 µL of ice-cold 96% ethanol under continuous swirling. PBS (1 mL at RT) was added and cells were centrifuged for 5 min at 500 × g and 4 °C. The supernatant was discarded and cells were resuspended in 200 µL of PI staining solution (20 µg/mL PI and 100 µg/mL RNAse A in PBS) in 300 µL of PBS (RT). Flow cytometry was performed as described for PI in section 2.3.11. The percentage of the cell population in the G0/G1 phase, S phase, and G2/M phase was calculated applying the Watson (Pragmatic) univariate model (61) in FlowJo.

2.4. Results and discussion

2.4.1. The utility of passive tumor targeting by metallated phthalocyanines as part of a comprehensive tumor-targeting photosensitizer platform and the need for systematic photosensitizer selection

Solid tumors in internal organs essentially have three druggable targets for PDT: the tumor cells that make up the tumor parenchyma, the intratumoral vasculature that supplies the tumor with oxygen and nutrients, and the tumor interstitial space that forms the tumor microenvironment (6). We have developed and tested PEGylated liposomal photomedicines for each of these targets, which are dubbed tumor cell-targeting liposomes (TTLs) (18), endothelium-targeting liposomes (ETLs) (10, 12, 17, 26, 62), and ITLs (9, 11), respectively. These liposomal formulations are intended to deliver PSs to the tumor (Figure 2.2) and can be combined into a single cocktail for intravenous administration to comprehensively photosensitize key anatomical sites of the tumor. Multi-targeted photosensitization reduces the opportunity for PDT-subjected tumor cells to recover from photochemically-induced hyperoxidative stress (63) via the activation of survival pathways (64), as has been shown to occur following PDT (11, 26).

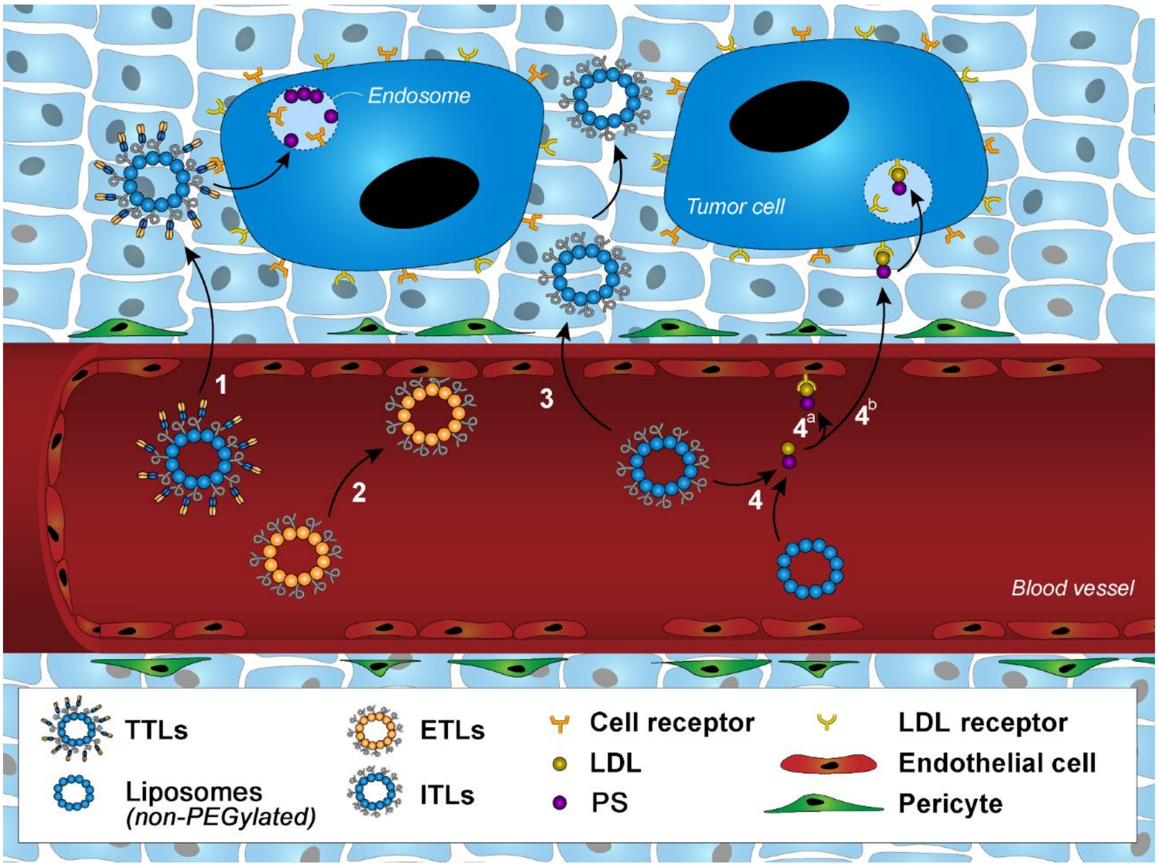

Figure 2.2 - Multi-targeted photonanomedicines platform for photodynamic therapy (PDT) of solid tumors. Photosensitizer (PS) molecules can be delivered to key tumor anatomical sites via 4 delivery routes, designated 1-4. For photosensitization of parenchymal cells (route 1), tumor cell-targeting liposomes (TTLs) can be used that are decorated with surface protein recognition domains (*e.g.*, nanobodies) designed against proteins that are overexpressed on tumor cells. Following extravasation through inter-endothelial gaps in the tumor vasculature, the TTLs bind to the cognate ligand and are subsequently internalized to deliver the PS cargo. PDT of TTL-delivered PS results in tumor cell death. Similarly, the tumor vasculature can be photosensitized using endothelium-targeting liposomes (ETLs; route 2), which are PS-encapsulating PEGylated cationic liposomes. The positive charge of the liposome surface leads to preferential association with the overly negative charge of the tumor endothelial glycocalyx, leading to liposomal uptake (19) and PS delivery. PDT of ETL-delivered PS results in vascular occlusion and tumor cell death due to anoxia and nutritional deprivation. The tumor microenvironment can be photosensitized by passive diffusion of PS-encapsulating PEGylated interstitially targeted liposomes (ITLs) into the stroma (route 3) via the enhanced permeability and retention (EPR) effect. PDT of ITL-delivered PS leads to oxidative damage to structural proteins and stromal cells, including resident immune cells. It has also been reported that the PS can be extracted from non-PEGylated ITLs in the circulation by low density lipoprotein (LDL) and delivered to tumor cells following LDL uptake by LDL receptors (41, 65, 66) (route 4). PDT of LDL-delivered PS leads to endothelial damage (thrombosis, vascular shutdown) and parenchymal damage (tumor cell death).

This study is centered on interstitial targeting and the ITL component of the platform. The lipophilic PS-containing ITLs are directed into the tumor by passive diffusion through leaky intratumoral vasculature in accordance with the enhanced permeability and retention (EPR) effect (52, 53). Compositionally similar formulations have been clinically approved and are used in oncological patients to deliver chemotherapeutics such as doxorubicin (67, 68), vincristine (69, 70), and irinotecan (71) to tumors. The EPR-based passive targeting equally applies to water-soluble PC derivatives (ZnPCS4 and AlPCS4); an alternative to ITL-based tumor photosensitization and second focus of this study. AlPCS4 was demonstrated to abundantly accumulate in tumor xenografts 2-4 h following intravenous administration (22, 25). The pharmacokinetics of hydrophilic PC derivatives depend on the degree of sulfonation and generally follow an inverse relationship between rate of intratumoral accumulation and the logP of the PC derivative (22, 72, 73).

The eventual localization of the PC-based PSs that passively diffuse into tumors is currently elusive. The intratumoral sites that become photosensitized ultimately dictate the tumoricidal efficacy (6, 74). Photosensitization of tumor cells is most critical insofar as hyperoxidative stress in parenchymal cells inflicts direct damage to key components that leads to activation and execution of cell death mechanisms that in turn prime a subsequent anti-tumor immune response (75). Photosensitization of multiple intracellular loci is preferable for therapeutic outcome (6, 74, 76). Oxidative damage to cellular and non-cellular constituents of the tumor microenvironment (77-79) and vascular shutdown (28, 80-83) is, in the broader context of PDT, considered a secondary phenomenon with largely an adjuvant contribution to PDT outcome.

Accordingly, uptake of ZnPC-ITLs, ZnPCS4, AlPC-ITLs, and AlPCS4 by tumor cells in addition to photosensitizing the tumor stroma and interstitial space would be beneficial to PDT efficacy and negates the necessity of co-administering TTLs. The TTLs are more difficult to mass-produce under GMP conditions and are also considerably more costly due to the use of biologicals (*e.g.*, nanobodies). Coincidentally, despite PEGylation and non-association of ITLs with certain blood cells (21, 84), ZnPC-ITLs were found to be taken up by and photosensitize tumor cells (9, 11) and therefore inherently possess multi-targeting properties, which may be advantageous to therapeutic efficacy. How the dark toxicity, uptake kinetics, intracellular distribution, and phototoxicity of ZnPC-ITLs compare to those of ZnPCS4, AlPC-ITLs, and AlPCS4 is currently elusive yet important to understand in a PS selection trajectory with clinical implementation as final aim. These parameters were therefore investigated by stepwise attrition in human epidermoid carcinoma (A431) cells to arrive at the most suitable PSs for PC-based PDT.

A431 cells were used because [1] these cells have a dysfunctional P53 tumor suppressor gene (85) – a feature shared by a plethora of cancers (86) – and [2] the cells overexpress epidermal growth factor receptor (EGFR) (87), which is a metabolically important receptor in many tumors (88) and is downregulated by PDT (26, 89). A431 cells therefore act as a generic test system that could be extended to spin-off PDT studies with specific cancer types.

2.4.2. Liposomal phthalocyanines are not cytotoxic up to 1.5 µM, while tetrasulfonated phthalocyanines induce mild-to-moderate dark toxicity at concentrations of ≥ 2.5 µM

In the absence of light, the PSs should not confer any toxicity (5). In a PS attrition approach, the manifestation of dark toxicity therefore constitutes a first-step measure that could signal the discontinuation of a PS. Accordingly, PS concentration-dependent and clinically relevant incubation time-dependent dark toxicity were determined with the WST-1 assay, given the preferential localization of ZnPC and AlPC to mitochondrial membranes (90, 91). Analysis of the mitochondrial redox state was ensued by the SRB assay of the same cell culture as a robust method for general cell death (57). DMSO (20%) was used as positive control for complete cell death and DMEM-/- as negative control.

Without photoactivation, the ZnPC-ITLs (122 ± 1 nm, PDI = 0.49 ± 0.02, ζ-potential = -10.1 ± 1.1 mV; Figure S2.1) and AlPC-ITLs (173 ± 7 nm, PDI = 0.68 ± 0.02, ζ-potential = -9.6 ± 1.1 mV; Figure S2.1) did not induce notable A431 cell death up to a PS concentration of 1.5 µM, equating to 500-µM final lipid concentration (Figure 2.3). This PS and lipid concentration range had been employed in previous work on ZnPC-ITLs (9, 11) with comparable results. Dark incubation of cholangiocarcinoma (Sk-Cha1) cells with ZnPC-ITLs at 1.5 µM:500 µM PS:lipid concentration produced no dark toxicity (9, 11). In toxicogenomics investigations, none of > 40,000 analyzed gene transcripts were dysregulated in Sk-Cha1 cells at these ZnPC and lipid concentrations compared to buffer control (11), underpinning the non-toxicity of ZnPC as well as the ITLs in the absence of light. The results were reproducible for AlPC-ITLs in A431 cells with both cell viability assays.

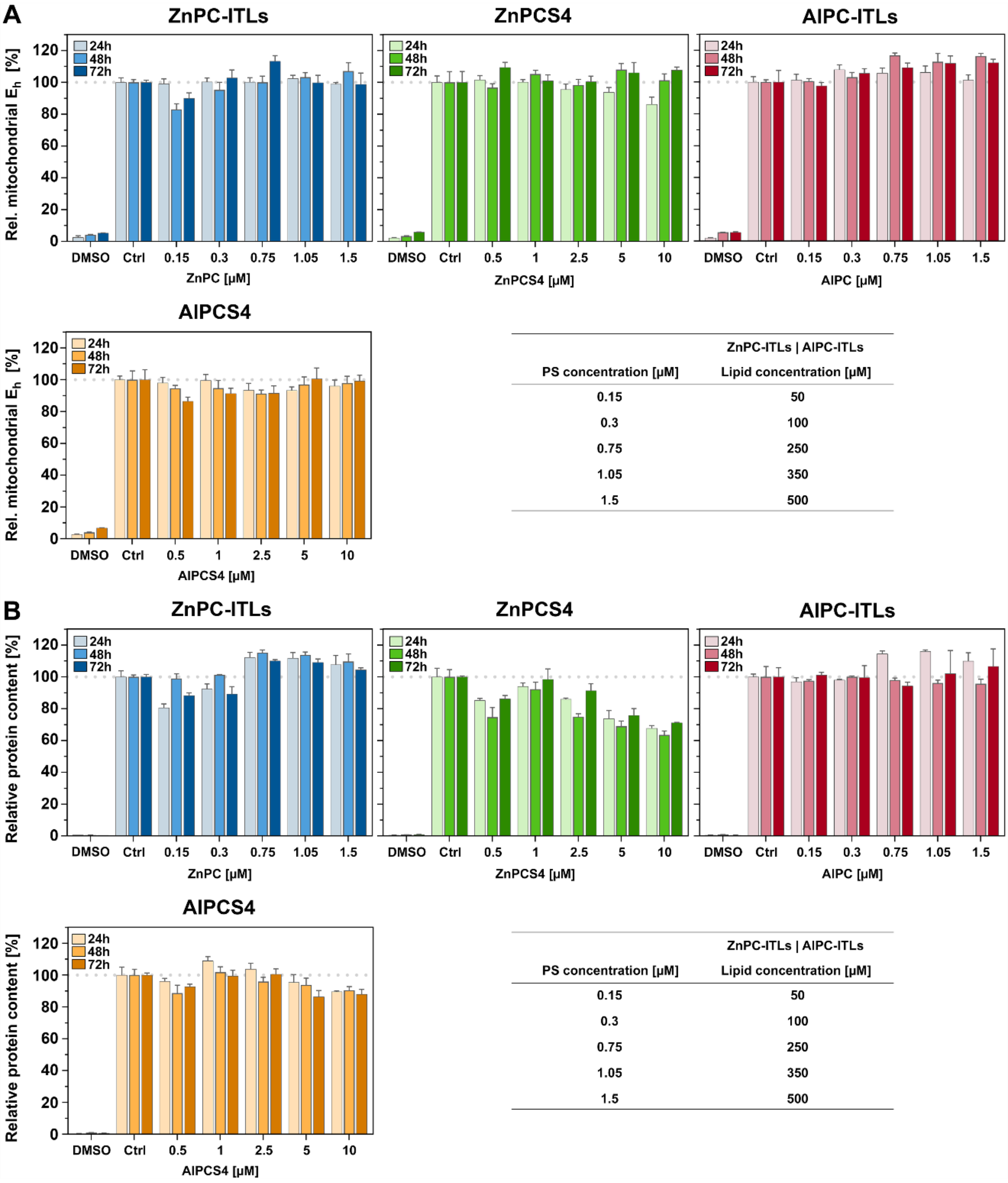

PS concentration [µM]	ZnPC-ITLs | AlPC-ITLs Lipid concentration [µM]
0.15	50
0.3	100
0.75	250
1.05	350
1.5	500

PS concentration [µM]	ZnPC-ITLs | AlPC-ITLs Lipid concentration [µM]
0.15	50
0.3	100
0.75	250
1.05	350
1.5	500

Figure 2.3 - *In vitro* dark toxicity. A431 cells were incubated with AlPC-ITLs and ZnPC-ITLs (0-1.5 µM final concentration) and AlPCS4 and ZnPCS4 (0-10 µM final concentration) in DMEM$^{-/-}$ and maintained under standard culture conditions for 24 h, 48 h, and 72 h. Cell were assayed by WST-1 for mitochondrial redox state **(A)** and by SRB for total protein content **(B)**, both used as indicator of cell viability. Positive control comprised 20% DMSO in DMEM$^{-/-}$ while the negative control was DMEM$^{-/-}$. Data (N = 3 per concentration per time point) were normalized to the control group mean. The tables provide the final lipid concentration of ITLs per photosensitizer concentration, all at a photosensitizer:lipid molar ratio of 0.003. Abbreviations: AlPC, aluminum phthalocyanine; AlPCS4, tetrasulfonated aluminum phthalocyanine; E_h, redox potential; ITLs, interstitially targeted liposomes; PS, photosensitizer; Rel., relative; ZnPC, zinc phthalocyanine; ZnPCS4, tetrasulfonated zinc phthalocyanine.

ZnPCS4 and AlPCS4 exhibited moderate (up to 30% cell death) and mild (up to 10% cell death) dark toxicity in A431 cells, respectively, that was concentration-dependent but not incubation time-dependent (Figure 2.3B). As opposed to the lipophilic PS, the tetrasulfonated species mainly occupy the cytoplasm and are excluded from mitochondria (92). In line with this localization pattern, cytotoxicity was revealed through the SRB assay but not the WST-1 assay. Contrastingly, Qualls et al. (92) reported no dark toxicity of AlPCS4 in human nasopharyngeal carcinoma (KB) cells following 4 h loading of up to 2.5 mM AlPCS4 and subsequent 48-h incubation. Similarly, no dark toxicity ($LC_{50} > 100$ μM) was observed for ZnPCS4 in human mammary carcinoma (MCF-7) cells, human oral squamous cell carcinoma (HSC-2) cells, and human colorectal carcinoma (HCT 116) cells (39), altogether indicating that the sensitivity to the tetrasulfonated PCs is cancer cell line-dependent. Neither ZnPCS4 nor AlPCS4 exhibited toxicity at the highest tested concentration of ZnPC and AlPC (1.5 μM) in A431 cells.

2.4.3. Liposomal and tetrasulfonated metallated phthalocyanines are taken up by cancer cells and rapidly disperse to multiple (intra)cellular loci

A compound can only exert cytotoxic effects if it associates with cells and is internalized. In the second attrition step, the association, internalization, and intracellular distribution of the PSs with cells were assayed by flow cytometry and confocal microscopy, respectively, using the intrinsic fluorescence properties of the metallated PCs (Figure S2.2). Inasmuch as the molar extinction coefficient, fluorescence quantum yield, molar absorptivity at 671 nm, and fluorescence lifetime differ among the PSs (6, 93, 94) the fluorescence intensity cannot be used for intergroup comparison, but only intragroup analysis to *e.g.*, monitor changes over time.

Flow cytometry revealed that all PSs associated with cells within 1 min of interaction and that the PS-cell interaction became more profuse with incubation time (Figure 2.4 A). All PSs entered the tumor cells and gradually distributed throughout the cells over the course of 1 h without entering the nucleus (Figure 2.4 B).

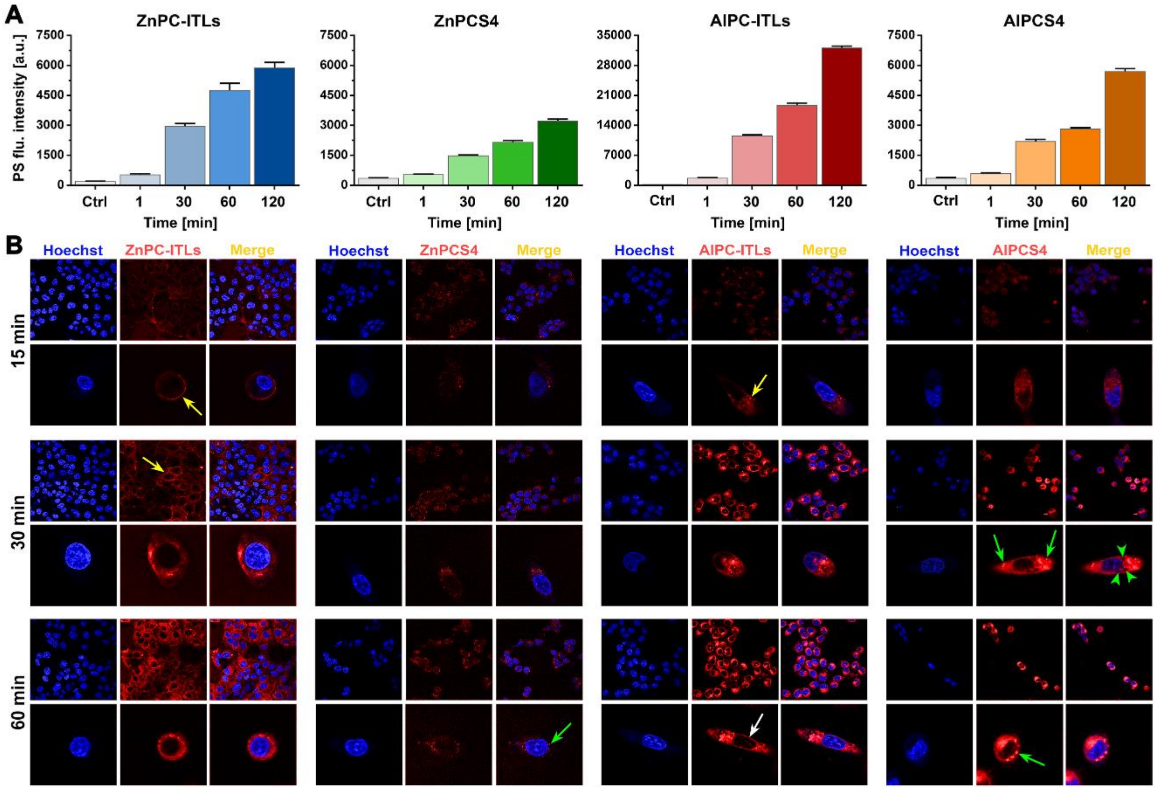

Figure 2.4 - Uptake and intracellular distribution of native and tetrasulfonated zinc- and aluminum phthalocyanine in A431 cells. (A) A431 cells were incubated with 0.375 μM of photosensitizer (PS) in DMEM$^{-/-}$ for 1-120 min and analyzed by flow cytometry. The mean PS autofluorescence intensity is plotted as a function of incubation time (N = 3 per time point). **(B)** A431 cells were incubated with AlPC-ITLs and ZnPC-ITLs (3 μM PS concentration, 1000 μM lipid concentration) and AlPCS4 and ZnPCS4 (10 μM) for 15-60 min and imaged by confocal microscopy (red fluorescence). Hoechst 33342 (blue fluorescence) was used to stain DNA. The yellow arrows designate photosensitizer accumulation in the cell membrane (ZnPC) and intracellular dispersion via vesicular trafficking (AlPC). The white arrow points to perinuclear accumulation of ITL-delivered AlPC. The green arrows point to hyperfluorescent compartmentalized ZnPCS4 and AlPCS4. The green arrowheads indicate perinuclear compartments devoid of AlPCS4. Additional exemplary images are provided in Figure S3. Abbreviations: AlPC, aluminum phthalocyanine; AlPCS4, tetrasulfonated aluminum phthalocyanine; flu., fluorescence; ITLs, interstitially targeted liposomes; PS, photosensitizer; ZnPC, zinc phthalocyanine; ZnPCS4, tetrasulfonated zinc phthalocyanine.

The current results regarding PC-ITLs corroborate our previous findings that ITLs are taken up by cultured human cholangiocarcinoma (Sk-Cha1) cells and therefore - at that time assumingly - deliver lipophilic PC molecules into the cell (9). In those prior studies we employed the lipophilic tracer rhodamine-PE as PC mimetic and observed its distribution across the cell and organelles (mitochondria) during 4-h incubation by fluorescence microscopy. Corroboratively, the uptake of different non-targeted liposomes has also been reported for other cancer cell lines by other research groups (90, 95). From previous work (9, 90, 95) together with the confocal microscopy data (Figure 2.4 B) it can be concluded that the entire macromolecular complex is internalized by cells, after which the individual components scatter to different subcellular loci (17). ITL uptake by A431 cells was not facilitated by proteins adsorbed to the liposome surface (96), as the ITLs were added to medium that was not supplemented with FBS or proteinaceous constituents. PEGylation did not impair cell entry, nor did it notably interfere with uptake dynamics (Figure 2.4 A), particularly when the intracellular ZnPC fluorescence pattern of PEGylated ZnPC-encapsulating liposomes (this study) is juxtaposed to that of ZnPC delivered into transformed rat embryo (4R) fibroblasts by non-PEGylated liposomes (ZnPC-liposomes from Ciba-Geigy composed of POPC and OOPS at a 9:1 w/w ratio) (90).

The intracellular distribution of ITL-delivered ZnPC occurred at a slower rate than ITL-delivered AlPC (Figure 2.4 B) despite an equal degree of PEGylation and liposomal membrane surface properties, which govern nanoparticle-cell interactions in our test system (95). Apparently, the central coordinated metal in phthalocyanines not only dictates photophysical and photochemical properties of phthalocyanines (94, 97-99) but also their intracellular distribution kinetics following liposomal delivery. Changes in localization are well-documented for PS that have been covalently modified with functional groups (100), but not per se as a result of coordinated metal substitution. The dissimilar distribution kinetics between ZnPC and AlPC are reflected in the differential compartmentalization in the early stages of ITL-cell interactions. After 15-min incubation, ZnPC mainly accumulated in the outer membrane (Figure 2.4 B, yellow arrows) and progressively populated intracellular sites. AlPC did not exhibit an initial accumulation in the cell membrane but rapidly dispersed throughout the cell via intracellular vesicles (Figure 2.4 B, yellow arrow). After 60-min incubation the intracellular presence and distribution of ZnPC and AlPC were mostly comparable. Both PCs photosensitized numerous (intra)cellular loci that are known to include the membranes of mitochondria, endoplasmic reticulum, Golgi apparatus, and lysosomes (51, 90, 101). AlPC also localized to or at the nuclear membrane at 60-min incubation (Figure 2.4 B, white arrow) while ZnPC did not. More detailed examples of the differential intracellular localization of the PSs are provided in Figure S2.3.

The differential uptake kinetics of ZnPC and AlPC over the course of 1 h are rather inconsequential to clinical PDT outcomes relative to the employed drug-light intervals, that are generally in the order of 1-2 days. Intracellular localization, on the other hand, is not trivial in clinical context insofar as nuclear membrane photosensitization may contribute to additional or preferential modes of cell death that could account for more profound phototoxicity and/or anti-tumor immune response, respectively (6).

The association profile of ZnPCS4 and AlPCS4 with A431 cells was comparable to that of ITL-delivered ZnPC and AlPC, respectively. Intracellular fluorescence of tetrasulfonated ZnPC and AlPC increased over time and did not reach saturation over the course of 1 h (Figure 2.4 A). In contrast to the parent compounds, AlPCS4 did not exhibit such profound compartmentalization initially, although fluorescent clusters were observed at longer incubation times (30 min and beyond) (Figure 2.4 B, green arrows). Instead, AlPCS4 distributed more homogenously throughout the entire cell except the nucleus and some perinuclear compartments (Figure 2.4 B, green arrowheads). Similar intracellular distribution patterns have been observed for AlPCS in Chinese hamster lung (V-79) fibroblasts (24 h incubation, 50 μM), where the extent of internalization and hence photosensitization was reliant on the degree of sulfonation and proceeded in the order of tetrasulfonated > trisulfonated > disulfonated (102). Compartmentalized AlPCS4 was also observed in KB cells following 4 h incubation at 12.5 μM PS concentration (92). Intracellular localization of ZnPCS4 was more difficult to assess by confocal microscopy due to the debilitating effect of the Zn atom on PC fluorescence quantum yield and fluorescence lifetime (94, 97-99) (Figure 2.4 B). Despite the hampered fluorescence intensity, the distribution pattern suggested early onset compartmentalization of ZnPCS4 (Figure 2.4 B, green arrows) in what are most likely lysosomes, given the strong negative charge of ZnPCS4 in combination with the near-immediate manifestation of clustering (Figure 2.4 B) (6, 100, 103).

The confocal microscopy results attest to the possibility to guide intracellular PC localization by the chemical composition of the PC, if intracellular delivery *in vivo* is successful. Photosensitization of specific intracellular loci is generally reserved for individual classes of PSs (6). For example, ALA can be used to photosensitize mitochondria after conversion to protoporphyrin IX (104, 105). Temoporfin (mTHPC) exhibits a preference for the endoplasmic reticulum and Golgi apparatus (106). Porfimer sodium chiefly localizes to the cell membrane and Golgi apparatus (107), while anionic PSs mostly end up in lysosomes (100, 103).

Damage to each subcellular structure triggers its unique cell death signaling cascade (108); intracellular PS localization is therefore important for therapeutic efficacy and outcome. Based on the confocal imaging, PCs can be directed to important intracellular sites by selecting the appropriate coordinated metal (109) and by employing tetrasulfonated derivatives, which are also commercially available, at least for ZnPC and AlPC. Accordingly, using multiple metallated PC(S4)s in a single PS delivery platform is expected to lead to more comprehensive photosensitization of tumor cells and consequently the photochemical activation of various critical modes of cell death (necrosis, apoptosis, necroptosis, and autophagy) upon PDT (6, 100, 103). It should be noted that most cell death pathways may diverge to necrotic cell death *in vivo* (6, 100, 103, 110) when these concur with vascular shutdown-mediated hypoxia (58, 59, 111-113) (*e.g.*, ATP depletion (114)) and metabolic catastrophe (*e.g.*, ceased nutrient supply (115) and ATP production (26)), which both favor necrosis (108). In any respect, the PS delivery platform illustrated in Figure 2.2 can be further finetuned by incorporating multiple metallated PCs and sulfonated derivatives for a comprehensive approach to photochemical cell death induction.

2.4.4. Aluminum-based phthalocyanines are more phototoxic than zinc-based phthalocyanines

The extent to which each light-exposed PS kills cancer cells constituted the next step in the attrition procedure. A431 cells were photosensitized at increasing PS concentration and the LC_{50} was calculated from the concentration-effect fitted curve functions as a measure of cell phototoxicity and PDT efficacy. Inter-PS differences between the Q-band absorption maximum of ZnPC, AlPC, and AlPCS4 (Figure 2.1 and S2.2) and the laser wavelength (671 nm) were discounted. The decrease in molar extinction coefficient, and hence the extent of ROS generation, due to a mismatch between the Q-band maximum and laser line was deemed too small to produce significant differences in outcome (*e.g.*, differences that would not exceed the standard deviation). For ZnPCS4, the absorption of 671 nm light is about 40% of that at the absorption maximum, translating to a molar absorptivity (ε = 118,000) that approximates the molar absorptivity of AlPC (ε = 126,000) and AlPCS4 (ε = 158,000) at their absorption maximum (Figure 2.1), which is near the 671-nm laser wavelength. At published triplet state quantum yields of 0.47, 0.41, and 0.38 of ZnPCS4, AlPC, and AlPCS4, respectively, and singlet oxygen (1O2) quantum yields of 0.43, 0.34, and 0.36, respectively (Figure 2.1), the amount of ROS produced by ZnPCS4 should theoretically not veer much from the amount of ROS produced by the Al-based PSs. In light of the intracellular distribution pattern (Figure 2.4 B), the aforementioned photophysical and photochemical properties, and experimental data, it was expected that phototoxicity would be most eminent for the ITL-delivered lipophilic PCs and proceed in the order of ZnPC-ITLs > AlPC-ITLs > AlPCS4 >> ZnPCS4. The (peri)nuclear localization of AlPC observed in this study (Figure 2.4 B) and the unexpectedly more overwhelming fluorogenic redox probe oxidation by AlPC versus ZnPC in physiological buffer published previously (6) could narrow or even tilt the phototoxicity in favor of AlPC.

Indeed, ITL-delivered AlPC was most phototoxic to A431 cells as evidenced by the LC_{50} values for both read-out parameters, which were in the low-nanomolar range (Figure 2.5). The LC_{50} values for ZnPC-ITLs were 5 fold (4 h post-PDT) and 3-10 fold higher (24 h post-PDT) compared to AlPC-ITLs. The LC_{50} could not be calculated for ZnPCS4, making the phototoxicity order AlPC-ITLs > ZnPC-ITLs > AlPCS4 >> ZnPCS4. The cellular phototoxicity of the photosensitizers mimics their ROS-generating capacity reported earlier (6). The fact that the degree of lethality was exacerbated for all PSs except ZnPCS4 at 24 h post-PDT compared to 4 h post-PDT indicates that the execution of cell death pathways predominated over any survival signaling (11, 26, 64), damage remediation, and salvage mechanisms. We could not confirm the utility of ZnPCS4 in PDT of A431 cells as reported previously for other cell types (28, 29, 32).

The pleiotropic photosensitization pattern of lipophilic metallated PCs (Figure 2.4 B) seems to be advantageous to photokilling efficacy (Figure 2.5), as was expected for membrane-targeting PSs and the lethality of multi-site-targeted PSs (74). PCs such as ZnPC produce ROS via type I (superoxide anion, hydroxyl radical (•OH), and hydrogen peroxide) (116) and type II photochemical reactions (1O2) (117, 118). 1O2 has a very short half-life (< 40 ns) in a biological milieu (119) because of its extreme reactivity towards lipids, proteins, and nucleic acids (120, 121). The same applies to •OH (122, 123), whose reactivity is so high that the reaction rate constants towards organic biomolecules (124) approximate the diffusion-controlled limit in aqueous solution (125). Accordingly, both ROS have a narrow action radius (119, 125) and inflict deleterious redox modifications proximal to their production site (9, 126).

Photogeneration of ROS in cellular and subcellular membranes, where phospholipids consequently undergo peroxidation by 1O2 (127) and •OH-induced radical chain-propagated oxidation (128), has lethal consequences on membrane function and (sub)cellular homeostasis (129). Oxidation of membrane constituents results in increased barrier permeability and leakage of content (9, 130), loss of mitochondrial membrane potential, and disruption of membrane-associated signaling systems (114, 131); *e.g.*, precursor events to various forms of cell death (132, 133). ROS produced by lipophilic PCs also oxidatively modify (transmembrane) proteins and deregulate vital systems in cell metabolism, damage remediation, and proliferation (26, 134). Ergo, when local PDT-induced hyperoxidative stress culminates in [1] metabolic catastrophe (redox damage to mitochondria); [2] the cell's inability to resolve the stress due to impaired protein and lipid synthesis (redox damage to the endoplasmic reticulum), and [3] hampered post-translational modifications to proteins and protein trafficking (redox damage to the Golgi apparatus), cell death signals are triggered that result in a mix of predominantly apoptosis and necrosis (9, 10, 17, 62, 135). Leakage of lysosomal content (redox damage to lysosomes) [4] will further amplify the cell death signaling (136).

The results in Figure 2.5 demonstrate that, at equimolar concentrations, photosensitization of most lipophilic subcellular compartments by ZnPC and AlPC translates to more cell death upon PDT than photosensitization of cytosolic regions and lysosomes by AlPCS4. As per attrition scheme, the multi-targeted photonanomedicines platform (Figure 2.2) would benefit most from AlPC compared to the other tested metallated PCs. Theoretically, equal tumoricidal effects could be realized with lower AlPC-ITL dosages compared to ZnPC-ITLs, which aligns with the aim to augment therapeutic efficacy while minimizing photoallergic skin reactions. To date we have been developing the PS delivery platform using ZnPC (9-12, 17, 18, 26, 62). Future research efforts will therefore be directed at head-to-head analysis of liposomal AlPC versus liposomal ZnPC with respect to *in vivo* skin phototoxicity, systemic toxicity, intratumoral PS accumulation, and PDT efficacy.

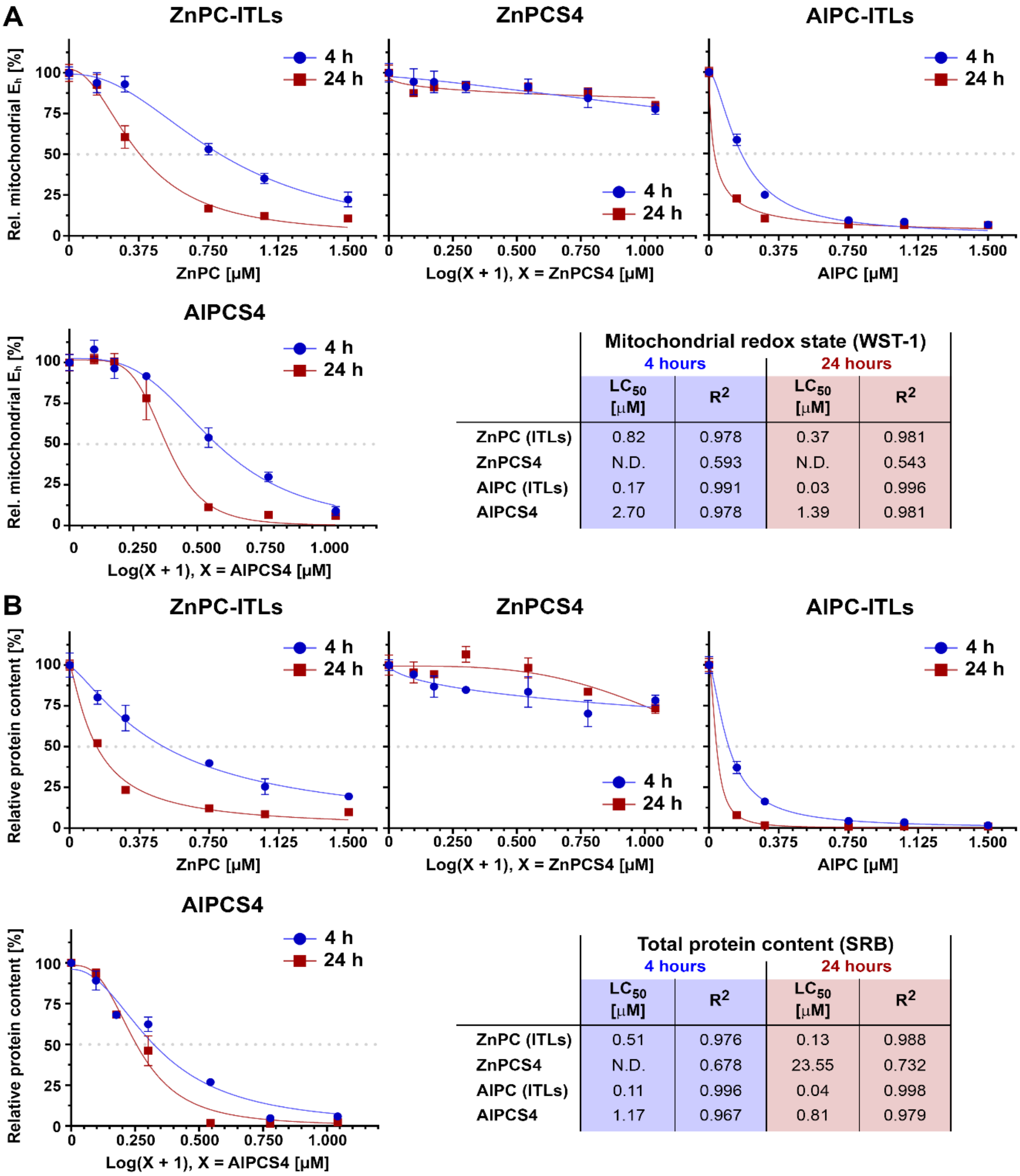

	Mitochondrial redox state (WST-1)			
	4 hours		24 hours	
	LC$_{50}$ [µM]	R^2	LC$_{50}$ [µM]	R^2
ZnPC (ITLs)	0.82	0.978	0.37	0.981
ZnPCS4	N.D.	0.593	N.D.	0.543
AlPC (ITLs)	0.17	0.991	0.03	0.996
AlPCS4	2.70	0.978	1.39	0.981

	Total protein content (SRB)			
	4 hours		24 hours	
	LC$_{50}$ [µM]	R^2	LC$_{50}$ [µM]	R^2
ZnPC (ITLs)	0.51	0.976	0.13	0.988
ZnPCS4	N.D.	0.678	23.55	0.732
AlPC (ITLs)	0.11	0.996	0.04	0.998
AlPCS4	1.17	0.967	0.81	0.979

Figure 2.5 - PDT-induced cell death as a function of photosensitizer (PS) concentration and incubation time. A431 cells were incubated for 1 h with ZnPC-ITLs, ZnPCS4, AlPC-ITLs, and AlPCS4 and

washed directly before PDT (cumulative radiant exposure of 15 J/cm²). Cell viability was assessed by the WST-1 assay (mitochondrial redox potential (E_h)) **(A)** and by the SRB assay (total protein content) **(B)** at 4 h and 24 h post-PDT (N = 3 per PS concentration per incubation time). PS incubation and post-PDT recovery were performed in DMEM$^{-/-}$ under standard culture conditions. Results were normalized to the mean value of the control group (medium only, cumulative radiant exposure of 15 J/cm²). Fits were generated using the non-linear fit data analysis function in GraphPad Prism, from which the median lethal PS concentration (LC_{50}) was calculated. The goodness of fit (R^2) value is provided for each fit. Abbreviations: AlPC, aluminum phthalocyanine; AlPCS4, tetrasulfonated aluminum phthalocyanine; ITLs, interstitially targeted liposomes; PS, photosensitizer; SRB, sulforhodamine B; WST-1, water-soluble tetrazolium 1; ZnPC, zinc phthalocyanine; ZnPCS4, tetrasulfonated zinc phthalocyanine; N.D., not determined.

2.4.5. PDT of A431 cells leads to a mixed mode of cell death dominated by apoptosis and cell cycle arrest

PDT can destroy tumors by vascular shutdown (28, 58, 59, 80-83), immunological cell death (137), and direct tumor cell death (74). Direct photokilling practically translates to in situ tumor debulking and prevents tumor cells from recovering via survival signaling (64, 138), the relevance of which has been attested *in vitro* (11, 26, 139), *in vivo* (140), and in the clinical setting (141). PDT triggers different modes of cell death that include necroptosis (programmed necrosis), secondary necrosis (apoptosis turned into necrosis, also referred to as late apoptosis), paraptosis, and apoptosis (especially due to ER stress) (74, 133, 142, 143). When irreparable damage occurs in the form of mitochondrial dysfunction, cell membrane damage, oxidative stress, and release of lysosomal enzymes (144), the abovementioned cell death programs generally execute and converge to a phenotype where phosphatidylserine is exposed on the outer membrane leaflet and/or the cell membrane becomes permeable (145, 146). Correspondingly, these hallmark events were measured by flow cytometry following annexin V and propidium iodide staining and stratified into healthy cells (annexin V-/-/PI-/-), early apoptotic (annexin V+/+/PI-/-), late apoptotic (annexin V+/+/PI+/+), and necrotic cells (annexin V-/-/PI+/+) (60).

In the first set of experiments, cells were incubated with increasing PS concentration for 1 h, subjected to PDT, and assayed by flow cytometry 4 h after treatment (Figure 2.6 A). The supernatant containing detached cells as well as the harvested cells were pooled for analysis. In line with the WST-1 and SRB data (Figure 2.5), cells that had been incubated with ZnPCS4 did not exhibit notable apoptotic or necrotic features at concentrations up to 5 μM. In other studies, substantially higher ZnPCS4 concentrations (IC50 and IC75 of 216 μM and 500 μM, respectively, in human cervical cancer (SiHa) cells) were required to achieve mainly necrotic cell death (147). However, photomedicines requiring such high concentrations are clinically not warranted or worth investigating further when superior PSs such as AlPC, ZnPC, and AlPCS4 are available. The liposomal PSs induced a mixed set of cell death modes where early apoptosis prevailed at the lower PS concentration (0.15 μM) while late apoptosis predominated at the higher PS concentration (1.5 μM). Necrosis was observed in 1-2% of the cells that had been photosensitized with ZnPC-ITLs and AlPC-ITLs at 0.75 and 1.5 μM PS concentration. In contrast, AlPCS4 at 0.75 μM induced early apoptosis, late apoptosis, and necrosis at an approximate ratio of 2:3:1. The fraction of early apoptotic cells did not change much at higher AlPCS4 concentrations, only the percentage of necrotic cells at the expense of late apoptotic cells.

An obvious difference between the hydrophilic AlPCS4 and ITL-delivered lipophilic AlPC was the extent of necrotic cell death that had manifested as early as 4 h after PDT. At 2.7 μM AlPCS4, which equates to the 4 h post-PDT LC_{50} value as determined by the WST-1 assay (Figure 2.5 A), there was 84% total cell death, of which 16 ± 10% was attributable to necrosis (Figure 2.6 A). This contrasts with the 25% total cell death and merely 1 ± 0% necrosis induced by liposomal AlPC at the near LC_{50} concentration of 0.17 μM at the same time interval (Figure 2.6 A versus Figure 2.5 A). We subsequently looked into post-PDT energy metabolism as a possible explanation, given that necrosis is an ATP depletion-depend phenomenon while apoptotic programs require energy (148). Ndhundhuma and Abrahamse (149) reported that human melanoma (A375) cells photosensitized with AlPCS4 (2.5 μM) and illuminated at a cumulative radiant exposure of 10 J/cm^2 lost ~80% of their baseline ATP levels at 4 h post-PDT. However, only 0.9% of the cells were necrotic, while 9.9% were early-apoptotic and 2.2% were late-apoptotic. In contrast, illumination (15 J/cm^2) of human biliary carcinoma (Sk-Cha1) cells photosensitized with ZnPC-ETLs did not lead to significant ATP depletion at 90 min post-PDT (26). In fact, only a ~15% drop in ATP concentration was measured at both LC_{50} and LC_{90} despite ample evidence of mitochondrial dysfunction. Both studies were performed with cells that had been exposed to a normoxic atmosphere after PDT, dismissing the possibility that the drop in ATP was caused by hypoxia. The reasons behind the AlPCS4-induced necrosis therefore does not seem to be related to disrupted energy metabolism per se. In an ancillary example, Kessel et al. (114) observed loss of mitochondrial membrane potential following PDT and consequent progression of apoptosis, which was incongruous with the depleted intracellular ATP levels.

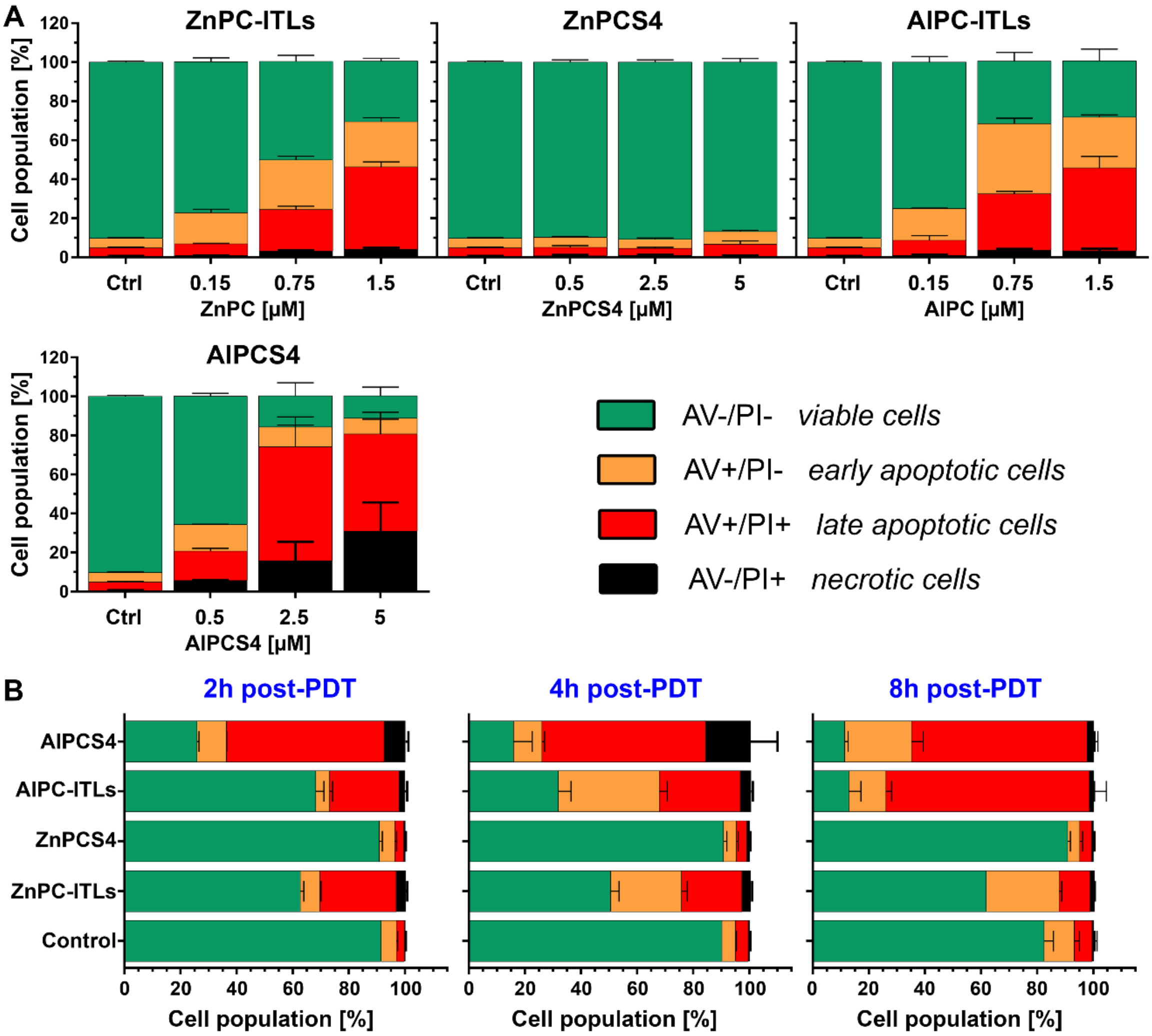

Figure 2.6 - Mode of cell death induced by PDT. A431 cells were incubated with PS in DMEM$^{-/-}$ for 1 h, washed, treated by PDT (cumulative radiant exposure of 15 J/cm^2) or left untreated (control), and stained with PI and annexin V after incubation in DMEM$^{-/-}$. The mode of cell death was analyzed by flow cytometry of both the supernatant fraction and harvested cells detached by trypsinization. **(A)** Photosensitizer concentration-dependent mode of cell death at 4 h post-PDT. Values are shown as mean ± SD for N = 3/group. **(B)** Mode of cell death evolution during the first 8 h after PDT (ZnPC and AlPC, 0.75 μM; ZnPCS4 and AlPCS4, 2.5 μM). Data represent mean ± SD for N = 3 per photosensitizer concentration and post-PDT incubation time. Abbreviations: AlPC, aluminum phthalocyanine; AlPCS4, tetrasulfonated aluminum phthalocyanine; AV, annexin V; ITLs, interstitially targeted liposomes; PI, propidium iodide; ZnPC, zinc phthalocyanine; ZnPCS4, tetrasulfonated zinc phthalocyanine.

In the second set of experiments, the mode of cell death was investigated as a function of time after PDT to assess how fast the cell death pathways were executed and to what extent. As presented in Figure 2.6 B, ZnPCS4 had no effect on cells, whereas AlPCS4 induced the most extensive cell death signaling 2 h after PDT (74%). With time, the percentage of dead/dying cells increased to 84% (4 h) and 89% (8 h). Although AlPC-ITLs inflicted roughly half of the degree of cell death at 2 h post-PDT compared to AlPCS4, at 8 h the fraction of dead/dying cells was comparable (87%), indicating that the progression of cell death signaling occurred at a slower pace for the lipophilic PS. This trend was echoed by ZnPC-

ITLs, albeit to a lesser extent (37%, 49%, and 38% at 2 h, 4 h, and 8 h, respectively), which is consistent with the WST-1 and SRB data obtained 4 h post-PDT (Figure 2.5). Moreover, the cells in the AlPCS4 group transitioned from a more severe form of cell death (late apoptosis) to a less severe form of cell death (early apoptosis). The same applied to cells in the ZnPC-ITL group, although a reversal in the magnitude of cell death signaling was found during the 4-8 h interval. These trends were absent in cells that had been treated with AlPC-ITLs, which progressed to a more severe cell death profile with time. The time required to count 10,000 cells in the gated region increased with post-PDT time in the AlPC-ITL and AlPCS4 group (Figure S2.4 A). Also, the amount of cell remnants, microparticles, and debris produced by dying and dead cells increased after PDT for all PSs that induced photokilling compared to control cells (Figure S2.4 B). The implications of these observations are discussed further in section S2.4.5 and Figures S2.4-S2.6.(9)

It is known that cell death signaling constitutes a sliding scale phenomenon where biochemical pro-survival stimuli (11, 64) may abrogate the death cascades and cause cells to undergo anastasis (cell survival and recovery through reversal of apoptosis (150)) or other modes of recovery (151-153). In fact, we reported this exact trend several years ago for human biliary carcinoma (Sk-Cha1) cells treated with ZnPC-ITLs (0.75 µM; cumulative radiant exposure of 15 J/cm^2) and ascribed it to cell survival, despite severely impaired mitochondrial redox capacity (9) (as was the case here too, Figure 2.5 A). These findings may have implications in translational studies. The mode of tumor cell death influences the post-PDT anti-tumor immune response (154) and abscopal effects (155). In juxtaposition to direct tumor cell photokilling, immunological cell death is additive and above all quintessential in long-term tumor control (137, 156). Qualified modes of cell death for immunological signaling are necroptosis, secondary necrosis, paraptosis, and apoptosis (146, 157-163). It will therefore be interesting to see whether [1] the reversal of cell death prevails *in vivo* for the AlPCS4 and ZnPC-ITLs and [2] whether it negatively impacts immunological tumor clearance.

In the final test arm, cells were treated by PDT and assayed for cell cycle arrest by PI staining in combination with flow cytometry at 24 h after PDT. As alluded to above, A431 cells are monoallelic for P53 (85), a tumor suppressor protein that under certain stress conditions can cause cell cycle arrest in G1 and G2 and apoptosis (164). An R273H missense mutation leads to gain of function in terms of increased propensity of evasion and migration but not increased cell cycle progression and cell survival (165). Conversely, cells were maintained in DMEM-/- following PDT to emulate post-PDT malnutrition and metabolic catastrophe (26) following vascular shutdown (28, 80-83). Serum deprivation can cause cell cycle arrest in G0 (166, 167), which we observed in control A431 cells (49.1 ± 0.3%; Figure 2.7) when compared to values reported elsewhere for A431 cells cultured in fully supplemented medium (39-43%) (168). Taken together, control cells had increased G0 arrest at baseline due to contrived culture conditions while the P53 gene status in itself was not expected to exacerbate cell cycle arrest and apoptosis.

In line with previous data, PDT of cells that had been incubated with ZnPCS4 resulted in cell cycle profiles that were comparable to control cells (Figure 2.7). Conversely, cells that had been photosensitized with ZnPC-ITLs, AlPC-ITLs, and AlPCS4 exhibited a reduction in the percentage of cells in G0/G1. Cells treated with AlPCS4 were arrested in the S-phase, suggesting perturbation of tightly controlled replication forks that mediate DNA replication. Cells that had been treated with AlPC-ITLs exhibited both S-phase and G2 arrest, which is in sync with the widespread apoptosis (Figure 2.6). The G2 phase is only entered if the DNA replication in the S-phase has proceeded successfully and embodies rapid cell growth and protein synthesis in preparation of division. Cells that had been subjected to ZnPC-ITL PDT also exhibited moderate arrest in the S-phase and G2, but less profoundly than the AlPC-ITLs and therefore in accordance with the mode of cell death data (Figure 2.6) and degree of cell death (Figure 2.5). The less extensive S-phase and G2 arrest in cells exposed to ZnPC-ITLs compared to the cell cycle fallout at equimolar AlPC concentration infers that AlPC is a more lethal PS capable of inducing downstream events that are more favorable for therapeutic efficacy; *e.g.*, photokilling of tumor cells and possibly more widespread anti-tumor immune responses.

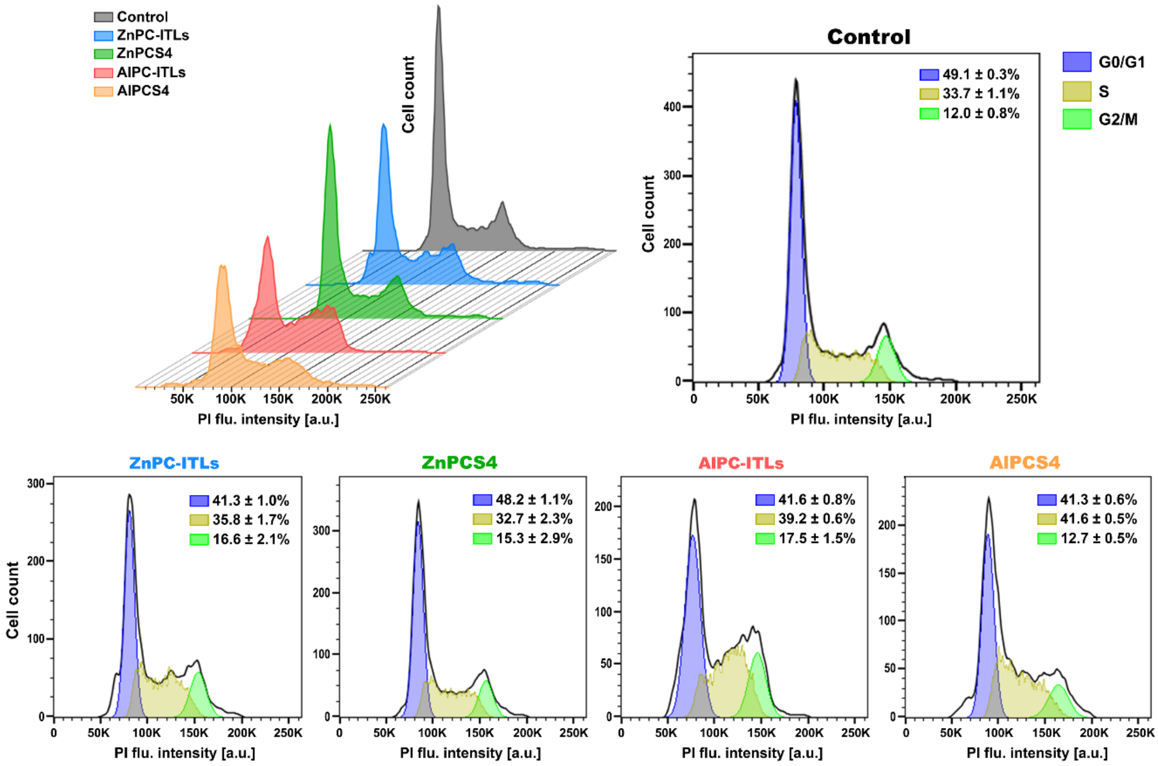

Figure 2.7 - Cell cycle analysis in A431 cells after PDT. Cells were incubated for 60 min with ZnPC-ITLs, AlPC-ITLs (both 31.25 µM), ZnPCS4, and AlPCS4 (both 0.31 µM), washed, illuminated at a cumulative radiant exposure of 15 J/cm^2, and harvested 24 h after PDT. Cells were washed twice and PI staining solution and RNAse A in PBS were added after fixation in ice-cold 96% ethanol. Analysis was performed by flow cytometry in the tumor cell gated region. Quantitative data represent mean ± SD for N = 3/group.

2.5. Summary and conclusions

This study entailed a head-to-head comparative analysis of four metallated phtahlocyanines for PDT of solid tumors; a study that hitherto had not been performed before. The study was conducted in an attritional sense to allow selection of the most optimal PS for further development of third- and fourth-generation PSs; *e.g.*, nanoparticulate second-generation PSs and nanoparticulate second-generation PSs co-encapsulating inhibitors of tumor cell survival pathways, respectively. AlPC encapsulated in ITLs was concluded to be the superior PS on the basis of: 1) no dark toxicity up to a concentration that was 37-50 times greater than its LC$_{50}$ value at 24 h post-PDT, [2] an LC$_{50}$ value that was 3 times lower than that of ZnPC and 20 times lower than that of AlPCS4 (at 24 h), [3] rapid and abundant uptake by tumor cells despite an absence of targeting ligands, [4] heterogeneous dispersion to numerous intracellular loci, and [5] extensive cell death induction by apoptosis that was accompanied by the most profound cell cycle arrest in the S-phase and G2. Research on the ZnPCS4 will be discontinued because it failed the attrition step regarding phototoxicity. Although phototoxic, ZnPC-ITLs were again shown to be associated with anastasis, which will need to be further explored before advancing the research with this formulation to *in vivo* and clinical stages.

Next, the results obtained with AlPC-ITLs and AlPCS4 will be validated in other cancer cell lines as well as *in vivo* with respect to systemic toxicity and toxicogenomics, skin phototoxicity, tumor photosensitization, and anti-tumor efficacy. Also, the combination of liposomal AlPC and AlPCS4 will be explored as a PS cocktail. This approach is expected to inflict oxidative damage at different subcellular structures and hence produce different modes of cell death and immunological responses that could be beneficial to therapeutic efficacy and long-term tumor control.

2.6. Acknowledgements

This work was supported by grants from the Dutch Cancer Foundation (KWF project # 10666), a Zhejiang Provincial Foreign Expert Program Grant, Zhejiang Provincial Key Natural Science Foundation of China (#Z20H160031), and a grant for the establishment of the Jiaxing Key Laboratory for Photonanomedicine and Experimental Therapeutics to MH. BD is sponsored by grants from the National Natural Science Foundation (81872220), a Basic Public Welfare Research Project of Zhejiang Province (LGF18H160034), and the Tumor Nanotargeting and TCM Technology Innovation Team (Key Science and Technology Innovation Team of Jiaxing, 2018). WP is sponsored by a grant from the National Natural Science Foundation of China (31871402). MH is chief formulation officer at Nurish.Me and Camelina Sun and has equity in those companies (whose business activities are unrelated to the present work).

References

1. Baskaran R, Lee J, and Yang SG. Clinical development of photodynamic agents and therapeutic applications. *Biomater Res*. 2018;22(25.
2. Shafirstein G, Battoo A, Harris K, Baumann H, Gollnick SO, Lindenmann J, and Nwogu CE. Photodynamic Therapy of Non-Small Cell Lung Cancer. Narrative Review and Future Directions. *Ann Am Thorac Soc*. 2016;13(2):265-75.
3. Kennedy JC, Pottier RH, and Pross DC. Photodynamic therapy with endogenous protoporphyrin IX: basic principles and present clinical experience. *J Photochem Photobiol B*. 1990;6(1-2):143-8.
4. Tan IB, Dolivet G, Ceruse P, Vander Poorten V, Roest G, and Rauschning W. Temoporfin-mediated photodynamic therapy in patients with advanced, incurable head and neck cancer: A multicenter study. *Head Neck*. 2010;32(12):1597-604.
5. Castano AP, Demidova TN, and Hamblin MR. Mechanisms in photodynamic therapy: part one-photosensitizers, photochemistry and cellular localization. *Photodiagnosis Photodyn Ther*. 2004;1(4):279-93.
6. Weijer R, Broekgaarden M, Kos M, van Vught R, Rauws EA, Breukink EJ, van Gulik TM, Storm G, and Heger M. Enhancing photodynamic therapy of refractory solid cancers: Combining second-generation photosensitizers with multi-targeted liposomal delivery. *J Photochem Photobiol C*. 2015;23(103-31.

7. Huggett MT, Jermyn M, Gillams A, Illing R, Mosse S, Novelli M, Kent E, Bown SG, Hasan T, Pogue BW, et al. Phase I/II study of verteporfin photodynamic therapy in locally advanced pancreatic cancer. *Br J Cancer.* 2014;110(7):1698-704.
8. Shen YJ, Cao J, Sun F, Cai XL, Li MM, Zheng NN, Qu CY, Zhang Y, Shen F, Zhou M, et al. Effect of photodynamic therapy with (17R,18R)-2-(1-hexyloxyethyl)-2-devinyl chlorine E6 trisodium salt on pancreatic cancer cells in vitro and in vivo. *World J Gastroenterol.* 2018;24(46):5246-58.
9. Broekgaarden M, de Kroon AI, Gulik TM, and Heger M. Development and in vitro proof-of-concept of interstitially targeted zinc- phthalocyanine liposomes for photodynamic therapy. *Curr Med Chem.* 2014;21(3):377-91.
10. Weijer R, Broekgaarden M, Krekorian M, Alles LK, van Wijk AC, Mackaaij C, Verheij J, van der Wal AC, van Gulik TM, Storm G, et al. Inhibition of hypoxia inducible factor 1 and topoisomerase with acriflavine sensitizes perihilar cholangiocarcinomas to photodynamic therapy. *Oncotarget.* 2016;7(3):3341-56.
11. Weijer R, Broekgaarden M, van Golen RF, Bulle E, Nieuwenhuis E, Jongejan A, Moerland PD, van Kampen AH, van Gulik TM, and Heger M. Low-power photodynamic therapy induces survival signaling in perihilar cholangiocarcinoma cells. *BMC Cancer.* 2015;15(1014.
12. Broekgaarden M, Weijer R, van Wijk AC, Cox RC, Egmond MR, Hoebe R, van Gulik TM, and Heger M. Photodynamic Therapy with Liposomal Zinc Phthalocyanine and Tirapazamine Increases Tumor Cell Death via DNA Damage. *J Biomed Nanotechnol.* 2017;13(2):204-20.
13. Valle J, Wasan H, Palmer DH, Cunningham D, Anthoney A, Maraveyas A, Madhusudan S, Iveson T, Hughes S, Pereira SP, et al. Cisplatin plus gemcitabine versus gemcitabine for biliary tract cancer. *N Engl J Med.* 2010;362(14):1273-81.
14. Zoepf T, Jakobs R, Arnold JC, Apel D, and Riemann JF. Palliation of nonresectable bile duct cancer: improved survival after photodynamic therapy. *Am J Gastroenterol.* 2005;100(11):2426-30.
15. Stan RV, Tse D, Deharvengt SJ, Smits NC, Xu Y, Luciano MR, McGarry CL, Buitendijk M, Nemani KV, Elgueta R, et al. The diaphragms of fenestrated endothelia: gatekeepers of vascular permeability and blood composition. *Dev Cell.* 2012;23(6):1203-18.
16. Sarin H. Physiologic upper limits of pore size of different blood capillary types and another perspective on the dual pore theory of microvascular permeability. *J Angiogenes Res.* 2010;2(14.
17. Broekgaarden M, Weijer R, Krekorian M, van den Ijssel B, Kos M, Alles LK, van Wijk AC, Bikadi Z, Hazai E, van Gulik TM, et al. Inhibition of hypoxia-inducible factor 1 with acriflavine sensitizes hypoxic tumor cells to photodynamic therapy with zinc phthalocyanine-encapsulating cationic liposomes. *Nano Res.* 2016;9(6):1639-62.
18. Broekgaarden M, van Vught R, Oliveira S, Roovers RC, van Bergen en Henegouwen PM, Pieters RJ, Van Gulik TM, Breukink E, and Heger M. Site-specific conjugation of single domain antibodies to liposomes enhances photosensitizer uptake and photodynamic therapy efficacy. *Nanoscale.* 2016;8(12):6490-4.
19. Thurston G, McLean JW, Rizen M, Baluk P, Haskell A, Murphy TJ, Hanahan D, and McDonald DM. Cationic liposomes target angiogenic endothelial cells in tumors and chronic inflammation in mice. *J Clin Invest.* 1998;101(7):1401-13.
20. Gilabert-Oriol R, Ryan GM, Leung AWY, Firmino NS, Bennewith KL, and Bally MB. Liposomal Formulations to Modulate the Tumour Microenvironment and Antitumour Immune Response. *Int J Mol Sci.* 2018;19(10).
21. van Raath MI, Weijer R, Nguyen GH, Choi B, de Kroon AI, and Heger M. Tranexamic Acid-Encapsulating Thermosensitive Liposomes for Site-Specific Pharmaco-Laser Therapy of Port Wine Stains. *J Biomed Nanotechnol.* 2016;12(8):1617-40.
22. Chan WS, Marshall JF, Svensen R, Bedwell J, and Hart IR. Effect of sulfonation on the cell and tissue distribution of the photosensitizer aluminum phthalocyanine. *Cancer Res.* 1990;50(15):4533-8.

23. Peng Q, and Moan J. Correlation of distribution of sulphonated aluminium phthalocyanines with their photodynamic effect in tumour and skin of mice bearing CaD2 mammary carcinoma. *Br J Cancer*. 1995;72(3):565-74.
24. Ochsner M. Light scattering of human skin: a comparison between zinc (II)-phthalocyanine and photofrin II. *J Photochem Photobiol B*. 1996;32(1-2):3-9.
25. Brasseur N, Ouellet R, La Madeleine C, and van Lier JE. Water-soluble aluminium phthalocyanine-polymer conjugates for PDT: photodynamic activities and pharmacokinetics in tumour-bearing mice. *Br J Cancer*. 1999;80(10):1533-41.
26. Weijer R, Clavier S, Zaal EA, Pijls MM, van Kooten RT, Vermaas K, Leen R, Jongejan A, Moerland PD, van Kampen AH, et al. Multi-OMIC profiling of survival and metabolic signaling networks in cells subjected to photodynamic therapy. *Cell Mol Life Sci*. 2017;74(6):1133-51.
27. Spikes JD. Phthalocyanines as photosensitizers in biological systems and for the photodynamic therapy of tumors. *Photochem Photobiol*. 1986;43(6):691-9.
28. Fingar VH, Wieman TJ, Karavolos PS, Doak KW, Ouellet R, and van Lier JE. The effects of photodynamic therapy using differently substituted zinc phthalocyanines on vessel constriction, vessel leakage and tumor response. *Photochem Photobiol*. 1993;58(2):251-8.
29. Huang Y, Xu G, Peng Y, Lin H, Zheng X, and Xie M. Zinc phthalocyanine tetrasulfonate (ZnPcS4): a new photosensitizer for photodynamic therapy in choroidal neovascularization. *J Ocul Pharmacol Ther*. 2007;23(4):377-86.
30. Lemos CN, de Souza JG, Simao PS, and Lopez RF. Iontophoresis Improved Growth Reduction of Invasive Squamous Cell Carcinoma in Topical Photodynamic Therapy. *PLoS One*. 2016;11(1):e0145922.
31. Viola A, Jeunet A, Decreau R, Chanon M, and Julliard M. ESR studies of a series of phthalocyanines. Mechanism of phototoxicity. Comparative quantitation of O2-. using ESR spin-trapping and cytochrome c reduction techniques. *Free Radic Res*. 1998;28(5):517-32.
32. Almeida EDP, Dipieri LV, Rossetti FC, Marchetti JM, Bentley M, Nunes RS, Sarmento VHV, Valerio MEG, Rodrigues Junior JJ, Montalvao MM, et al. Skin permeation, biocompatibility and antitumor effect of chloroaluminum phthalocyanine associated to oleic acid in lipid nanoparticles. *Photodiagnosis Photodyn Ther*. 2018;24(262-73.
33. Goto PL, Siqueira-Moura MP, and Tedesco AC. Application of aluminum chloride phthalocyanine-loaded solid lipid nanoparticles for photodynamic inactivation of melanoma cells. *Int J Pharm*. 2017;518(1-2):228-41.
34. Siqueira-Moura MP, Primo FL, Espreafico EM, and Tedesco AC. Development, characterization, and photocytotoxicity assessment on human melanoma of chloroaluminum phthalocyanine nanocapsules. *Mater Sci Eng C Mater Biol Appl*. 2013;33(3):1744-52.
35. Rocha MS, Lucci CM, Longo JP, Galera PD, Simioni AR, Lacava ZG, Tedesco AC, and Azevedo RB. Aluminum-chloride-phthalocyanine encapsulated in liposomes: activity against naturally occurring dog breast cancer cells. *J Biomed Nanotechnol*. 2012;8(2):251-7.
36. Longo JP, Leal SC, Simioni AR, de Fatima Menezes Almeida-Santos M, Tedesco AC, and Azevedo RB. Photodynamic therapy disinfection of carious tissue mediated by aluminum-chloride-phthalocyanine entrapped in cationic liposomes: an in vitro and clinical study. *Lasers Med Sci*. 2012;27(3):575-84.
37. Komatsu K. Photodynamic cell killing effects and acute skin photosensitivity of aluminum-chloro-tetrasulfonated phthalocyanine and hematoporphyrin derivative. *Jpn J Cancer Res*. 1991;82(5):599-606.
38. Tetko IV. Virtual Computational Chemistry Laboratory. http://www.vcclab. Accessed May, 2020.
39. Chin Y, Lim SH, Zorlu Y, Ahsen V, Kiew LV, Chung LY, Dumoulin F, and Lee HB. Improved photodynamic efficacy of Zn(II) phthalocyanines via glycerol substitution. *PLoS One*. 2014;9(5):e97894.

40. Polo L, Segalla A, Jori G, Bocchiotti G, Verna G, Franceschini R, Mosca R, and De Filippi PG. Liposome-delivered 131I-labelled Zn(II)-phthalocyanine as a radiodiagnostic agent for tumours. *Cancer Lett.* 1996;109(1-2):57-61.
41. Reddi E, Zhou C, Biolo R, Menegaldo E, and Jori G. Liposome- or LDL-administered Zn (II)-phthalocyanine as a photodynamic agent for tumours. I. Pharmacokinetic properties and phototherapeutic efficiency. *Br J Cancer.* 1990;61(3):407-11.
42. Reddi E, Lo Castro G, Biolo R, and Jori G. Pharmacokinetic studies with zinc(II)-phthalocyanine in tumour-bearing mice. *Br J Cancer.* 1987;56(5):597-600.
43. van Leengoed HL, van der Veen N, Versteeg AA, Ouellet R, van Lier JE, and Star WM. In vivo fluorescence kinetics of phthalocyanines in a skin-fold observation chamber model: role of central metal ion and degree of sulfonation. *Photochem Photobiol.* 1993;58(2):233-7.
44. Tapajos EC, Longo JP, Simioni AR, Lacava ZG, Santos MF, Morais PC, Tedesco AC, and Azevedo RB. In vitro photodynamic therapy on human oral keratinocytes using chloroaluminum-phthalocyanine. *Oral Oncol.* 2008;44(11):1073-9.
45. Ricci-Junior E, and Marchetti JM. Zinc(II) phthalocyanine loaded PLGA nanoparticles for photodynamic therapy use. *Int J Pharm.* 2006;310(1-2):187-95.
46. Taillefer J, Jones MC, Brasseur N, van Lier JE, and Leroux JC. Preparation and characterization of pH-responsive polymeric micelles for the delivery of photosensitizing anticancer drugs. *J Pharm Sci.* 2000;89(1):52-62.
47. Amin RM, Hauser C, Kinzler I, Rueck A, and Scalfi-Happ C. Evaluation of photodynamic treatment using aluminum phthalocyanine tetrasulfonate chloride as a photosensitizer: new approach. *Photochem Photobiol Sci.* 2012;11(7):1156-63.
48. Muehlmann LA, Ma BC, Longo JP, Almeida Santos Mde F, and Azevedo RB. Aluminum-phthalocyanine chloride associated to poly(methyl vinyl ether-co-maleic anhydride) nanoparticles as a new third-generation photosensitizer for anticancer photodynamic therapy. *Int J Nanomedicine.* 2014;9(1199-213.
49. Zhang M, Naik RR, and Dai L. *Carbon nanomaterials for biomedical applications.* Cham Springer International Publishing; 2016.
50. Muehlmann LA, Rodrigues MC, Longo JP, Garcia MP, Py-Daniel KR, Veloso AB, de Souza PE, da Silva SW, and Azevedo RB. Aluminium-phthalocyanine chloride nanoemulsions for anticancer photodynamic therapy: Development and in vitro activity against monolayers and spheroids of human mammary adenocarcinoma MCF-7 cells. *J Nanobiotechnology.* 2015;13(36.
51. Henderson BW, and Dougherty TJ. *Photodynamic therapy : basic principles and clinical applications.* New York: Marcel Dekker; 1992.
52. Bovis MJ, Woodhams JH, Loizidou M, Scheglmann D, Bown SG, and Macrobert AJ. Improved in vivo delivery of m-THPC via pegylated liposomes for use in photodynamic therapy. *J Control Release.* 2012;157(2):196-205.
53. Buchholz J, Kaser-Hotz B, Khan T, Rohrer Bley C, Melzer K, Schwendener RA, Roos M, and Walt H. Optimizing photodynamic therapy: in vivo pharmacokinetics of liposomal meta-(tetrahydroxyphenyl)chlorin in feline squamous cell carcinoma. *Clin Cancer Res.* 2005;11(20):7538-44.
54. Rouser G, Fkeischer S, and Yamamoto A. Two dimensional then layer chromatographic separation of polar lipids and determination of phospholipids by phosphorus analysis of spots. *Lipids.* 1970;5(5):494-6.
55. Berridge MV, Herst PM, and Tan AS. Tetrazolium dyes as tools in cell biology: new insights into their cellular reduction. *Biotechnol Annu Rev.* 2005;11(127-52.
56. Bock FJ, and Tait SWG. Mitochondria as multifaceted regulators of cell death. *Nat Rev Mol Cell Biol.* 2020;21(2):85-100.
57. Vichai V, and Kirtikara K. Sulforhodamine B colorimetric assay for cytotoxicity screening. *Nat Protoc.* 2006;1(3):1112-6.
58. Seshadri M, Spernyak JA, Mazurchuk R, Camacho SH, Oseroff AR, Cheney RT, and Bellnier DA. Tumor vascular response to photodynamic therapy and the antivascular agent 5,6-dimethylxanthenone-4-acetic acid: implications for combination therapy. *Clin Cancer Res.* 2005;11(11):4241-50.

59. Wang W, Moriyama LT, and Bagnato VS. Photodynamic therapy induced vascular damage: an overview of experimental PDT. *Laser Physics Letters*. 2012;10(2):023001.
60. Wlodkowic D, Skommer J, and Darzynkiewicz Z. Flow cytometry-based apoptosis detection. *Methods Mol Biol*. 2009;559(19-32.
61. Watson JV, Chambers SH, and Smith PJ. A pragmatic approach to the analysis of DNA histograms with a definable G1 peak. *Cytometry*. 1987;8(1):1-8.
62. Broekgaarden M, Kos M, Jurg FA, van Beek AA, van Gulik TM, and Heger M. Inhibition of NF-kappaB in Tumor Cells Exacerbates Immune Cell Activation Following Photodynamic Therapy. *Int J Mol Sci*. 2015;16(8):19960-77.
63. Reiniers MJ, van Golen RF, Bonnet S, Broekgaarden M, van Gulik TM, Egmond MR, and Heger M. Preparation and Practical Applications of 2',7'-Dichlorodihydrofluorescein in Redox Assays. *Anal Chem*. 2017;89(7):3853-7.
64. Broekgaarden M, Weijer R, van Gulik TM, Hamblin MR, and Heger M. Tumor cell survival pathways activated by photodynamic therapy: a molecular basis for pharmacological inhibition strategies. *Cancer Metastasis Rev*. 2015;34(4):643-90.
65. Allison BA, Pritchard PH, and Levy JG. Evidence for low-density lipoprotein receptor-mediated uptake of benzoporphyrin derivative. *Br J Cancer*. 1994;69(5):833-9.
66. Polo L, Bianco G, Reddi E, and Jori G. The effect of different liposomal formulations on the interaction of Zn(II)-phthalocyanine with isolated low and high density lipoproteins. *Int J Biochem Cell Biol*. 1995;27(12):1249-55.
67. Arrieta O, Medina LA, Estrada-Lobato E, Ramirez-Tirado LA, Mendoza-Garcia VO, and de la Garza-Salazar J. High liposomal doxorubicin tumour tissue distribution, as determined by radiopharmaceutical labelling with (99m)Tc-LD, is associated with the response and survival of patients with unresectable pleural mesothelioma treated with a combination of liposomal doxorubicin and cisplatin. *Cancer Chemother Pharmacol*. 2014;74(1):211-5.
68. Crivellari D, Gray KP, Dellapasqua S, Puglisi F, Ribi K, Price KN, Lang I, Gianni L, Spazzapan S, Pinotti G, et al. Adjuvant pegylated liposomal doxorubicin for older women with endocrine nonresponsive breast cancer who are NOT suitable for a "standard chemotherapy regimen": the CASA randomized trial. *Breast*. 2013;22(2):130-7.
69. Bedikian AY, Silverman JA, Papadopoulos NE, Kim KB, Hagey AE, Vardeleon A, Hwu WJ, Homsi J, Davies M, and Hwu P. Pharmacokinetics and safety of Marqibo (vincristine sulfate liposomes injection) in cancer patients with impaired liver function. *J Clin Pharmacol*. 2011;51(8):1205-12.
70. Rodriguez MA, Pytlik R, Kozak T, Chhanabhai M, Gascoyne R, Lu B, Deitcher SR, Winter JN, and Marqibo I. Vincristine sulfate liposomes injection (Marqibo) in heavily pretreated patients with refractory aggressive non-Hodgkin lymphoma: report of the pivotal phase 2 study. *Cancer*. 2009;115(15):3475-82.
71. DiGiulio S. FDA approves Onivyde combo regimen for advanced pancreatic cancer. *Oncology Times*. 2015;37(22):8.
72. Rousseau J, Langlois R, Ali H, and van Lier JE. Biological activities of phthalocyanines. XII: Synthesis tumor uptake and biodistribution of 14C-labeled disulfonated and trisulfonated gallium phthalocyanine in C3H mice. *J Photochem Photobiol B*. 1990;6(1-2):121-32.
73. Tralau CJ, Barr H, Sandeman DR, Barton T, Lewin MR, and Bown SG. Aluminum sulfonated phthalocyanine distribution in rodent tumors of the colon, brain and pancreas. *Photochem Photobiol*. 1987;46(5):777-81.
74. Kessel D, and Oleinick NL. Cell Death Pathways Associated with Photodynamic Therapy: An Update. *Photochem Photobiol*. 2018;94(2):213-8.
75. Donohoe C, Senge MO, Arnaut LG, and Gomes-da-Silva LC. Cell death in photodynamic therapy: From oxidative stress to anti-tumor immunity. *Biochim Biophys Acta Rev Cancer*. 2019;1872(2):188308.
76. Martins WK, Santos NF, Rocha CS, Bacellar IOL, Tsubone TM, Viotto AC, Matsukuma AY, Abrantes ABP, Siani P, Dias LG, et al. Parallel damage in

mitochondria and lysosomes is an efficient way to photoinduce cell death. *Autophagy*. 2019;15(2):259-79.

77. Edwardson DW, Parissenti AM, and Kovala AT. Chemotherapy and Inflammatory Cytokine Signalling in Cancer Cells and the Tumour Microenvironment. *Adv Exp Med Biol*. 2019;1152(173-215.
78. Singh SV, Ajay AK, Mohammad N, Malvi P, Chaube B, Meena AS, and Bhat MK. Proteasomal inhibition sensitizes cervical cancer cells to mitomycin C-induced bystander effect: the role of tumor microenvironment. *Cell Death Dis*. 2015;6(e1934.
79. McCann JV, Null JL, and Dudley AC. Deadly DAaRTS destroy cancer cells via a tumor microenvironment-mediated trigger. *J Clin Invest*. 2018;128(7):2750-3.
80. Henderson BW, Waldow SM, Mang TS, Potter WR, Malone PB, and Dougherty TJ. Tumor destruction and kinetics of tumor cell death in two experimental mouse tumors following photodynamic therapy. *Cancer Res*. 1985;45(2):572-6.
81. Fingar VH, Wieman TJ, and Doak KW. Role of thromboxane and prostacyclin release on photodynamic therapy-induced tumor destruction. *Cancer Res*. 1990;50(9):2599-603.
82. Henderson BW, Owczarczak B, Sweeney J, and Gessner T. Effects of photodynamic treatment of platelets or endothelial cells in vitro on platelet aggregation. *Photochem Photobiol*. 1992;56(4):513-21.
83. Reed MW, Miller FN, Wieman TJ, Tseng MT, and Pietsch CG. The effect of photodynamic therapy on the microcirculation. *J Surg Res*. 1988;45(5):452-9.
84. Heger M, Salles, II, van Vuure W, Hamelers IH, de Kroon AI, Deckmyn H, and Beek JF. On the interaction of fluorophore-encapsulating PEGylated lecithin liposomes with hamster and human platelets. *Microvasc Res*. 2009;78(1):57-66.
85. Reiss M, Brash DE, Munoz-Antonia T, Simon JA, Ziegler A, Vellucci VF, and Zhou ZL. Status of the p53 tumor suppressor gene in human squamous carcinoma cell lines. *Oncol Res*. 1992;4(8-9):349-57.
86. Kaelin WG, Jr. The p53 gene family. *Oncogene*. 1999;18(53):7701-5.
87. Gulli LF, Palmer KC, Chen YQ, and Reddy KB. Epidermal growth factor-induced apoptosis in A431 cells can be reversed by reducing the tyrosine kinase activity. *Cell Growth Differ*. 1996;7(2):173-8.
88. Normanno N, De Luca A, Bianco C, Strizzi L, Mancino M, Maiello MR, Carotenuto A, De Feo G, Caponigro F, and Salomon DS. Epidermal growth factor receptor (EGFR) signaling in cancer. *Gene*. 2006;366(1):2-16.
89. Tsai T, Ji HT, Chiang PC, Chou RH, Chang WS, and Chen CT. ALA-PDT results in phenotypic changes and decreased cellular invasion in surviving cancer cells. *Lasers Surg Med*. 2009;41(4):305-15.
90. Fabris C, Valduga G, Miotto G, Borsetto L, Jori G, Garbisa S, and Reddi E. Photosensitization with zinc (II) phthalocyanine as a switch in the decision between apoptosis and necrosis. *Cancer Res*. 2001;61(20):7495-500.
91. Ben-Hur E, Green M, Prager A, Kol R, and Rosenthal I. Phthalocyanine photosensitization of mammalian cells: biochemical and ultrastructural effects. *Photochem Photobiol*. 1987;46(5):651-6.
92. Qualls MM, and Thompson DH. Chloroaluminum phthalocyanine tetrasulfonate delivered via acid-labile diplasmenylcholine-folate liposomes: intracellular localization and synergistic phototoxicity. *Int J Cancer*. 2001;93(3):384-92.
93. Idowu M, and Nyokong T. Photophysical and photochemical properties of zinc and aluminum phthalocyanines in the presence of magnetic fluid. *J Photochem Photobiol A*. 2007;188(2):200-6.
94. Owens JW, Smith R, Robinson R, and Robins M. Photophysical properties of porphyrins, phthalocyanines, and benzochlorins. *Inorg Chim Acta*. 1998;279(2):226-31.
95. Dan N. Effect of liposome charge and PEG polymer layer thickness on cell-liposome electrostatic interactions. *Biochim Biophys Acta*. 2002;1564(2):343-8.

96. Corbo C, Molinaro R, Taraballi F, Toledano Furman NE, Sherman MB, Parodi A, Salvatore F, and Tasciotti E. Effects of the protein corona on liposome-liposome and liposome-cell interactions. *Int J Nanomedicine*. 2016;11(3049-63.
97. Allison JB, and Becker RS. Effect of Metal Atom Perturbations on the Luminescent Spectra of Porphyrins. *J Chem Phys*. 1960;32(5):1410-7.
98. Seybold PG, and Gouterman M. Porphyrins: XIII: Fluorescence spectra and quantum yields. *J Mol Spectrosc*. 1969;31(1):1-13.
99. McCubbin I, and Phillips D. The photophysics and photostability of zinc(II) and aluminium(III) sulphonated naphthalocyanines. *J Photochem*. 1986;34(2):187-95.
100. Woodburn KW, Vardaxis NJ, Hill JS, Kaye AH, and Phillips DR. Subcellular localization of porphyrins using confocal laser scanning microscopy. *Photochem Photobiol*. 1991;54(5):725-32.
101. Soriano J, Villanueva A, Stockert JC, and Canete M. Vehiculization determines the endocytic internalization mechanism of Zn(II)-phthalocyanine. *Histochem Cell Biol*. 2013;139(1):149-60.
102. Paquette B, Ali H, Langlois R, and van Lier JE. Biological activities of phthalocyanines--VIII. Cellular distribution in V-79 Chinese hamster cells and phototoxicity of selectively sulfonated aluminum phthalocyanines. *Photochem Photobiol*. 1988;47(2):215-20.
103. Tsubone TM, Martins WK, Pavani C, Junqueira HC, Itri R, and Baptista MS. Enhanced efficiency of cell death by lysosome-specific photodamage. *Sci Rep*. 2017;7(1):6734.
104. Wilson BC, Olivo M, and Singh G. Subcellular localization of Photofrin and aminolevulinic acid and photodynamic cross-resistance in vitro in radiation-induced fibrosarcoma cells sensitive or resistant to photofrin-mediated photodynamic therapy. *Photochem Photobiol*. 1997;65(1):166-76.
105. Ji Z, Yang G, Vasovic V, Cunderlikova B, Suo Z, Nesland JM, and Peng Q. Subcellular localization pattern of protoporphyrin IX is an important determinant for its photodynamic efficiency of human carcinoma and normal cell lines. *J Photochem Photobiol B*. 2006;84(3):213-20.
106. Teiten MH, Bezdetnaya L, Morliere P, Santus R, and Guillemin F. Endoplasmic reticulum and Golgi apparatus are the preferential sites of Foscan localisation in cultured tumour cells. *Br J Cancer*. 2003;88(1):146-52.
107. Hsieh YJ, Wu CC, Chang CJ, and Yu JS. Subcellular localization of Photofrin determines the death phenotype of human epidermoid carcinoma A431 cells triggered by photodynamic therapy: when plasma membranes are the main targets. *J Cell Physiol*. 2003;194(3):363-75.
108. Jain MV, Paczulla AM, Klonisch T, Dimgba FN, Rao SB, Roberg K, Schweizer F, Lengerke C, Davoodpour P, Palicharla VR, et al. Interconnections between apoptotic, autophagic and necrotic pathways: implications for cancer therapy development. *J Cell Mol Med*. 2013;17(1):12-29.
109. Kadish KM, Smith KM, and Guilard R. *The porphyrin handbook - Vol. 17: Phthalocyanines: properties and materials*. San Diego: Academic Press; 2003.
110. Ris HB, Altermatt HJ, Nachbur B, Stewart JC, Wang Q, Lim CK, Bonnett R, and Althaus U. Effect of drug-light interval on photodynamic therapy with meta-tetrahydroxyphenylchlorin in malignant mesothelioma. *Int J Cancer*. 1993;53(1):141-6.
111. Henderson BW, and Fingar VH. Relationship of tumor hypoxia and response to photodynamic treatment in an experimental mouse tumor. *Cancer Res*. 1987;47(12):3110-4.
112. Hirsch BD, Walz NC, Meeker BE, Arnfield MR, Tulip J, McPhee MS, and Chapman JD. Photodynamic therapy-induced hypoxia in rat tumors and normal tissues. *Photochem Photobiol*. 1987;46(5):847-52.
113. Chapman JD, McPhee MS, Walz N, Chetner MP, Stobbe CC, Soderlind K, Arnfield M, Meeker BE, Trimble L, and Allen PS. Nuclear magnetic resonance spectroscopy and

sensitizer-adduct measurements of photodynamic therapy-induced ischemia in solid tumors. *J Natl Cancer Inst*. 1991;83(22):1650-9.

114. Kessel D, and Luo Y. Mitochondrial photodamage and PDT-induced apoptosis. *J Photochem Photobiol B*. 1998;42(2):89-95.

115. Dolmans DE, Kadambi A, Hill JS, Waters CA, Robinson BC, Walker JP, Fukumura D, and Jain RK. Vascular accumulation of a novel photosensitizer, MV6401, causes selective thrombosis in tumor vessels after photodynamic therapy. *Cancer Res*. 2002;62(7):2151-6.

116. Hadjur C, Wagnieres G, Ihringer F, Monnier P, and van den Bergh H. Production of the free radicals O2.- and .OH by irradiation of the photosensitizer zinc(II) phthalocyanine. *J Photochem Photobiol B*. 1997;38(2-3):196-202.

117. Rosenthal I, Murali Krishna C, Riesz P, and Ben-Hur E. The role of molecular oxygen in the photodynamic effect of phthalocyanines. *Radiat Res*. 1986;107(1):136-42.

118. Valduga G, Nonell S, Reddi E, Jori G, and Braslavsky SE. The production of singlet molecular oxygen by zinc(II) phthalocyanine in ethanol and in unilamellar vesicles. Chemical quenching and phosphorescence studies. *Photochem Photobiol*. 1988;48(1):1-5.

119. Ogilby PR. Singlet oxygen: there is indeed something new under the sun. *Chem Soc Rev*. 2010;39(8):3181-209.

120. Ryter SW, and Tyrrell RM. Singlet molecular oxygen ((1)O2): a possible effector of eukaryotic gene expression. *Free Radic Biol Med*. 1998;24(9):1520-34.

121. Davies MJ. Reactive species formed on proteins exposed to singlet oxygen. *Photochem Photobiol Sci*. 2004;3(1):17-25.

122. Cheng FC, Jen JF, and Tsai TH. Hydroxyl radical in living systems and its separation methods. *J Chromatogr B Analyt Technol Biomed Life Sci*. 2002;781(1-2):481-96.

123. Sueishi Y, Hori M, Ishikawa M, Matsu-Ura K, Kamogawa E, Honda Y, Kita M, and Ohara K. Scavenging rate constants of hydrophilic antioxidants against multiple reactive oxygen species. *J Clin Biochem Nutr*. 2014;54(2):67-74.

124. van Golen RF, van Gulik TM, and Heger M. Mechanistic overview of reactive species-induced degradation of the endothelial glycocalyx during hepatic ischemia/reperfusion injury. *Free Radic Biol Med*. 2012;52(8):1382-402.

125. Mitroka S, Zimmeck S, Troya D, and Tanko JM. How solvent modulates hydroxyl radical reactivity in hydrogen atom abstractions. *J Am Chem Soc*. 2010;132(9):2907-13.

126. Yuan Y, Zhang CJ, Xu S, and Liu B. A self-reporting AIE probe with a built-in singlet oxygen sensor for targeted photodynamic ablation of cancer cells. *Chem Sci*. 2016;7(3):1862-6.

127. Reis A, and Spickett CM. Chemistry of phospholipid oxidation. *Biochim Biophys Acta*. 2012;1818(10):2374-87.

128. Yin H, Xu L, and Porter NA. Free radical lipid peroxidation: mechanisms and analysis. *Chem Rev*. 2011;111(10):5944-72.

129. Gaschler MM, and Stockwell BR. Lipid peroxidation in cell death. *Biochem Biophys Res Commun*. 2017;482(3):419-25.

130. Tai WY, Yang YC, Lin HJ, Huang CP, Cheng YL, Chen MF, Yen HL, and Liau I. Interplay between structure and fluidity of model lipid membranes under oxidative attack. *J Phys Chem B*. 2010;114(47):15642-9.

131. Vantieghem A, Xu Y, Declercq W, Vandenabeele P, Denecker G, Vandenheede JR, Merlevede W, de Witte PA, and Agostinis P. Different pathways mediate cytochrome c release after photodynamic therapy with hypericin. *Photochem Photobiol*. 2001;74(2):133-42.

132. Lemasters JJ, Nieminen AL, Qian T, Trost LC, Elmore SP, Nishimura Y, Crowe RA, Cascio WE, Bradham CA, Brenner DA, et al. The mitochondrial permeability transition in cell death: a common mechanism in necrosis, apoptosis and autophagy. *Biochim Biophys Acta*. 1998;1366(1-2):177-96.

133. Mroz P, Yaroslavsky A, Kharkwal GB, and Hamblin MR. Cell death pathways in photodynamic therapy of cancer. *Cancers (Basel)*. 2011;3(2):2516-39.

134. Tsaytler PA, M COF, Sakharov DV, Krijgsveld J, and Egmond MR. Immediate protein targets of photodynamic treatment in carcinoma cells. *J Proteome Res.* 2008;7(9):3868-78.
135. Morgan J, and Oseroff AR. Mitochondria-based photodynamic anti-cancer therapy. *Adv Drug Deliv Rev.* 2001;49(1-2):71-86.
136. Aits S, and Jaattela M. Lysosomal cell death at a glance. *J Cell Sci.* 2013;126(Pt 9):1905-12.
137. Beltran Hernandez I, Yu Y, Ossendorp F, Korbelik M, and Oliveira S. Preclinical and Clinical Evidence of Immune Responses Triggered in Oncologic Photodynamic Therapy: Clinical Recommendations. *J Clin Med.* 2020;9(2).
138. Sun G, and Montell DJ. Q&A: Cellular near death experiences-what is anastasis? *BMC Biol.* 2017;15(1):92.
139. Bazak J, Fahey JM, Wawak K, Korytowski W, and Girotti AW. Enhanced aggressiveness of bystander cells in an anti-tumor photodynamic therapy model: Role of nitric oxide produced by targeted cells. *Free Radic Biol Med.* 2017;102(111-21.
140. Solban N, Selbo PK, Sinha AK, Chang SK, and Hasan T. Mechanistic investigation and implications of photodynamic therapy induction of vascular endothelial growth factor in prostate cancer. *Cancer Res.* 2006;66(11):5633-40.
141. Shim CS, Cheon YK, Cha SW, Bhandari S, Moon JH, Cho YD, Kim YS, Lee LS, Lee MS, and Kim BS. Prospective study of the effectiveness of percutaneous transhepatic photodynamic therapy for advanced bile duct cancer and the role of intraductal ultrasonography in response assessment. *Endoscopy.* 2005;37(5):425-33.
142. Thompson SA, Aggarwal A, Singh S, Adam AP, Tome JPC, and Drain CM. Compromising the plasma membrane as a secondary target in photodynamic therapy-induced necrosis. *Bioorg Med Chem.* 2018;26(18):5224-8.
143. Zhang Y, Cheung YK, Ng DKP, and Fong WP. Immunogenic necroptosis in the anti-tumor photodynamic action of BAM-SiPc, a silicon(IV) phthalocyanine-based photosensitizer. *Cancer Immunol Immunother.* 2020.
144. Miller MA, and Zachary JF. Mechanisms and Morphology of Cellular Injury, Adaptation, and Death. *Pathologic Basis of Veterinary Disease.* 2017:2-43.e19.
145. Poon IK, Hulett MD, and Parish CR. Molecular mechanisms of late apoptotic/necrotic cell clearance. *Cell Death Differ.* 2010;17(3):381-97.
146. Vanden Berghe T, Vanlangenakker N, Parthoens E, Deckers W, Devos M, Festjens N, Guerin CJ, Brunk UT, Declercq W, and Vandenabeele P. Necroptosis, necrosis and secondary necrosis converge on similar cellular disintegration features. *Cell Death Differ.* 2010;17(6):922-30.
147. Haywood-Small SL, Vernon DI, Griffiths J, Schofield J, and Brown SB. Phthalocyanine-mediated photodynamic therapy induces cell death and a G0/G1 cell cycle arrest in cervical cancer cells. *Biochem Biophys Res Commun.* 2006;339(2):569-76.
148. Tsujimoto Y. Apoptosis and necrosis: intracellular ATP level as a determinant for cell death modes. *Cell Death Differ.* 1997;4(6):429-34.
149. Ndhundhuma IM, and Abrahamse H. Susceptibility of In Vitro Melanoma Skin Cancer to Photoactivated Hypericin versus Aluminium(III) Phthalocyanine Chloride Tetrasulphonate. *Biomed Res Int.* 2017;2017(5407012.
150. Tang HL, Tang HM, Mak KH, Hu S, Wang SS, Wong KM, Wong CS, Wu HY, Law HT, Liu K, et al. Cell survival, DNA damage, and oncogenic transformation after a transient and reversible apoptotic response. *Mol Biol Cell.* 2012;23(12):2240-52.
151. Tang HM, and Tang HL. Cell recovery by reversal of ferroptosis. *Biol Open.* 2019;8(6).
152. Gong YN, Guy C, Olauson H, Becker JU, Yang M, Fitzgerald P, Linkermann A, and Green DR. ESCRT-III Acts Downstream of MLKL to Regulate Necroptotic Cell Death and Its Consequences. *Cell.* 2017;169(2):286-300 e16.
153. Overholtzer M, and Brugge JS. The cell biology of cell-in-cell structures. *Nat Rev Mol Cell Biol.* 2008;9(10):796-809.

154. Hamblin M, and Abrahamse H. Factors Affecting Photodynamic Therapy and Anti-Tumor Immune Response. *Anticancer Agents Med Chem*. 2020.

155. Kepp O, Marabelle A, Zitvogel L, and Kroemer G. Oncolysis without viruses - inducing systemic anticancer immune responses with local therapies. *Nat Rev Clin Oncol*. 2020;17(1):49-64.

156. Hwang HS, Shin H, Han J, and Na K. Combination of photodynamic therapy (PDT) and anti-tumor immunity in cancer therapy. *J Pharm Investig*. 2018;48(2):143-51.

157. Zhou J, Wang G, Chen Y, Wang H, Hua Y, and Cai Z. Immunogenic cell death in cancer therapy: Present and emerging inducers. *J Cell Mol Med*. 2019;23(8):4854-65.

158. Sachet M, Liang YY, and Oehler R. The immune response to secondary necrotic cells. *Apoptosis*. 2017;22(10):1189-204.

159. Gamrekelashvili J, Greten TF, and Korangy F. Immunogenicity of necrotic cell death. *Cell Mol Life Sci*. 2015;72(2):273-83.

160. Dhuriya YK, and Sharma D. Necroptosis: a regulated inflammatory mode of cell death. *J Neuroinflammation*. 2018;15(1):199.

161. Hoa N, Myers MP, Douglass TG, Zhang JG, Delgado C, Driggers L, Callahan LL, VanDeusen G, Pham JT, Bhakta N, et al. Molecular mechanisms of paraptosis induction: implications for a non-genetically modified tumor vaccine. *PLoS One*. 2009;4(2):e4631.

162. Krysko O, Aaes TL, Kagan VE, D'Herde K, Bachert C, Leybaert L, Vandenabeele P, and Krysko DV. Necroptotic cell death in anti-cancer therapy. *Immunol Rev*. 2017;280(1):207-19.

163. Vandenabeele P, Vandecasteele K, Bachert C, Krysko O, and Krysko DV. Immunogenic Apoptotic Cell Death and Anticancer Immunity. *Adv Exp Med Biol*. 2016;930(133-49.

164. Pucci B, Kasten M, and Giordano A. Cell cycle and apoptosis. *Neoplasia*. 2000;2(4):291-9.

165. Muller PA, and Vousden KH. Mutant p53 in cancer: new functions and therapeutic opportunities. *Cancer Cell*. 2014;25(3):304-17.

166. Langan TJ, Rodgers KR, and Chou RC. Synchronization of Mammalian Cell Cultures by Serum Deprivation. *Methods Mol Biol*. 2017;1524(97-105.

167. Narasimha AM, Kaulich M, Shapiro GS, Choi YJ, Sicinski P, and Dowdy SF. Cyclin D activates the Rb tumor suppressor by mono-phosphorylation. *Elife*. 2014;3(

168. Ahmad N, Feyes DK, Agarwal R, and Mukhtar H. Photodynamic therapy results in induction of WAF1/CIP1/P21 leading to cell cycle arrest and apoptosis. *Proc Natl Acad Sci U S A*. 1998;95(12):6977-82.

SUPPLEMENTAL INFORMATION OF PAPER I

S2.3. Materials and methods

S2.3.1. Chemicals and reagents

Table S2.1 - List of chemicals and reagents used. N.S. = not specified.

Compound	Purity	Supplier	Additional information
1,2-Dipalmitoyl-*sn*-glycero-3-phosphocholine (DPPC)	> 99%	Avanti Polar Lipids[$]	Product # 850355P; dissolved in $CHCl_3$, stored under N_2 atmosphere at -20 °C
2',7'-Dichlorodihydrofluorescein-diacetate ($DCFH_2$-DA)	N.S.	Molecular Probes | Life Technologies[†]	Product # D399, dissolved in DMSO and stored at 4 °C
Chloroform ($CHCl_3$)	≥ 99%	Sigma-Aldrich[#]	Product # 288306
Paraformaldehyde aqueous solution (PFA)	8%	Electron Microscopy Science[€]	Product # 157-8
Accutase	N.S.	Innovative Cell Technologies[¥]	Product # AT104; stored at 4 °C
Dimethyl sulfoxide (DMSO)	≥ 99.5%	Sigma-Aldrich[#]	Product # D4540
Dulbecco's modified Eagle medium (DMEM)	N.S.	Lonza[†]	Phenol red-containing (product # BE12-604F) or phenol red-free (product # BE12-917F), depending on the type of experiment. Stored at 4 °C
Fetal bovine serum (FBS)	N.S.	Bodinco[‡]	10% final concentration in medium, stored at -20 °C
Propidium Iodide (PI)	N.S.	Molecular Probes | Life Technologies[†]	Product # P3566; 1.0 mg/mL Solution in Water, stored at 4 °C
HEPES (sodium salt)	≥ 99.5%	Sigma-Aldrich[#]	Product # H7006
Dead Cell Apoptosis Kit	N.S.	Molecular Probes | Life Technologies[†]	Product # V13245; contains Annexin V - Alexa Fluor 488 conjugate (250 μL), propidium iodide (PI, 100 μL), and annexin binding buffer (5X solution, 15 mL); stored at 4 °C
Hoechst 33342	N.S.	Sigma-Aldrich[#]	Product # H3570; 10 mg/mL solution in water
L-α-phosphatidylethanolamine, distearoyl methoxypolyethylene glycol conjugate (DSPE-PEG)	N.S.	Sigma-Aldrich[#]	Product # P7840; average PEG molecular mass of 2,000, dissolved in $CHCl_3$, stored under N_2 atmosphere at -20 °C
RNAse A	N.S.	Sigma-Aldrich[#]	Product # 109169; from bovine pancreas, stored at 4 °C
L-glutamine	N.S.	Lonza[†]	Product # BE17-605E, 2 mM final concentration in medium, stored at -20 °C
Ethanol (absolute)	≥ 99.9%	Sigma-Aldrich[#]	Product # RH 34870
Sulforhodamine B sodium salt (SRB)	N.S.	Sigma-Aldrich[#]	Product # S1402
Trichloroacetic acid (TCA)	≥ 99%	Sigma-Aldrich[#]	Product # T6399, stored at 4 °C
Acetic acid (glacial)	100%	Merck KGaA[*]	Product # 100063
Tris(hydroxymethyl)-aminomethane (TRIS)	N.S.	Merck KGaA[*]	Product # 108382
Cell Proleferation Reagent WST-1	N.S.	Sigma-Aldrich[#]	Cat.No. 0501594400; stored at -20 °C
Phosphate-buffered saline (PBS)	N.S.	Fresenius Kabi[§]	Sterile
Penicillin/streptomycin	N.S.	Lonza[†]	Product # 17-602E; final concentration of 100 U/mL penicillin, 100 μg/mL streptomycin in medium
Pyridine	≥ 99%	Sigma-Aldrich[#]	Product # 437611
Sodium chloride	99.99%	Merck KGaA[*]	Product # 106406

Sodium hydroxide	≥ 99%	Merck KGaA*	Product # 106462
Aluminum (III) phthalocyanine chloride tetrasulfonic acid	N.S.	Frontier Scientific£	CAS: 100180-30-1; dissolved in PBS at 1 mM stock concentration, stored under N_2 atmosphere at 4 °C
Zinc (II) phthalocyanine tetrasulfonic acid	N.S.	Frontier Scientific£	CAS: 61586-86-5; dissolved in PBS at 1 mM stock concentration, stored under N_2 atmosphere at 4 °C
Aluminum (III) phthalocyanine chloride	85%	Sigma-Aldrich#	Product # 362530; dissolved in pyridine at 150 µM stock concentration, stored under N_2 atmosphere at RT
Zinc (II) phthalocyanine	97%	Sigma-Aldrich#	Product # 341169; dissolved in pyridine at 178 µM stock concentration, stored under N_2 atmosphere at RT

* Darmstadt, Germany
\# St. Louis, MO, USA
† Basel, Switzerland
$ Alabaster, AL, USA
§ Bad Homburg, Germany
‡ Alkmaar, the Netherlands
┼ Carlsbad, CA, USA
¥ San Diego, CA, USA
£ Logan, UT, USA
€ Hatfield, PA, USA

Table S2.2 - List of instruments and materials.

Instrument / technique	**Supplier**	**Additional information**
Tip sonifier	Branson	Model 450 Danbury, CT, USA
Hemocytometer	Blaubrand	0.100 mm depth, 0.0025 mm^2 Wertheim, Germany
Dynamic light scattering	Malvern Instruments	Model ALV CGS-3 Malvern, UK
Electrophoretic mobility	Malvern Instruments	Model Zetasizer Nano Z Malvern, UK
Absorbance spectrophotometer	Perkin Elmer	Model Lambda 18 Waltham, MA
Fluorescence spectrometer	Varian	Model Cary Eclipse Palo Alto, CA
1-cm path length quartz cuvette	Hellma Analytics	Model QS 10 × 4 mm Müllheim, Germany
FacsCanto II flow cytometer	BD Bioscience	Franklin Lakes, NJ, USA
Centrifuge	Hettich	Model Rotina 380 R Tuttlingen, Germany
Leica SP8-X SMD confocal laser scanning microscope	Leica Microsystems	Wetzlar, Germany
Synergy HT microplate reader	BioTek Instruments	Winooski, VT, USA
671-nm diode laser	CNI Laser	Changchun, China
Field-Mate power meter	Coherent	Santa Clara, CA, USA
Hotplate stirrer	VWR (cat.no. 97042-616)	Radnor, PA, USA
Rocker (microplate shaker)	Brinkmann	Titermix 100 Riverview, FL, USA
Materials/disposables	**Supplier**	**Additional information**
T75 culture flasks	Cellstar, Greiner Bio-One	Solingen, Germany
6, 12, 24 and 96 wells culture plates (flat bottom)	Cellstar, Greiner Bio-One	Solingen, Germany
2-mL centrifuge tubes (safe-lock)	Eppendorf	Hamburg, Germany
Circular coverslip (25 mm)	Menzel Gläser | Thermo Fisher Scientific	Waltham, Massachusetts, USA
15 mL polystyrene tubes (sterile)	Greiner Bio-One	Solingen, Germany
5 mL round-bottom polypropylene tubes	Falcon, Corning Life Science	Tewksbury, MA, USA

S2.4. Results and discussion

S2.4.2 Liposomal phthalocyanines are not cytotoxic up to 1.5 μM, while tetrasulfonated phthalocyanines induce mild-to-moderate dark toxicity at concentrations of ≥ 2.5 μM

The size, PDI, and ζ-potential of ZnPC-ITLs and AlPC-ITLs is presented in Figure S2.1.

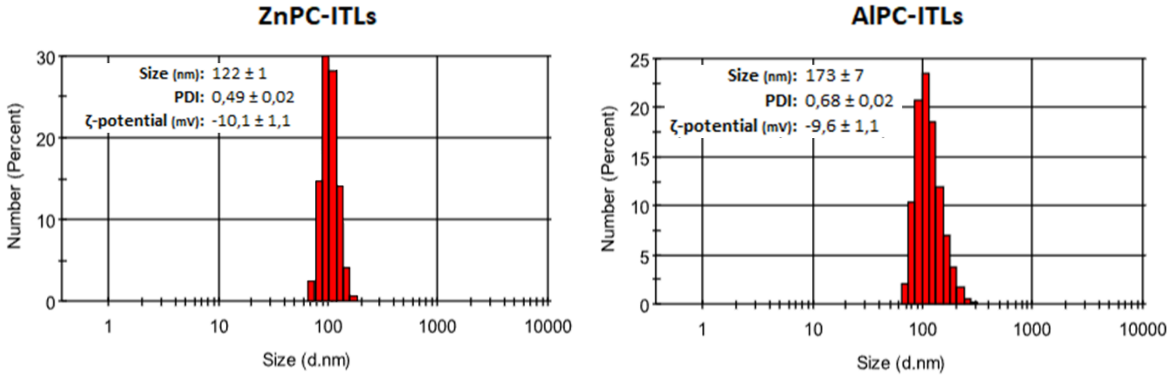

Figure S2.1 - Characterization of ITLs. Size histograms of ZnPC-ITLs and AlPC-ITLs. Size, polydispersion index (PDI), and zeta (ζ)-potential are expressed as mean ± SD of 3 repeated measurements.

S2.4.3 Liposomal and tetrasulfonated metallated phthalocyanines are taken up by cancer cells and rapidly disperse to multiple (intra)cellular loci

The spectral properties of the metallated phthalocyanines are presented in Figure S2.2. The absorption maximum was 673 nm for ZnPC, 614 nm for ZnPCS4, 674 nm for AlPC, and 676 nm for AlPCS4. The fluorescence excitation maximum was 673 nm for ZnPC, 687 nm for ZnPCS4, 675 nm for AlPC, and 675 nm for AlPCS4. The fluorescence emission maximum was 677 nm for ZnPC, 692 nm for ZnPCS4, 680 nm for AlPC, and 679 nm for AlPCS4.

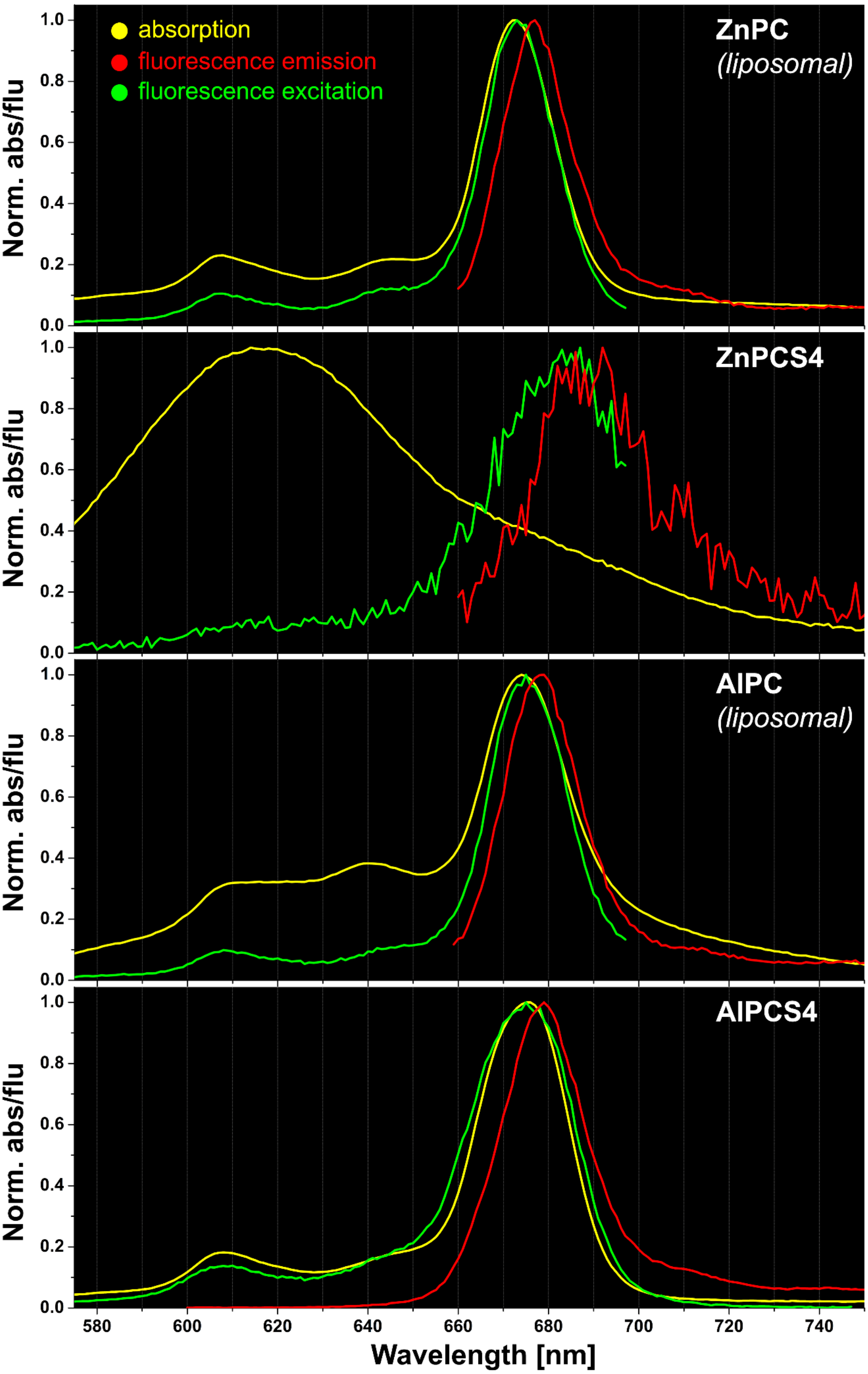

Figure S2.2 - Normalized absorption, fluorescence emission, and fluorescence excitation spectra of liposomal zinc phthalocyanine (ZnPC), tetrasulfonated ZnPC (ZnPCS4), liposomal aluminum phthalocyanine (AlPC), and tetrasulfonated AlPC (AlPCS4). Liposomes were composed of DPPC and DSPE-PEG at a 96:4 molar ratio. ZnPC and AlPC were encapsulated at a 0.003 photosensitizer:lipid ratio. All (liposomal) photosensitizers were suspended/dissolved in physiological buffer (10 mM HEPES, 0.88% (w/v) NaCl, pH = 7.4, 0.293 osmol/kg). ZnPCS4 and AlPCS4 were dissolved and tested in PBS. Spectra were normalized to the Q band maximum.

1) ITL-delivered ZnPC that initially accumulates in the cell membrane

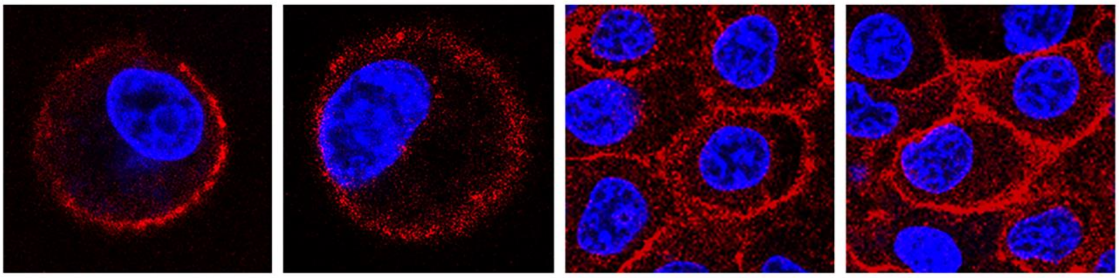

2) ITL-delivered AlPC internalized by intracellular vesicles

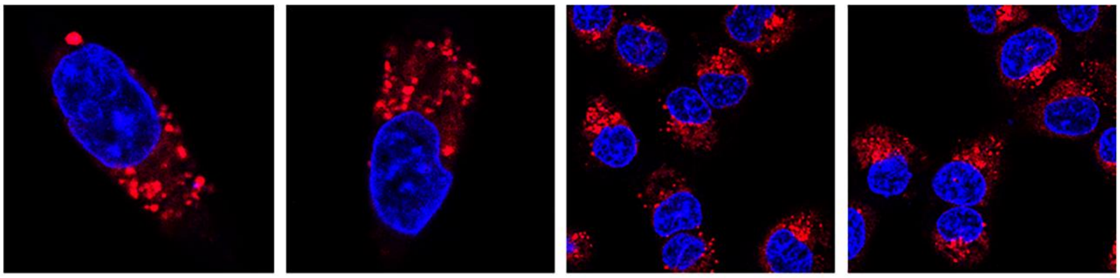

3) Perinuclear localization of ITL-delivered AlPC

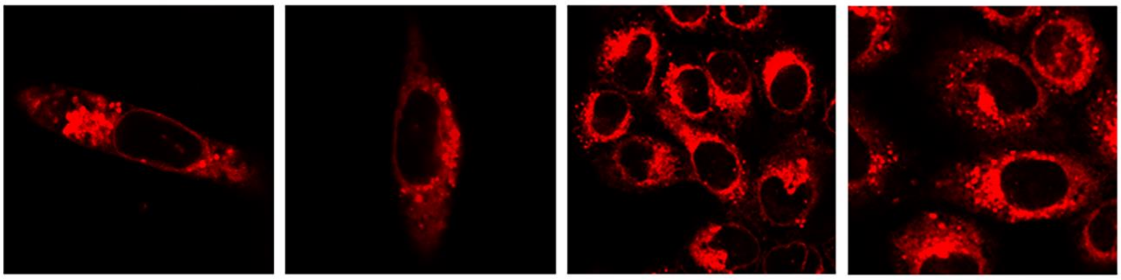

4) Vesicular accumulation of AlPCS4

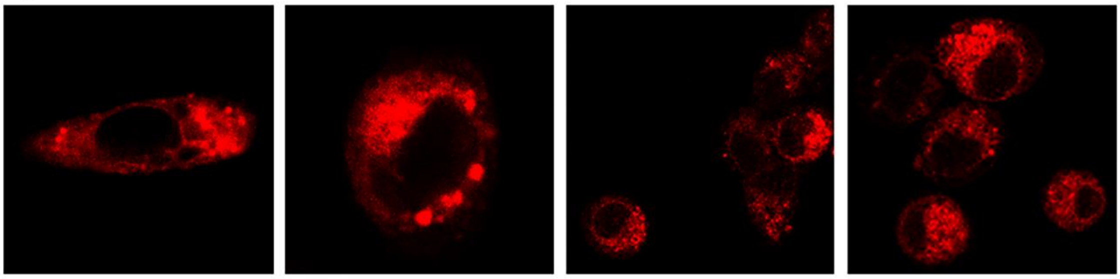

Figure S2.3 - Intracellular localization of the different metallated phthalocyanines.

S2.4.5. PDT of A431 cells leads to a mixed mode of cell death dominated by apoptosis and cell cycle arrest

Mode of cell death analysis was performed by pooling the cell culture supernatant with the harvested cells following trypsinization at different time frames after PDT. PDT triggers cell death signaling that encompasses apoptosis and necrosis, depending on the PS, whereby apoptosis predominated (Figure 2.6). The key changes of apoptosis that are relevant for flow cytometry are depicted in Figure S2.4. Particularly late apoptosis has consequences on certain read-out parameters that can be used to explain or substantiate certain observations.

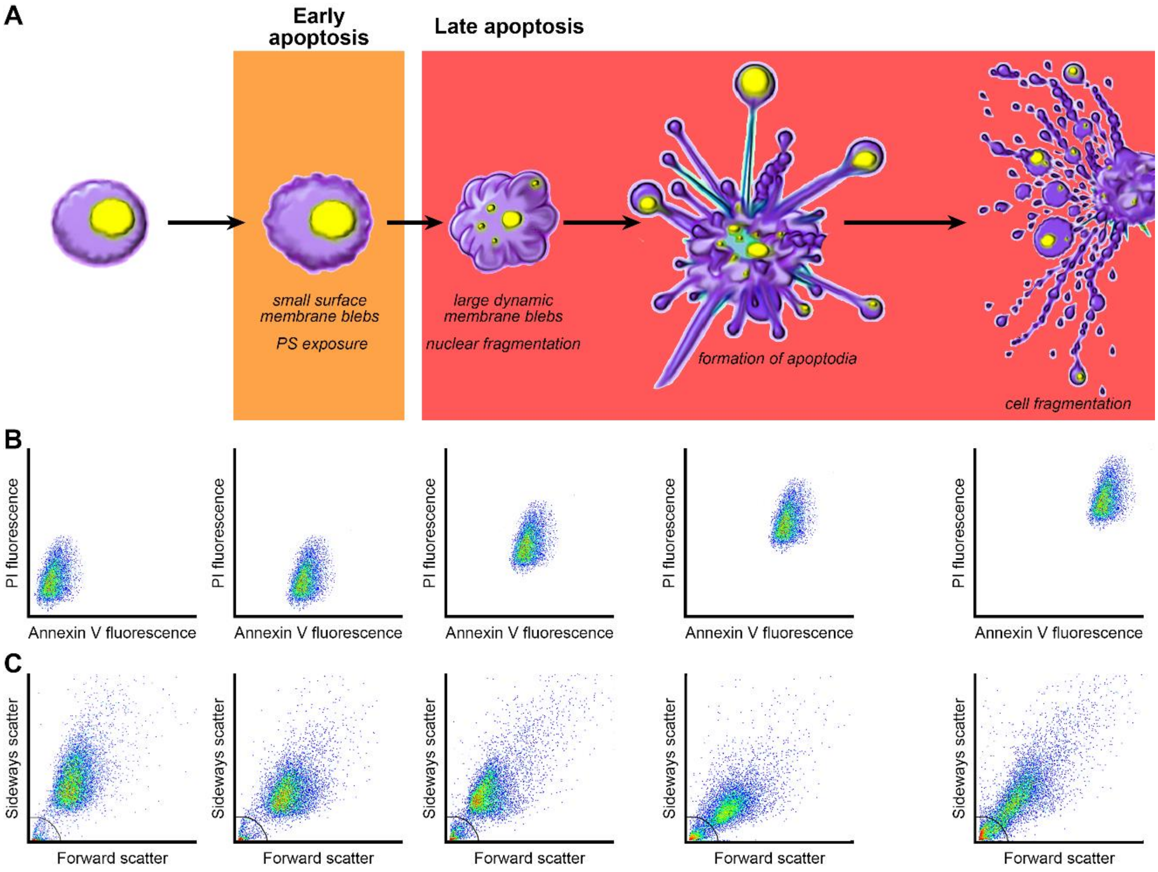

Figure S2.4 - Exemplary flow cytograms for key cellular changes during apoptosis. (**A**) Five key stages of apoptosis spanning from a healthy cell (left) to cell fragmentation (right). (**B**) Hypothetical flow cytogram profiles in terms of annexin V positivity (indicating the exposure of phosphatidylserine on the outer membrane leaflet) and propidium iodide (PI) positivity (indicating outer and nuclear membrane permeability). (**C**) Hypothetical flow cytograms in regard to forward scattering (size) and sideways scattering (granularity). The panels in (**B**) and (**C**) should be read vertically in relation to the cell's stage in panel (**A**).

First, late apoptosis is characterized by the release of apoptotic bodies that are smaller than cells and contain less granules. This translates to reduced forward scatter and sideways scatter intensity, respectively, as a result of which the flow cytometer takes longer to reach the preprogrammed 10,000 count stop command for the gated region (assuming samples are plated and/or treated at equal starting cell density). The gated region was calibrated around healthy tumor cells in all experiments. The time required to collect 10,000 counted events in the gated region was calculated and plotted in Figure S2.5 A. PDT of cells photosensitized with AlPC-ITLs and especially AlPCS4 resulted in longer acquisition times, which is in agreement with the trends in $V^{+/+}/PI^{+/+}$ cells as a function of time (Figure 2.6 B). Second, the formation of apoptotic bodies, cell remnants, and cell debris will lead to an increase in event counts outside of the gated region, particularly in the bottom left corner of the cytogram (low-intensity forward and sideways scatter) (Figure 2.3 B). When analyzing the cell remnants, microparticles, and debris we indeed found an increase in counts in the groups treated with ZnPC-ITLs, AlPC-ITLs, and AlPCS4 (Figure S2.5 B and Figure S2.6), corresponding to the cell death data (Figure 2.5 and Figure 2.6). One major exception was cells treated with ZnPC-ITLs. In a previous study with Sk-Cha1 cells (9) as well as in this study with A431 cells less extensive cell death was observed at 8 h post-PDT compared to 4 h post-PDT (Figure 2.6). The acquisition was shorter in the former (Figure S2.5 A) while the amount of non-intact cellular entities increased drastically (Figure S2.5 B), suggesting that the residually viable cells may have recovered and proliferated during the assay time (population doubling time is short for A431 cells; 18-20 h) while the lethally afflicted cells proceeded through apoptosis to account for the vast amount of cell-derived constituents at 8 h post-PDT. PDT with ZnPC-ITLs was performed at near LC$_{50}$ concentration for the 4 h time point (Figure 2.5 A), so about half of the cells would have been viable and hence able to undergo survival/anastasis (11, 150).

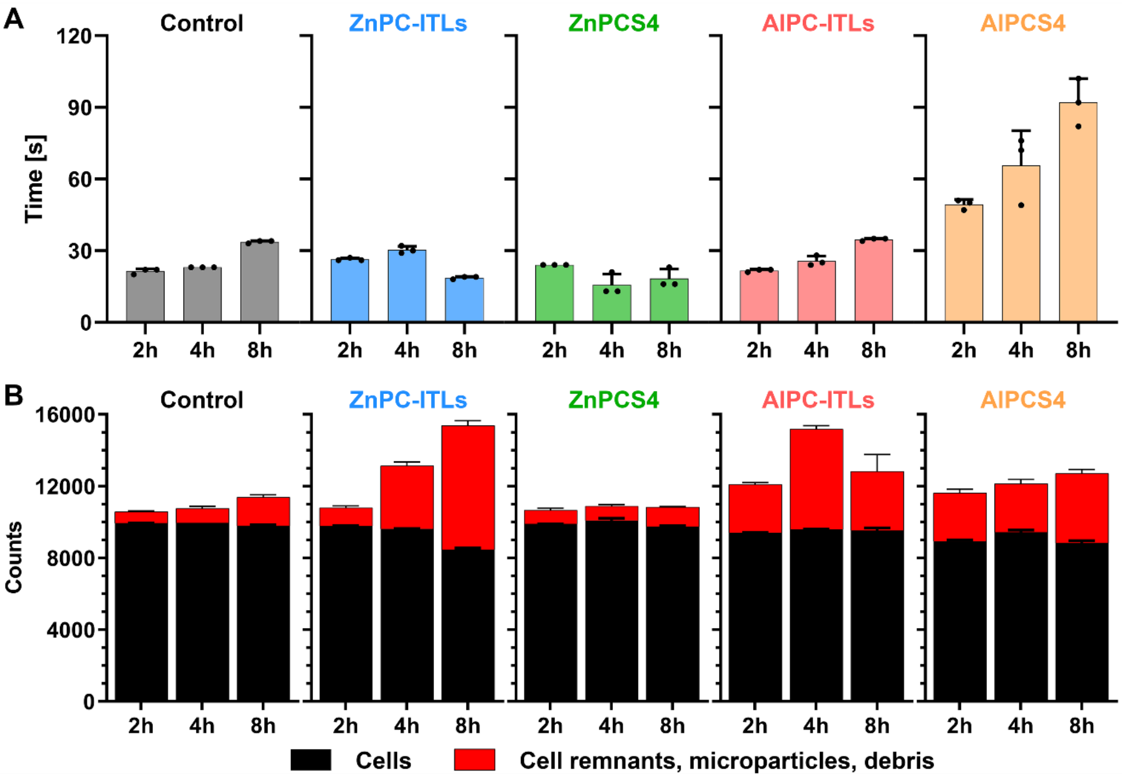

Figure S2.5 - Flow cytometry outcomes in mode of cell death experiments. A431 cells were incubated with PS in DMEM$^{-/-}$ for 1 h, washed, treated by PDT (cumulative radiant exposure of 15 J/cm^2), and stained with PI and annexin V after incubation in DMEM$^{-/-}$ for the indicated time frame. PDT was performed at the following concentrations: ZnPC and AlPC, 0.75 µM; ZnPCS4 and AlPCS4, 2.5 µM. (**A**) The time required to reach 10,000 counts in the gated region around intact tumor cells. (**B**) Amount of non-gated events (cell remnants, particles, and debris) per 10,000 gated events (tumor cells).

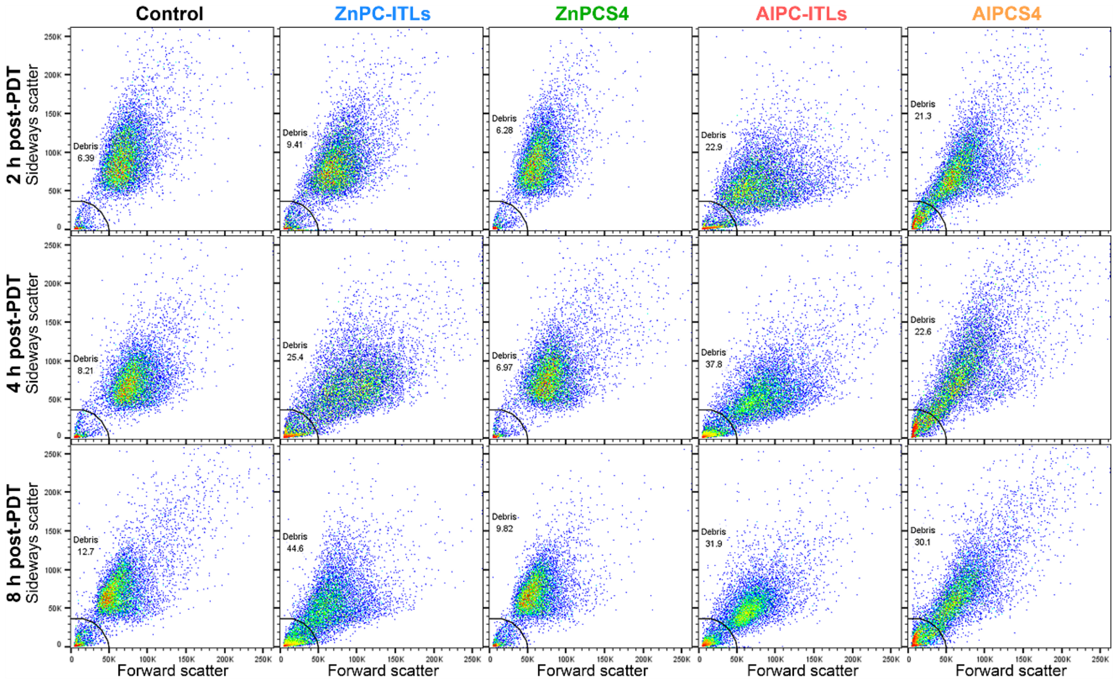

Figure S2.6 - Representative flow cytograms of A431 cells and cell remnants, microparticles, and debris after PDT. A431 cells were incubated with PS in DMEM$^{-/-}$ for 1 h, washed, treated by PDT (cumulative radiant exposure of 15 J/cm^2), and stained with PI and annexin V after incubation in DMEM$^{-/-}$ for the indicated time frame. PDT was performed at the following concentrations: ZnPC and AlPC, 0.75 μM; ZnPCS4 and AlPCS4, 2.5 μM. Quantitative data on the cell remnants, microparticles, and debris was collected from the gated region in the bottom left corner (Figure S2.4 B).

Chapter 3

Paper II

Journal of Photochemistry & Photobiology, B: Biology 234 (2022) 112500

Contents lists available at ScienceDirect

Journal of Photochemistry & Photobiology, B: Biology

journal homepage: www.elsevier.com/locate/jphotobiol

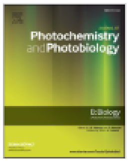

Metallated phthalocyanines and their hydrophilic derivatives for multi-targeted oncological photodynamic therapy

Lionel Mendes Dias [a,b,c,d], Mark J. de Keijzer [a,e,f,1], Daniel Ernst [a,d,1], Farangis Sharifi [c,g,1], Daniel J. de Klerk [a,d], Tony G. Kleijn [a,d,h], Emilie Desclos [c,g], Jakub A. Kochan [c,g], Lianne R. de Haan [a,d], Leonardo P. Franchi [i], Albert C. van Wijk [j], Enzo M. Scutigliani [c,g], Marcel H. Fens [e], Arjan D. Barendrecht [k], Jos´e E.B. Cavaco [b], Xuan Huang [a], Ying Xu [l], Weiwei Pan [l], Marjo J. den Broeder [m], Jan Bogerd [m], Rüdiger W. Schulz [m], Kitty C. Castricum [n], Victor L. Thijssen [n], Shuqun Cheng [o], Baoyue Ding [a,**,2], Przemek M. Krawczyk [c,g,2], Michal Heger [a,d,e,f,*,2], on behalf of the Photodynamic Therapy Study Group

[a] Jiaxing Key Laboratory for Photonanomedicine and Experimental Therapeutics, Department of Pharmaceutics, College of Medicine, Jiaxing University, Jiaxing, Zhejiang, PR China

[b] CICS-UBI, Health Sciences Research Center, University of Beira Interior, Covilhã, Portugal

[c] Department of Medical Biology, Cancer Center Amsterdam, Amsterdam UMC Location Academic Medical Center, Amsterdam, the Netherlands

[d] Laboratory of Experimental Oncology, Department of Pathology, Erasmus MC, Rotterdam, the Netherlands

[e] Department of Pharmaceutics, Utrecht Institute for Pharmaceutical Sciences, Utrecht University, Utrecht, the Netherlands

[f] Membrane Biochemistry and Biophysics, Department of Chemistry, Faculty of Science, Utrecht University, Utrecht, the Netherlands

[g] Laboratory of Experimental Oncology and Radiobiology (LEXOR), Cancer Center Amsterdam, Amsterdam UMC Location Academic Medical Center, Amsterdam, the Netherlands

[h] Department of Pathology and Medical Biology, University Medical Center Groningen, University of Groningen, Groningen, the Netherlands

[i] Department of Biochemistry and Molecular Biology, Institute of Biological Sciences (ICB 2), Federal University of Goiás (UFG), Goiânia, Goiás, Brazil

[j] Department of Surgery, Amsterdam UMC location VUmc, Amsterdam, the Netherlands

[k] CDL Research, University Medical Center Utrecht, Utrecht, the Netherlands

[l] Department of Cell Biology, College of Medicine, Jiaxing University, Jiaxing, PR China

[m] Reproductive Biology Group, Division Developmental Biology, Institute of Biodynamics and Biocomplexity, Department of Biology, Faculty of Science, Utrecht University, the Netherlands

[n] Department of Radiation Oncology, Cancer Center Amsterdam, Amsterdam UMC Location VUmc, Amsterdam, the Netherlands

[o] Department of Hepatic Surgery VI, The Eastern Hepatobiliary Surgery Hospital, The Second Military Medical University, Shanghai, PR China

[*] Corresponding author at: Jiaxing Key Laboratory for Photonanomedicine and Experimental Therapeutics, Department of Pharmaceutics, College of Medicine, Jiaxing University, Jiaxing, Zhejiang, PR China.

[**] Corresponding author.

[1] Shared second authorship.

[2] Shared senior authorship.

3. Chapter 3 - Paper II: Metallated phthalocyanines and their hydrophilic derivatives for multi-targeted oncological photodynamic therapy

3.1. Abstract

Background and aim: A photosensitizer (PS) delivery and comprehensive tumor targeting platform was developed that is centered on the photosensitization of key pharmacological targets in solid tumors (cancer cells, tumor vascular endothelium, and cellular and non-cellular components of the tumor microenvironment) before photodynamic therapy (PDT). Interstitially targeted liposomes (ITLs) encapsulating zinc phthalocyanine (ZnPC) and aluminum phthalocyanine (AlPC) were developed for passive targeting of the tumor microenvironment. In previous work it was established that the PEGylated ITLs were taken up by cultured cholangiocarcinoma cells. The aim of this study was to verify previous results in cancer cells and determine whether the ITLs can also be used to photosensitize cells in the tumor microenvironment. Following positive results, rudimentary *in vitro* and *in vivo* experiments were performed with ZnPC-ITLs and AlPC-ITLs as well as their water-soluble tetrasulfonated derivatives (ZnPCS4 and AlPCS4) to assemble a research dossier and bring this platform closer to clinical transition.

Methods: Flow cytometry and confocal microscopy were employed to determine ITL uptake and PS distribution in cholangiocarcinoma (SK-ChA-1) cells, endothelial cells (HUVECs), fibroblasts (NIH-3T3), and macrophages (RAW 364.7). Uptake of ITLs by endothelial cells was verified under flow conditions in a flow chamber. Dark toxicity and PDT efficacy were determined by cell viability assays, while the mode of cell death and cell cycle arrest were assayed by flow cytometry. *In vivo* systemic toxicity was assessed in zebrafish and chicken embryos, whereas skin phototoxicity was determined in BALB/c nude mice. A PDT efficacy pilot was conducted in BALB/c nude mice bearing human triple-negative breast cancer (MDA-MB-231) xenografts.

Results: The key findings were that [1] photodynamically active PSs (all except ZnPCS4) were able to effectively photosensitize cancer cells and non-cancerous cells; [2] following PDT, photodynamically active PSs were highly toxic to potent as per anti-cancer compound classification; [3] the photodynamically active PSs did not elicit notable systemic toxicity in zebrafish and chicken embryos; [4] ITL-delivered ZnPC and ZnPCS4 were associated with skin phototoxicity, while the aluminum-containing PSs did not exert detectable skin phototoxicity; and [5] ITL-delivered ZnPC and AlPC are equally effective in their tumor-killing capacity in human tumor breast cancer xenografts and superior to other non-phthalocyanine PSs when appraised on a per mole administered dose basis.

Conclusions: AlPC(S4) are the safest and most effective PSs to integrate into the comprehensive tumor targeting and PS delivery platform.

Keywords: photonanomedicine; interstitially targeted liposomes; *in vitro* pharmacokinetics; mode of cell death; toxicity; skin phototoxicity; pharmacodynamics; therapeutic efficacy; mouse xenograft tumor model

3.2. Introduction

Photodynamic therapy (PDT) is a non-to-minimally invasive light-based modality for the treatment of a variety of diseases such as psoriasis, age-related macular degeneration, and cancer. The cancer types that have been clinically addressed by PDT include skin-, lung-, brain-, ovarian-, bladder-, prostate-, liver-, bile duct-, pancreatic-, esophageal-, and head and neck cancer (1). PDT is doubly selective towards the tumor mass owing to the preponderant photosensitization of the tumor relative to surrounding healthy tissue and the confinement of illumination to the tumor bulk. The therapeutic efficacy of oncological PDT emanates from the induction of tumor cell death, damage to the tumor microenvironment, metabolic catastrophe in tumor cells due to hypoxia and malnutrition following vascular shutdown, and activation of an anti-tumor immune response with potential abscopal effects (2-5). Notwithstanding the fact that the modality is generally used as a last-line treatment option, the abovementioned effects have rendered PDT superior to second-line treatment options such as chemotherapy and radiotherapy in terms of select clinical outcome parameters for certain cancers (6-11). Nonetheless, several factors have deterred widespread clinical adoption of PDT, which comprise skin phototoxicity (12), the activation of tumor cell survival signaling following PDT (2, 13-16) and consequent tumor regrowth or recurrence (17, 18), the inability to treat large tumors due to the limited optical penetration depth of laser light and heterogeneous photon coverage of target tissue (19), and the requirement for specialized clinical teams and long post-treatment dark periods for patients (20). The latter is ethically problematic in case of aggressive terminal cancer with short median life expectancy (21).

To counter these clinical bottlenecks our group has developed a comprehensive tumor photosensitization strategy (20, 21) based on three distinct liposomal photosensitizer (PS) delivery systems that target pharmacologically critical locations in the tumor, namely the tumor cells (22), the tumor interstitial space (13, 23), and the intratumoral vasculature (2, 24). Photosensitizer encapsulation into liposomes will sterically hinder extravasation of PS molecules through the fenestrations in the dermal microcirculation, thereby ameliorating PS accumulation in the skin and the incidence of phototoxic reactions (25, 26). Consequently, the circulatory confinement of PS molecules will translate to effective therapeutic outcomes at lower PS dosage. Both will concurrently reduce the required post-treatment dark periods, making the treatment more patient-friendly. By photosensitizing and oxidatively damaging distinct structural elements of the tumor, the ability of sublethally afflicted tumor cells to recover from photo-induced hyperoxidative stress will be impaired. This comprehensive photosensitization strategy therefore also tackles potential tumor regrowth or recurrence. To further offset tumor cell survival in predominantly distal tumor regions (2), our group has developed fourth-generation photosensitizers that encompass the co-encapsulation of small-molecular drugs into PS-carrying liposomes so as to curtail post-PDT survival. Proof-of-concept with the hypoxic cytotoxin tirapazamine and the HIF-1α and topoisomerase II inhibitor acriflavine has been established (14, 15, 27).

The most basic formulation of the PS delivery platform concerns interstitially targeted liposomes (ITLs) composed of dipalmitoylphosphatidylcholine and a molar fraction of PEG-conjugated disteroylphosphatidylethanolamine. ITLs were designed to target the tumor stroma (28) by virtue of the enhanced permeability and retention (EPR) effect exhibited by many solid tumors (29, 30), a phenomenon exploited by several approved liposomal chemotherapy carriers (31-35). The tumor microenvironment is an established target for cancer treatment, including PDT (3). In previous studies it was demonstrated that PS-encapsulating ITLs, which do not bear targeting moieties or possess uptake-enhancing properties, were endocytosed by cultured biliary cancer (SK-ChA-1) (13, 23) and skin cancer (A431) cells (21), thereby fundamentally enabling multi-targeting. It was further shown that, upon illumination, the metallated phthalocyanine-containing ITLs produced reactive transients capable of oxidizing (bio)molecules (20, 23, 36), culminating mainly in apoptotic and necrotic cell death at half maximum lethal concentration (LC_{50}) values in the low nM range for both zinc phthalocyanine (ZnPC) and aluminum phthalocyanine (AlPC) and their hydrophilic tetrasulfonated derivatives ZnPCS4 and AlPCS4 (13, 21, 23).

In light of the abovementioned properties, the non-toxicity of the formulation in chicken embryos and mice (13), and the GMP scaling possibilities it was decided to further develop the formulation in the context of extrahepatic cholangiocarcinoma (EHCC). Presently, non-resectable EHCC (~80% of patients (37)) is incurable and responds poorly to standard and palliative chemotherapy (38). Accordingly, there is a strong medical need to develop effective therapies for EHCC. PDT constitutes a promising last-line therapy for EHCC, as corroborated in numerous clinical trials (17, 39-42). EHCCs have a major stromal component that is replete with neoangiogenic vasculature (14), rendering these tumors eligible for ITL-based photosensitization.

This study therefore aimed to validate previous results obtained with abovementioned PSs in SK-ChA-1 (23) and A431 cells (21) in cells that are instrumental in tumor biology and comprise key elements in our comprehensive tumor targeting strategy: SK-ChA-1 cells that are representative of the tumor parenchyma (43), RAW 264.7 cells that mimic tumor-resident macrophages (44), NIH 3T3 cells as substitutes for stromal fibroblasts (45), and human umbilical vein endothelial cells (HUVECs) that are analogous to the endothelial cells lining the intratumoral microvasculature (14). ITLs encapsulating ZnPC and AlPC as well as non-encapsulated ZnPCS4 and AlPCS4 were assayed for uptake, intracellular localization, dark toxicity, photodynamic efficacy, and PDT-induced mode of cell death and cell cycle arrest. Given the encouraging *in vitro* data, the ITLs were screened for systemic toxicity in zebrafish and chicken embryos and for skin phototoxicity in nude mice. Finally, an *in vivo* pharmacodynamic efficacy pilot study was conducted with the liposomal PSs in mice bearing human triple-negative mammary carcinoma (MDA-MB-231) xenografts.

3.3. Materials and methods

Supplemental material is designated with prefix 'S' and the section numbering in the supplemental material corresponds to that in the main text. A list of abbreviations is provided in the supplemental material. The chemicals/compounds, buffers, and reagents/kits are summarized in Table S3.1. Equipment and materials/disposables are listed in Table S3.2. Cells and animals and their required paraphernalia are summarized in Table S3.3. The concentrations listed are final unless specified otherwise. All procedures involving PSs were performed under dim light.

3.3.1. Photosensitizers, phospholipids, and buffers

ZnPC and AlPC were dissolved in pyridine at a 178 µM and 150 µM stock concentration, respectively. ZnPCS4 and AlPCS4 were dissolved in phosphate-buffered saline (PBS) at a 1 mM stock concentration. All PS stock solutions were stored under a nitrogen atmosphere at room temperature (RT) (ZnPC and AlPC) or 4 °C (ZnPCS4 and AlPCS4) in the dark.

Phospholipids (Table S3.1) were dissolved in chloroform and stored under a nitrogen atmosphere at -20 °C. The phospholipid concentration of stock solutions was determined spectrophotometrically by an inorganic phosphate quantification method modified from Rouser et al. (23, 46).

Physiological buffer was composed of 10 mM HEPES, 0.88% (w/v) NaCl, pH = 7.4 that was attuned to physiological conditions (0.293 osmol/kg) (23).

3.3.2. Cell culture

3.3.2.1. Cell culture for in vitro experiments

HUVECs were isolated from fresh umbilical cords obtained at the Department of Obstetrics and Gynecology of the Academic Medical Center (Amsterdam University Medical Centers) and processed as described previously (47). SK-ChA-1 cells were obtained from malignant ascites of a patient with primary adenocarcinoma of the extrahepatic biliary tree (43). Cell and cell line details are provided in section S3.3.2 (Table S3.4). Cells were grown under standard culture conditions (dark, 37 °C, humidified atmosphere composed of 5% CO2 and 95% air). Readers are referred to section S3.3.2 for cell culture details.

The cells were washed with PBS (RT, 10 mL/T75 flask) prior to detachment by Accutase treatment (1 mL/T75 flask) for 10 min under standard culture conditions or by using a cell scraper in the case of RAW 264.7 macrophages (to prevent cell activation). Cells were harvested by the addition of fully supplemented culture medium and transferred to a new T75 flask.

Cells, detached as described above, were seeded into 24 well plates 24 h prior to an experiment unless stated otherwise. The seeding density (section S3.3.2) was such that ~90% confluence was reached at the time of the experiment. Cell counting was performed with an aliquot of 10 µL using a hemocytometer and a brightfield microscope.

During the experiments, medium without fetal bovine serum (FBS) and phenol red (medium-/-) was used when cells were incubated with PSs or reagents.

3.3.2.2. Cell culture for in vivo experiments

Human triple-negative breast cancer (MDA-MB-231) cells were grown in T25 culture flasks under standard culture conditions in RPMI 1640 (further detailed in section S3.3.2 (Table S3.4). The medium was supplemented with 10% FBS, 100 µg/mL streptomycin, and 100 U/mL penicillin. The cells were washed once with PBS (RT) and detached by trypsin (1 mL per T25 flask, 2 min). Cells were resuspended in cell culture medium and centrifuged at 100 × g for 15 min at RT. The cell pellet was resuspended in cell culture medium at 3 × 106 cells/mL and Matrigel at a 1:1 ratio. The mixture was kept on ice until subcutaneous injection into the right dorsal flank of the animal (see further section 3.3.14.2).

3.3.3. Preparation, characterization, and functional testing of ITLs

3.3.3.1. Preparation

ITLs composed of 1,2-dipalmitoyl-sn-glycero-3-phosphocholine (DPPC) and L-α-phosphatidylethanolamine, distearoyl methoxypolyethylene glycol conjugate (DSPE-PEG) (96:4) molar ratio were prepared by the lipid film hydration technique as described previously (23). Briefly, the phospholipids and ZnPC or AlPC were premixed at the desired ratios and the organic phase was evaporated under a stream of nitrogen gas at 40 °C in a water bath. The lipid film was vacuum exsiccated for 30 min and hydrated with physiological buffer (section 3.3.1). The suspension was tip sonicated and the liposomes were stored at 4 °C under a nitrogen atmosphere in the dark for a maximum of 2 months (15). The PS:phospholipid molar ratio was 0.003 (21, 23).

Where indicated, fluorescently labeled ITLs were prepared by the incorporation of 1,2-dipalmitoyl-sn-glycero-3-phosphoethanolamine-N-(lissamine rhodamine B sulfonyl) (rhodamine-PE, headgroup-labeled) and/or 1-palmitoyl-2-{6-[(7-nitro-2-1,3-benzoxadiazol-4-yl)amino]hexanoyl}-sn-glycero-3-phosphocholine (NBD-PC, acyl chain-labeled) into the lipid bilayer at the expense of DPPC. Rhodamine-PE was incorporated at a 1.0% molar fraction while NBD-PC was included at a 5.0% molar fraction.

The ITLs that were used in the chicken embryo toxicity studies were prepared at a 20 mM phospholipid concentration and a 0.003 PS:phospholipid molar ratio. Instead of physiological buffer, 0.75% (w/v) NaCl in sterile MilliQ was used as lipid film hydration solution. ZnPCS4 and AlPCS4 were dissolved in PBS at a 3 mM stock concentration and diluted with MilliQ to arrive at a final concentration of 2.56 mM.

3.3.3.2. Characterization

Liposomes were characterized for size and polydispersity as well as zeta-potential by dynamic light scattering and electrophoretic mobility analysis, respectively, as described in (21, 23). The mean ± SD size [range] of ZnPC-ITLs and AlPC-ITLs used in the experiments was 120 ± 8 nm [109-127 nm] and 175 ± 10 nm [162-189 nm], respectively, with a mean ± SD polydispersity index of 0.374 ± 0.133 and 0.612 ± 0.098. The mean ± SD size [range] zeta-potential was -6.3 ± 5.4 [-2.3 to -10.1] for ZnPC-ITLs and -7.6 ± 4.5 [-3.2 to -9.6] for AlPC-ITLs.

3.3.4. *Temperature-dependent uptake of ITLs (flow cytometry)*

The effect of temperature on ITL association was investigated by incubation of rhodamine-PE-labeled ITLs with cells at 4 °C and 37 °C. A solution containing ITLs in medium-/- was prepared at 50, 100, and 250 µM final phospholipid concentration. The upper concentration limit was selected because roughly 5% of injected PEGylated lecithin liposomes passively target to the tumor following 24 h of circulation in mice (48) and PEGylated lecithin liposomes are typically administered at a systemic phospholipid concentration range of 0.02-3.3 mM in mice (49). ITLs were added to cells cultured in 12-well plates to ~90% confluence and incubated for 2 h under normoatmospheric conditions at 4 °C (refrigerator) and 37 °C (stove). Next, cells were washed with PBS (1 mL/well) and harvested using 50 µL/well of Accutase for 10 min at standard culture conditions or by scraping (RAW 264.7 cells). Harvested cells were collected in 500 µL medium-/-, transferred to 2 mL centrifuge tubes, and kept on ice until centrifugation. Following centrifugation (5 min, 200 × g, 4 °C) the supernatant was discarded and cells were resuspended in 500 µL of medium-/- before transfer to 5 mL round-bottom polypropylene tubes for flow cytometric analysis.

Viable cells were gated based on forward scatter and side scatter properties. Rhodamine-PE fluorescence was measured at λ_{ex} = 488 nm and λ_{em} = 585 ± 42 nm as an indicator of ITL-cell association (section S3.3.4). Ten thousand counts were collected in the gated region. Fluorescence intensity was averaged from 3 experimental replicates per concentration. Data were processed in FlowJo software and plotted in GraphPad Prism.

3.3.5. *ITL internalization and intracellular distribution (confocal microscopy)*

ITL internalization and intracellular localization were studied by confocal microscopy. The cells were seeded on fibronectin-coated 24 mm circular coverslips placed in 6 well plates as described in (15, 27) and grown overnight as described in section S3.3.2 until 60-70% confluence. After washing once with PBS (37 °C), ITLs labeled with NBD-PC and rhodamine-PE were added at final phospholipid concentration of 250 µM to medium-/- and incubated for 15, 30, and 60 min under standard culture conditions. Next, cells were washed and imaged as further detailed in section S3.3.5 and Tables S3.5 and S3.6.

3.3.6. Uptake of ITLs by endothelial cells under flow

Rhodamine-PE-labeled ITLs were prepared and characterized as described in section 3.3.3.1 . HUVECs were purchased from Lonza and seeded in Ibidi perfusion slides at a density of 2.4 × 10^5 cells/slide in a total volume of 150 µL complete EBM-2 medium containing SupplementMix and antibiotics (GA-1000) and allowed to attach for 2 h. Subsequently, the slides were connected to a yellow/green pump-controlled perfusion set (50 cm, internal diameter 1.6 mm, 10 mL reservoirs, Ibidi) and cultured for 3 d under continuous unidirectional flow (shear rate 300 s^{-1}, shear stress 0.3 N/m^2 (3.0 dyn/cm^2), viscosity 1 mPa•s (0.01 dyn•s/cm^2), and pressure 9.3 mbar) using PumpControl v1.5.4 software at 37 °C and 5% CO_2 in complete EBM-2 medium.

Just before the addition of the different liposomes, the old medium was removed from the pump system and flushed with 10 mL of fresh EBM-2 medium without growth factors and serum, that was in turn removed. Subsequently, 10 mL of sample in EBM-2 medium without growth factors, antibiotics, and serum was added to the 2 mL of medium remaining in the pump system, and liposomes were added at a final lipid concentration of 150 µM. HUVECs were incubated with the liposomes for 30 min at aforementioned unidirectional flow settings. Subsequently, the slides were disconnected and washed twice with 2.5 mL of EBM-2 medium. The cells were then fixed with 4% paraformaldehyde in PBS. After fixation, the nuclei were stained with 1 µg/mL Hoechst 33342 in PBS for 20 min and washed once with PBS. The F-actin cytoskeleton was stained with Alexa Fluor 488 (AF488)-conjugated phalloidin (1:50 in PBS) for 30 min and washed once with PBS. Finally, the cells were mounted with FluorSave reagent. Imaging was performed using a Zeiss Axio Observer Z1 microscope and images were processed using ZEN 2 Blue software and ImageJ software as further detailed in section S3.3.6.

3.3.7. Cell photosensitization (flow cytometry and confocal microscopy)

The relative degree of cell photosensitization was studied by flow cytometry. All four PS were diluted in medium-/- to a PS concentration of 375 nM, corresponding to a final phospholipid concentration of 125 µM for ZnPC-ITLs and AlPC-ITLs.

PSs were added to cells cultured in 12 wells-plates to 80% confluence. The plates were incubated for 1, 30, and 60 min under standard culture conditions. After harvesting with 100 µL of Accutase for 10 min at standard culture conditions (or scraping in the case of RAW

264.7 cells), cells were collected in 500 µL of medium-/- at RT, transferred to a 2 mL centrifuge tube, and centrifuged (5 min, 500 × g, 4 °C). The supernatant was discarded and the cells were resuspended in 500 µL of medium-/- (RT) for flow cytometric analysis.

Viable cells were gated based on their preset forward-scatter and side-scatter properties. PS autofluorescence was measured at λex = 633 nm and λem = 661 ± 20 nm and a fixed detector voltage (625 V). The excitation wavelength coincides with the blue Q-band absorption shoulder of the photosensitizers (20), and causes autofluorescence as a result of radiative S1 -> S0 state decay of a small fraction of the excited state electrons. Ten thousand events were collected in the gated region. Association was calculated from the difference between the mean fluorescence intensity of photosensitized cells relative to the mean fluorescence intensity of non-photosensitized cells (N = 3 independent experiments per incubation time). Data were processed in FlowJo software and GraphPad Prism.

After washing with PBS (37 °C), cells were incubated with 10 µM of AlPCS4 or ZnPCS4 or 3 µM of ZnPC or AlPC (1 mM phospholipid concentration) for 1, 30, and 60 min at standard culture conditions.

3.3.8. Dark toxicity in cultured cells

The toxicity of each PS was assessed in SK-ChA-1, HUVEC, NIH-3T3, and RAW 264.7 cells in the absence of illumination. Cells seeded in 24-wells plates were washed with PBS at RT, and PS in medium-/- was added at concentrations ranging from 0-1.5 µM for ZnPC-ITLs and AlPC-ITLs (0-500 µM phospholipid concentration, equating to 0-1.5 µM PS concentration) and 0-10 µM for ZnPCS4 and AlPCS4. Medium-/- containing 20% DMSO was used as positive control for complete cell death and medium-/- as negative control. After 24, 48, and 72 h incubation at standard culture conditions, WST-1 and SRB assays were performed in sequence on the same cell population as described previously (21) and detailed in section S3.3.8. Experiments in each group (PS concentration and incubation time) were performed in triplicate.

3.3.9. PDT of cultured cells

To compare photodynamic efficacy between the PSs, mitochondrial redox state and total protein content were measured after PDT. Cells seeded in 24 wells plates were incubated for 1 h with PS in medium-/- under standard culture conditions. The volume of physiological buffer containing the PS (50 µL added to 450 µL medium-/-) was kept constant while initial PS concentration was controlled via dilution with physiological buffer. Following photosensitization, cells were washed once with PBS (RT, 500 µL/well) and received fresh medium-/- (37 °C, 500 µL/well). The cells were illuminated with a 671 nm solid state diode laser at 500 mW for 57 s/well (the diameter of the beam was equal to the diameter of a well), yielding a cumulative radiant exposure of 15 J/cm^2. The laser output power was confirmed with a power meter before PDT. The plate was kept at 37 °C using a plate heater during PDT. Following illumination, the cells were incubated in medium-/- for 4 h or 24 h (N = 3 independent experiments per time point and PS concentration) under standard culture conditions to emulate PDT-induced malnutrition due to vascular shutdown (50, 51). Lastly, the WST-1 assay and subsequent SRB assay were performed as described in sections S3.3.8.1 and S3.3.8.2, respectively. The results were normalized to the mean of the control group that had been illuminated but not photosensitized. LC_{50} values were obtained using the non-linear fit function in GraphPad Prism.

3.3.10. Cell cycle analysis

To determine the effect of PDT on the cell cycle, PDT-treated cells were stained with propidium iodide (PI) and analyzed by flow cytometry (14, 15, 27). PDT was performed on photosensitized cells in medium-/-, illumination for 1 min and 54 s at 500 mW (cumulative radiant exposure of 15 J/cm^2 per well), with N = 3 independent experiments per PS. The percentage of the cell population in the G0/G1 phase, S phase, and G2/M phase was calculated using the Watson (Pragmatic) univariate model (52) in FlowJo software. Additional details are provided in section S3.3.10.

3.3.11. Analysis of mode of cell death

The mode of cell death was analyzed by flow cytometry. Cells were photosensitized and treated by PDT as described in section 3.3.9 and analyzed at 2 h, 4 h, and 8 h post-PDT (N = 3 independent experiments per time point). The experiment was repeated for the 4 h post-PDT incubation group, where the PS concentration effects were studied. Viable cells were quantified as AV-negative / PI-negative, while cells that were in early apoptosis were quantified as AV-positive / PI-negative. Cells in late apoptosis and necrosis were clustered and quantified as AV-positive / PI-positive and AV-negative / PI-positive, respectively (modified from (53)). Data were plotted in GraphPad Prism. More information on experimental detail is provided in section S3.3.11.

3.3.12.Systemic toxicity in zebrafish embryos

Wild-type, AB strain, Danio rerio adults were bred and raised in the aquatic facility of the Faculty of Science, Utrecht University. Institutional review board approval regarding the zebrafish experiments was exempted inasmuch as the embryos were in a non-vertebrate stage (≤ 5 days post-fertilization (dpf)) throughout the experiment and hence did not meet the animal ethics review criteria under Dutch legislation. Zebrafish care is described in section S3.3.12.

The fertilized eggs were collected 30 min after spawning, washed with sterile water, and transferred to E3 medium (5 mM NaCl, 0.17 mM KCl, 0.33 mM $CaCl2•2H2O$, 0.33 mM $MgSO4•7H2O$) in a 100 × 15 mm Petri dish. The fertilization rate was observed under a Nikon SMZ-800 stereomicroscope and the experiment was continued if fertilization was greater than 90%. An embryo in 4 to 32 cell stage was selected and transferred to a 96 wells plate with 100 µL test solution comprising 95% E3 medium and 5% PS, with a final PS concentrations ranging from 0.19-1.5 µM for liposomal ZnPC and AlPC (62.5-500 µM final phospholipid concentration) and from 16.25-150 µM ZnPCS4 and AlPCS4. The volume containing the PS was kept constant. One embryo was used per well, with a total of 8 embryo per PS concentration. The embryos were kept in an incubator at 28.0 ± 0.5 °C in the dark to prevent phototoxicity. Medium was refreshed every 24 h with medium containing the same concentration of PS.

Survival and hatch rate of embryos were recorded daily, and morphology and teratogenicity at 120 h post fertilization (hpf) were scored by two researchers (Daniel Ernst and Marjo den Broeder) as described in (54) and detailed in section S3.3.12. Group results were discarded when morphological effects had materialized in more than 20% of the control embryos. On the last day of the experiment, images were taken after anesthetizing the zebrafish embryos with 1 drop of MS222 using a Motic SMZ-171T stereomicroscope equipped with a Moticam 5 digital camera. Images were processed with Motic Images Plus 3.0 software.

3.3.13.Systemic toxicity in chicken embryos

In vivo toxicity was further evaluated in chicken embryos at the Department of Radiation Oncology, Cancer Center Amsterdam. In the Netherlands, chicken embryos are not considered vertebrates until embryonic development day 18 (EDD18). Approval by the animal ethics committee was therefore not required.

PS were introduced into chicken embryos by intravenous injection as described previously (55). Briefly, fertilized white Leghorn chicken eggs were incubated and rotated in a fan-assisted humidified incubator at a relative air humidity of 65% and a temperature of 37.8 °C for 3 d. On EDD3, a small opening of approximately 3 mm in diameter was made in the eggshell at the top of the egg and sealed with tape. The eggs were then incubated for 3 d with the opening facing upwards and without rotation. On EDD6, the small opening was enlarged to a 0.5 mm^2 window, sealed with tape, and the eggs were placed back in the incubator. On EDD10, 50 µL of control or PS formulation was slowly (2-5 min) injected intravenously under a stereomicroscope using a 33-G Hamilton needle and a 100 µL Hamilton syringe. The PS stock solutions were not further diluted (section 3.3.3), yielding a systemic PS concentration of 0.8 µM (injected dose of 1.2 nmol of ZnPC and AlPC) and 85 µM (injected dose of 128 nmol of ZnPCS4 and AlPCS4) when a blood volume of 1.5 mL is accounted for on EDD10 (56). Two control groups were included in this experiment, receiving 0.75% NaCl or 0.82× PBS, which are iso-osmolar relative to chicken embryo blood. Following injection, eggs were placed back in the incubator and viability of the embryo was monitored daily (except for the weekend) until EDD18. At the end of the experiment, embryos were cryogenically euthanized at -20 °C for 24 h. Experiments were performed at least in duplicate and a minimum of 10 eggs were evaluated for each treatment/controls. Formulation toxicity was determined by death rate and plotted in Kaplan-Meier format as a function of EDD in GraphPad Prism.

3.3.14. Phototoxicity and PDT efficacy experiments in mice

Mouse experiments were performed at the Jiaxing Key Laboratory for Photonanomedicine and Experimental Therapeutics of Jiaxing University's College of Medicine. All animal procedures were approved by the animal ethics and welfare committee of Jiaxing University Medical College under protocol number JUMC2019-003 (phototoxicity) and JUMC2019-059 (PDT efficacy). Animals were treated in accordance with the Guide for the Care and Use of

Laboratory Animals (8th edition, National Institutes of Health, Bethesda, MD) and institutional guidelines.

3.3.14.1. Skin phototoxicity in BALB/c nude mice

The experimental setup was custom-built and integrated into the animal housing facility infrastructure (Figure 3.1).

Figure 3.1 - Experimental setup for skin phototoxicity analysis in nude mice. (**A**) Anesthesia induction chamber. (**B**) LED panel (18 W) that was used as a source of light to emulate typical outdoor and indoor lighting conditions that photosensitized patients could be exposed to, producing an incident illuminance of 3,982-5,033 lux (mean ± SD = 4,558 ± 537 lux) at the level of the animals. The insert shows the LED panel in on mode. (**C**) Cage setup with the created window to which the LED panel was affixed for light exposure. The sides and bottom of the cage were covered in aluminum foil. (**D** and **E**) Individual ventilated cage setup during the skin phototoxicity study, which lasted 24 h. Active climatization of the cages prevented animal exposure to hyperthermic conditions.

Specific pathogen-free male BALB/c nude mice (N = 17) weighing between 20.5 and 23.7 g (mean ± SD = 21.9 ± 0.9 g) on the day of PS infusion were purchased from Changzhou Cavens Laboratory Animals Co. (Changzhou, Jiangsu, China). Animal care is detailed in section S3.3.14.1.

On day 1, the mice were weighed and anesthetized with diethyl ether in a drying chamber (Figure 3.1 A). The diethyl ether was dripped on a bed of cotton placed on the bottom of the chamber. The bottom compartment was closed off with filter 18 cm-diameter laboratory filter paper positioned between the cotton and the hole-containing ceramic base on which the animals were placed. Anesthetic depth was confirmed by monitoring motion, breathing rate, and the response to pain stimuli (pinching of the paw). Upon reaching a desired analgesic state, the animals were transferred to a sterile surgical pad and the legs were secured to the pad with tape. The mice received a single bolus of PS (10 mM phospholipid concentration, 0.003 PS:phospholipid molar ratio) via the penile vein (0.3 nmol/g body weight, equating to 10 µL/g) as described in (36, 57) using a 1-mL insulin syringe with a 30-G needle (Microfine, BD Biosciences). With a blood volume of 78-80 mL/kg body weight and a mean weight of 22 g, the systemic PS concentration was ~4 µM. It is recommended to use insulin syringes for accurate dosing because these syringes have minimal dead volume. Group sizes were N = 4 (ZnPC-ITLs, ZnPCS4, AlPCS4) and N = 5 (AlPC-ITLs). The animals were placed back in the cage and, upon completion of a group, the side and bottom of the cage was sealed with aluminum foil to shield the photosensitized mice from light.

Twenty-four hours after PS injection (day 2), all added nesting material was removed. An 18-W LED panel (Figure 3.1 B) emitting white light (Figure 3.1 C) was used as PS excitation source to emulate outdoor and indoor lighting conditions that photosensitized patients are subjected to. The emission spectrum of sunlight and the LED panels was measured with an Ocean Optics QE65000 spectrometer. The spectrometer was connected to a modified Leica M165 FC fluorescence stereomicroscope (36) in case of LED panel measurements. The emission spectrum of the LED panel presented against the visible light spectrum of daylight and the absorption spectrum of each PS in Figure S3.4. One LED panel was fixed to the side of each cage where the aluminum foil had been removed (Figure 3.1 D-E). This configuration yielded an illuminance ranging from 3,982-5,033 lux (mean ± SD = 4,558 ± 537 lux) in the center of the cage at the level of the bedding. The rest of the aluminum cover was not removed to ensure light reflection throughout the cage and to keep out stray light from neighboring cages. Mice received 125 µL of butorphanol (1 mg/mL injection solution that was diluted 5× with PBS, ~1.3 µg/g) subcutaneously in the dorsal neck region for analgesic purposes. Next, the LEDs were turned on for 24 h light exposure.

After 24 h illumination (day 3), the animals were terminated by cervical dislocation following diethyl ether anesthesia. Mice were inspected macroscopically for skin damage (burns, erythema, crusting, hemorrhage) and photographed (Galaxy S8, Samsung Electronics). Skin biopsies were fixed in formalin for 6 h at RT and for 24 h at 4 °C, dehydrated in graded steps of ethanol (50%, 70%, 80%, 95%, and 100%, 1 h 2×/step), cleared in xylene (30 min, 2×), and embedded in paraffin. Five-µm thick sections were cut with a microtome, stained with hematoxylin & eosin (H&E), and mounted on standard light microscopy slides. Three to 10 sections per mouse were assessed by two histopathologists (YX and TGK) blinded to the groups at 100, 200, and 400× magnification. Abnormalities such as erosions, ulceration, epidermal changes, hemorrhage, edema, influx of inflammatory cells, destruction of dermal adnexa, and fat necrosis were evaluated. The influx of inflammatory cells was scored as absent/normal (0), mild (1), and moderate (2) and the score was averaged per group.

3.3.14.2. In vivo PDT efficacy in human tumor-bearing BALB/c nude mice

A total of 25 male BALB/c nude mice (4 - 6 weeks old) weighing between 19.9 and 25.3 g on the day of PS injection (day 0) were included in this pilot study and maintained as described in section S3.3.14.2. Mice were acclimated to laboratory conditions for 2 weeks before xenografting.

Cultured MDA-MB-231 cells were cultured and injected as described in section 3.3.2.2. Upon reaching a tumor volume between 100 - 200 mm^3 the animals were randomly assigned to 1 of 3 groups: control (N = 7), ZnPC-ITLs (N = 6), AlPC-ITLs (N = 7). A total of 4 mice did not develop a tumor and 1 animal died from anesthesia.

Mice were weighed and anesthetized with diethyl ether in an anesthesia induction chamber (Figure 3.1 A) as described in section 3.3.14.1. When a desired analgesic depth was achieved, the animals were transferred to a sterile surgical pad and the legs were secured to the pad with tape (Figure S3.5 A). Mice received a single bolus of ZnPC-ITLs or AlPC-ITLs (10 mM final lipid concentration, 200 µL injection volume, 6 nmol PS per animal) or PBS (control group) via the penile vein, using a 1 mL insulin syringe with a 30-G needle, yielding a systemic PS concentration of ~3 µM. A maintenance anesthesia chamber comprising diethyl ether-primed cotton balls placed in a 500 mL Erlenmeyer flask (Figure S3.5 B) was used when necessary to properly sedate the animals during the injection procedure. The animals were placed back in the cage and controlled housing environment (dim light) until PDT was performed.

PDT was performed 24 h after PS administration. Mice were anesthetized as described in section 3.3.14.1 and transferred to a sterile surgical pad where the animals were secured with surgical tape on their ventral side to expose the tumor region (Figure S3.5 C). A 671 nm solid state diode laser coupled to an optical fiber (inner diameter of 400 µm) was allowed to equilibrate for 30 min prior to PDT to ensure constant power output. The laser probe was secured in a portable retort stand and clamp and positioned approximately 3 cm from the tumor surface, accounting for an incident spot diameter of 1 cm. PDT was performed at 200 mW output power (incident irradiance of 255 mW/cm^2), confirmed with a power meter before illumination, for 13 min and 6 seconds to yield a cumulative radiant exposure of 200 J/cm^2.

Following PDT, the animals were returned to their cage and light-controlled environment. Mice were inspected macroscopically for skin damage and general wellbeing every day during 20 d post-administration. The animals were weighed every 2 d and tumor length (L) and width (W) were measured with a digital Vernier caliper. Tumor volume (V) was calculated by $V = 0.5\ [L^2 \times W]$ (58). A tumor volume of 1,800 mm^3 was set as human endpoint, the reaching of which resulted in the sacrifice of diethyl ether-anesthetized mice by cervical translocation. Tumors were removed with surgical scissors and tweezers, weighed, and stored at -20 °C for future analyses.

3.3.15. Statistical analysis

Statistical analysis was performed on Kaplan-Meier data sets in GraphPad Prism. The ZnPC-ITL and AlPC-ITL group was compared to the control group using a log-rank Mantel-Cox test and a Gehan-Breslow-Wilcoxon test. The highest P-value was noted in the results. A P-value of ≤ 0.05 was considered statistically significant.

3.4. Results and discussion

In previous work (21) we employed an attritional approach to study the most important aspects of PDT in an *in vitro* setting. The approach was based on association and uptake analyses to determine whether cells were photosensitized, which is essential for a therapeutic effect. When photosensitization was confirmed, the dark toxicity of the PSs was assessed inasmuch as non-illuminated PSs should not be toxic to cells in the absence of light (59) because of non-selective tissue distribution and uptake (60-62) and hence potential organ damage. When the PSs exerted no dark toxicity, PDT efficacy was confirmed based on cell viability, mode of cell death, and cell cycle arrest assays, *e.g.*, key events in therapeutic tumor killing. A similar approach was applied in the current study and ensued by additional assessment of systemic toxicity and skin phototoxicity *in vivo* to build a preclinical dossier for further translational research prior to clinical trials.

3.4.1. Tumor-comprising cells take up ITLs in a concentration- and incubation time-dependent manner

Previously it was found that PS-encapsulating ITLs were internalized by cultured biliary cancer (SK-ChA-1) (13, 23) and skin cancer (A431) cells (21). This behavior may not only enable passive targeting of PS to the tumor stroma via the EPR effect (63), but also facilitate subsequent tumor cell photosensitization, which is advantageous in terms of a therapeutic net effect. In the current study, flow cytometry and confocal microscopy imaging were used to verify the uptake of fluorescently labeled ITLs in SK-ChA-1 cells as well as in tumor stromal cells, *e.g.*, fibroblasts (NIH-3T3), endothelial cells (HUVECs), and monocyte/macrophage-like cells (RAW 264.7).

As shown in Figure 3.2 A, both tumor and non-tumor stromal cells were fluorescently labeled by ITLs after 2 h incubation at 37 °C in a phospholipid concentration-dependent manner. Incubation at 4 °C, at which endocytosis and intracellular transport processes are halted (64, 65), augmented the fluorescence staining intensity of SK-ChA-1 cells, had no notable effect in NIH-3T3 cells, and reduced it in HUVECs and RAW 264.7 cells compared to the data at body temperature (Figure 3.2 A). These findings not only suggest uptake of the ITLs (instead of merely adhesion) but also indicate that uptake is receptor-mediated in endothelial cells and macrophages but not in cancer cells and fibroblasts. Of note, membrane-membrane contact and subsequent fusion (66) are deterred by the PEG chains, making coalescence of phospholipid bilayers unlikely at 4 °C. Confocal microscopy (Figure 3.2 B) confirmed that the association observed by flow cytometry was caused by the uptake of the PEGylated liposomes and not merely adhesion to the cells' membrane surface. The uptake mechanism was not further studied at this stage because the *in vitro* uptake dynamics may misrepresent the more relevant *in vivo* cellular internalization processes, which are dominated by the presence and composition of the plasma protein-replete corona covering the PEGylated liposome surface (67). The unhindered uptake of PEGylated liposomes by cells is in lockstep with other studies (68), and some have even reported increased uptake of nanoparticles as a result of PEGylation (69). The current findings indicate that cell type is a determinant factor in ITL uptake rate. Fibroblasts had reached a near-saturated state after 15-min incubation while the other cell types exhibited a gradual increase in staining intensity over the course of 60 min. The staining pattern was generally homogeneous across the intracellular space for both fluorescently labeled phospholipids but also revealed localized focal and granular rhodamine-PE concentration. The deviation from the NBD-PC distribution profile indicates differential distribution kinetics of the phospholipids following internalization, which was characteristic for all cell types but was most clearly visible in HUVECs following 60-min incubation (Figure

3.2 B). In any case, the ITLs were not retained in endosomes as intact particles - a common fate of PEGylated nanocarriers upon endocytosis (70). A widespread dispersion throughout the cell is potentially beneficial for PDT efficacy with lipophilic PSs as it is expected that multiple cellular structures will be photosensitized. Indeed, multi-site photosensitization leads to the induction of more profound cell death compared to single site photosensitization (20, 21).

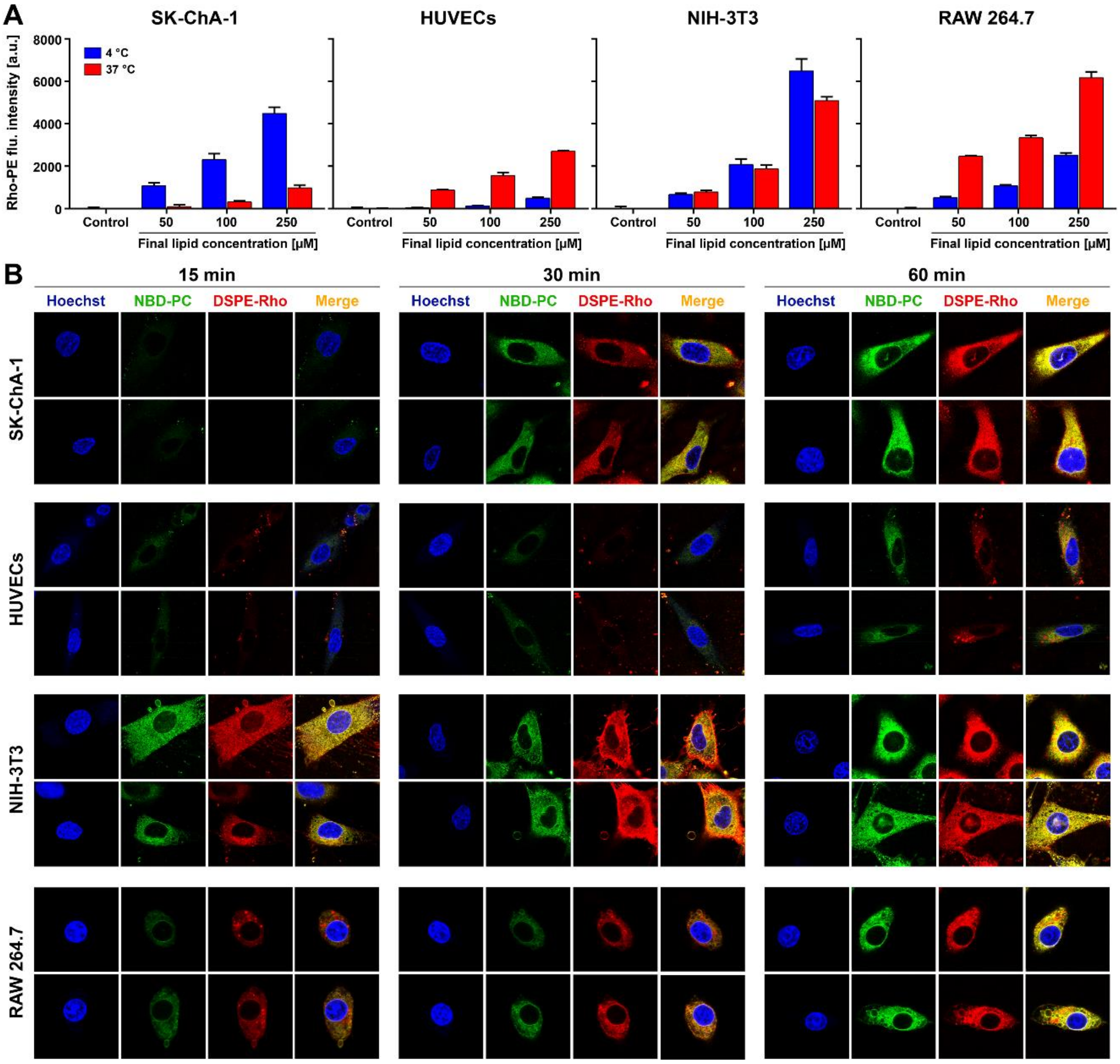

Figure 3.2 - Uptake and intracellular distribution of fluorescently labeled ITLs in cultured cells. (**A**) Cells were incubated with 50, 100, and 250 μM of ITLs (final phospholipid concentration) labeled with 1 mol% rhodamine-PE for 2 h at 4 °C and 37 °C. ITL association with cells was analyzed by flow cytometry based on rhodamine-PE fluorescence. Data are presented as mean ± SD of N = 3 experimental replicates per group. (**B**) Cells were incubated with 250 μM of ITLs (final phospholipid concentration) containing 5 mol% of NBD-PC (green) and 1 mol% of rhodamine-PE (red) for 15, 30, and 60 min, fixed, and imaged by confocal microscopy. Hoechst 33342 was used to stain the cell nucleus (blue) post-fixation. Experimental detail is provided in section 3.3.5 and S3.3.5. Images were edited in Adobe Photoshop for hue, lightness, saturation, and contrast in a clustered manner to preserve relative differences in fluorescence intensity.

In contrast to tumor cells, tumor-resident macrophages, and fibroblasts, ITLs interact with endothelial cells under hemodynamic conditions. Accordingly, ITL uptake by cultured

HUVECs was assayed in Ibidi flow chambers (36) using parameters that mimic the lower bound flow rates in microvasculature (71) in the absence of plasma proteins and FBS. ITLs were taken up by HUVECs (Figure 3.3 A) to different degrees (Figure 3.3 B). The distribution of intracellular fluorescence was comparable to what was observed under static incubation conditions (Figure 3.2 B), namely patches of homogeneously dispersed rhodamine-PE (Figure 3.3 B, green arrows) and fluorescence-dense clusters that likely comprise various organelles (Figure 3.3 B, red and yellow arrows). Photochemical damage to the cell and organelle membranes is expectedly beneficial to indirect tumor killing effects via vascular occlusion, which has been observed following PDT of human tumor xenografts (72) and chicken chorioallantoic membrane vasculature (73). Photochemical disruption of cell integrity, endothelial cell activation, and exposure of the basement membrane are vaso-occlusive events in that these trigger coagulation and thrombosis (73, 74). The corollary hemostasis then leads to anoxia, metabolic catastrophe (2), and cell death. It remains to be seen what the effect of plasma proteins will be on ITL uptake by HUVECs under flow and hence on photosensitization of tumor endothelium in a normophysiological setting.

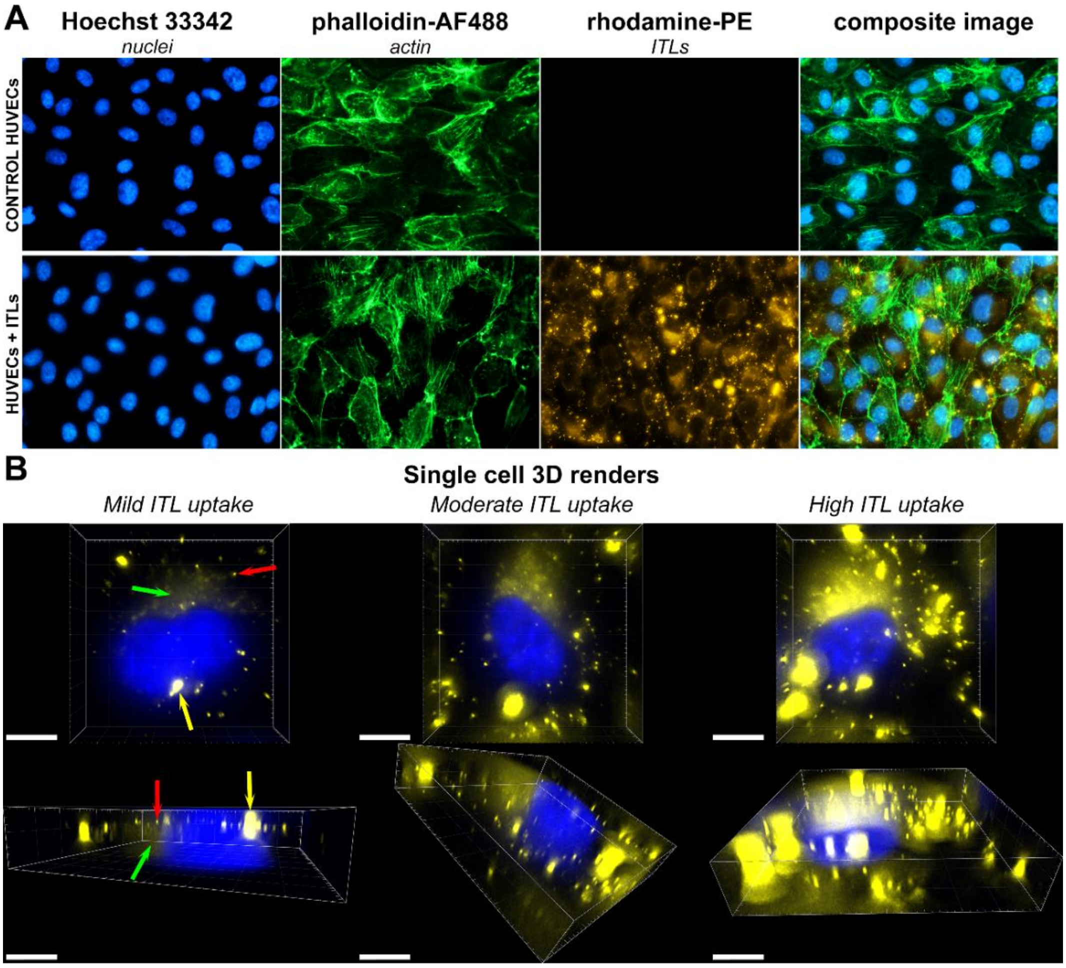

Figure 3.3 - ITL uptake by endothelial cells under flow conditions. HUVECs were cultured in Ibidi flow chambers under continuous flow conditions for 3 d and subsequently exposed to 150 µM of rhodamine-PE-labeled

ITLs (yellow) in EBM-2 medium without growth factors, antibiotics, and serum for 30 min during unidirectional flow (shear rate 300 s^{-1}, shear stress 0.3 N/m^2 (3.0 dyn/cm^2), viscosity 1 mPa•s (0.01 dyn•s/cm^2), and a pressure of 9.3 mbar). Cells were fixed and counterstained with phalloidin-AF488 (actin cytoskeleton, green) and Hoechst 33342 (nuclei, blue) and imaged by fluorescence microscopy (**A**). Control HUVECs were not exposed to ITLs. (**B**) 3D renders of single cells to demonstrate spatial distribution of rhodamine-PE fluorescence in cells with mild, moderate, and high ITL uptake. Green arrows point to dispersed rhodamine-PE, red arrows indicate small clusters of rhodamine-PE fluorescence, whereas yellow arrows designate large conglomerates of fluorescence. Scale bar = 3 μm.

3.4.2. Tumor-comprising cells are ubiquitously photosensitized by liposomal and tetrasulfonated metallated phthalocyanines

After confirming the uptake of the liposomal constituents of ITLs by target cells, we investigated whether and to what extent liposomal PS delivery occurred and how the PS molecules were distributed intracellularly. Photosensitization by ZnPC and AlPC derivatives was also determined. Photosensitization was screened using PS autofluorescence (21). It should be noted that, since the photophysical and photochemical properties differ among the PSs, only intragroup comparisons can be made (20, 21).

All cell types had internalized PS molecules during 60-min incubation but the level of photosensitization was PS- and cell type-dependent (Figure 3.4 A). No plateau in intracellular PS concentration was reached during 60 min incubation in any of the cell types (Figure S3.6). For the ITLs it was hypothesized that the degree of photosensitization would be proportional to the intensity of phospholipid fluorescence. However, this was nullified, as for example RAW 264.7 macrophages exhibited the most intense rhodamine-PE fluorescence (indicating greatest ITL internalization; Figure 3.2 A) but the lowest ZnPC and AlPC fluorescence (indicating lowest photosensitization). The disconnect could not be explained by technical reasons given that the uptake experiments had been performed under the same conditions. Moreover, it is unclear why a change in the central core elements of the PSs (chloro(29H,31H-phthalocyaninato)aluminum (III) vs. zinc (IV) phthalocyanine), which is located in the most lipophilic region of the lipid bilayer with no direct impact on membrane-membrane interactions, would have a profound effect on cell uptake (see uptake of ZnPC-ITLs in SK-ChA-1 cells versus HUVECs compared to the uptake of AlPC-ITLs in those cells; Figure 3.4 A). Stark differences also manifested at the level of intracellular distribution kinetics. ITL-delivered ZnPC accumulated in the cell membrane during the first 30 min of incubation and gradually scattered across the rest of the cellular milieu in the subsequent 15 min (Figures S3.7-S3.9). Contrastingly, ITL-delivered AlPC had already homogenously diffused throughout the cell at the 15 min assessment point (Figures S3.7-S3.9). The implications of these observations should be considered when designing *in vitro* experiments since intracellular PS localization and mode of cell death are interrelated (20). Some PSs require more than 60 min to reach uniform distribution in cells.

Nevertheless, the intracellular PS distribution patterns after 60 min of ITL exposure (Figure 3.4 B) were comparable to the labeled phospholipid distribution patterns (Figure 3.2B). In fact, both types of PSs were replete throughout the cell with a few notable exceptions addressed below, whereby ZnPC and AlPC occupied lipophilic domains and ZnPCS4 and AlPCS4 were enriched in the hydrophilic regions of the cell based on their chemical properties (20). ZnPCS4 has a low fluorescence quantum yield and was therefore difficult to image. ZnPC distribution appeared more granular than AlPC distribution in SK-ChA-1 cells, implying that ZnPC may be enriched in organelles relative to other structures in cancer cells. Almost exclusive endovesicularization was noted for AlPCS4 in HUVECs, suggesting pinocytic uptake and endosomal confinement of the PS. In contrast, the other cell types exhibited pleiotropic distribution of AlPCS4. Homogeneous distribution patterns were also observed in SK-ChA-1 cells (23) and human epidermoid carcinoma (A431) cells (21) and therefore appear to be the main dispersion mode. As alluded to previously, multitargeted cytosolic photosensitization is desirable for optimal PDT efficacy.

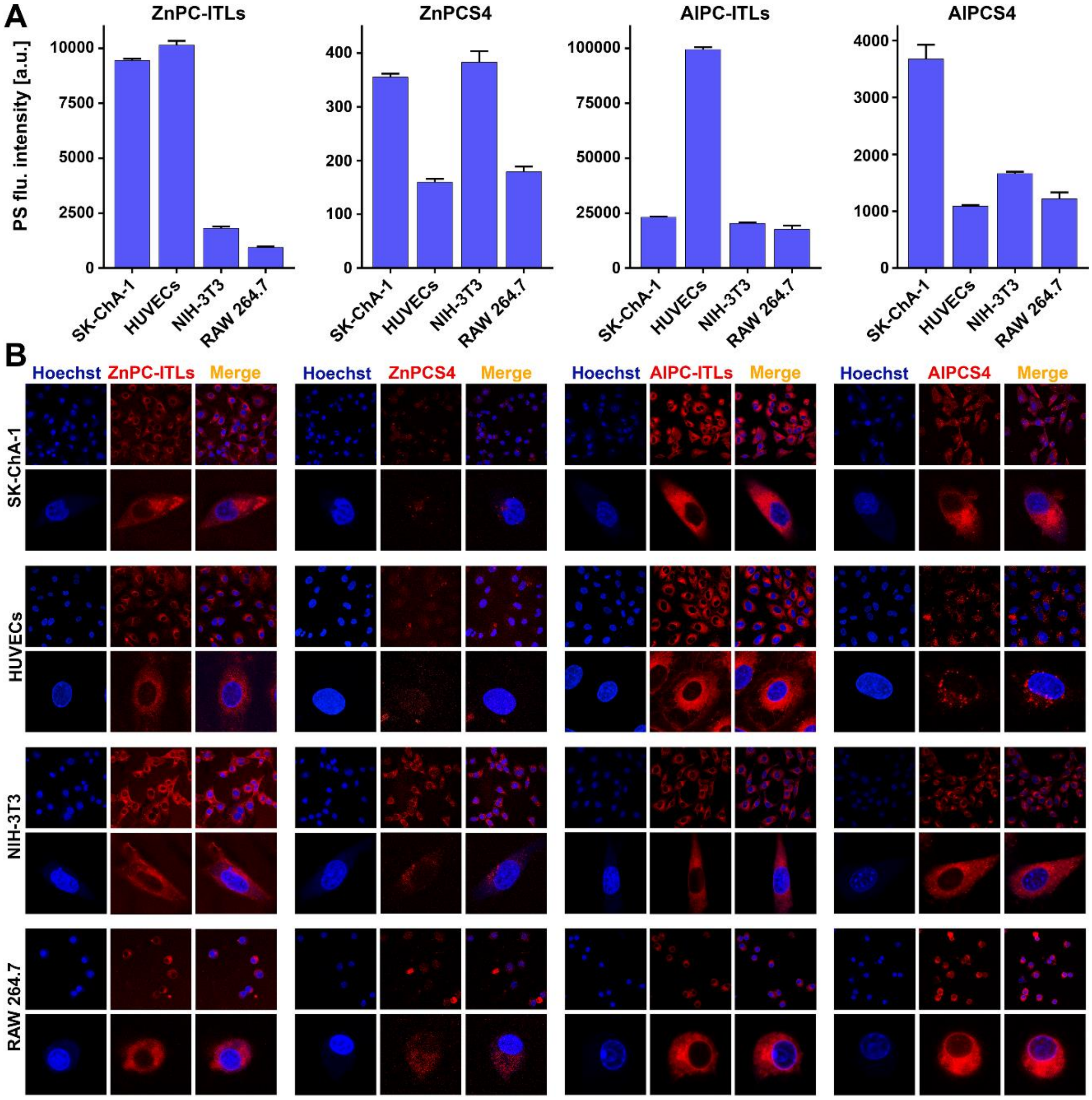

Figure 3.4 - Photosensitization of cultured cancer cells. (**A**) Cells were incubated either with ZnPC-ITLs or AlPC-ITLs (125-μM final phospholipid concentration, equating to 0.375 μM PS concentration) or with 0.375 μM of ZnPCS4 and AlPCS4 for 60 min under standard culture conditions (N = 3 per group) and analyzed by flow cytometry. The fluorescence intensity was background-corrected for cell autofluorescence. (**B**) Cells were incubated with either ITL-delivered ZnPC or AlPC (1,000 μM final phospholipid concentration, equivalent to 3 μM PS concentration) or with 10 μM of ZnPCS4 or AlPCS4 for 60 min under standard culture conditions. Following fixation, cells were imaged with confocal microscopy using PS autofluorescence (red). Hoechst 33342 was used to stain nuclei (blue).

3.4.3. Lipophilic and hydrophilic metallated phthalocyanines exhibit no-to-moderate dark toxicity

The toxicity of PSs in the absence of light was determined using the WST-1 assay, reflecting the mitochondrial redox potential, and the SRB assay, which is a measure of the total protein content. In principle, afflicted cells undergo mitochondrial perturbation and uncoupling of the electron transport chain before detaching from the well surface, so the assays reflect early and late events in the death cascade.

At the longest incubation time (3 d) and highest concentration (Figure 3.5), none of the PSs exerted toxicity in cancer cells, which is consistent with earlier reports on Sk-ChA-1 cells (13, 23) and A431 cells (21). The non-cancerous cells were more susceptible to the PSs. ZnPCS4 showed the highest toxicity (SRB assay) in endothelial cells, fibroblasts, and macrophages. Toxicity generally set in or was exacerbated after longer incubation times and higher PS concentrations (Figures S3.10 and S3.11). The degree of toxicity was mild-to-moderate in the non-cancerous cells. It should be noted that the experiments were performed in medium-/- that lacked FBS. Although this did not affect cancer cells, the absence of FBS may have rendered the non-cancerous cells more susceptible to stress (in this case from potentially toxic compounds) and may hence be an overestimation of toxicity before illumination. Naturally, after PDT the liposomal constituents and PSs will remain in the non-cancerous cells and could, based on the data in Figure 3.5, confer an additional boost in toxicity in photochemically damaged cells suffering from hyponutrition and metabolic crisis.

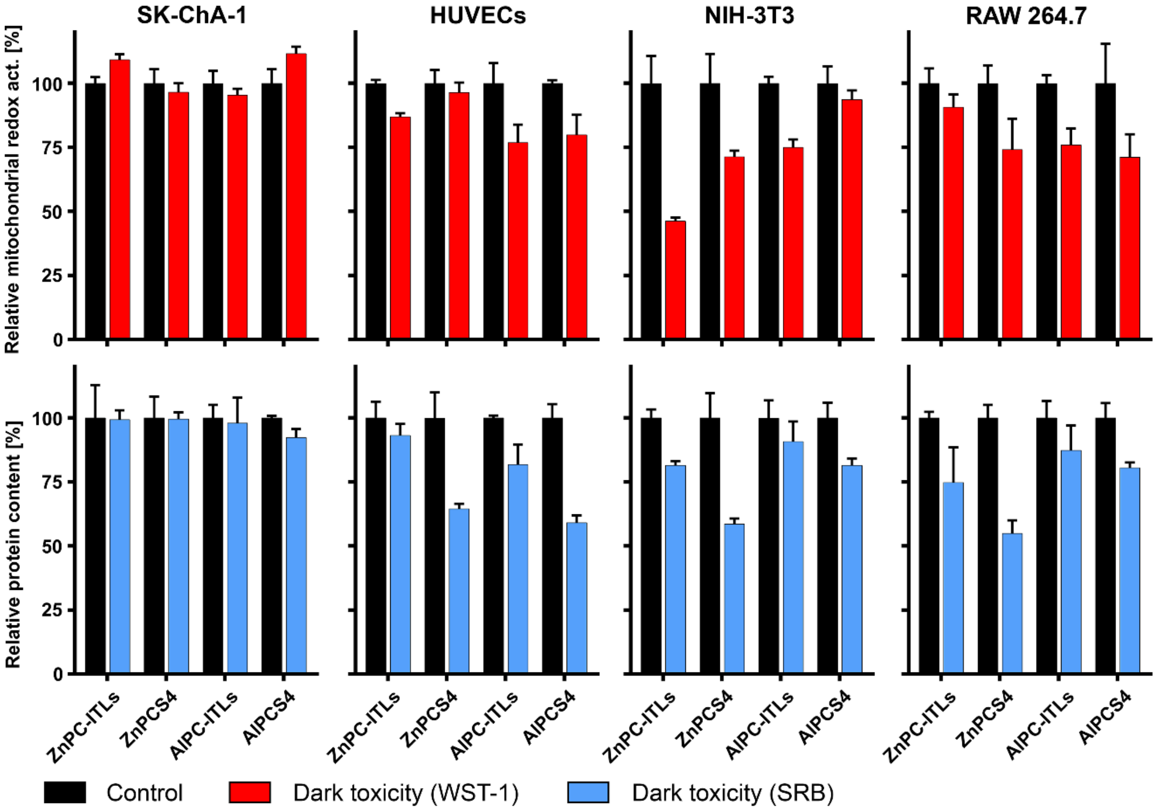

Figure 3.5 - Dark toxicity in cultured tumor-comprising cells. SK-ChA-1, HUVEC, NIH-3T3, and RAW 264.7 cells were incubated with 500 µM of ZnPC-ITLs and AlPC-ITLs (equivalent to 1.5 µM PS concentration) or 10 µM of ZnPCS4 and AlPCS4 for 72 h in the dark under standard culture conditions. Toxicity was analyzed using a WST-1 assay (mitochondrial activity; red bars) followed by the SRB assay (total protein content; blue bars). Cells in the control group were not exposed to PSs. Individual results were normalized to the mean of the control group. Data are reported as mean ± SD for N = 3 independent experiments per group. Readers are referred to Figures S3.10 and S3.11 for dark toxicity at earlier time points and lower PS concentrations.

It is questionable whether the tumor-comprising cells will reach the ITL exposure levels *in vivo* as applied in the *in vitro* assays. As summarized in (49), liposomal formulations are injected into animals at a plasma concentration of maximally 3 mM phospholipids. It is therefore improbable (and unfortunate) that passively targeted ITLs will attain an intratumoral concentration of 0.5 mM (*e.g.*, ~15% of total injected dose), especially since comparable formulations of doxorubicin (Caelyx) accumulate in the tumor at a ~4% fraction of the injected dose after 24 h and 48 h circulation (75). The highest evaluated phospholipid concentration is even more unlikely to be achieved in the plasma of human patients because that would require the administration of a large volume of a highly concentrated liposomal suspension. Consequences for non-malignant endothelial cells, fibroblasts, and macrophages that the injected liposomes come in contact with are therefore unwarranted. Accordingly, the *in vitro* toxicity results pose no practical concern at this stage with respect to the ITL formulations.

For the water-soluble AlPCS4 the systemic concentration can be easily increased compared to what was used in the *in vitro* dark toxicity studies, although toxicity to non-cancerous cells should be taken into account. In unpublished pilot experiments we injected 2 µmol/mouse and 1 µmol/mouse of AlPCS4, which translates to a systemic concentration of 1.2 mM and 0.6 mM at a blood volume of 80 µL/g body weight. These high concentrations resulted in 100% (3/3) and 67% (2/3) mortality 24 h after intravenous administration. Consequently, *in vivo* toxicological testing was performed in two animal models below to curtail any detrimental systemic effects of the PS before PDT *in vivo*.

3.4.4. All PSs except ZnPCS4 exhibit strong-to-potent toxicity in illuminated tumor-comprising cells

PDT was performed at the same settings as in the previous study with A431 cells (21) to make comparative analysis possible. In A431 cells and the cell lines investigated in the present experiments, PDT with ZnPCS4 conferred no notable light-mediated toxicity (Table 3.1) (21), which is in agreement with the inability of ZnPCS4 to generate ROS upon illumination (20) and the absence of protein oxidation (Figure S3.14). ZnPCS4 was therefore deemed ill-suited for further development of the PDT platform (21), corroborated here. When grouped, the remaining PSs were associated with the following mean ± SD LC_{50} values: 1.17 ± 1.80 µM (range 0.11-5.72 µM), WST-1 at 4 h; 2.11 ± 2.68 µM (range 0.50-9.80 µM), SRB at 4 h; 0.74 ± 1.12 µM (range 0.05-4.04 µM), WST-1 at 24 h; and 1.22 ± 1.41 µM (range 0.01-4.80 µM), SRB at 24 h. Compounds with an LC_{50} value of < 1 µM were classified as potent, whereas compounds with an LC_{50} in the range of 1-20 μM were classified as having very strong toxicity (76). ZnPC-ITLs, AlPC-ITLs, and AlPCS4 gyrated between these classifications depending on the cell line, assay method, and the time interval between treatment and assessment. The PSs can therefore be considered good-to-excellent oncotherapeutics in the framework of our comprehensive PDT platform targeting the most important tumor-comprising cells.

Table 3.1 - PDT-mediated half maximum lethal concentration (LC_{50}) of lipophilic and hydrophilic metalated phthalocyanines. The LC_{50} values (in μM) were calculated from the non-linear fit function (Figures S3.12 and S3.13) and are given as mean ± SD of N = 3 independent experiments per group.

		WST-1		**SRB**	
		Incubation time [h]		**Incubation time [h]**	
PS	**Cell type**	**4h**	**24h**	**4h**	**24h**
ZnPC (ITLs)	SK-ChA-1	**0.22** ± 0.01	**0.25** ± 0.01	**1.14** ± 0.15	**0.16** ± 0.02
	HUVECs	**3.93** ± 0.93	**4.04** ± 0.75	**2.27** ± 0.47	**1.87** ± 0.16
	NIH-3T3	**5.72** ± 1.38	**0.60** ± 0.04	**3.17** ± 0.52	**2.03** ± 0.42
	RAW 264.7	**0.62** ± 0.03	**0.48** ± 0.01	**1.12** ± 0.03	**0.91** ± 0.07
ZnPCS4	SK-ChA-1	**26.0** ± 0.6	**N.D.**	**18.1** ± 1.3	**N.D.**
	HUVECs	**N.D.**	**N.D.**	**N.D.**	**25.7** ± 0.8
	NIH-3T3	**N.D.**	**N.D.**	**N.D.**	**N.D.**
	RAW 264.7	**N.D.**	**N.D.**	**N.D.**	**N.D.**
AlPC (ITLs)	SK-ChA-1	**0.35** ± 0.2	**0.05** ± 0.01	**0.97** ± 0.18	**0.01** ± 0.00
	HUVECs	**0.21** ± 0.01	**0.19** ± 0.01	**0.68** ± 0.17	**0.41** ± 0.08
	NIH-3T3	**0.52** ± 0.02	**1.53** ± 0.05	**1.59** ± 0.11	**1.73** ± 0.20
	RAW 264.7	**1.66** ± 0.09	**0.98** ± 0.04	**1.66** ± 0.08	**1.34** ± 0.03
AlPCS4	SK-ChA-1	**0.29** ± 0.01	**0.16** ± 0.01	**0.50** ± 0.05	**0.16** ± 0.04
	HUVECs	**0.20** ± 0.01	**0.16** ± 0.01	**9.80** ± 0.70	**0.05** ± 0.03
	NIH-3T3	**0.11** ± 0.02	**0.13** ± 0.02	**N.D.**	**N.D.**
	RAW 264.7	**0.15** ± 0.01	**0.36** ± 0.02	**0.33** ± 0.04	**4.80** ± 0.20

From the dark toxicity (Figures 3.5, S3.10, S3.11) and LC_{50} values (Table 3.1), a selectivity index (SI) can be extrapolated. In the context of PDT, the SI can be defined as the ratio of the PS's dark toxicity concentration against its pharmacologically active concentration (77). The ideal PS should have a relatively high dark toxicity concentration and a very low photoactive concentration (78). For anti-cancer pharmaceuticals, an SI value of ≥ 10 is deemed worthy of further investigation (79). To approximate the SI, the most profound dark toxicity was determined per PS in each cell line irrespective of post-PDT incubation time (Figures S3.10 and S3.11) and the corresponding PS concentration was divided by the LC_{50} value at 24 h (Table 3.1) in an assay-matched manner (*e.g.*, WST-1 dark toxicity versus WST-1 LC_{50}). The dark toxicity LC_{50} values were calculated where necessary, assuming a linear concentration-toxicity relationship. For ZnPC-ITLs, the mean ± SD [range; percentage of data points with SI ≥ 10] SI was 1.8 ± 1.8 [0.2-3.1; 0%], indicating that this PS and delivery system combination may be too toxic in the absence of a light stimulus. For AlPC-ITLs the SI values were 11.2 ± 20.1 [0.2-55.9; 29%], whereas for AlPCS4 the SI values were 72.9 ± 72.6 [0.2-212.7; 71%], reflecting a higher safety profile compared to the zinc-containing PC counterpart. Only certain cells were too susceptible to aluminum-containing PCs. AlPC-ITLs and AlPCS4 were least tolerated by macrophages, which may in fact be advantageous for PDT. It is known that tumor-associated macrophages of the M2 phenotype inhibit T cell-mediated anti-tumor immune responses (80) and that the T cell response that is inherent to post-PDT immune signaling is quintessential for tumor clearance and long-term tumor control (4, 5, 81). By inflicting toxicity in M2 macrophages via inherent PS dark toxicity the post-PDT immune response may be exacerbated, on top of being triggered by the M2 to M1 phenotype switch by PDT itself (82). Contrastingly, the M1 phenotype is hostile towards tumor cells (80). PDT with aluminum-containing PCs may therefore relay a beneficial kill-and-switch effect in tumor-associated macrophages.

Several other conclusions can be derived from the data. Firstly, there was no correlation between the extent of photosensitization (based on PS fluorescence intensity measured by flow cytometry) and 24 h LC_{50} values when the data were ranked per individual PS for the 4 cell lines. For example, HUVECs had top rank in terms of ZnPC-ITL uptake (Figure 3.4 A) but bottom rank with respect to LC_{50} (WST-1; Table 3.1). In fact, only 2 of the 24 matrix entries had equal rank (ZnPC-ITLs, uptake versus WST-1 LC_{50} in NIH-3T3 cells; AlPCS4, uptake versus SRB LC_{50} in RAW 264.7 cells). Accordingly, PS uptake has no prognostic value for PDT efficacy. Secondly, cancer cells tested to date have proven to be highly amenable to PDT with the metallated PSs, with a mean ± SD LC_{50} value of 0.30 ± 0.41 when the LC_{50} values for A431 cells (21) and Sk-ChA-1 cells (this study) were grouped for the WST-1 and SRB assay performed at 24 h post-PDT. These LC_{50} values belong in the potent anti-cancer agent stratum (76). Parenchymal cells are the primary targets in the PDT platform, with the other pharmacologically relevant loci acting as 'adjuvant targets' (21). Finally, AlPCS4 inflicted the most profound damage across the board with very low LC_{50} values based on the WST-1 assay, which relies on mitochondrial redox potential (83). AlPC-ITLs were slightly more phototoxic to cells than ZnPC-ITLs, although both PS also performed well in terms of cell-killing potency. Hybrid modalities should therefore be considered comprising ITL-delivered lipophilic PS such as AlPC-ITLs to target membrane structures and hydrophilic AlPCS4 to target the aqueous compartments of the cell, with the aim to induce maximal photochemical damage to the widest possible range of biomolecules.

3.4.5. ITL-delivered metallated phthalocyanines are more potent inducers of cell cycle arrest, apoptosis, and necrosis

Cell cycle stages and mode of cell death were measured following the protocol used previously for A431 cells (21) as a metric of the PSs' phototoxicity, secondary to the WST-1 and SRB data. Furthermore, the mode of cell death, which is a culminant of cell cycle arrest, is a gauge for a cell's ability to recover and dictates post-PDT immunological clearance. Sublethally afflicted cells can cope with hyperoxidative stress by activating survival pathways (2, 13-16) that lead to anastasis (cell survival and recovery through reversal of apoptosis) (84) and other forms of post-traumatic recovery (85-87). These processes require energy in the form of ATP. Apoptosis, necroptosis, secondary necrosis, and paraptosis are also energy-demanding cell death cascades. Cells undergoing a predominantly apoptotic mode of cell death (AV+/PI-) are therefore fundamentally capable of reverting death signals and recover. Contrastingly, necrosis results from energy depletion and is not compatible with recovery. The mode of cell death in turn shapes the anti-tumor immune response (88), which is required for long-term tumor control (81, 89), and abscopal effects (90) that bear clinical relevance in cases of viable tumor residuals post-PDT and (micro)metastases that may have escaped detection by imaging.

PDT generally resulted in an increase in the fraction of cells arrested in the S-phase and G2/M-phase (Figure 3.6). The extent to which S-phase and G2/M-phase arrest occurred depended on the type of PS, with ITL-delivered lipophilic PSs inducing more profound cell cycle arrest than their hydrophilic counterparts at roughly 3 fold lower PS concentration. Moreover, the non-cancerous cells, and HUVECs in particular, displayed greater cell cycle arrest (Figure 3.6) than the SK-ChA-1 cells, while the LC_{50} values in the former cells were typically higher than in SK-ChA-1 cells (Table 3.1) as well as A431 cells (21). Similar trends in LC_{50} values were found for apoptosis/necrosis (Figure 3.7). These data represent another example of the disconnect between inter-assay results. Plausible explanations are that post-PDT recovery processes in the non-cancerous cells are more resolute than in the cancer cells, that cancer cells become more frail than non-cancerous cells when serum-deprived, and/or that paracrine death signaling loops are more detrimental in cancer cells (*e.g.*, through PDT-induced tumor necrosis factor (TNF) release and locoregional signal transduction (24, 91)). It is known that serum deprivation, as implemented here and in our previous studies (14, 15, 21), arrests certain cells in the G0/G1-phase, including fibroblasts (92, 93) and cancer cells (94, 95). A double-digit percentual increase in G0/G1-phase arrest following 24 h serum starvation has been reported in cancer cells (95), leading some to propose this form of metabolic deprivation as a potential therapeutic avenue (96). This avenue is particularly pertinent to PDT when the treatment leads to vascular shutdown, as multiple metabolic hubs in cancer cells become congested in consequence to the direct photodynamic effects on cells (2) and hence could account for synergism in treatment efficacy. The serum deprivation-enhanced sensitivity of G0/G1-phase arrested cancer cells was reported to emanate from signaling by TNF-related apoptosis-inducing ligand (TRAIL) (96), a protein that binds to the death receptors (DR)4 and DR5 and induces apoptosis. Moreover, PDT can invoke susceptibility of TRAIL-resistant cancer cells to TRAIL (97) while at the same time increasing TRAIL release by PDT-treated cells (98), creating another paracrine death signaling loop. It should be noted, though, that HUVECs and RAW 264.7 cells were not considerably affected by serum deprivation and G0/G1-phase arrest per se inasmuch as such an arrest would preclude the cells from being arrested in the S-phase (both HUVECs and RAW 264.7 cells) and the G2/M-phase (mainly HUVECs) after PDT (Figure 3.6).

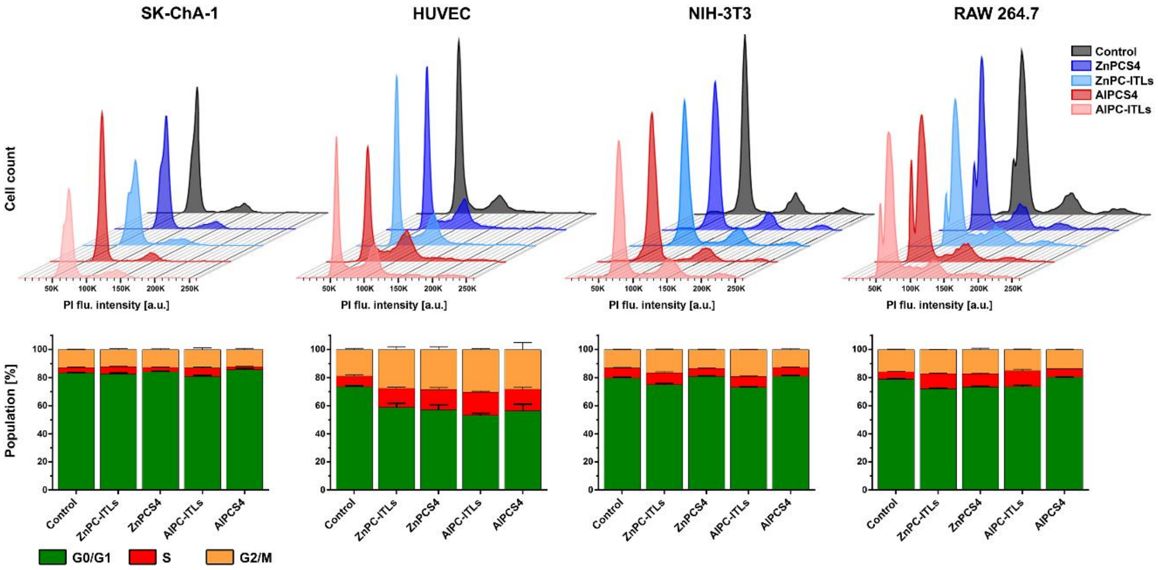

Figure 3.6 - Cell cycle profile in PDT-treated tumor-comprising cells. Cells were photosensitized with ZnPC-ITLs and AlPC-ITLs (31.25 µM phospholipid concentration, 0.09 µM PS concentration) and ZnPCS4 and AlPCS4 (0.31 µM) during 60 min incubation under standard culture conditions. Cells were illuminated (15 J/cm^2), harvested 24 h after PDT, fixed, and stained with PI before flow cytometry. Data are presented as mean ± SD for N = 3 independent experiments per group.

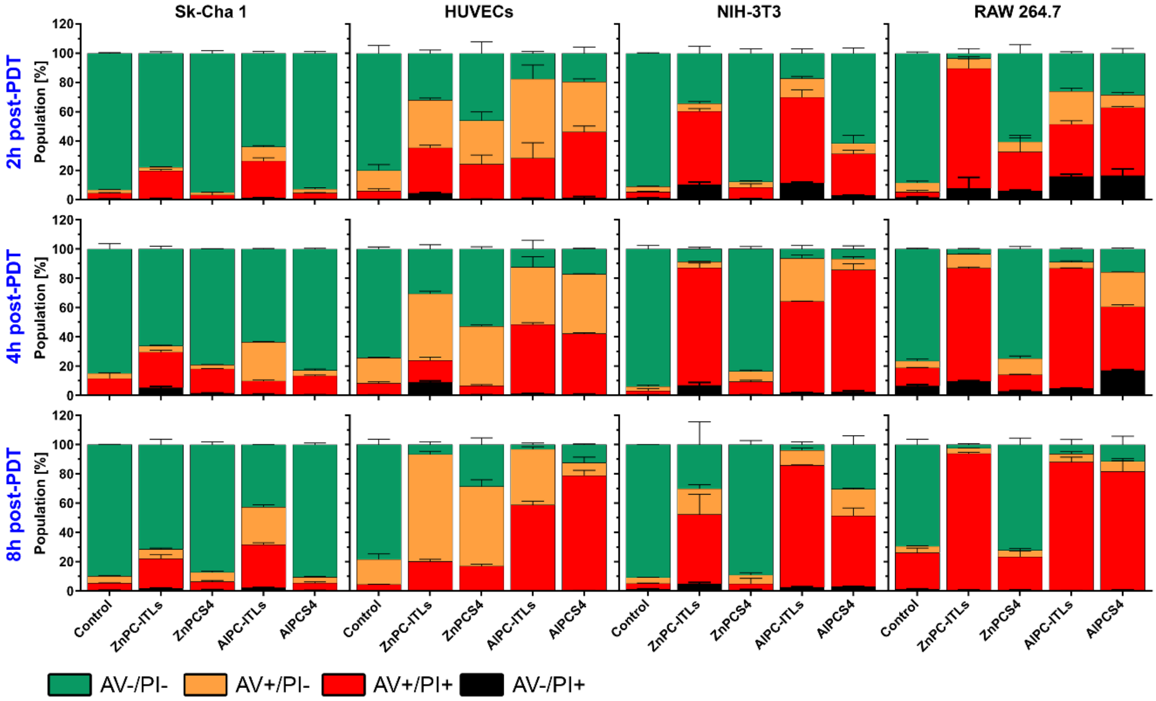

Figure 3.7 - Mode of cell death in PDT-treated tumor-comprising cells. Cells were photosensitized with ZnPC-ITLs and AlPC-ITLs (250 µM phospholipid concentration, 0.75 µM PS concentration) and ZnPCS4 and AlPCS4 (2.5 µM) during 60 min incubation under standard culture conditions. Cells were stained with PI and Alexa Fluor 488-conjugated annexin V (AV) at 2, 4, and 8 hours of post-PDT (15 J/cm^2) and assayed by flow cytometry. Data are presented as mean ± SD for N = 3 independent experiments per group. Corresponding quantitative data are provided in Table S3.7. Classification: AV-/PI-, viable cells; AV+/PI-, early apoptotic cells; AV+/PI+ and AV-/PI+, cells in late apoptosis or necrosis.

The cell cycle arrest patterns (Figure 3.6) were broadly reflected in the cell death patterns in isolated cell lines (Figure 3.7). Most notably, the non-cancerous cells exhibited more apoptosis and necrosis after PDT than SK-ChA-1 cells. The fraction of cells undergoing any mode of cell death increased with time after PDT. The ITL-delivered PSs were more phototoxic than their hydrophilic counterparts, with AlPC being a more potent inducer of cell death than ZnPC except in RAW 264.7 macrophages, echoing previous results in A431 cells (21). ZnPCS4 imparted no cytotoxicity in cells except in HUVECs, where cell death was disproportionally sizeable and dominated by apoptosis. Previous studies in cancer cells such as A431 cells (99, 100) have demonstrated phototoxic responses to ZnPCS4, which were ascribed to possibly the formation of oxygen-free radicals (101), but which could not be reproduced in our previous work at the level of radical production (20) and cellular phototoxicity (21). Although it is peculiar why oxygen-free radicals would be toxic to select cells (radicals react with electron acceptor sites on any biomolecule), the cytotoxicity of ZnPCS4 in HUVECs was significant enough to warrant *in vivo* investigation as a selective tumor endothelium PS. Necrotic cell death constituted the main mode of cell death in all cell types but HUVECs, the only primary cells in this study. At the earlier time points (2 h and 4 h post-PDT) a remarkable fraction of cells was AV-/PI+, suggesting that PDT induced temporary membrane permeability allowing PI to enter the cell and stain DNA. The membrane permeability abated in time (8 h post-PDT). The early-onset permeability of the outer membrane, albeit transient, may have contributed to cell death, predominantly necrosis, as a result of perturbation of cellular homeostasis (102). These phenomena are reminiscent of ferroptosis, characterized by the accumulation of oxidized polyunsaturated fatty acids and inherently linked to PDT (103).

In the attritional study conducted in A431 cells (21) it was determined that AlPC-ITLs comprised the most suitable PS delivery system for PDT, with AlPCS4 as a possible co-PS for the pleiotropic photosensitization of the intracellular environment. Given the dark toxicity data, intracellular PS distribution pattern, and photo-induced toxicity it can be surmised that the previous conclusion was reasserted in this study, noting that ZnPC-ITLs are not considerably inferior to AlPC-ITLs.

3.4.6. Liposomal photosensitizers and AlPCS4 exhibit minimal dark toxicity in zebrafish and chicken embryos

To get more insight in the *in vivo* application of the PSs, dark toxicity was measured in zebrafish and chicken embryos. Zebrafish share many toxicological pathways with mammals and therefore constitute a reliable means to assess the hazards that a drug could pose to humans (104). Chicken embryos are equally suitable test systems (105), especially because they are more sensitive indicators of drug toxicity owing to low-threshold lethality.

Zebrafish embryos were exposed to up to 1.5 μM of liposomal ZnPC and AlPC and up to 150 μM ZnPCS4 and AlPCS4. No morphological or teratogenic abnormalities were observed in any of the fish (Figure 3.8 A and S3.3), and no aberrant zebrafish hatching (determined 72 h post-hatching) or lethality were observed between day 1 and day 5 regardless of PS concentration (Figure 3.8 B). Lethality was mainly noted in the first 24 h, which was equally divided over all groups, with the sole exception of the 0.75 μM ZnPC group, and not dose-dependent (Figure 3.8 B).

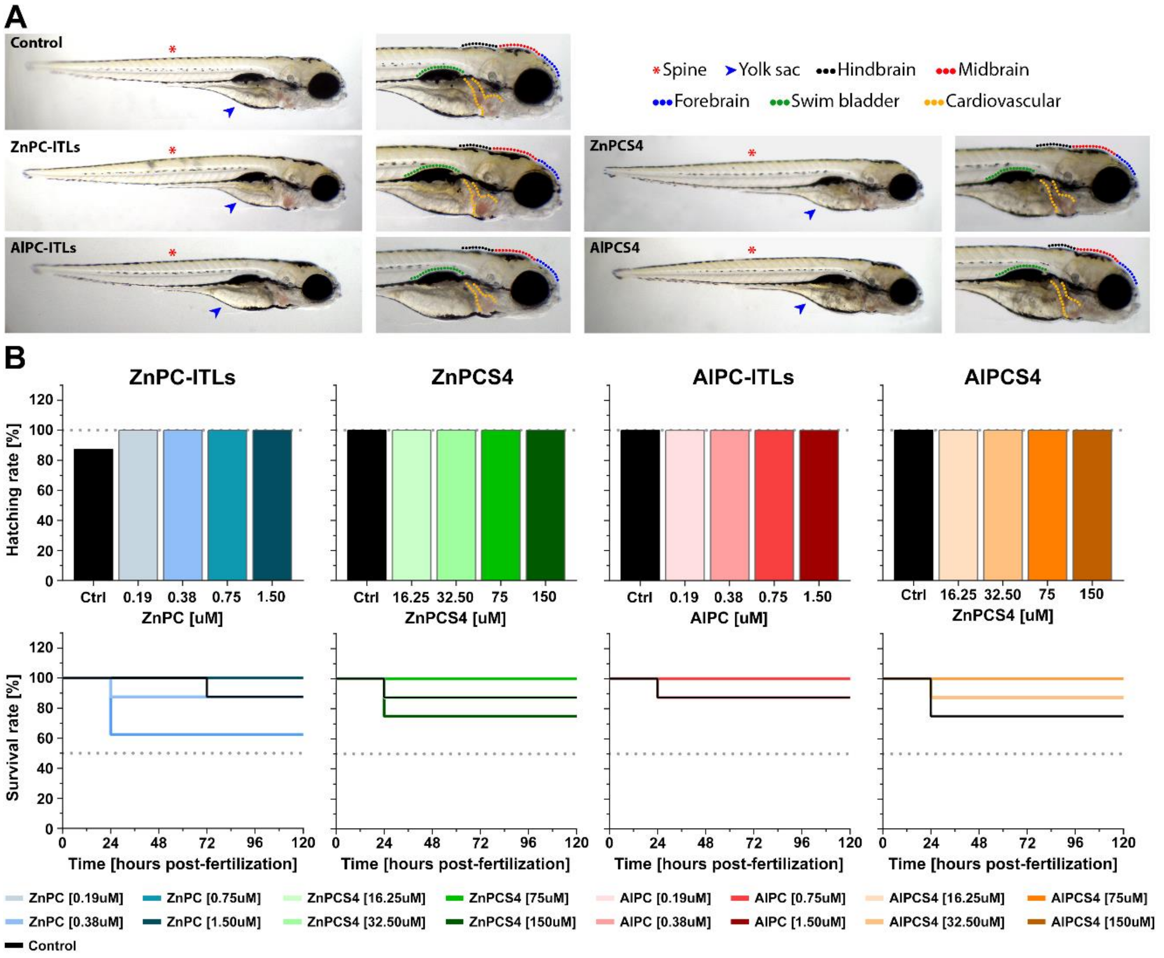

Figure 3.8 - Systemic toxicity in zebrafish. (**A**) Representative whole-body images and magnified snapshots of hatched zebrafish indicate no anatomical anomalies at key locations where drug toxicity is expected manifest (legend top right). Images were taken at 120 h post-fertilization after embryos had been exposed to 1.5 µM ZnPC and AlPC and 150 µM ZnPCS4 and AlPCS4. (**B**) Hatching rate (top panel) as a function of PS concentration (N = 8 per concentration) and survival rate (bottom panel) plotted as a function of time (N = 8) for the highest PS concentration measured in each group.

Chicken embryos received a single bolus of PS in iso-osmolar buffer solution via the chorioallantoic membrane vasculature on EDD10 to actualize systemic exposure to 0.8 µM ZnPC and AlPC (injected dose of 1.2 nmol) and 85 µM ZnPC and AlPC (injected dose of 128 nmol). The embryos were screened for viability on a daily basis up to EDD18. As presented in Figure 3.9, the only PS that induced notable toxicity was ZnPCS4, while the other PSs were more or less comparable to the respective control groups.

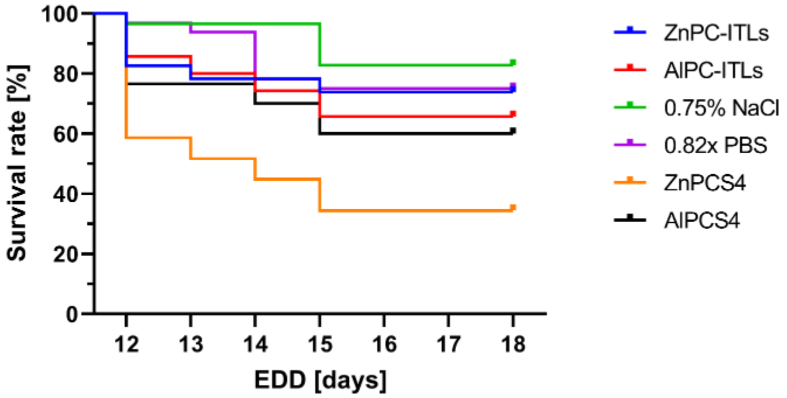

Figure 3.9 - Systemic toxicity in chicken embryos. Kaplan-Meier plot of chicken embryos who had received a single bolus of 1.2 nmol ZnPC and AlPC in ITLs and 128 nmol of ZnPCS4 and AlPCS4, accounting for a systemic PS concentration of 0.8 µM and 85 µM, respectively, in a 50-µL injection volume. Control group injections consisted of 0.75% NaCl solution and 0.82× PBS. Data encompasses duplicate experiments with N ≥ 10/group.

The toxicity determined in both animal models was less grave than initially reflected by the dark toxicity results in cultured non-cancerous cells (Figure 3.5). Non-cancerous cells were exposed to an equimolar concentration of liposomal ZnPC and AlPC (in zebrafish) and a 15 fold and 8.5 fold lower tetrasulfonated PS derivative concentration (in zebrafish and chickens, respectively). Each PS exhibited some level of toxicity with up to ~50% cell death (NIH-3T3, ZnPC-ITLs, WST-1 assay); a degree that was not observed in animals. The data suggest that dark toxicity assessment in cultured cell monolayers may lead to an overestimation of toxicity, and that therefore *in vitro* toxicological studies constitute a more sensitive gauge. On the other hand, transcriptomics analyses in SK-ChA-1 cells revealed no dysregulation of any of the microarrayed genes by ZnPC-ITLs in the absence of light (13), albeit the exposure time was significantly shorter (2 h) than used here (72 h). Nevertheless, transcriptomic processes are typically very sensitive to external stimuli with detectable early-onset modulation, as was evident from the vast array of changes induced by sublethal PDT at the 90 min post-PDT mark (13) and with cationic liposomes in the absence of light (manuscript in preparation). Furthermore, chicken embryos could withstand ZnPC-ITL concentrations, although these were three-fold lower than what had been previously tested (up to 0.7 mM systemic lipid concentration, 2.1 µM ZnPC concentration) (13). In mice, a single intravenous bolus of ZnPC-ITLs (2.5 mM final lipid concentration and 7.5 µM ZnPC concentration in blood) resulted in no body weight alterations during the 4 weeks monitoring period, no deleterious changes in clinical biochemistry and hematological parameters, and no histological anomalies at animal sacrifice (4 weeks after intravenous administration). Accordingly, the photosensitization protocol to be used for *in vivo* PDT efficacy studies is not expected to produce a level of systemic toxicity in mouse models that would constitute a stop signal for further investigations.

3.4.7. In vivo skin phototoxicity manifested in nude mice exposed to ZnPC and ZnPCS4 but not AlPC and AlPCS4

In addition to systemic toxicity, skin phototoxicity is a potentially serious side-effect of clinical PDT that is experienced by some patients even long after PS administration (Figure 3.10). In fact, based on the cases presented in Figure 3.10, the short median survival time of hilar cholangiocarcinoma patients, and the recommended post-PDT dark periods for clinical PSs, the gastroenterologist decided to discontinue PDT for said patients at our institute (20). Preventing ambient/sun light-induced burns and photoallergic reactions should therefore be routinely investigated in preclinical research to minimize sequelae in subsequent clinical trials and ultimately increase adoption of the modality by physicians, especially since PDT can increase median life expectancy of cholangiocarcinoma patients compared to palliative chemotherapy (38, 39).

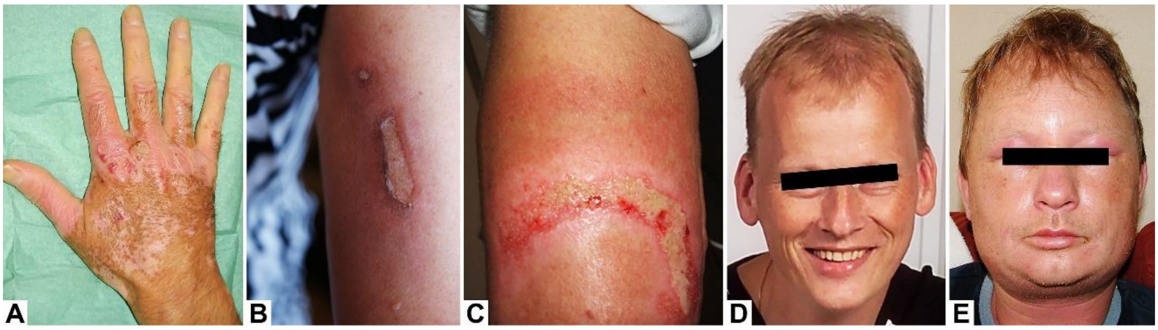

Figure 3.10 - Clinical phototoxicity cases in non-resectable hilar cholangiocarcinoma patients who had undergone PDT with intravenously administered Photofrin (porfimer sodium) or Foscan (mTHPC) as a last-line treatment (palliative). Phototoxicity was most prominent in regions most susceptible to light exposure (*e.g.*, extremities, head, and neck) as well as at the infusion site (typically the vena cubiti). (**A**) Photo of a hand made after healing of severe burns with blisters, 3 months after injection of Photofrin in the vena cubiti. (**B**) and (**C**) Skin lesions both 2 months after intravenous injection of mTHPC, which ultimately healed by scarring (not shown). (**D**) and (**E**) Patient before (**D**) and 3 months after Photofrin-PDT (**E**) following a visit to an amusement park. The patient was wearing light-protective clothing, including a hat, but still experienced a severe photoallergic reaction in the face as evidenced by the degree of swelling. All patients were included in a clinical trial that had been approved by the institutional review board of the Academic Medical Center (AMC), University of Amsterdam, and registered under trial number NCT01016002. The trial was discontinued after inclusion of 5 patients due to the severity of adverse events. Explicit written informed consent for the publication of the images in (**D**) and (**E**) was provided posthumously to MH by the patient's spouse. Images and clinical metadata were provided to MH by Dr. Erik Rauws (AMC, retired).

To this end, we have designed a simple yet useful skin phototoxicity setup (Figure 3.1) and assessment approach, where we can determine light-induced macroscopic damage in mouse ears and microscopic damage at the histological level in dorsal skin following 24-h exposure to light of a relevant wavelength range (Figure S3.4) and intensity. Mouse ears are well-vascularized and translucent, and therefore an ideal tool for visual inspection of overt phototoxicity. Also, the anatomy allows for pertinent physiological and pharmacodynamic processes such as PS extravasation and perivascular accumulation. As can be seen in Figure

3.11 A, ITL-delivered ZnPC inflicted numerous burn-like and erythemic wounds, often at multiple sites per ear, in 5 of the 8 ears (63%). Such damage patterns were absent in the ears of animals that had received AlPC-ITLs. ZnPCS4 induced similar type of damage in 3 of the 8 ears (38%), with one ear bearing a sizeable eschar. This was somewhat surprising given the photo-inactive character of ZnPCS4 reported above and in published work (20, 21). AlPCS4 was not associated with any apparent skin phototoxicity.

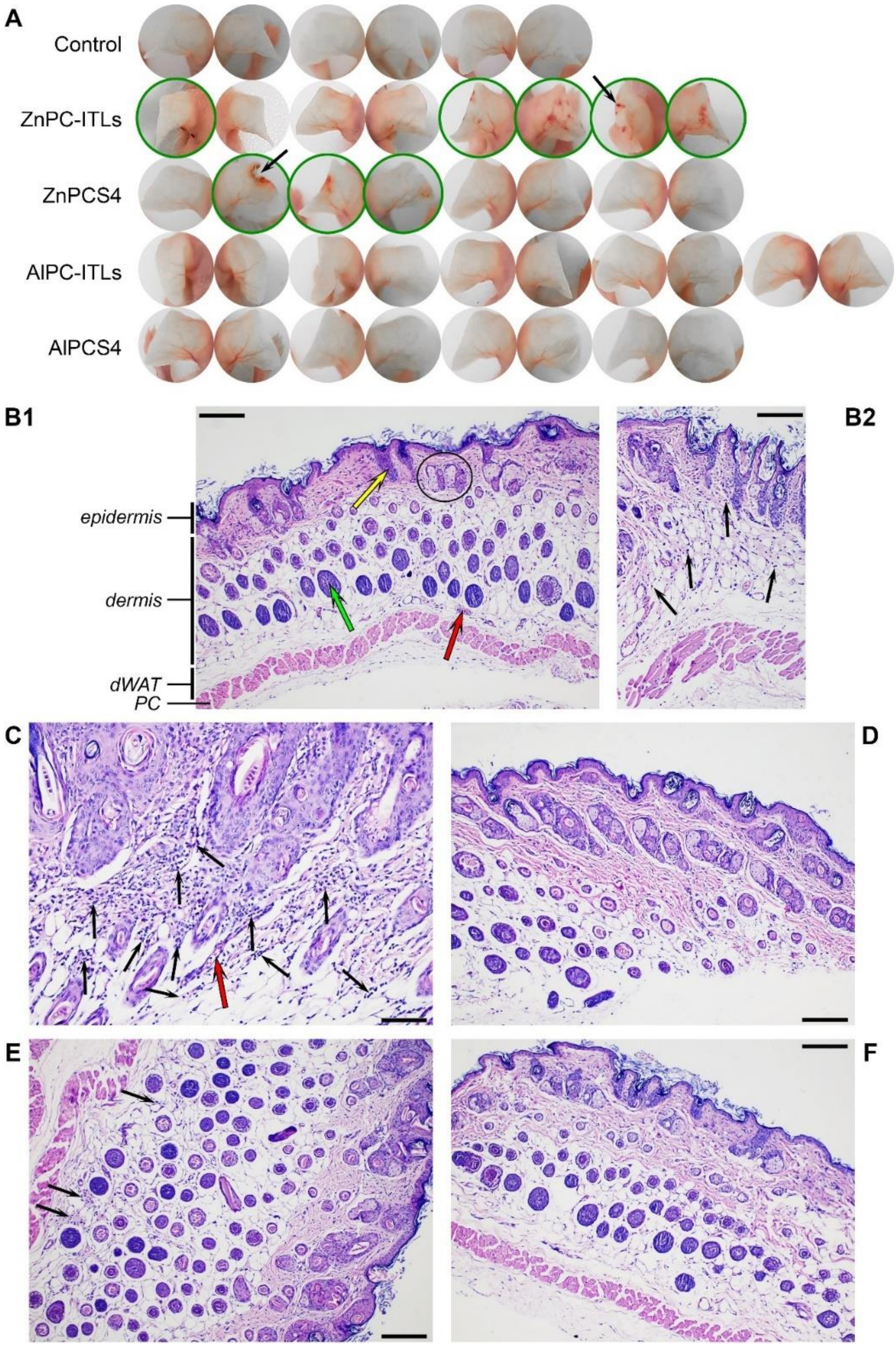

Figure 3.11 - PS phototoxicity in the skin of nude mice. (**A**) Light-induced tissue injury in mouse ears 24 h after intravenous PS injection and continuous LED light exposure. The left and right ear of all animals included in the experiment were photographed and assessed for tissue injury resulting from PS activation by LED light (Figure S3.4). Macroscopic tissue injury entailed visible burns characterized by eschars (ZnPCS4, arrow) and focal

burn-like patches (ZnPC-ITLs, arrow). The panels depicting ears marked by photo-induced damage are outlined in green. Representative histology micrographs of dorsal skin of nude mice in the control group (not photosensitized; **B1**, **B2**) and animals that had received an intravenous bolus of ZnPC-ITLs (**C**), ZnPCS4 (**D**), AlPC-ITLs (**E**), and AlPCS4 (**F**). Legend for B1: green arrow, basis of a hair follicle; yellow arrow, hair follicle at the dermo-epidermal junction; red arrow, blood vessel; encircled, sebaceous glands surrounding two hair follicles. Abbreviations: dWAT, dermal white adipose tissue; PC, panniculus carnosus (muscle layer) (106). The black arrows point to sites of inflammatory cell infiltrates as identified by the pathologist (TGK). Scale bar: 200 μm (**B1**, **D**, **E**, **F**), 180 μm (B2), 100 μm (**C**). Histopathological scoring was performed as follows: 0, absence of inflammatory cell influx (*e.g.*, **D**, **F**); 1, mild inflammatory cell influx (*e.g.*, **B2**, **E**); 2, moderate inflammatory cell influx (*e.g.*, **C**).

The most clear-cut histological sign of photochemical damage to the skin is the corollary immunological response; *e.g.*, infiltration of the affected skin regions by inflammatory cells (107). Accordingly, the degree of inflammatory cell influx was scored by a histopathologist as described in the legend of Figure 3.11. The scores are largely consistent with the macroscopic assessment, although the damage to ears induced by ZnPCS4 was not necessarily reflected in the histological appraisal. Control animals had a mean ± SD score of 0.44 ± 0.53, while mice subjected to AlPC-ITLs and AlPCS4 were scored as 0.33 ± 0.52 and 0.0 ± 0.0, respectively. Skin sections of mice that were photosensitized with ITL-delivered ZnPC and ZnPCS4 were scored as 1.50 ± 0.53 and 0.25 ± 0.50, respectively. The predominant site of inflammatory cell influx was the dermis (Figure 3.11 B-F), which is highly vascularized and allows immune cells to extravasate into photochemically afflicted zones along a chemotactic gradient (20, 108).

It is not clear why ZnPC-ITLs caused significantly more skin phototoxicity than AlPC-ITLs. One possible explanation may be related to the relationship between particle diameter and the size of interendothelial junctions in the auricular microcirculation. The liposomal PS delivery systems were originally designed to prevent PS diffusion into skin as a result of the physical mismatch between the PEGylated liposomes and the endothelial fenestrations (20). Although the ZnPC-ITLs and AlPC-ITLs had a mean diameter of 120 ± 8 nm and 175 ± 10 nm, respectively, that is larger than the 60-nm gaps between endothelial cells (109, 110), particle sizes abide by a Gaussian distribution (21, 23). The smaller nanoparticle diameter shoulder may have overlapped with the larger size shoulder of the fenestration size histogram. Compared to the AlPC-ITLs, the smaller ZnPC-ITLs likely had a larger fraction of ITLs that could have passed through the fenestrations and accumulated in the perivascular space of mouse ears, causing more extensive damage during the 24 h light exposure. Liposomal efflux from the microcirculation was observed with intravital fluorescence microscopy with NBD-labeled liposomes of similar composition and properties in hamster dorsal skin (111, 112). The same applied to the monovalent and tetravalent anionic fluorophores 5(6)-carboxyfluorescein and calcein, respectively, in intravital feasibility studies (111, 112). However, damage-based signs of intra-auricular accumulation of the tetrasulfonated PS derivatives, which are small, charged molecules like 5(6)-

carboxyfluorescein and calcein, were not observed. This dichotomy gives rise to another possible explanation, which is that ZnPC may have been extracted out of the phospholipid bilayer by a biomolecule such as low-density lipoprotein that facilitated the PS diffusion in a by proxy manner (20, 21), as has been reported for non-PEGylated lecithin liposomes (113-115). Whether PS extraction occurs with PEGylated liposomes and whether the phenomenon is more pronounced for ZnPC versus AlPC, which would add credence to the latter explanation, is currently being investigated.

3.4.8. ZnPC-ITLs and AlPC-ITLs extend the time to sacrifice in a mouse model of human triple negative breast cancer

In the final set of pilot experiments, human triple-negative breast cancer (MDA-MB-231) cells were xenografted into BALB/c nude mice and left untreated (control) or subjected to PDT after photosensitization with ZnPC-ITLs and AlPC-ITLs (single bolus of 6 nmol PS, approximately 0.17 mg/kg body weight, 24 h dark-light interval). This tumor model was chosen because MDA-MB-231 xenografts are properly vascularized (116), which is necessary for optimal PS delivery (14, 20), and because of precedent PDT studies (117-119), making benchmarking possible.

Mice did not respond adversely to the injection of PS or PDT as evidenced by comparable body weights relative to control animals (Figure 3.12 A). PDT resulted in smaller tumor volumes at every measurement point, with no pharmacodynamic potency difference between ZnPC and AlPC (Figure 3.12 B). PDT resulted in the typical skin necrosis (dark patches) at the site of laser incidence (Figure 3.12 D) and caused a 4 d (33%) delay in the tumors reaching the human endpoint for both ZnPC-ITLs and AlPC-ITLs (Figure 3.12 C). To get a general perspective of the PDT efficacy versus other PSs, the results were juxtaposed to results from other studies using the same xenograft model. Theodossiou et al. (119) used hypericin (12.5 mg/kg intraperitoneally, 2 h dark-light interval) to photosensitize tumors. PDT (cumulative radiant exposure of 40 J/cm^2, Lumisource lamp with 530 nm long pass filter) resulted in a 14 d (47%) delay in the tumor volume reaching the predefined endpoint (≥ 1,000 mm^3). In the study by Wang et al. (118) BALB/c nude mice were photosensitized with 5aminolevulinic acid (250 mg/kg intraperitoneally, 4h dark-light interval) and subjected to PDT (cumulative radiant exposure of 120 J/cm^2, 400-700 nm filtered LED light). Extrapolation of the tumor volume-time curves yielded a 29% increase in the number of days (49 d in PDT group versus 38 d in control group) to reach an equivalent tumor volume, measured by fluorescence whole body imaging. Finally, Zhu et al. (117) photosensitized athymic nude mice with methyl pyropheophenylchlorin (15 mg/kg, 18 h dark-light interval) and performed PDT at a cumulative radiant exposure of 120 J/cm^2 using a 630 nm laser. Tumor volumes were plotted as a function of time after PDT, revealing a 46% reduction in tumor volume 23 d after PDT (data extrapolated from the graph). Our PDT efficacy results are therefore non-inferior to those obtained using other PSs from a tumor volume perspective and superior in light of the fact that the PS dose administered was at least 2 orders of magnitude lower than the dose used in the other studies.

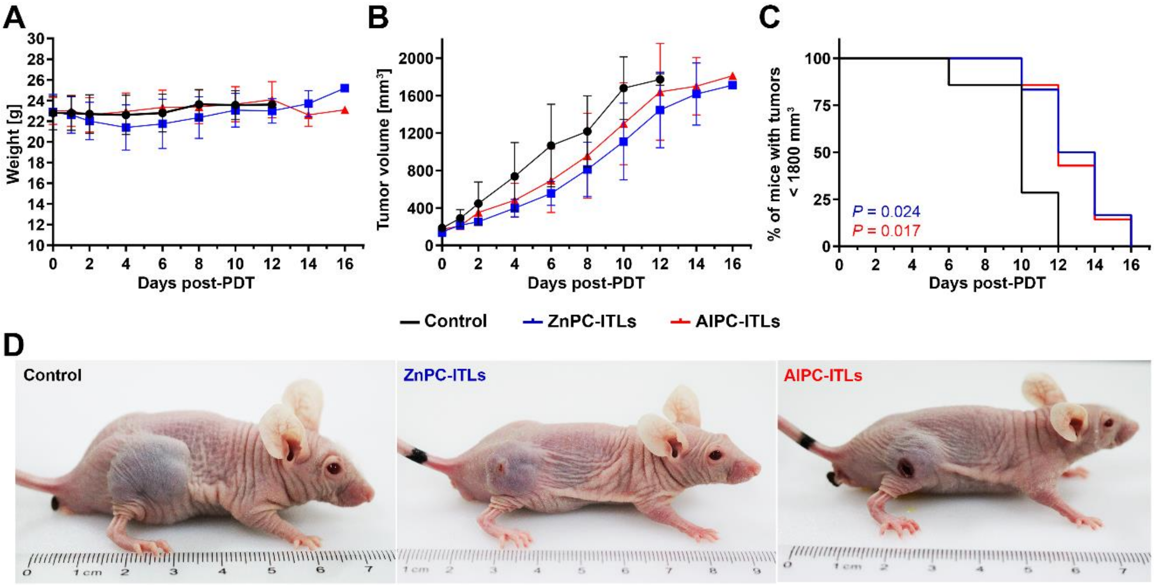

Figure 3.12 - PDT efficacy with ZnPC-ITLs and AlPC-ITLs in BALB/c nude mice bearing MDA-MB-231 xenografts. After reaching a tumor volume of 100 - 200 mm^3 the animals were photosensitized with a single bolus of 6 nmol PS /animal and subjected to PDT (cumulative radiant exposure of 200 J/cm^2) following a 24-h dark-light interval. Animal weights (**A**) were recorded and the tumor volume was measured and plotted as a function of time post-PDT (**B**). A Kaplan-Meier plot was constructed for the percentage of animals reaching a human endpoint (tumor volume of ≥ 1,800 mm^3) versus time post-PDT (**C**). Data are plotted as mean ± SD. Starting group size was N = 6 for ZnPC-ITLs and N = 7 for the control and AlPC-ITL group. Color-coded *P*-values are provided and are relative to the control group. Representative tumors are shown for mice on day 12 post-PDT (**D**).

The efficacy of the current modality could be optimized in several ways. Firstly, the PS:phospholipid molar ratio could be increased to augment the number of PS molecules delivered to a cell on a per liposome basis. A molar ratio of 0.003 has been used in all ITL studies conducted to date because this ratio was deemed optimal from a ROS production standpoint (23). At higher ratios the ZnPC dimerizes or multimerizes (120), which results in photochemical deactivation and hampered biomolecule oxidation capacity (23). However, ITLs should not be viewed as concrete ROS-generating entities in a tumor biological context. Liposomal constituents coalesce with cellular structures following ITL uptake (Figure 3.2) and ZnPC and AlPC disperse homogeneously across the cellular environment (Figure 3.4). As a result, liposomal PS dimerization/multimerization is of no concern due to dilution in the intracellular lipophilic compartment. ITLs with a PS:phospholipid molar ratio of 0.01 have been prepared before (23) and the ratio could be increased even further (unpublished results). Secondly, hybrid PS delivery systems could be prepared encompassing *e.g.*, AlPC in the lipid bilayer of liposomes and AlPCS4 in the lipid film hydration buffer, which would result in non-encapsulated as well as encapsulated AlPCS4 in the injectable bolus. If a high systemic presence of free AlPCS4 leads to any form of toxicity, the liposomes could be passed over a size exclusion chromatography column (121) to remove unencapsulated AlPCS4. The AlPCS4 would only be released from the liposome's aqueous compartment following ITL uptake or following an external stimulus, such as heat (111, 121). Thirdly, PSs other than AlPC or AlPCS4 can be loaded into the other platform components if warranted by preclinical research. A cocktail of PS-encapsulating ITLs, ETLs, and TTLs or permutations thereof could be administered as proposed earlier (20, 21).

3.5. Conclusions

This study focused on the ITL component of the multi-component PS delivery platform designed to photosensitize the most relevant pharmacological target sites in a tumor: the tumor cells, the tumor vascular endothelium, and the tumor microenvironment including its cellular components. The ITLs encapsulating ZnPC and AlPC were further compared to their water-soluble tetrasulfonated counterparts in an array of rudimentary *in vitro* and *in vivo* experiments. The key findings were that [1] all PSs except for ZnPCS4 are able to effectively photosensitize cancer cells and non-cancerous cells, granted that the PSs actually reach the tumor environment after intravenous administration; [2] the pharmacodynamic potency of the photodynamically active PSs is considered highly toxic to potent as per anti-cancer compound classification; [3] the photodynamically active PSs do not elicit notable systemic toxicity in zebrafish and chicken embryos; [4] ITL-delivered ZnPC and ZnPCS4 are associated with skin phototoxicity, while the aluminum-containing PSs do not exert detectable skin phototoxicity; and [5] ITL-delivered ZnPC and AlPC are equally effective in their tumor-killing capacity in human tumor breast cancer xenografts and superior to other non-phthalocyanine PSs when appraised on a per mole administered basis. The cutaneous phototoxicity of ZnPC(S4) in mice is worrisome. It is therefore concluded that AlPC(S4) are the least toxic and most effective and promising PSs to advance towards clinical translation using our comprehensive tumor targeting and PS delivery platform.

3.6. Acknowledgements

This work was supported by grants from the Dutch Cancer Foundation (KWF project # 10666), a Zhejiang Provincial Foreign Expert Program Grant, Zhejiang Provincial Key Natural Science Foundation of China (#Z20H160031), and a grant for the establishment of the Jiaxing Key Laboratory for Photonanomedicine and Experimental Therapeutics to MH. BD is sponsored by grants from the National Natural Science Foundation (81872220), a Basic Public Welfare Research Project of Zhejiang Province (LGF18H160034), and the Tumor Nanotargeting and TCM Technology Innovation Team (Key Science and Technology Innovation Team of Jiaxing, 2018). WP is sponsored by a grant from the National Natural Science Foundation of China (31871402). MH is chief formulation officer at Nurish.Me and Camelina Sun and has equity in those companies (whose business activities are unrelated to the present work).

The authors are grateful to Dr. Ruud Weijer for the BSA oxidation experiments and Dr. Marije Hoogland (pathologist at Isala, Zwolle, the Netherlands) for input on mouse histopathology.

3.7. References

1. dos Santos AFdA, D. R.; Terra, L. F.; Baptista, M. S.; Labriola, L. Photodynamic therapy in cancer treatment - an update review. *J Cancer Metastasis Treat.* 2019;5(25).
2. Weijer R, Clavier S, Zaal EA, Pijls MM, van Kooten RT, Vermaas K, Leen R, Jongejan A, Moerland PD, van Kampen AH, et al. Multi-OMIC profiling of survival and metabolic signaling networks in cells subjected to photodynamic therapy. *Cell Mol Life Sci.* 2017;74(6):1133-51.
3. Sorrin AJ, Kemal Ruhi M, Ferlic NA, Karimnia V, Polacheck WJ, Celli JP, Huang HC, and Rizvi I. Photodynamic Therapy and the Biophysics of the Tumor Microenvironment. *Photochem Photobiol.* 2020;96(2):232-59.
4. Korbelik M. Induction of tumor immunity by photodynamic therapy. *J Clin Laser Med Surg.* 1996;14(5):329-34.
5. Korbelik M, Sun J, and Cecic I. Photodynamic therapy-induced cell surface expression and release of heat shock proteins: relevance for tumor response. *Cancer Res.* 2005;65(3):1018-26.
6. Jayadevappa R, Chhatre S, Soukiasian HJ, and Murgu S. Outcomes of patients with advanced non-small cell lung cancer and airway obstruction treated with photodynamic therapy and non-photodynamic therapy ablation modalities. *J Thorac Dis.* 2019;11(10):4389-99.
7. Bath-Hextall FJ, Matin RN, Wilkinson D, and Leonardi-Bee J. Interventions for cutaneous Bowen's disease. *Cochrane Database Syst Rev.* 20136):CD007281.
8. Gonzalez-Carmona MA, Bolch M, Jansen C, Vogt A, Sampels M, Mohr RU, van Beekum K, Mahn R, Praktiknjo M, Nattermann J, et al. Combined photodynamic therapy with systemic chemotherapy for unresectable cholangiocarcinoma. *Aliment Pharmacol Ther.* 2019;49(4):437-47.

9. McCaughan JS, Jr., Ellison EC, Guy JT, Hicks WJ, Jones JJ, Laufman LR, May E, Nims TA, Spiridonidis CH, and Williams TE. Photodynamic therapy for esophageal malignancy: a prospective twelve-year study. *Ann Thorac Surg*. 1996;62(4):1005-9; discussion 9-10.
10. Lindenmann J, Matzi V, Neuboeck N, Anegg U, Baumgartner E, Maier A, Smolle J, and Smolle-Juettner FM. Individualized, multimodal palliative treatment of inoperable esophageal cancer: clinical impact of photodynamic therapy resulting in prolonged survival. *Lasers Surg Med*. 2012;44(3):189-98.
11. Kostron H. Photodynamic diagnosis and therapy and the brain. *Methods Mol Biol*. 2010;635(261-80.
12. Baskaran R, Lee J, and Yang SG. Clinical development of photodynamic agents and therapeutic applications. *Biomater Res*. 2018;22(25.
13. Weijer R, Broekgaarden M, van Golen RF, Bulle E, Nieuwenhuis E, Jongejan A, Moerland PD, van Kampen AH, van Gulik TM, and Heger M. Low-power photodynamic therapy induces survival signaling in perihilar cholangiocarcinoma cells. *BMC Cancer*. 2015;15(1014.
14. Weijer R, Broekgaarden M, Krekorian M, Alles LK, van Wijk AC, Mackaaij C, Verheij J, van der Wal AC, van Gulik TM, Storm G, et al. Inhibition of hypoxia inducible factor 1 and topoisomerase with acriflavine sensitizes perihilar cholangiocarcinomas to photodynamic therapy. *Oncotarget*. 2016;7(3):3341-56.
15. Broekgaarden M, Weijer R, Krekorian M, van den Ijssel B, Kos M, Alles LK, van Wijk AC, Bikadi Z, Hazai E, van Gulik TM, et al. Inhibition of hypoxia-inducible factor 1 with acriflavine sensitizes hypoxic tumor cells to photodynamic therapy with zinc phthalocyanine-encapsulating cationic liposomes. *Nano Res*. 2016;9(6):1639-62.
16. Broekgaarden M, Weijer R, van Gulik TM, Hamblin MR, and Heger M. Tumor cell survival pathways activated by photodynamic therapy: a molecular basis for pharmacological inhibition strategies. *Cancer Metastasis Rev*. 2015;34(4):643-90.
17. Shim CS, Cheon YK, Cha SW, Bhandari S, Moon JH, Cho YD, Kim YS, Lee LS, Lee MS, and Kim BS. Prospective study of the effectiveness of percutaneous transhepatic photodynamic therapy for advanced bile duct cancer and the role of intraductal ultrasonography in response assessment. *Endoscopy*. 2005;37(5):425-33.
18. Lindberg-Larsen R, Solvsten H, and Kragballe K. Evaluation of recurrence after photodynamic therapy with topical methylaminolaevulinate for 157 basal cell carcinomas in 90 patients. *Acta Derm Venereol*. 2012;92(2):144-7.
19. Jacques SL. How tissue optics affect dosimetry of photodynamic therapy. *J Biomed Opt*. 2010;15(5):051608.
20. Weijer R, Broekgaarden M, Kos M, van Vught R, Rauws EA, Breukink EJ, van Gulik TM, Storm G, and Heger M. Enhancing photodynamic therapy of refractory solid cancers: Combining second-generation photosensitizers with multi-targeted liposomal delivery. *J Photochem Photobiol C*. 2015;23(103-31.
21. Dias LM, Sharifi F, de Keijzer MJ, Mesquita B, Desclos E, Kochan JA, de Klerk DJ, Ernst D, de Haan LR, Franchi LP, et al. Attritional evaluation of lipophilic and hydrophilic metallated phthalocyanines for oncological photodynamic therapy. *J Photochem Photobiol B*. 2021;216(112146.
22. Broekgaarden M, van Vught R, Oliveira S, Roovers RC, van Bergen en Henegouwen PM, Pieters RJ, Van Gulik TM, Breukink E, and Heger M. Site-specific conjugation of single domain antibodies to liposomes enhances photosensitizer uptake and photodynamic therapy efficacy. *Nanoscale*. 2016;8(12):6490-4.
23. Broekgaarden M, de Kroon AI, Gulik TM, and Heger M. Development and in vitro proof-of-concept of interstitially targeted zinc- phthalocyanine liposomes for photodynamic therapy. *Curr Med Chem*. 2014;21(3):377-91.
24. Broekgaarden M, Kos M, Jurg FA, van Beek AA, van Gulik TM, and Heger M. Inhibition of NF-kappaB in Tumor Cells Exacerbates Immune Cell Activation Following Photodynamic Therapy. *Int J Mol Sci*. 2015;16(8):19960-77.
25. Derycke AS, and de Witte PA. Liposomes for photodynamic therapy. *Adv Drug Deliv Rev*. 2004;56(1):17-30.

26. Jori G. Factors controlling the selectivity and efficiency of tumour damage in photodynamic therapy. *Lasers Med Sci*. 1990;5(2):115-20.
27. Broekgaarden M, Weijer R, van Wijk AC, Cox RC, Egmond MR, Hoebe R, van Gulik TM, and Heger M. Photodynamic Therapy with Liposomal Zinc Phthalocyanine and Tirapazamine Increases Tumor Cell Death via DNA Damage. *J Biomed Nanotechnol*. 2017;13(2):204-20.
28. Peng Q, and Nesland JM. Effects of photodynamic therapy on tumor stroma. *Ultrastruct Pathol*. 2004;28(5-6):333-40.
29. Bovis MJ, Woodhams JH, Loizidou M, Scheglmann D, Bown SG, and Macrobert AJ. Improved in vivo delivery of m-THPC via pegylated liposomes for use in photodynamic therapy. *J Control Release*. 2012;157(2):196-205.
30. Buchholz J, Kaser-Hotz B, Khan T, Rohrer Bley C, Melzer K, Schwendener RA, Roos M, and Walt H. Optimizing photodynamic therapy: in vivo pharmacokinetics of liposomal meta-(tetrahydroxyphenyl)chlorin in feline squamous cell carcinoma. *Clin Cancer Res*. 2005;11(20):7538-44.
31. Arrieta O, Medina LA, Estrada-Lobato E, Ramirez-Tirado LA, Mendoza-Garcia VO, and de la Garza-Salazar J. High liposomal doxorubicin tumour tissue distribution, as determined by radiopharmaceutical labelling with (99m)Tc-LD, is associated with the response and survival of patients with unresectable pleural mesothelioma treated with a combination of liposomal doxorubicin and cisplatin. *Cancer Chemother Pharmacol*. 2014;74(1):211-5.
32. Crivellari D, Gray KP, Dellapasqua S, Puglisi F, Ribi K, Price KN, Lang I, Gianni L, Spazzapan S, Pinotti G, et al. Adjuvant pegylated liposomal doxorubicin for older women with endocrine nonresponsive breast cancer who are NOT suitable for a "standard chemotherapy regimen": the CASA randomized trial. *Breast*. 2013;22(2):130-7.
33. Bedikian AY, Silverman JA, Papadopoulos NE, Kim KB, Hagey AE, Vardeleon A, Hwu WJ, Homsi J, Davies M, and Hwu P. Pharmacokinetics and safety of Marqibo (vincristine sulfate liposomes injection) in cancer patients with impaired liver function. *J Clin Pharmacol*. 2011;51(8):1205-12.
34. Rodriguez MA, Pytlik R, Kozak T, Chhanabhai M, Gascoyne R, Lu B, Deitcher SR, Winter JN, and Marqibo I. Vincristine sulfate liposomes injection (Marqibo) in heavily pretreated patients with refractory aggressive non-Hodgkin lymphoma: report of the pivotal phase 2 study. *Cancer*. 2009;115(15):3475-82.
35. DiGiulio S. FDA approves Onivyde combo regimen for advanced pancreatic cancer. *Oncology Times*. 2015;37(22):8.
36. Reiniers MJ, van Golen RF, Bonnet S, Broekgaarden M, van Gulik TM, Egmond MR, and Heger M. Preparation and Practical Applications of 2',7'-Dichlorodihydrofluorescein in Redox Assays. *Anal Chem*. 2017;89(7):3853-7.
37. Matsuo K, Rocha FG, Ito K, D'Angelica MI, Allen PJ, Fong Y, Dematteo RP, Gonen M, Endo I, and Jarnagin WR. The Blumgart preoperative staging system for hilar cholangiocarcinoma: analysis of resectability and outcomes in 380 patients. *J Am Coll Surg*. 2012;215(3):343-55.
38. Valle J, Wasan H, Palmer DH, Cunningham D, Anthoney A, Maraveyas A, Madhusudan S, Iveson T, Hughes S, Pereira SP, et al. Cisplatin plus gemcitabine versus gemcitabine for biliary tract cancer. *N Engl J Med*. 2010;362(14):1273-81.
39. Zoepf T, Jakobs R, Arnold JC, Apel D, and Riemann JF. Palliation of nonresectable bile duct cancer: improved survival after photodynamic therapy. *Am J Gastroenterol*. 2005;100(11):2426-30.
40. Wiedmann M, Berr F, Schiefke I, Witzigmann H, Kohlhaw K, Mossner J, and Caca K. Photodynamic therapy in patients with non-resectable hilar cholangiocarcinoma: 5-year follow-up of a prospective phase II study. *Gastrointest Endosc*. 2004;60(1):68-75.
41. Ortner ME, Caca K, Berr F, Liebetruth J, Mansmann U, Huster D, Voderholzer W, Schachschal G, Mossner J, and Lochs H. Successful photodynamic therapy for

nonresectable cholangiocarcinoma: a randomized prospective study. *Gastroenterology*. 2003;125(5):1355-63.

42. Dumoulin FL, Gerhardt T, Fuchs S, Scheurlen C, Neubrand M, Layer G, and Sauerbruch T. Phase II study of photodynamic therapy and metal stent as palliative treatment for nonresectable hilar cholangiocarcinoma. *Gastrointest Endosc*. 2003;57(7):860-7.
43. Knuth A, Gabbert H, Dippold W, Klein O, Sachsse W, Bitter-Suermann D, Prellwitz W, and Meyer zum Buschenfelde KH. Biliary adenocarcinoma. Characterisation of three new human tumor cell lines. *J Hepatol*. 1985;1(6):579-96.
44. Pansa MF, Lamberti MJ, Cogno IS, Correa SG, Rumie Vittar NB, and Rivarola VA. Contribution of resident and recruited macrophages to the photodynamic intervention of colorectal tumor microenvironment. *Tumour Biol*. 2016;37(1):541-52.
45. Chuaysri C, Thuwajit P, Paupairoj A, Chau-In S, Suthiphongchai T, and Thuwajit C. Alpha-smooth muscle actin-positive fibroblasts promote biliary cell proliferation and correlate with poor survival in cholangiocarcinoma. *Oncol Rep*. 2009;21(4):957-69.
46. Rouser G, Fkeischer S, and Yamamoto A. Two dimensional then layer chromatographic separation of polar lipids and determination of phospholipids by phosphorus analysis of spots. *Lipids*. 1970;5(5):494-6.
47. Post IC, de Boon WM, Heger M, van Wijk AC, Kroon J, van Buul JD, and van Gulik TM. Endothelial cell preservation at hypothermic to normothermic conditions using clinical and experimental organ preservation solutions. *Exp Cell Res*. 2013;319(17):2501-13.
48. Harrington KJ, Rowlinson-Busza G, Syrigos KN, Uster PS, Abra RM, and Stewart JS. Biodistribution and pharmacokinetics of 111In-DTPA-labelled pegylated liposomes in a human tumour xenograft model: implications for novel targeting strategies. *Br J Cancer*. 2000;83(2):232-8.
49. Heger M, Salles, II, van Vuure W, Hamelers IH, de Kroon AI, Deckmyn H, and Beek JF. On the interaction of fluorophore-encapsulating PEGylated lecithin liposomes with hamster and human platelets. *Microvasc Res*. 2009;78(1):57-66.
50. Seshadri M, Spernyak JA, Mazurchuk R, Camacho SH, Oseroff AR, Cheney RT, and Bellnier DA. Tumor vascular response to photodynamic therapy and the antivascular agent 5,6-dimethylxanthenone-4-acetic acid: implications for combination therapy. *Clin Cancer Res*. 2005;11(11):4241-50.
51. Wang W, Moriyama LT, and Bagnato VS. Photodynamic therapy induced vascular damage: an overview of experimental PDT. *Laser Physics Letters*. 2012;10(2):023001.
52. Watson JV, Chambers SH, and Smith PJ. A pragmatic approach to the analysis of DNA histograms with a definable G1 peak. *Cytometry*. 1987;8(1):1-8.
53. Wlodkowic D, Skommer J, and Darzynkiewicz Z. Flow cytometry-based apoptosis detection. *Methods Mol Biol*. 2009;559(19-32.
54. Hermsen SA, van den Brandhof EJ, van der Ven LT, and Piersma AH. Relative embryotoxicity of two classes of chemicals in a modified zebrafish embryotoxicity test and comparison with their in vivo potencies. *Toxicol In Vitro*. 2011;25(3):745-53.
55. Castricum KC, and Thijssen VL. Method to study the role of galectins in angiogenesis in vivo using the chick chorioallantoic membrane assay. *Methods Mol Biol*. 2022:in press.
56. Barnes AE, and Jensen WN. Blood volume and red cell concentration in the normal chick embryo. *Am J Physiol*. 1959;197(403-5.
57. van Golen RF, Reiniers MJ, Heger M, and Verheij J. Solutions to the discrepancies in the extent of liver damage following ischemia/reperfusion in standard mouse models. *J Hepatol*. 2015;62(4):975-7.
58. Jensen MM, Jorgensen JT, Binderup T, and Kjaer A. Tumor volume in subcutaneous mouse xenografts measured by microCT is more accurate and reproducible than determined by 18F-FDG-microPET or external caliper. *BMC Med Imaging*. 2008;8(16.

59. Abrahamse H, and Hamblin MR. New photosensitizers for photodynamic therapy. *Biochem J*. 2016;473(4):347-64.
60. Chan WS, Marshall JF, Svensen R, Bedwell J, and Hart IR. Effect of sulfonation on the cell and tissue distribution of the photosensitizer aluminum phthalocyanine. *Cancer Res*. 1990;50(15):4533-8.
61. Qian P, Evensen JF, Rimington C, and Moan J. A comparison of different photosensitizing dyes with respect to uptake C3H-tumors and tissues of mice. *Cancer Lett*. 1987;36(1):1-10.
62. Cramers P, Ruevekamp M, Oppelaar H, Dalesio O, Baas P, and Stewart FA. Foscan uptake and tissue distribution in relation to photodynamic efficacy. *Br J Cancer*. 2003;88(2):283-90.
63. Jain RK, and Stylianopoulos T. Delivering nanomedicine to solid tumors. *Nat Rev Clin Oncol*. 2010;7(11):653-64.
64. Silverstein SC, Steinman RM, and Cohn ZA. Endocytosis. *Annu Rev Biochem*. 1977;46(669-722.
65. Dunn WA, Hubbard AL, and Aronson NN, Jr. Low temperature selectively inhibits fusion between pinocytic vesicles and lysosomes during heterophagy of 125I-asialofetuin by the perfused rat liver. *J Biol Chem*. 1980;255(12):5971-8.
66. Knoll G, Burger KN, Bron R, van Meer G, and Verkleij AJ. Fusion of liposomes with the plasma membrane of epithelial cells: fate of incorporated lipids as followed by freeze fracture and autoradiography of plastic sections. *J Cell Biol*. 1988;107(6 Pt 2):2511-21.
67. Montizaan D, Yang K, Reker-Smit C, and Salvati A. Comparison of the uptake mechanisms of zwitterionic and negatively charged liposomes by HeLa cells. *Nanomedicine*. 2020;30(102300.
68. Suk JS, Xu Q, Kim N, Hanes J, and Ensign LM. PEGylation as a strategy for improving nanoparticle-based drug and gene delivery. *Adv Drug Deliv Rev*. 2016;99(Pt A):28-51.
69. Sadzuka Y, Kishi K, Hirota S, and Sonobe T. Effect of polyethyleneglycol (PEG) chain on cell uptake of PEG-modified liposomes. *J Liposome Res*. 2003;13(2):157-72.
70. Hatakeyama H, Akita H, and Harashima H. The polyethyleneglycol dilemma: advantage and disadvantage of PEGylation of liposomes for systemic genes and nucleic acids delivery to tumors. *Biol Pharm Bull*. 2013;36(6):892-9.
71. Buchanan CF, Verbridge SS, Vlachos PP, and Rylander MN. Flow shear stress regulates endothelial barrier function and expression of angiogenic factors in a 3D microfluidic tumor vascular model. *Cell Adh Migr*. 2014;8(5):517-24.
72. Engbrecht BW, Menon C, Kachur AV, Hahn SM, and Fraker DL. Photofrin-mediated photodynamic therapy induces vascular occlusion and apoptosis in a human sarcoma xenograft model. *Cancer Res*. 1999;59(17):4334-42.
73. Debefve E, Pegaz B, van den Bergh H, Wagnieres G, Lange N, and Ballini JP. Video monitoring of neovessel occlusion induced by photodynamic therapy with verteporfin (Visudyne), in the CAM model. *Angiogenesis*. 2008;11(3):235-43.
74. Yau JW, Teoh H, and Verma S. Endothelial cell control of thrombosis. *BMC Cardiovasc Disord*. 2015;15(130.
75. Hagtvet E, Evjen TJ, Nilssen EA, and Olsen DR. Assessment of liposome biodistribution by non-invasive optical imaging: a feasibility study in tumour-bearing mice. *J Nanosci Nanotechnol*. 2012;12(3):2912-8.
76. Indrayanto G, Putra GS, and Suhud F. In: Al-Majed AA ed. *Profiles of Drug Substances, Excipients and Related Methodology*. Academic Press; 2021:273-307.
77. Pritchett JC, Naesens L, and Montoya J. In: Flamand L, Lautenschlager I, Krueger GRF, and Ablashi DV eds. *Human Herpesviruses HHV-6A, HHV-6B & HHV-7 (Third Edition)*. Boston: Elsevier; 2014:311-31.
78. Castano AP, Demidova TN, and Hamblin MR. Mechanisms in photodynamic therapy: part one-photosensitizers, photochemistry and cellular localization. *Photodiagnosis Photodyn Ther*. 2004;1(4):279-93.

79. Pena-Moran OA, Villarreal ML, Alvarez-Berber L, Meneses-Acosta A, and Rodriguez-Lopez V. Cytotoxicity, Post-Treatment Recovery, and Selectivity Analysis of Naturally Occurring Podophyllotoxins from Bursera fagaroides var. fagaroides on Breast Cancer Cell Lines. *Molecules*. 2016;21(8).
80. Pan Y, Yu Y, Wang X, and Zhang T. Tumor-Associated Macrophages in Tumor Immunity. *Front Immunol*. 2020;11(583084.
81. Beltran Hernandez I, Yu Y, Ossendorp F, Korbelik M, and Oliveira S. Preclinical and Clinical Evidence of Immune Responses Triggered in Oncologic Photodynamic Therapy: Clinical Recommendations. *J Clin Med*. 2020;9(2).
82. Soyama T, Sakuragi A, Oishi D, Kimura Y, Aoki H, Nomoto A, Yano S, Nishie H, Kataoka H, and Aoyama M. Photodynamic therapy exploiting the anti-tumor activity of mannose-conjugated chlorin e6 reduced M2-like tumor-associated macrophages. *Transl Oncol*. 2021;14(2):101005.
83. Berridge MV, Herst PM, and Tan AS. Tetrazolium dyes as tools in cell biology: new insights into their cellular reduction. *Biotechnol Annu Rev*. 2005;11(127-52.
84. Tang HL, Tang HM, Mak KH, Hu S, Wang SS, Wong KM, Wong CS, Wu HY, Law HT, Liu K, et al. Cell survival, DNA damage, and oncogenic transformation after a transient and reversible apoptotic response. *Mol Biol Cell*. 2012;23(12):2240-52.
85. Tang HM, and Tang HL. Cell recovery by reversal of ferroptosis. *Biol Open*. 2019;8(6).
86. Gong YN, Guy C, Olauson H, Becker JU, Yang M, Fitzgerald P, Linkermann A, and Green DR. ESCRT-III Acts Downstream of MLKL to Regulate Necroptotic Cell Death and Its Consequences. *Cell*. 2017;169(2):286-300 e16.
87. Overholtzer M, and Brugge JS. The cell biology of cell-in-cell structures. *Nat Rev Mol Cell Biol*. 2008;9(10):796-809.
88. Kepp O, Marabelle A, Zitvogel L, and Kroemer G. Oncolysis without viruses - inducing systemic anticancer immune responses with local therapies. *Nat Rev Clin Oncol*. 2020;17(1):49-64.
89. Hwang HS, Shin H, Han J, and Na K. Combination of photodynamic therapy (PDT) and anti-tumor immunity in cancer therapy. *J Pharm Investig*. 2018;48(2):143-51.
90. Zhou J, Wang G, Chen Y, Wang H, Hua Y, and Cai Z. Immunogenic cell death in cancer therapy: Present and emerging inducers. *J Cell Mol Med*. 2019;23(8):4854-65.
91. Wang X, and Lin Y. Tumor necrosis factor and cancer, buddies or foes? *Acta Pharmacol Sin*. 2008;29(11):1275-88.
92. Wittayarat M, Thongphakdee A, Saikhun K, Chatdarong K, Otoi T, and Techakumphu M. Cell cycle synchronization of skin fibroblast cells in four species of family Felidae. *Reprod Domest Anim*. 2013;48(2):305-10.
93. Dalman A, Eftekhari-Yazdi P, Valojerdi MR, Shahverdi A, Gourabi H, Janzamin E, Fakheri R, Sadeghian F, and Hasani F. Synchronizing cell cycle of goat fibroblasts by serum starvation causes apoptosis. *Reprod Domest Anim*. 2010;45(5):e46-53.
94. Davis PK, Ho A, and Dowdy SF. Biological methods for cell-cycle synchronization of mammalian cells. *Biotechniques*. 2001;30(6):1322-6, 8, 30-1.
95. Shin JS, Hong SW, Lee SL, Kim TH, Park IC, An SK, Lee WK, Lim JS, Kim KI, Yang Y, et al. Serum starvation induces G1 arrest through suppression of Skp2-CDK2 and CDK4 in SK-OV-3 cells. *Int J Oncol*. 2008;32(2):435-9.
96. Jin Z, Dicker DT, and El-Deiry WS. Enhanced sensitivity of G1 arrested human cancer cells suggests a novel therapeutic strategy using a combination of simvastatin and TRAIL. *Cell Cycle*. 2002;1(1):82-9.
97. Szliszka E, Czuba ZP, Kawczyk-Krupka A, Sieron-Stoltny K, Sieron A, and Krol W. Chlorin-based photodynamic therapy enhances the effect of tumor necrosis factor-related apoptosis-inducing ligand (TRAIL) in bladder cancer cells. *Med Sci Monit*. 2012;18(1):BR47-53.
98. Tudor D, Nenu I, Filip GA, Olteanu D, Cenariu M, Tabaran F, Ion RM, Gligor L, and Baldea I. Combined regimen of photodynamic therapy mediated by Gallium phthalocyanine chloride and Metformin enhances anti-melanoma efficacy. *PLoS One*. 2017;12(3):e0173241.

99. Fingar VH, Wieman TJ, Karavolos PS, Doak KW, Ouellet R, and van Lier JE. The effects of photodynamic therapy using differently substituted zinc phthalocyanines on vessel constriction, vessel leakage and tumor response. *Photochem Photobiol.* 1993;58(2):251-8.
100. Huang Y, Xu G, Peng Y, Lin H, Zheng X, and Xie M. Zinc phthalocyanine tetrasulfonate (ZnPcS4): a new photosensitizer for photodynamic therapy in choroidal neovascularization. *J Ocul Pharmacol Ther.* 2007;23(4):377-86.
101. Viola A, Jeunet A, Decreau R, Chanon M, and Julliard M. ESR studies of a series of phthalocyanines. Mechanism of phototoxicity. Comparative quantitation of O2-. using ESR spin-trapping and cytochrome c reduction techniques. *Free Radic Res.* 1998;28(5):517-32.
102. Zhang Y, Chen X, Gueydan C, and Han J. Plasma membrane changes during programmed cell deaths. *Cell Res.* 2018;28(1):9-21.
103. Bacellar IOL, and Baptista MS. Mechanisms of Photosensitized Lipid Oxidation and Membrane Permeabilization. *ACS Omega.* 2019;4(26):21636-46.
104. Cornet C, Calzolari S, Minana-Prieto R, Dyballa S, van Doornmalen E, Rutjes H, Savy T, D'Amico D, and Terriente J. ZeGlobalTox: An Innovative Approach to Address Organ Drug Toxicity Using Zebrafish. *Int J Mol Sci.* 2017;18(4).
105. Vargas A, Zeisser-Labouebe M, Lange N, Gurny R, and Delie F. The chick embryo and its chorioallantoic membrane (CAM) for the in vivo evaluation of drug delivery systems. *Adv Drug Deliv Rev.* 2007;59(11):1162-76.
106. Naldaiz-Gastesi N, Bahri OA, Lopez de Munain A, McCullagh KJA, and Izeta A. The panniculus carnosus muscle: an evolutionary enigma at the intersection of distinct research fields. *J Anat.* 2018.
107. Fantini F, Greco A, Cesinaro AM, Surrenti T, Peris K, Vaschieri C, Marconi A, Giannetti A, and Pincelli C. Pathologic changes after photodynamic therapy for Basal cell carcinoma and Bowen disease: a histologic and immunohistochemical investigation. *Arch Dermatol.* 2008;144(2):186-94.
108. Falk-Mahapatra R, and Gollnick SO. Photodynamic Therapy and Immunity: An Update. *Photochem Photobiol.* 2020;96(3):550-9.
109. Sarin H. Physiologic upper limits of pore size of different blood capillary types and another perspective on the dual pore theory of microvascular permeability. *J Angiogenes Res.* 2010;2(14.
110. Ono S, Egawa G, and Kabashima K. Regulation of blood vascular permeability in the skin. *Inflamm Regen.* 2017;37(11.
111. Li M, van Raath MI, Khakpour S, Secilir A, Sliggers BC, Huang X, Ding B, Storm G, van der Hulst RR, de Kroon A, et al. In Vivo Assessment of Thermosensitive Liposomes for the Treatment of Port Wine Stains by Antifibrinolytic Site-Specific Pharmaco-Laser Therapy. *Pharmaceutics.* 2020;12(6).
112. Heger M, Salles, II, Bezemer R, Cloos MA, Mordon SR, Begu S, Deckmyn H, and Beek JF. Laser-induced primary and secondary hemostasis dynamics and mechanisms in relation to selective photothermolysis of port wine stains. *J Dermatol Sci.* 2011;63(3):139-47.
113. Reddi E, Zhou C, Biolo R, Menegaldo E, and Jori G. Liposome- or LDL-administered Zn (II)-phthalocyanine as a photodynamic agent for tumours. I. Pharmacokinetic properties and phototherapeutic efficiency. *Br J Cancer.* 1990;61(3):407-11.
114. Allison BA, Pritchard PH, and Levy JG. Evidence for low-density lipoprotein receptor-mediated uptake of benzoporphyrin derivative. *Br J Cancer.* 1994;69(5):833-9.
115. Polo L, Bianco G, Reddi E, and Jori G. The effect of different liposomal formulations on the interaction of Zn(II)-phthalocyanine with isolated low and high density lipoproteins. *Int J Biochem Cell Biol.* 1995;27(12):1249-55.
116. Warin R, Xiao D, Arlotti JA, Bommareddy A, and Singh SV. Inhibition of human breast cancer xenograft growth by cruciferous vegetable constituent benzyl isothiocyanate. *Mol Carcinog.* 2010;49(5):500-7.
117. Zhu J, Tian S, Li KT, Chen Q, Jiang Y, Lin HD, Yu LH, and Bai DQ. Inhibition of breast cancer cell growth by methyl pyropheophenylchlorin photodynamic therapy is

mediated though endoplasmic reticulum stress-induced autophagy in vitro and vivo. *Cancer Med.* 2018;7(5):1908-20.

118. Weng X, Wei D, Yang Z, Pang W, Pang K, Gu B, and Wei X. Photodynamic therapy reduces metastasis of breast cancer by minimizing circulating tumor cells. *Biomed Opt Express.* 2021;12(7):3878-86.

119. Theodossiou TA, Ali M, Grigalavicius M, Grallert B, Dillard P, Schink KO, Olsen CE, Walchli S, Inderberg EM, Kubin A, et al. Simultaneous defeat of MCF7 and MDA-MB-231 resistances by a hypericin PDT-tamoxifen hybrid therapy. *NPJ Breast Cancer.* 2019;5(13.

120. Nunes SM, Sguilla FS, and Tedesco AC. Photophysical studies of zinc phthalocyanine and chloroaluminum phthalocyanine incorporated into liposomes in the presence of additives. *Braz J Med Biol Res.* 2004;37(2):273-84.

121. van Raath MI, Weijer R, Nguyen GH, Choi B, de Kroon AI, and Heger M. Tranexamic Acid-Encapsulating Thermosensitive Liposomes for Site-Specific Pharmaco-Laser Therapy of Port Wine Stains. *J Biomed Nanotechnol.* 2016;12(8):1617-40.

SUPPLEMENTAL INFORMATION OF PAPER II

S3.3. Materials and methods

S3.3.1. Chemicals and reagents

Table S3.1 - List of chemicals/compounds, buffers, and reagents/kits (categorically, alphabetically).

Chemical / compound	**Purity**	**Supplier**	**Additional information**
1,2-Dipalmitoyl-*sn*-glycero-3-phosphocholine (DPPC)	> 99%	Avanti Polar Lipids[$]	Product # 850355P; dissolved in $CHCl_3$, stored under N_2 atmosphere at -20 °C
1,2-Dipalmitoyl-sn-glycero-3-phosphoethanolamine-N-(lissamine rhodamine B sulfonyl) (ammonium salt) (rhodamine-PE)	> 99%	Avanti Polar Lipids[$]	Product # 810158P; dissolved in $CHCl_3$, stored under N_2 atmosphere (by supplier) at -20 °C
1-Palmitoyl-2-{6-[(7-nitro-2-1,3-benzoxadiazol-4-yl)amino]hexanoyl}-*sn*-glycero-3-phosphocholine (NBD-PC)	> 99%	Avanti Polar Lipids[$]	Product # 810131C; dissolved in $CHCl_3$, stored under N_2 atmosphere (by supplier) at -20 °C
Acetic acid (glacial)	100%	Merck KGaA[*]	Product # 100063
Alexa Fluor 488-conjugated phalloidin	N.A.	Life Technologies[†]	Supplied by Thermo Fisher Scientific under product # A12379
Aluminum (III) phthalocyanine chloride	85%	Sigma-Aldrich[#]	Product # 362530; dissolved in pyridine at 150-µM stock concentration, stored under N_2 atmosphere at RT
Aluminum (III) phthalocyanine chloride tetrasulfonic acid	N.S.	Frontier Scientific[£]	CAS: 100180-30-1; dissolved in PBS at 1 mM stock concentration, stored under N_2 atmosphere at 4 °C
Bovine serum albumin	≥ 98%	Sigma-Aldrich[#]	Product # A7906
Chloroform ($CHCl_3$)	≥ 99%	Sigma-Aldrich[#]	Product # 288306
Dimethyl sulfoxide (DMSO)	≥ 99.5%	Sigma-Aldrich[#]	Product # D4540
Ethanol (absolute)	≥ 99.9%	Sigma-Aldrich[#]	Product # RH 34870
Hoechst 33342	N.S.	Sigma-Aldrich[#]	Product # H3570; 10 mg/mL MilliQ water
L-α-phosphatidylethanolamine, distearoyl methoxypolyethylene glycol conjugate (DSPE-PEG)	N.S.	Sigma-Aldrich[#]	Product # P7840; average PEG molecular mass of 2,000, dissolved in $CHCl_3$, stored under N_2 atmosphere at -20 °C
Propidium iodide (PI)	N.S.	Molecular Probes | Life Technologies[†]	Product # P3566; 1.0 mg/mL MilliQ water, stored at 4 °C
Pyridine	≥ 99%	Sigma-Aldrich[#]	Product # 437611
Sodium chloride	99.99%	Merck KGaA[*]	Product # 106406
Sodium hydroxide	≥ 99%	Merck KGaA[*]	Product # 106462
Sulforhodamine B sodium salt (SRB)	N.S.	Sigma-Aldrich[#]	Product # S1402
Trichloroacetic acid (TCA)	≥ 99%	Sigma-Aldrich[#]	Product # T6399, stored at 4 °C
Zinc (II) phthalocyanine	97%	Sigma-Aldrich[#]	Product # 341169; dissolved in pyridine at 178 µM stock concentration, stored under N_2 atmosphere at RT
Zinc (II) phthalocyanine tetrasulfonic acid	N.S.	Frontier Scientific[£]	CAS: 61586-86-5; dissolved in PBS at 1 mM stock concentration, stored under N_2 atmosphere at 4 °C

Buffer	**Purity**	**Supplier**	**Additional information**
HEPES (sodium salt)	≥ 99.5%	Sigma-Aldrich[#]	Product # H7006
Phosphate-buffered saline (PBS)	N.S.	Fresenius Kabi[§]	Sterile solution
Tris(hydroxymethyl)-aminomethane (TRIS)	≥ 99.8%	Merck KGaA[*]	Product # 108382

Reagent / kit	Purity	Supplier	Additional information
Cell proliferation reagent WST-1	N.A.	Sigma-Aldrich[#]	Cat.No. 0501594400; stored at -20 °C
Dead Cell Apoptosis Kit	N.A.	Molecular Probes | Life Technologies[†]	Product # V13245; contains Annexin V - Alexa Fluor 488 conjugate (250 µL), propidium iodide (PI, 100 µL), and annexin binding buffer (5× solution, 15 mL); stored at 4 °C
FluorSave reagent	N.A.	Calbiochem[&]	Supplied by Merck KGaA under product # 345789. Stored between 15 - 30 °C
RNAse A	N.S.	Sigma-Aldrich[#]	Product # 109169; from bovine pancreas, stored at 4 °C

Abbreviations: N.A., not applicable; N.S., not specified

[$] Alabaster, AL, USA

[*] Darmstadt, Germany

[†] Carlsbad, CA, USA

[#] St. Louis, MO, USA

[£] Logan, UT, USA

[§] Bad Homburg, Germany

[&] San Diego, CA, USA

Table S3.2 - List of instruments and materials/disposables (chronologically).

Instrument / technique	Model / type	Supplier
Hemocytometer	0.100 mm depth and 0.0025 mm^2	Blaubrand, Wertheim, Germany
Light microscope	Model CK2	Olympus, Tokyo, Japan
Tip sonicator	Model 450	Branson, Danbury, CT, USA
Dynamic light scattering	Model 3000 and ALV CGS-3	Malvern Instruments, Malvern, UK
Electrophoretic mobility	Model 3000 and Nano Z	Malvern Instruments, Malvern, UK
Quartz cuvettes (QS)	Model 109004F-10-40; 10 × 4 mm, 1,500 µL, magnetic stirrer	Hellma Analytics, Müllheim, Germany
Fluorescence spectrometer	Cary Eclipse	Varian, Palo Alto, CA, USA
Graphics software	Origin	Microcal, Los Angeles, CA, USA
Centrifuge (for 2 mL tubes)	Model 5417R	Eppendorf, Hamburg, Germany
Flow cytometer	FacsCanto II	BD Biosciences, Franklin Lakes, NJ, USA
Flow cytometry software	FloJo	BD Biosciences, Franklin Lakes, NJ, USA
Graphics software	GraphPad Prism	GraphPad Software, San Diego, CA, USA
Confocal laser scanning microscope	SP8-X SMD	Leica Microsystems, Wetzlar, Germany
Perfusion slides	µ-Slide I 0.6 Luer, single channel, cat # 80186	Ibidi, Gräfelfing, Germany
Fluorescence microscope	Axio Observer Z1	Carl Zeiss Microscopy, Oberkochen, Germany
Image processing software	ZEN 2 Blue	Carl Zeiss Microscopy, Oberkochen, Germany
Image processing software	ImageJ	National Institutes of Health, Bethesda, MD, USA
Microplate reader	Synergy HT	BioTek Instruments, Winooski, VT, USA
Hotplate stirrer	17.8 × 17.8 cm, aluminum; cat # 97042-616	VWR, Radnor, PA, USA
Power meter	Field-Mate	Coherent, Santa Clara, CA, USA
Laser	Solid state diode laser, 671 nm, tunable power (0-1.5 W), fiber-based	CNI Laser, Changchun, China
Rocker (microplate shaker)	Titermix 100	LAUDA-Brinkmann, Delran, NJ, USA
Centrifuge (for 15 mL tubes)	Model Rotina 380 R	Hettich, Tuttlingen, Germany
Aquatic tank	Active Blue ZebTec standalone unit	Tecniplast, Buguggiate, Italy
Stereomicroscope	SMZ-800	Nikon, Tokyo, Japan
Stereomicroscope	SMZ-171T	Motic, Kowloon, Hong Kong
Digital camera	Moticam 5, 5.0 MP (2592 × 1944), CMOS sensor	Motic, Kowloon, Hong Kong

Dedicated image processing software	Images Plus 3.0	Motic, Kowloon, Hong Kong
Hamilton syringe	100 µL	Hamilton Company, Reno, NV, USA
Hamilton needle	33-G	Hamilton Company, Reno, NV, USA
Digital lux meter	AS-V8	Aicevoos, Beijing, China
Insulin syringe and needle	Microfine, 1 mL, 33-G	BD Biosciences, Franklin Lakes, NJ, USA
LED panel	18 W	Qiang Lighting Products
Spectrometer	QE65000	Ocean Optics, Dunedin, FL, USA
Fluorescence stereomicroscope	M165 FC, custom-modified	Leica Microsystems, Wetzlar, Germany
Camera (macroscopy)	Galaxy	S8Samsung Electronics, Seoul, South Korea
Microtome	Microm EC 350-2 workstation	Thermo Scientific, Waltham, MA, USA
Materials / disposables	**Model / type**	**Supplier**
Cell culture flasks	Cellstar; T75 T25 Rectangular Canted Neck Cell Culture Flask	Greiner Bio-One, Solingen, Germany Corning, Corning, NY, USA
Cell culture plates	Cellstar; 6,12, 24, 96 wells, flat bottom	Greiner Bio-One, Solingen, Germany
Centrifuge tubes	2 mL, safe lock	Eppendorf, Hamburg, Germany
Centrifuge tubes	15 mL, sterile, polystyrene	Greiner Bio-One, Solingen, Germany
Circular coverslip for confocal microscopy	24 mm	Thermo Fisher Scientific, Waltham, MA, USA
Round-bottom flow cytometry tubes	Falcon, 5 mL, polypropylene	Corning Life Science, Tewksbury, MA, USA
Perfusion slides	µ-Slide I$^{0.6}$ Luer	Ibidi, Martinsried, Germany
Petri dish	100 × 15 mm, polystyrene	Sigma Aldrich, St. Louis, MO, USA
Microscope slides	76 × 26 mm, 1.0 mm thick	Thermo Fisher Scientific, Waltham, MA, USA
Microscope cover slips	24 × 24 mm, 0.17 mm thick	Thermo Fisher Scientific, Waltham, MA, USA

Table S3.3 - List of cells and animals and required paraphernalia (chronologically).

Cell line/primary cells *Origin*	**Supplier**	**Additional information**
SK-ChA1 *malignant ascites of patient with primary adenocarcinoma of the extrahepatic biliary tree*	Dr. Alexander Knuth, Ms. Claudia Matter; University Hospital Zürich, Switzerland	Negative for mycoplasma
HUVECs (primary cells) *human umbilical vein, isolated directly post-birth*	Freshly isolated from primary source	
NIH-3T3 *Swiss mouse embryonic fibroblasts*	Dr. Riekelt Houtkooper, Amsterdam UMC, location AMC	Negative for mycoplasma
RAW 264.7 *mouse (Balb/c) leukemic monocyte-macrophage*	Dr. Joan Kwakkel, Amsterdam UMC, location AMC	Negative for mycoplasma
HUVECs	Lonza, Basel, Switzerland; cat # C2519A	Negative for mycoplasma, bacteria, yeast, and fungi, HIV-1, hepatitis B, and hepatitis C; express CD31/105
MDA-MB-231	Cell Bank of the Chinese Academy of Sciences	Negative for mycoplasma
Cell culture paraphernalia	**Supplier**	**Additional information**
Dulbecco's modified Eagle medium (DMEM)	Lonza, Basel, Switzerland	Phenol red-containing (product # BE12-604F) or phenol red-free (product # BE12-917F), depending on the type of experiment. Stored at 4 °C

Roswell Park Memorial Institute (RPMI) 1640	Gibco | Thermo Fisher Scientific, Waltham, MA, USA (SK-ChA1) Sangon Biotech, Shanghai, China (MDA-MB-231)	Phenol red-containing (product # 21875034) and phenol red -free (product # 11835-063). Stored at 4 °C
EndoGRO-LS	Merck | Millipore, Burlington, MA, USA	Product # SCME001, Stored at 4 °C (basal medium) and at -21 °C (supplement kit)
L-glutamine	Lonza, Basel, Switzerland	Product # BE17-605E, 2 mM final concentration in medium, stored at -20 °C
Fetal bovine serum (FBS)	Bodinco, Alkmaar, the Netherlands (cell cultures for *in vitro* studies) Beyotime Biotech, Shanghai, China	10% final concentration in medium, stored at -20 °C
Penicillin/streptomycin	Lonza, Basel, Switzerland	Product # 17-602E; final concentration of 100 U/mL penicillin, 100 µg/mL streptomycin in medium. Used in cell culture for *in vitro* studies
Streptomycin	NCPC, Hebei, China	Used in cell culture for *in vivo* studies
Penicillin	NCPC, Hebei, China	Used in cell culture for *in vivo* studies
Accutase	Innovative Cell Technologies, San Diego, CA, USA	Product # AT104; stored at 4 °C
Trypsin	Beyotime Biotech, Shanghai, China	Product # C0202
Paraformaldehyde aqueous solution (PFA)	Electron Microscopy Science, Hatfield, PA, USA	Cat # 157-8
Endothelial Cell Basal Medium 2 (EBM-2)	PromoCell, Heidelberg, Germany	cat # C-22211
SupplementMix	PromoCell, Heidelberg, Germany	cat # C-39216
Gentamicin sulfate-amphotericin (GA-1000)	Lonza, Basel, Switzerland	Product # CC-4083. Used in ITL-HUVEC flow assays.
Animal (strain)	**Supplier**	**Additional information**
Zebrafish (Danio rerio)	Aquatic facility of the Faculty of Science, Utrecht University	
White Leghorn chicken embryos	Het Anker, Ochten, the Netherlands	
BALB/c nude mice, male	Changzhou Cavens Laboratory Animals Co., Changzhou, Jiangsu, China	
Animal paraphernalia	**Supplier**	**Additional information**
Fish feed	Skretting | Nutreco, Amersfoort, the Netherlands	Gemma Micron 300
Fish feed	Hobby, Schoten, the Netherlands	Artemia
E3 medium	Chemicals obtained from Sigma-Aldrich, St. Louis, MO, USA	5 mM NaCl, 0.17 mM KCl, 0.33 mM $CaCl_2 \cdot 2H_2O$, 0.33 mM $MgSO_4 \cdot 7H_2O$
Fish anesthesia	Sigma-Aldrich, St. Louis, MO, USA	Tricaine 0.4% (MS222), CAS 888-86-2
Humidified egg incubator	FIEM, Guanzate, Italy	MG140/200 Rural
Mouse IVC housing	Suzhou SuHang Technology Equipment Company, Suzhou, Jiangsu, China	Makrolon type II with filter top
Mouse pelleted food	Jiangsu Xietong Pharmaceutical Bio-Engineering Company,	Sterilized

	Nanjing, Jiangsu, China	
Anesthesia (mice)	Guangdong longhui Chemical & Industry Co., Guangdong, China	Diethyl ether
Analgesia (mice)	Shanghai Hengrui Pharmaceutical Co., Shanghai, China	Butorphanol
Matrigel	Corning, Shanghai, China	Stored frozen, kept at 4 °C before use
Fixative solution	Sigma-Aldrich, St. Louis, MO, USA	Formalin
Tissue dehydration solution	Qingchen Chemical Preparation Factory, Hangzhou, China	Ethanol
Tissue clearing solution	Qingchen Chemical Preparation Factory, Hangzhou, China	Xylene
Tissue embedding material	Nanjing Tianshi New Material Technology Co., Jiangsu, China	Paraffin
Histological stains	Beyotime Biotechnology Co., Shanghai, China	Hematoxylin and eosin

S3.3.2. Cell culture

Cells were grown under standard culture conditions (37 °C, humidified atmosphere of 5% CO2 and 95% air) in T75 culture flasks and subcultured twice per week as described in Table S3. All cell culture media were supplemented with 10% (v/v) fetal bovine serum (FBS), 100 U/mL penicillin, 100 µg/mL streptomycin, and 2 mM glutamine unless noted otherwise. Cells were washed in phosphate-buffered saline (PBS) equilibrated at 37 °C. The degree of confluence was assessed by standard light microscopy (Olympus CK2) and cell density of harvested cells in suspension was determined with a hemocytometer. Cells were harvested following Accutase treatment (maximum 10 min incubation at standard culture conditions), except for RAW 264.7 cells that were harvested using a 25 cm sterile cell scraper (Sarstedt, Nümbrecht, Germany) to prevent macrophage activation. Cells were seeded 24 h prior to experiments in 12 wells or 24 wells plates at a volume of 1 mL/well or 500 µL/well, respectively.

Table S3.4 - Cell culture specifics for all experiments excluding the HUVEC flow experiments.

Cells / cell line	**Medium**	**Passage ratio**	**Seeding density** [cells/mL]	
			24 and 12 well plates*	**6 well plates#**
HUVECs	EndoGRO-LS	1:4 (2×/wk)	2.0×10^5	1.0×10^5
RAW 264.7	DMEM	1:8 (2×/wk)	1.8×10^5	1.0×10^5
3T3-NIH	DMEM	1:14 (2×/wk)	1.5×10^5	0.5×10^5
SK-ChA-1	RPMI 1640	1:8 (2×/wk)	1.8×10^5	1.0×10^5
MDA-MB-231	RPMI 1640	1:3 (3×/wk)	N.A.	N.A.

* Cell seeding density for ~90% confluence after 24 h at standard incubation conditions.
# Cell seeding density for ~60% confluence after 24 h at standard incubation conditions.

S3.3.3. Preparation, characterization, and functional testing of ITLs

S3.3.3.3. Functional testing

The decrease in fluorescence emission with increasing ROS generation and oxidative tryptophan modification was determined by time-based fluorescence spectroscopy. A quartz cuvette containing a magnetic stirrer was placed in a temperature-controlled cuvette holder of a fluorescence spectrometer (Cary Eclipse). The spectrometer was operated in time-based acquisition mode with constant stirring and a set cuvette temperature of 20 °C. The procedure entailed: t = -1 min: addition of 1080 µL of 1 mg/mL BSA in equilibration buffer to the cuvette, t = 0 min: start spectral acquisition (λex = 279 ± 5 nm, λem = 344 ± 5 nm), t = 1 min: addition of 120 µL of the ZnPC-ITL or AlPC-ITL suspension (0.5 mM final lipid concentration, 1.5 µM final PS concentration), empty ITLs (0.5 mM final lipid concentration, control), or ZnPCS4/AlPCS4 (1.5 µM final PS concentration), t = 2 min: 671-nm laser illumination for 2 min at 500 mW, and t = 5 min: end spectral acquisition. Data (N = 3 experimental replicates) were normalized to the maximum fluorescence emission intensity between t = 0-1 min and plotted as a function of time in MicroCal Origin.

S3.3.4. Temperature-dependent uptake of ITLs (flow cytometry)

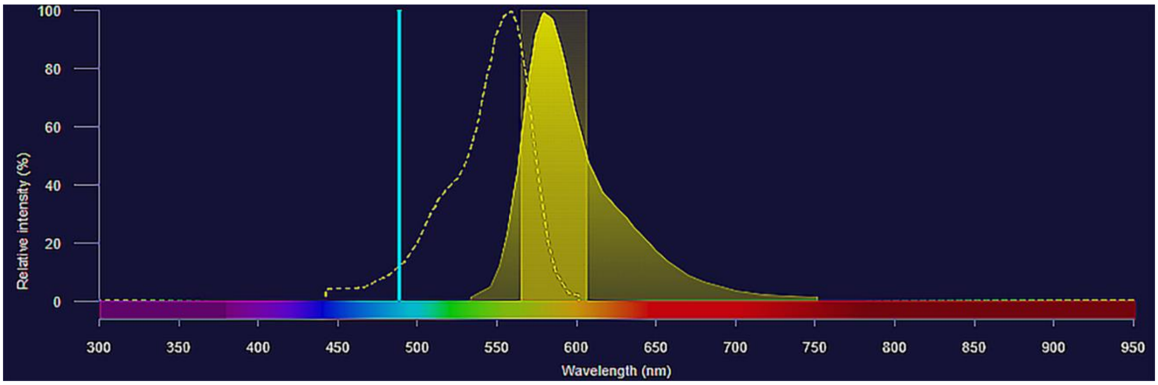

Figure S3.1 - Spectral properties of rhodamine in the context of ITL-cell association analysis. The normalized excitation (dashed) and fluorescence emission (solid, filled) spectrum is presented against the laser excitation line (vertical cyan line) and the fluorescence detection range (vertical yellow marquee) of the flow cytometer. Data were plotted in SpectraViewer (Thermo Fisher Scientific).

S3.3.5. ITL internalization and intracellular distribution (confocal microscopy)

After photosensitization, cells were washed with PBS (RT, 1 mL/well) prior to fixation with 2% paraformaldehyde (PFA, 1 mL/well) in PBS (RT) for 15 min in the dark. The fixative solution was decanted, cells were washed once with PBS (RT), and 1 mL of ice-cold PBS was added per well for storage at 4 °C until confocal microscopy imaging (typically within 24 h) on a Leica SP8-X SMD system. Directly before imaging, 10 µL of Hoechst 33342 (0.5 mg/mL in MilliQ) was added to each sample and incubated for 3 min at RT to stain the nucleus. Subsequently, the cover slip was secured in the steel ring of the microscope stage, 1 mL of PBS (RT) was added, and the cells were imaged.

Table S3.5 - Confocal microscopy settings.

Name	Value
Rotator Angle	0 °
Scan Mode	xyz
Scan Direction X	Bidirectional
Scan Speed	400 Hz
Magnification	63
Objective	HC PL APO CS2 63×/1.40 OIL
Immersion	Oil
Numerical Aperture	1.4
Refraction Index	1.518
Zoom	3
Pinhole	95.6 µm
Pinhole Airy	1 AU
Emission Wavelength for Pinhole Airy Calculation	580 nm
Laser	405 Diode
Laser Power	16383,0000 W
Detectors:	HyD (660nm - 800nm) Standard mode
	HyD (571nm - 648nm) Standard mode
	HyD (501nm - 551nm) Standard mode

Table S3.6 - Laser settings used for confocal microscopy.

	ZnPC-ITLs	ZnPCS4	AlPC-ITLs	AlPCS4	ITLs		Hoechst 33342
					NBD-PC	DSPE-Rho	
λ_{ex} [nm]	660	633	660	650	488	561	405
Int. (%)	25.16	79.80	17.00	35.00	15.00	10.00	0.10
λ_{em} [nm]	790	790	790	790	541	638	479

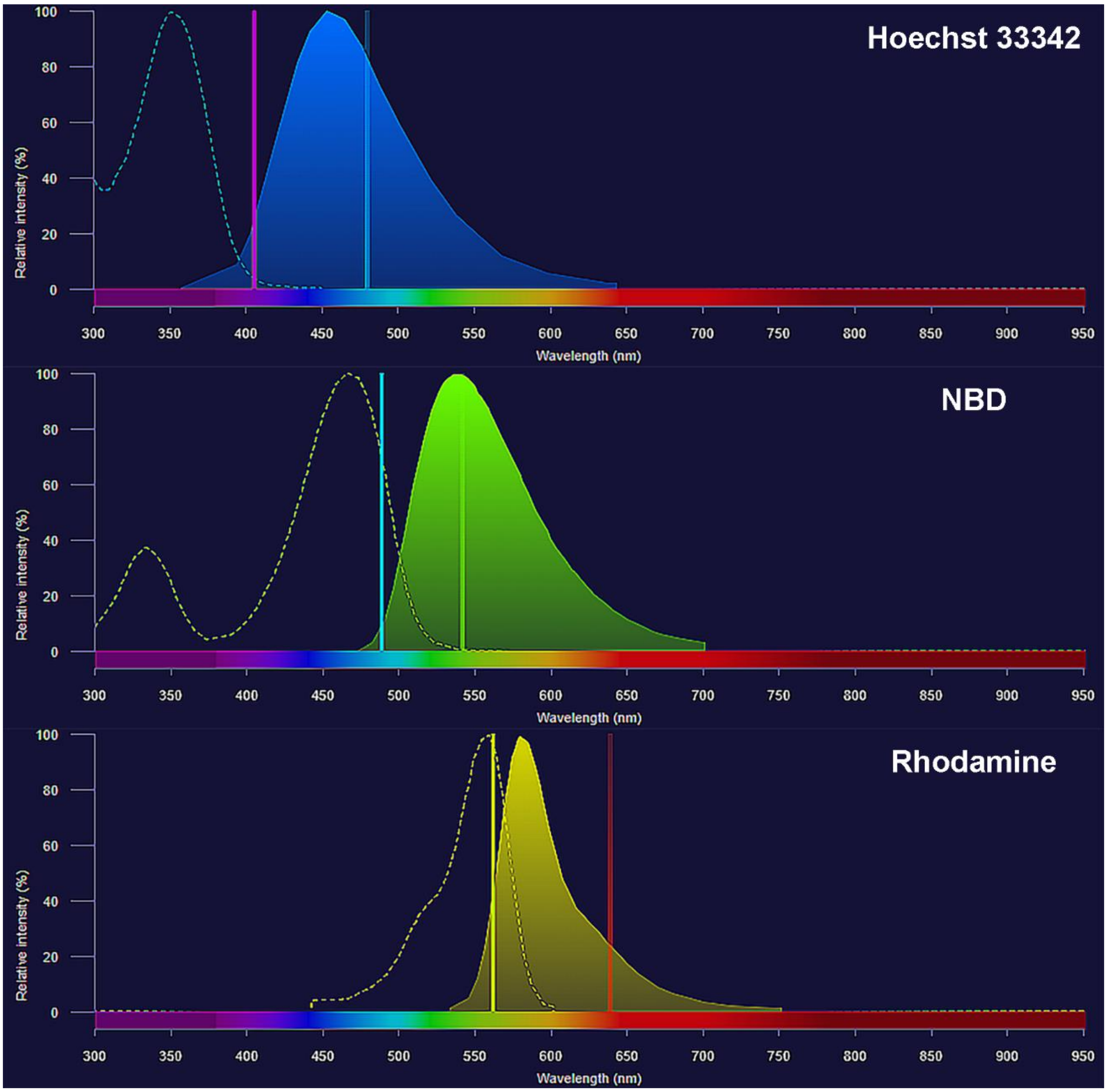

Figure S3.2 - Spectral properties of the non-photosensitizer fluorophores used in the confocal microscopy experiments. The normalized excitation (dashed) and fluorescence emission (solid, filled) spectra are presented against the laser excitation line (left vertical line) and the fluorescence detection wavelength (right vertical line). Data were plotted in SpectraViewer (Thermo Fisher Scientific). The absorption spectra of the photosensitizers are plotted in Figure S3.4.

S3.3.6. Uptake of ITLs by endothelial cells under flow

Imaging was performed using a Zeiss Axio Observer Z1 microscope equipped with Colibri LEDs (Carl Zeiss filter set 49 for Hoechst 33342 (λex = 350 nm, λem = 461 nm), filter set 10 for phalloidin-AF488 (λex = 495 nm, λem = 518 nm), filter set 20 for rhodamine-PE (λex = 510 nm, λem = 562 nm)) using a 40 × objective (Fluor 40 ×/1.30 oil), and an AxioCam MRm. Twenty Z-stacks were captured per slide (range 8.12 μm, slices 30, interval 0.28 μm) and were processed using ZEN 2 Blue software and ImageJ software.

S3.3.8. Dark toxicity

S3.3.8.1. Mitochondrial redox (WST-1) assay

The WST-1 colorimetric assay was performed to determine mitochondrial redox state (1) as part of viability analysis (2). The ZnPC and AlPC have a logP of > 8 and hence localize to cell and organelle membranes, including mitochondria (3). Inasmuch as mitochondria play a key role in cell death, particularly when the electron transport chain is dysregulated (4), a mitochondrial redox function assay was selected to gauge dark toxicity of the PSs. The WST-1 assay is ideal because it does not notably interfere in cell physiology, allowing subsequent cell viability analysis by other methods.

Briefly, cells were washed once with PBS (37 °C). WST-1 reagent was added to medium-/- at a 1:25 volume ratio. A 300 μL aliquot was transferred to each well (for 24-wells plates) and cells were incubated for 20 min under standard culture conditions. After incubation, 100 μL of the medium containing WST-1 was transferred in duplicate to a 96 wells plate. The absorption was read using a plate reader at 450 nm and a reference wavelength of 620 nm for background subtraction. The mean ± SD absorption at 450 nm was calculated per concentration and incubation time (N = 3) and normalized to the mean WST-1 absorbance of untreated cells (N = 3). Finally, the remainder of the WST-1 containing medium was removed by washing once with PBS (37 °C) using a squirt bottle and processed further for total protein content as described in the next section.

S3.3.8.2. Total protein (SRB) assay

The sulforhodamine B (SRB) colorimetric assay was used to measure total protein content as a more definitive parameter of cytotoxicity. This assay is based on the premise that dead and late-stage dying cells detach from the well plate bottom, leaving only viable cells that are stained and semi-quantified (5).

Following the single wash, cells were tapped dry and fixed with 300 µL of 10% ice-cold trichloroacetic acid in MilliQ for at least 1 h at 4 °C. Next, the cells were washed 5 × with MilliQ (RT) using a squirt bottle and stained with 0.4% SRB dissolved in 1% acetic acid in MilliQ for at least 15 min (300 µL/well for a 24 well plate). The SRB solution was decanted, and the cells were washed 4 × with 1% acetic acid in a squirt bottle (RT) to remove unbound SRB. The well plate was left to dry at 37 °C for at least 15 min. Once dried, 500 µL of 10 mM unbuffered TRIS base in MilliQ (RT) was added to each well and the plate was gently rocked for at least 1 min to completely dissolve the SRB. Absorption was measured in a microplate reader at 564 nm and 600 nm and a reference wavelength of 690 nm for background removal. The mean ± SD absorption at 564 nm was calculated per concentration and incubation time and normalized to the mean SRB absorbance of untreated cells (N = 3/group). Absorbance data at 600 nm were used to determine cell viability when the optical density of the 564 nm read was > 1.3.

S3.3.10. Cell cycle analysis

Cells seeded in 12-well plates were incubated for 60 min with PS in medium-/- (37 °C, 1000 µL/well; ZnPC-ITLs and AlPC-ITLs, 31.25 µM phospholipid concentration, 0.09 µM PS concentration; ZnPCS4 and AlPCS4, 0.31 µM) under standard culture conditions. After washing with PBS (37 °C), fresh medium-/- was added and cells were illuminated at 500 mW for 1 min and 54 s, accounting for a cumulative radiant exposure of 15 J/cm^2 per well (N = 3 independent experiments per PS). The plate was kept at 37 °C using a plate heater during PDT. Cells were harvested 24 h after PDT with Accutase (100 µL/well, 10 min at standard culture conditions) or scraped (RAW 264.7 cells) in 1 mL of PBS (RT). The cells were transferred to 15 mL sterile centrifuge tubes and washed twice by centrifugation at 500 × g for 5 min at 4 °C. Following the second centrifugation step, the supernatant was decanted and the pellet was resuspended in 300 µL of PBS (RT). Cells were fixed by dropwise addition of 700 µL of ice-cold 96% ethanol under continuous swirling. PBS (1 mL at RT) was added and cells were centrifuged for 5 min at 500 × g and 4 °C. The supernatant was discarded and cells were resuspended in 200 µL of PI staining solution (20 µg/mL PI and 100 µg/mL RNAse A in PBS) in 300 µL of PBS (RT). Before flow cytometric measurement of PI fluorescence, cells were gated based on forward scatter and sideways scatter properties to ensure that cell remnants and cell-derived microparticles were gated out. PI fluorescence was measured at λex = 488 nm and λem = 670 nm long pass. Ten thousand events were collected in the gated region.

S3.3.11. Analysis of mode of cell death

Cells seeded in 12 well plates were photosensitized and treated by PDT as described in section 3.3.9. After 2 h, 4 h, and 8 h of incubation at standard culture conditions (N = 3 independent experiments per time point), the medium was transferred into 15 mL sterile centrifuge tubes and combined with the detached cells that had been harvested following proteolytic and collagenolytic enzyme treatment (100 µL of Accutase for 10 min at standard culture conditions) or scraping (RAW 264.7 cells). Cells were then centrifuged at 500 × g for 5 min at 4 °C. The supernatant was decanted, and the cell pellet was resuspended in 100 µL of 1 × annexin V (AV) binding buffer (RT) containing 5 µL of Alexa Fluor 488-conjugated AV. The AV binding buffer was diluted 5 × with MilliQ water. After 15 min incubation at RT, 399 µL of diluted AV binding buffer was added and the cell suspension was transferred to 5-mL round-bottom flow cytometry tubes. Subsequently, 1 µL of PI (0.1 mg/mL, diluted with annexin V binding buffer) was added 5 min before flow cytometry.

The experiment was repeated for the 4 h post-PDT incubation group, where the PS concentration effects were studied. Cells were incubated with ZnPC-ITLs or AlPC-ITLs (50-, 250-, and 500-µM final phospholipid concentration; 0.15-, 0.75-, and 1.5-µM final PS concentration) and 0.5, 2.5, and 5 µM of ZnPCS4 or AlPCS4 for 60 min and subjected to PDT as described in section 3.3.9 . The same procedural steps were followed after PDT as described above.

Cells were gated based on forward scatter and sideways scatter properties. Cell remnants and cell-derived microparticles were gated out. AV and PI fluorescence was measured at λex = 488 nm, λem = 530 ± 30 nm and λex = 488 nm, λem = 670 nm long pass, respectively. Ten thousand events were collected in the gated region. The scatterplots were analyzed in FlowJo software, where quadrants were positioned based on the green and red fluorescence of untreated cells.

S3.3.12. Systemic toxicity in zebrafish embryos

The zebrafish were maintained in tanks within an Active Blue ZebTec standalone unit at 28.0 ± 0.5 °C with continuous water flow under a 14:10 h light/dark period (standard conditions). The fish were fed three times a day, twice with Gemma Micron 300 and once with fresh Artemia. Males and females were separated in spawning boxes 16 h before spawning at a ratio of 5:5. Spawning was triggered once the light was turned on and the divider was removed, after which the spawning was usually completed within 30 min.

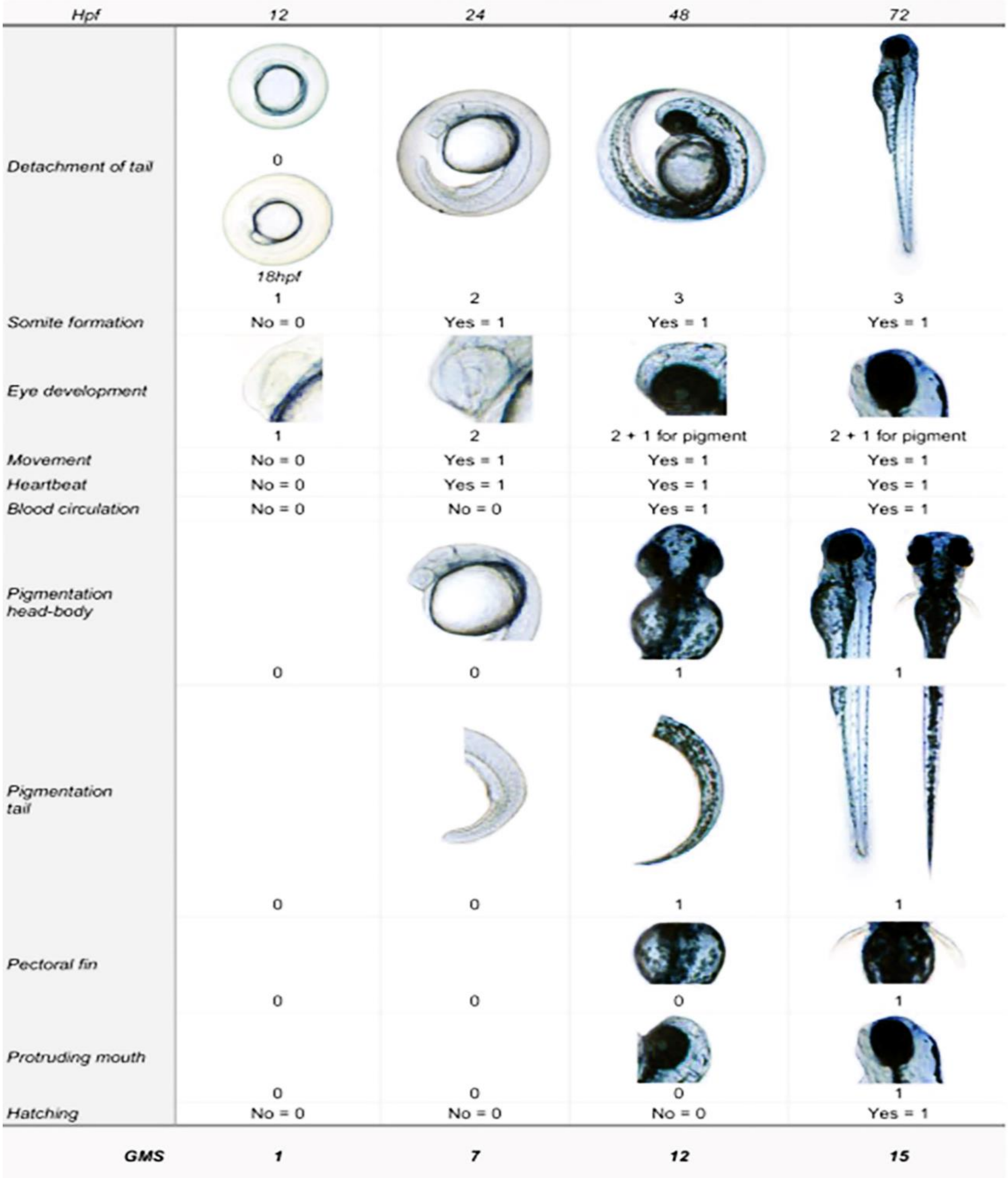

Hpf	*12*	*24*	*48*	*72*
Detachment of tail	0 *18hpf* 1	2	3	3
Somite formation	No = 0	Yes = 1	Yes = 1	Yes = 1
Eye development	1	2	2 + 1 for pigment	2 + 1 for pigment
Movement	No = 0	Yes = 1	Yes = 1	Yes = 1
Heartbeat	No = 0	Yes = 1	Yes = 1	Yes = 1
Blood circulation	No = 0	No = 0	Yes = 1	Yes = 1
Pigmentation head-body	0	0	1	1
Pigmentation tail	0	0	1	1
Pectoral fin	0	0	0	1
Protruding mouth	0	0	0	1
Hatching	No = 0	No = 0	No = 0	Yes = 1
GMS	***1***	***7***	***12***	***15***

Lethality	Yes
Coagulation	

Teratogenicity	Yes
Pericardial edema	 Treated vs. control (Sultana_2008)
Yolk sac edema (arrow)	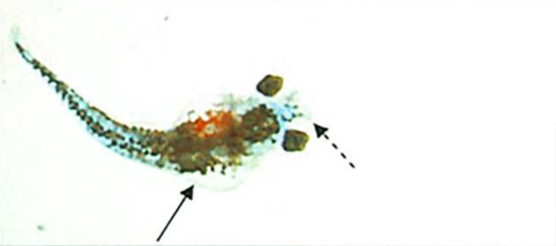
Eye edema (dashed arrow)	
Malformation of the head	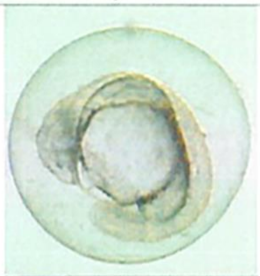
Absence/ malformation of sacculi / otoliths	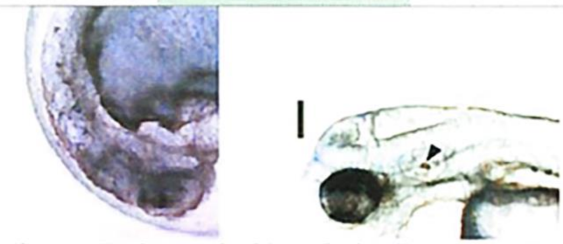 Absence (Bachmann thesis) Fusion (Razzaque_2007)
Malformation of tail	 (Bachmann thesis)
Malformation of heart	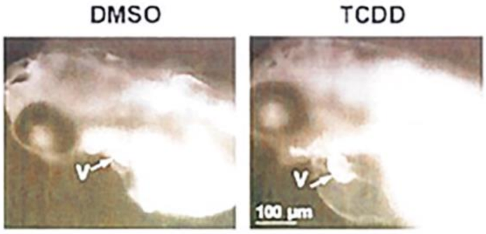 v=ventricle (Antkiewicz_2005)

Figure S3.3 - Scoring system used for photosensitizer-induced toxicity analysis in zebrafish embryos. The scoring system was adapted from (6).

S3.3.14.1. Skin phototoxicity in BALB/c nude mice

The mice were acclimated for 4 d in temperature- and humidity-controlled individually ventilated cages with ad libitum access to food and sterilized, mildly acidified water. The animals were housed in a restricted access facility at the Jiaxing University Medical College under sterile conditions (nightly disinfection of facility by ultraviolet germicidal illumination, sterile bedding) and handled in sterile cleanroom garments and attire.

All procedures with photosensitized animals were performed under dim light conditions. All materials and equipment that were brought in contact with the animals were steam-sterilized.

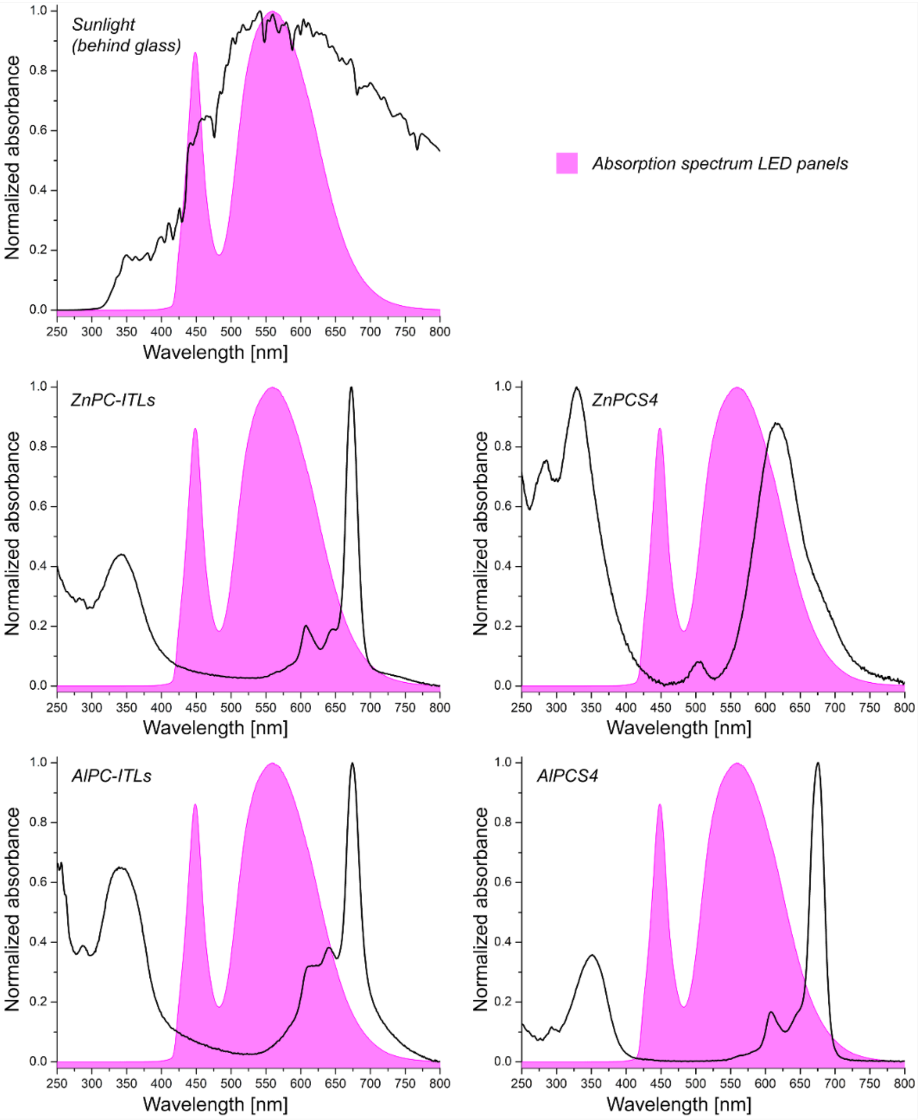

Figure S3.4 - Normalized absorption spectra of sunlight, the LED panels used to emulate indoors and outdoors light conditions, and the photosensitizers. The LED panels emit light in a wavelength range that largely overlaps with the spectral output of sunlight and the absorption spectrum of the photosensitizers.

S3.3.14.2. In vivo PDT efficacy in human tumor-bearing BALB/c nude mice

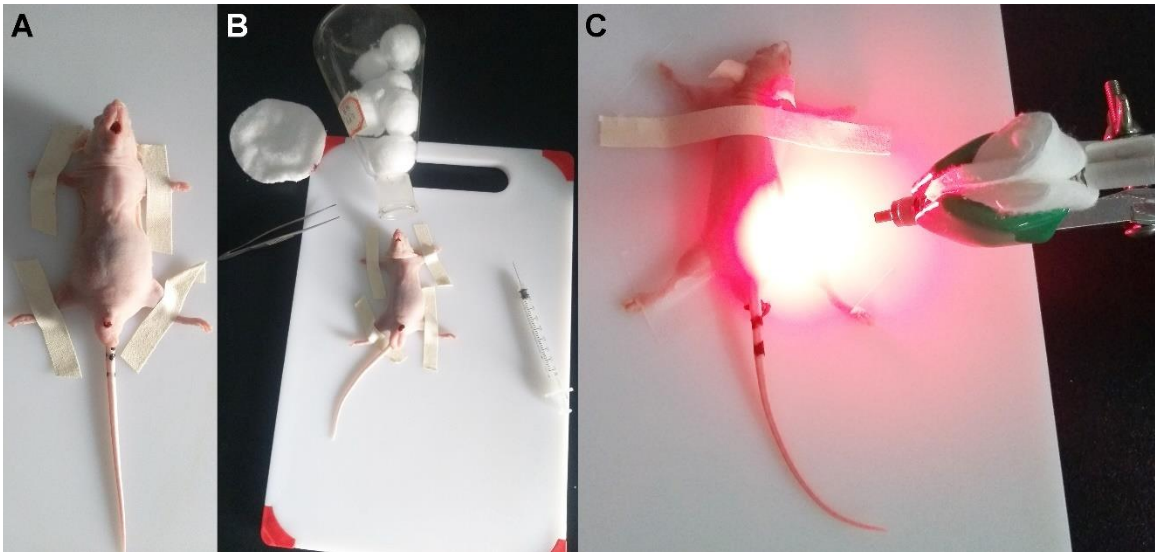

Figure S3.5 - Intravenous injection and PDT protocol in mice. (**A**) For penile vein injections, diethyl ether-anesthetized mice were positioned on their back and their legs were taped to a sterile cutting board to immobilize the animals. In some cases (**B**), the depth of anesthesia had to be increased with an improvised maintenance anesthesia setup (diethyl ether-drenched cotton balls in an Erlenmeyer flask). For PDT (**C**), the mice were immobilized onto the sterile cutting board under mild diethyl ether anesthesia by surgical tape over their legs and neck. PDT was performed without anesthesia in awake state.

S3.4. Results

S3.4.2. Tumor-comprising cells are ubiquitously photosensitized by liposomal and tetrasulfonated metallated phthalocyanines

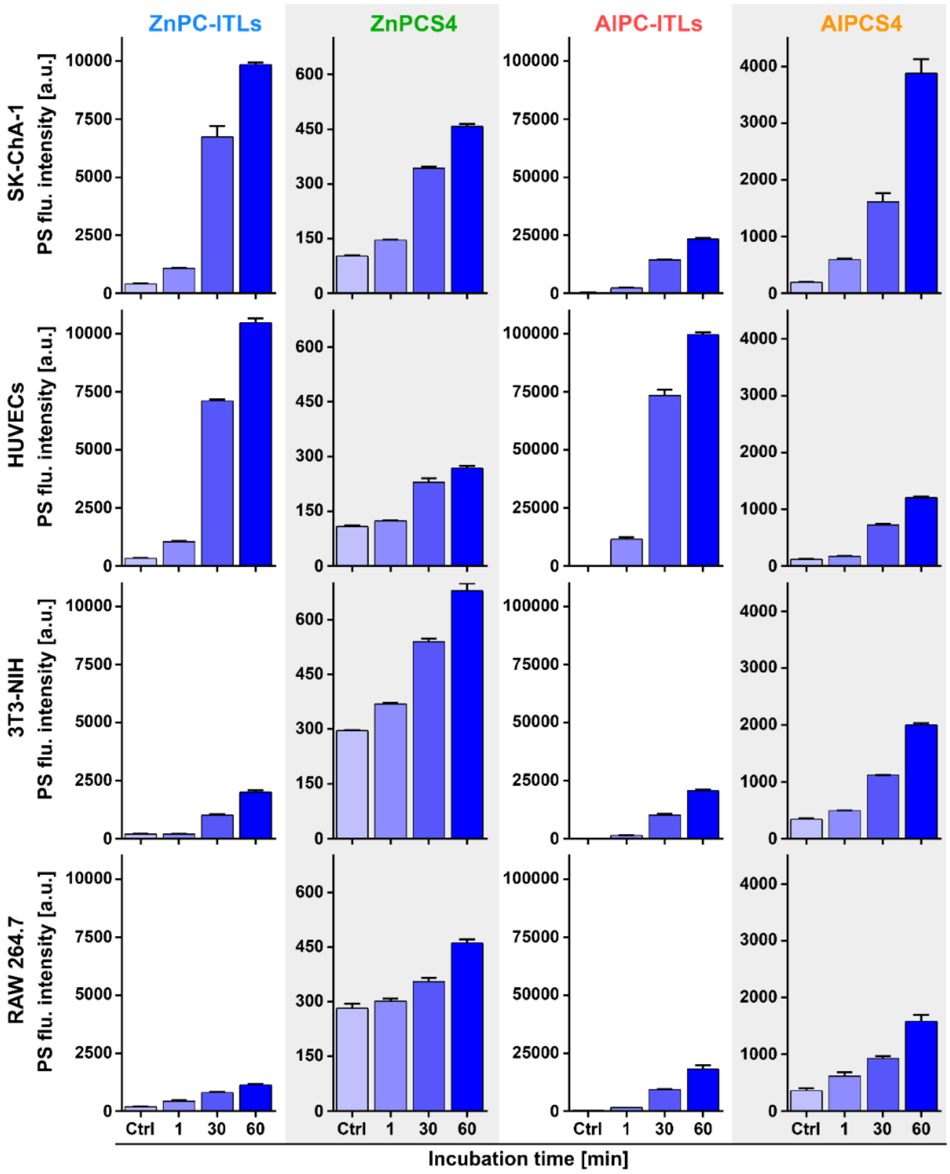

Figure S3.6 - Photosensitization of cells that normally comprise a tumor with liposomal and tetrasulfonated metallated phthalocyanines. SK-ChA-1, HUVECs, 3T3-NIH, and RAW 264.7 cells were incubated either with ZnPC-ITLs or AlPC-ITLs (125 µM final phospholipid concentration, 0.375 µM PS concentration) or with 0.375 µM of ZnPCS4 or AlPCS4 for 1, 30, or 60 min at standard culture conditions. Photosensitization was measured by flow cytometry using PS autofluorescence. Abbreviations: AlPC, aluminum phthalocyanine, AlPCS4, tetrasulfonated AlPC; Ctrl, control; flu. int., fluorescence intensity; ITLs, interstitially targeted liposomes; PS, photosensitizer; ZnPC, zinc phthalocyanine; ZnPCS4, tetrasulfonated ZnPC. Data represent mean ± SD of N = 3 experimental replicates.

The PS distribution kinetics are presented in Figures S3.7-S3.9. It should be noted that confocal microscopy experiments under these conditions could not be performed with HUVECs because the cells displayed apoptotic features when incubated in medium-/-.

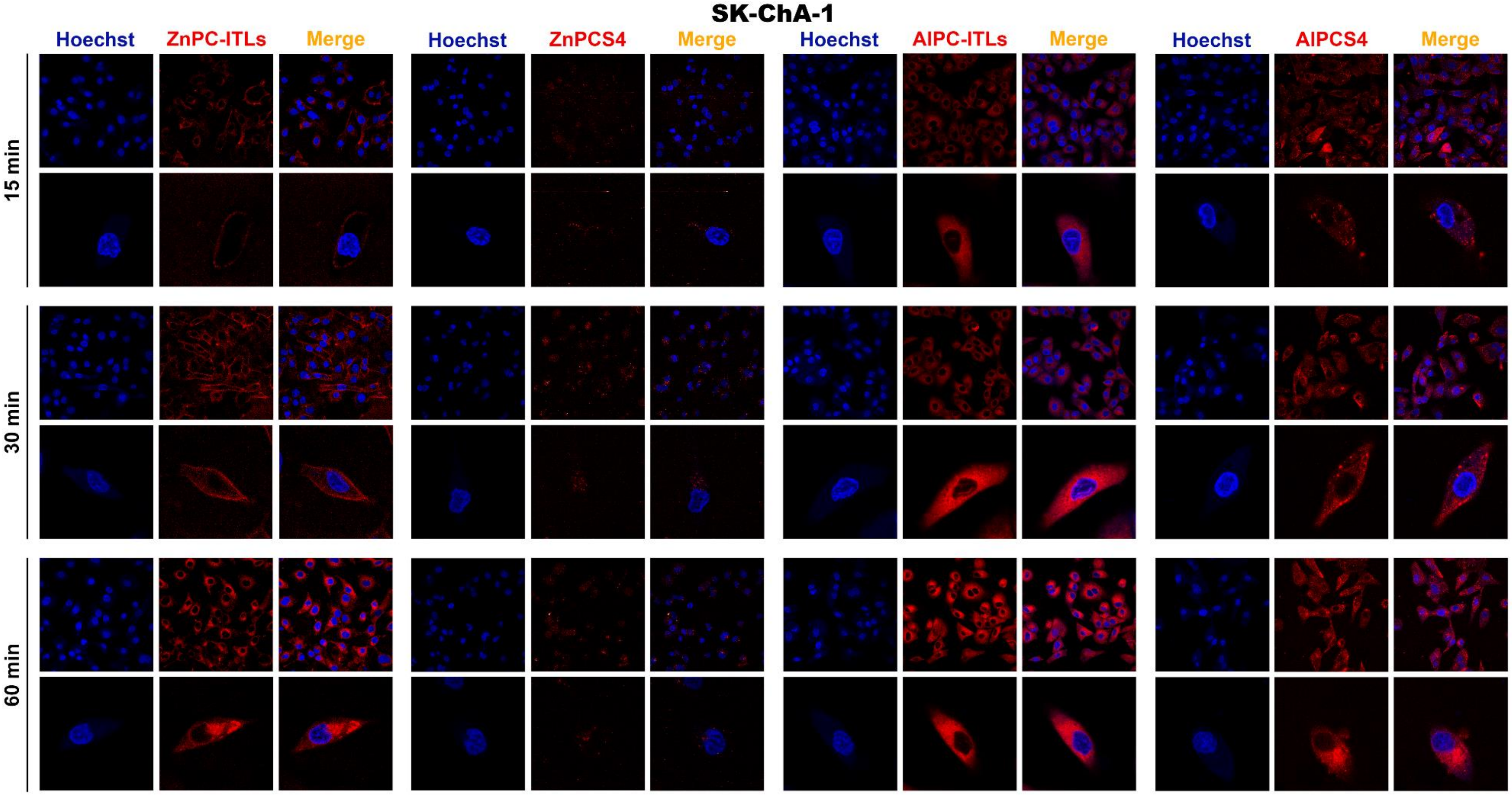

Figure S3.7 - Uptake and intracellular distribution of hydrophilic and liposome-delivered photosensitizers in SK-ChA-1 cells. SK-ChA-1 cells were incubated either with 10 μM of AlPCS4 or ZnPCS4 or 1,000 μM (final phospholipid concentration; 3 μM PS concentration) of AlPC-ITLs or ZnPC-ITLs for 15, 30, and 60 min. Uptake and distribution was assessed by confocal microscopy using PS autofluorescence (red). Nuclei are stained with Hoechst 33342 (blue). Detailed information is provided in section 3.3.5 and S3.3.5. Images were edited in Adobe Photoshop for hue, lightness, saturation, and contrast in a clustered manner per PS so as to preserve relative differences in staining pattern. Abbreviations: AlPC, aluminum phthalocyanine, AlPCS4, tetrasulfonated AlPC; ITLs, interstitially targeted liposomes; min, minutes; ZnPC, zinc phthalocyanine; ZnPCS4, tetrasulfonated ZnPC.

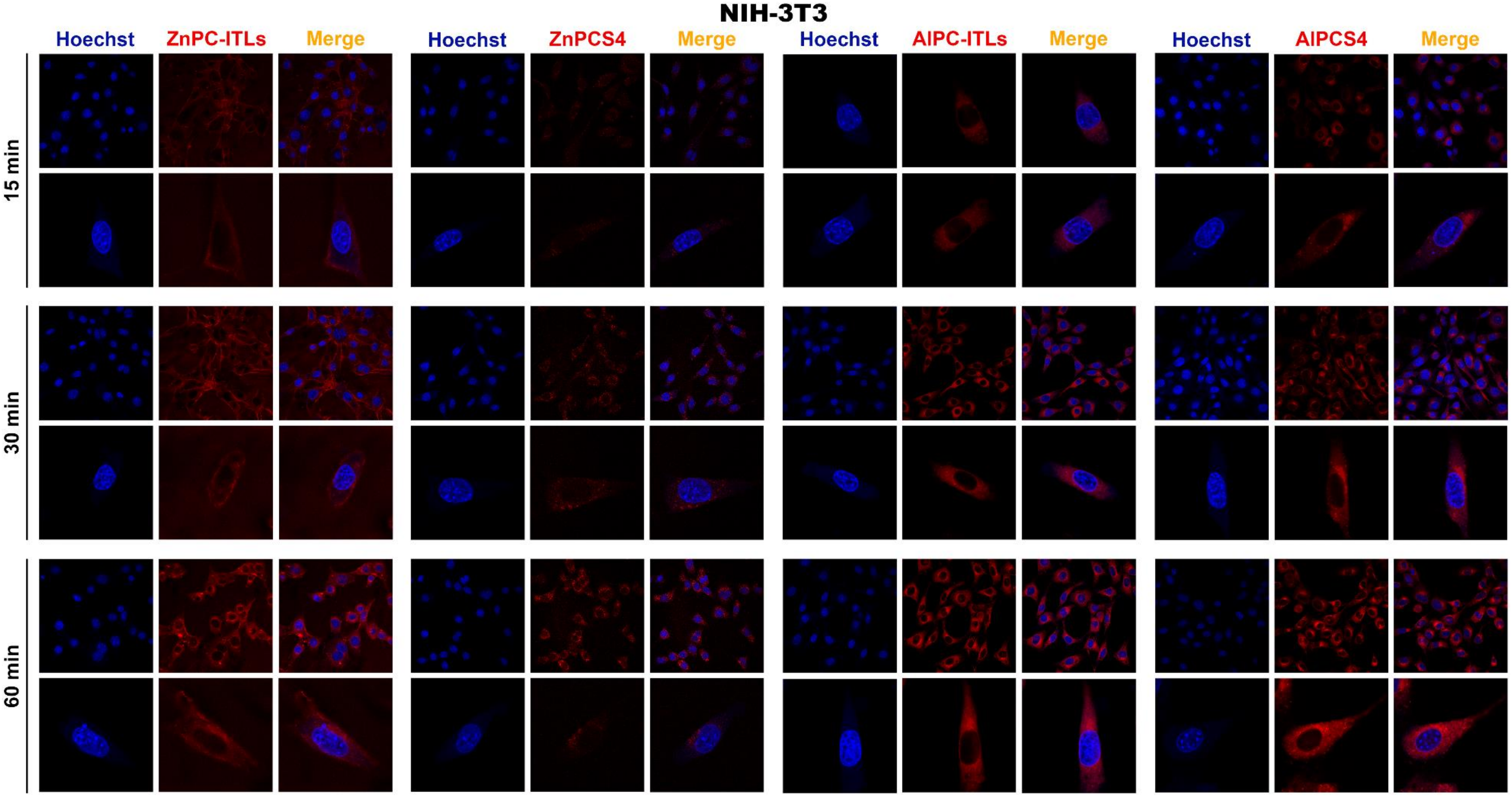

Figure S3.8 - Uptake and intracellular distribution of hydrophilic and liposome-delivered photosensitizers in NIH-3T3 cells. NIH-3T3 cells were incubated either with 10 µM of AlPCS4 or ZnPCS4 or 1,000 µM (final phospholipid concentration; 3 µM PS concentration) of AlPC-ITLs or ZnPC-ITLs for 15, 30, and 60 min. Uptake and distribution was assessed by confocal microscopy using PS autofluorescence (red). Nuclei are stained with Hoechst 33342 (blue). Detailed information is provided in section 3.3.5 and S3.3.5. Images were edited in Adobe Photoshop for hue, lightness, saturation, and contrast in a clustered manner per PS so as to preserve relative differences in staining pattern. Abbreviations: AlPC, aluminum phthalocyanine, AlPCS4, tetrasulfonated AlPC; ITLs, interstitially targeted liposomes; min, minutes; ZnPC, zinc phthalocyanine; ZnPCS4, tetrasulfonated ZnPC.

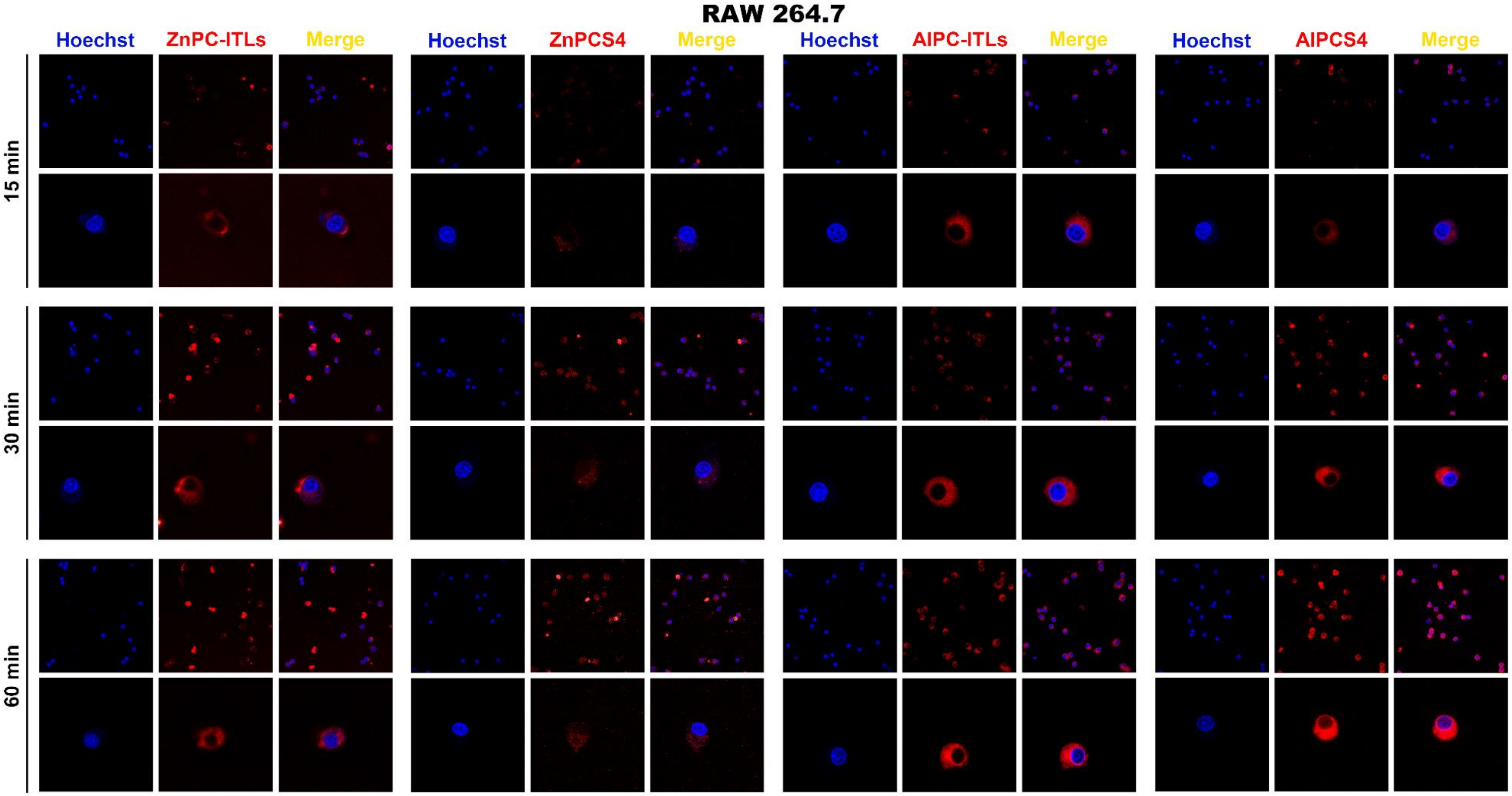

Figure S3.9 - Uptake and intracellular distribution of hydrophilic and liposome-delivered photosensitizers in RAW 264.7 macrophages. RAW 264.7 cells were incubated either with 10 µM of AlPCS4 or ZnPCS4 or 1,000 µM (final phospholipid concentration; 3 µM PS concentration) of AlPC-ITLs or ZnPC-ITLs for 15, 30, and 60 min. Uptake and distribution was assessed by confocal microscopy using PS autofluorescence (red). Nuclei are stained with Hoechst 33342 (blue). Detailed information is provided in section 3.3.5 and S3.3.5. Images were edited in Adobe Photoshop for hue, lightness, saturation, and contrast in a clustered manner per PS so as to preserve relative differences in staining pattern. Abbreviations: AlPC, aluminum phthalocyanine, AlPCS4, tetrasulfonated AlPC; ITLs, interstitially targeted liposomes; min, minutes; ZnPC, zinc phthalocyanine; ZnPCS4, tetrasulfonated ZnPC.

S3.4.3. Lipophilic and hydrophilic metalated phthalocyanines exhibit no-to-moderate dark toxicity

S3.4.3.1. Dark toxicity – WST-1

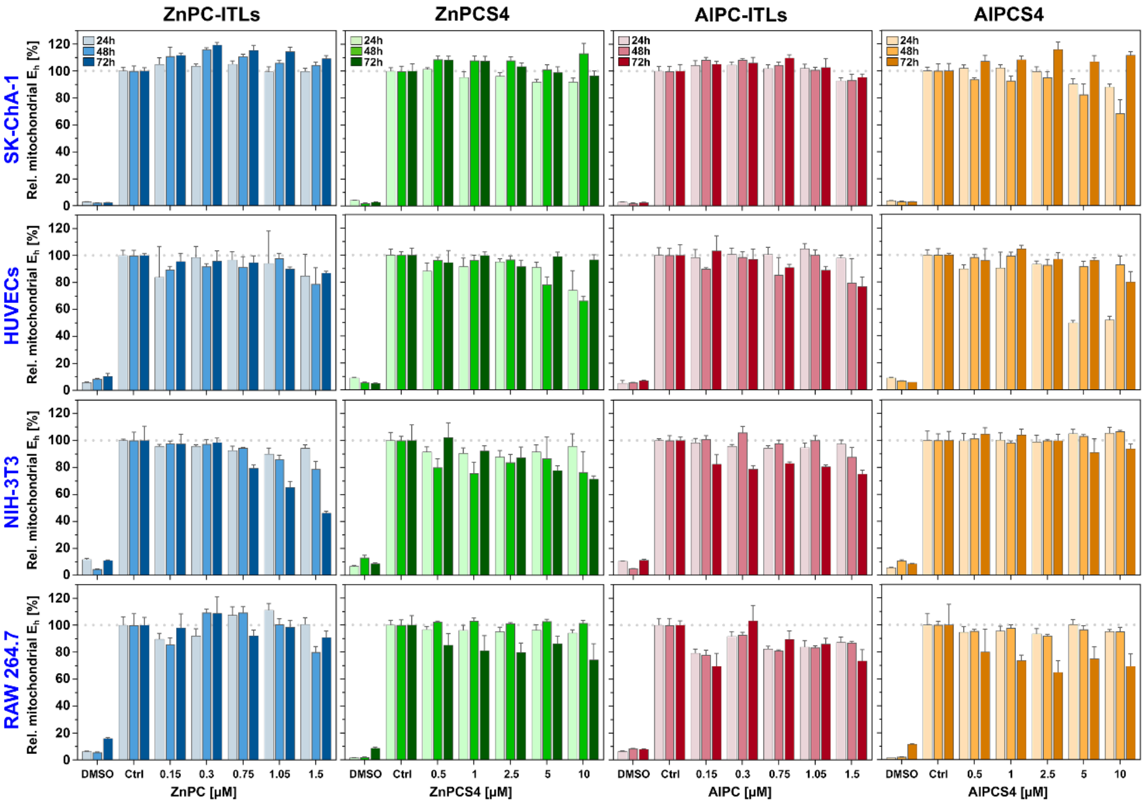

Figure S3.10 - Dark toxicity in cultured cells via WST-1 assay. Viability of SK-ChA-1, HUVEC, 3T3-NIH, and RAW 264.7 cells after incubation with ZnPC-ITLs, ZnPCS4, AlPC-ITLs, and AlPCS4 at standard culture conditions for 24 h, 48 h, and 72 h in the dark. Cell viability was measured using the WST-1 assay, which reflects mitochondrial redox activity. PS was diluted with medium$^{-/-}$. Cells in the negative control group were exposed to medium$^{-/-}$ only while the positive control group was subjected to 20% DMSO (v/v) in medium$^{-/-}$. Data were normalized to the control group mean value and are plotted as mean ± SD of N = 3 experimental replicates.

S3.4.3.2. Dark toxicity - SRB

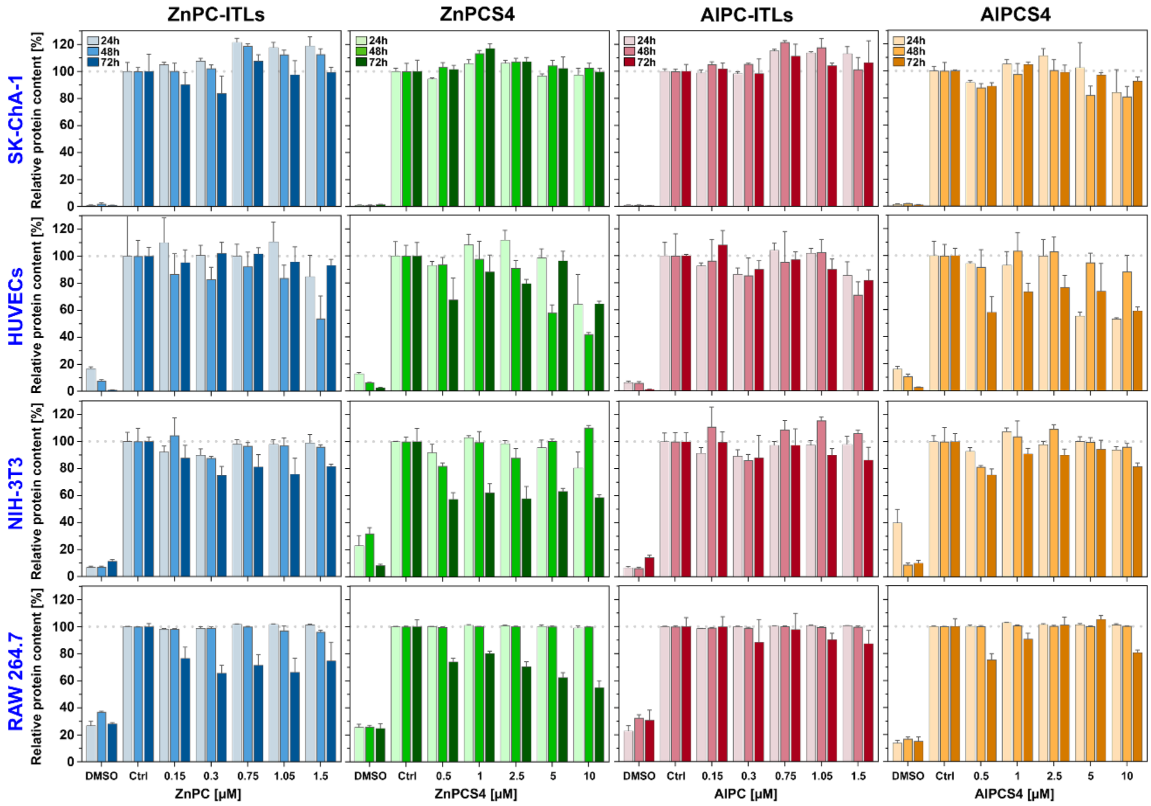

Figure S3.11 - Dark toxicity in cultured cells via SRB assay. Viability of SK-ChA-1, HUVEC, 3T3-NIH, and RAW 264.7 cells after incubation with ZnPC-ITLs, ZnPCS4, AlPC-ITLs, and AlPCS4 at standard culture conditions for 24 h, 48 h, and 72 h in the dark. Cell viability was measured using the sulforhodamine B assay, which reflects total protein content. PS was diluted with medium$^{-/-}$. Cells in the negative control group were exposed to medium$^{-/-}$ only while the positive control group was subjected to 20% DMSO (v/v) in medium$^{-/-}$. Data were normalized to the control group mean value and are plotted as mean ± SD of N = 3 experimental replicates.

S3.4.4. All PSs except ZnPCS4 exhibit strong-to-potent toxicity in illuminated tumor-comprising cells

S3.4.4.1. PDT efficacy: WST-1

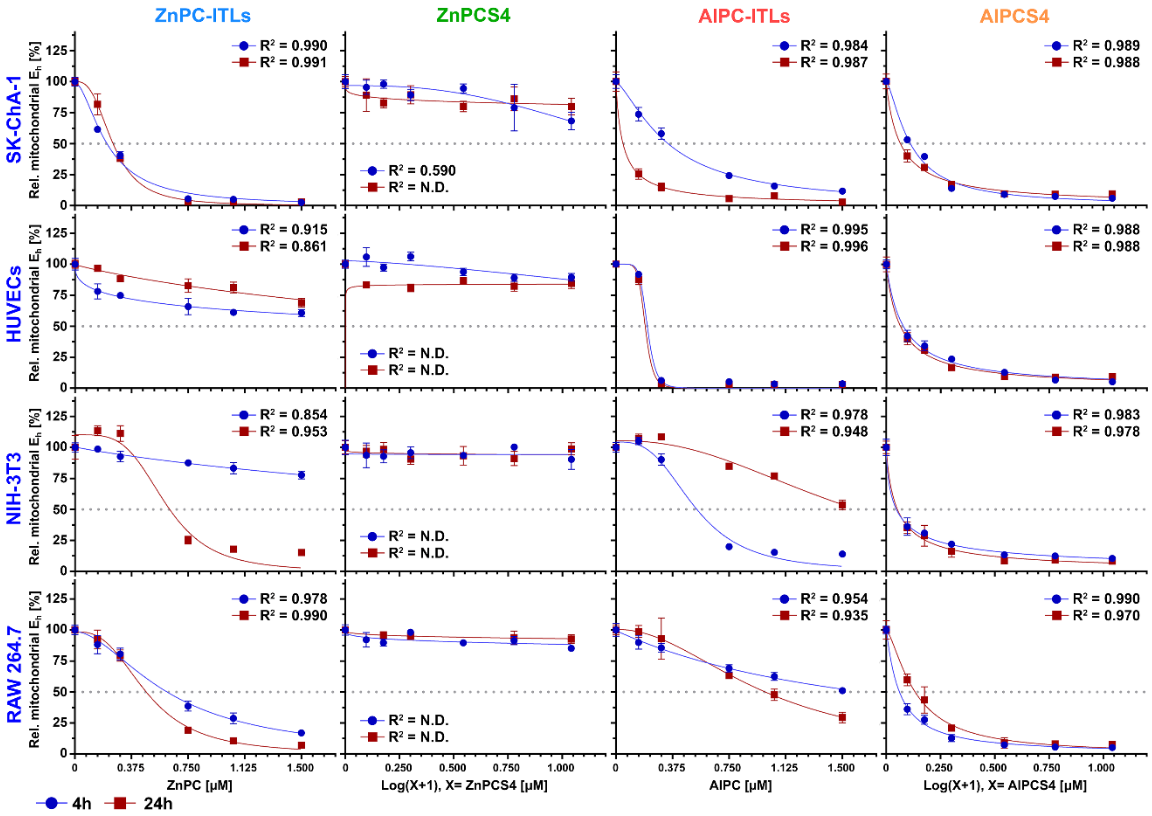

Figure S3.12 - PDT efficacy in cultured cells via WST-1 assay. Viability of SK-ChA-1, HUVEC, 3T3-NIH, and RAW 264.7 cells 4 h and 24 h after PDT. Cells were incubated for 1 h with ZnPC-ITLs, ZnPCS4, AlPC-ITLs, and AlPCS4 prior to PDT (cumulative radiant exposure of 15 J/cm^2). Cell viability was determined with the WST-1 assay. PS was diluted with medium$^{-/-}$. Cells in the control group were incubated with medium$^{-/-}$ and illuminated. Data were normalized to the mean viability of cells in the control group and are plotted as mean ± SD of N = 3 experimental replicates.

S3.4.4.2. PDT efficacy: SRB

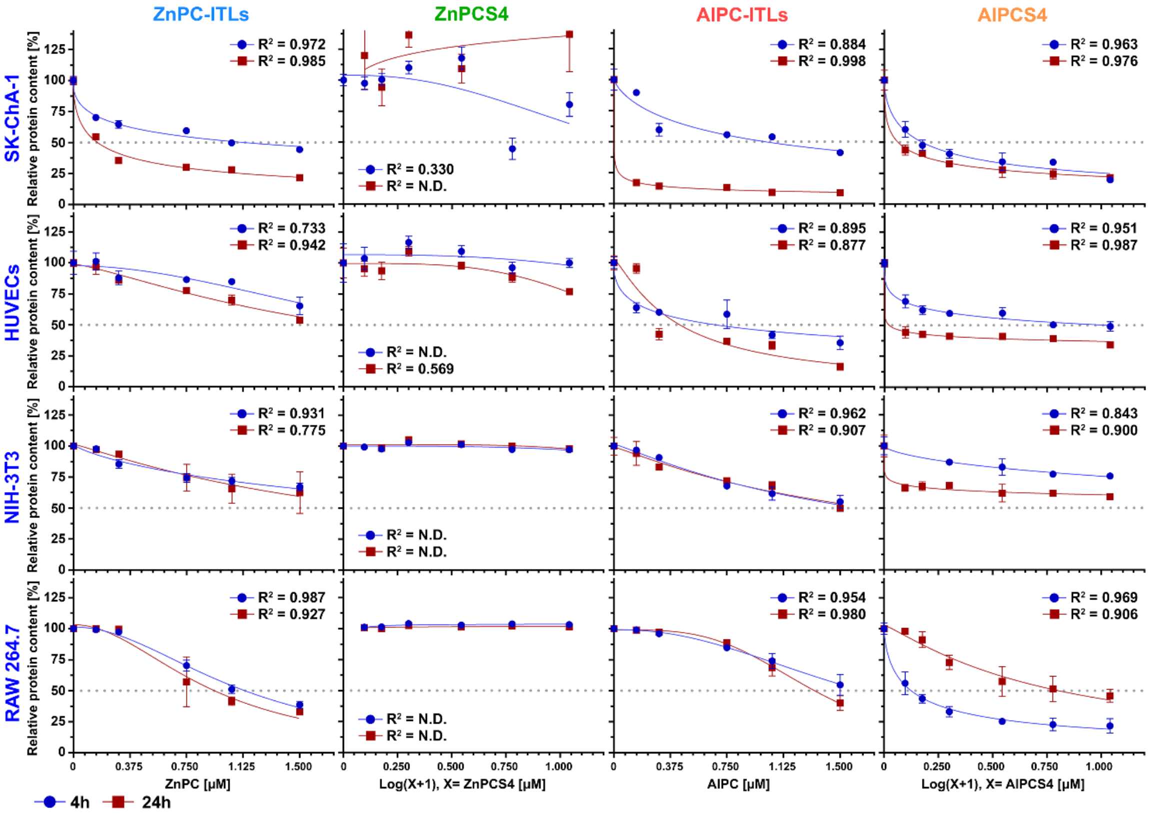

Figure S3.13 - PDT efficacy in cultured cells via SRB assay. Viability of SK-ChA-1, HUVEC, 3T3-NIH, and RAW 264.7 cells 4 h and 24 h after PDT. Cells were incubated for 1 h with ZnPC-ITLs, ZnPCS4, AlPC-ITLs, and AlPCS4 prior to PDT (cumulative radiant exposure of 15 J/cm²). Cell viability was determined with the SRB assay. PS was diluted with medium$^{-/-}$. Cells in the control group were incubated with medium$^{-/-}$ and illuminated. Data were normalized to the mean viability of cells in the control group and are plotted as mean ± SD of N = 3 experimental replicates.

S3.4.5. All PSs except ZnPCS4 exhibit strong-to-potent toxicity in illuminated tumor-comprising cells

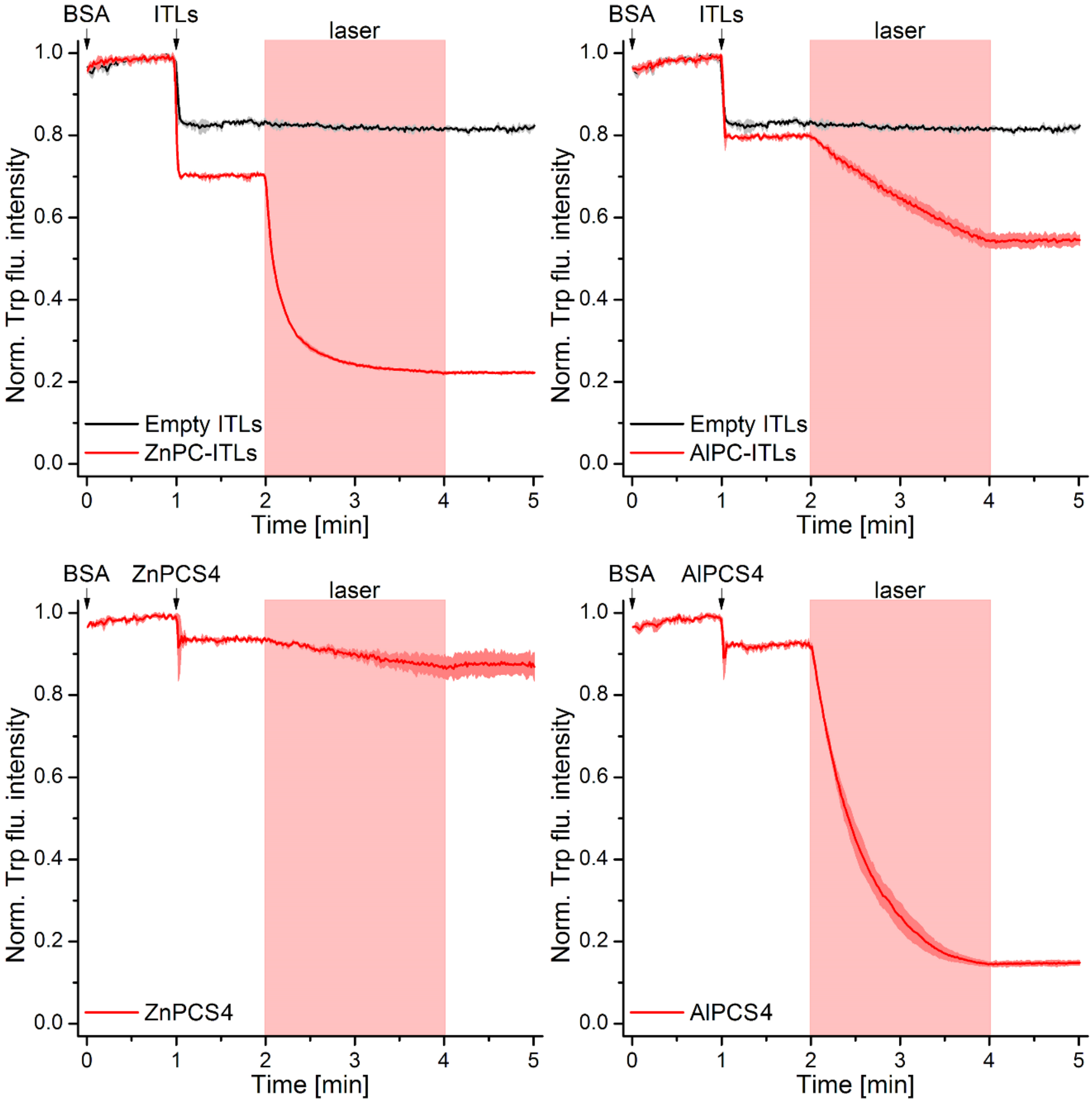

Figure S3.14 - Time-based acquisition of tryptophan (Trp) fluorescence as a marker for protein oxidation after PDT with metallated PCs. Protein (BSA) oxidation coincided with a decrease in Trp fluorescence upon PDT. A final PS concentration of 1.5 µM and 0.1% BSA (w/v) in physiological buffer were used. Trp fluorescence was normalized to the maximum fluorescence intensity recorded before the addition of PS (t = 1 min). The arrows indicate the addition of the corresponding compound and the pink area represent the application of PDT with 671 nm laser light (500 mW, 1 min). All traces are presented with their SD (N = 3 experimental replicated per PS).

S3.4.6. ITL-delivered metallated phthalocyanines are more potent inducers of cell cycle arrest, apoptosis, and necrosis

Table S3.7 - Percentage of the population of cells that were viable (AV-/PI-), early apoptotic (AV+/PI-), and late apoptotic and necrotic (AV+/PI+, AV-/PI+) after PDT, measured at different time intervals. Depicted are quantitative data (mean ±SD) that were used to construct Figure 3.7 in the main text (N = 3 per group).

2 h after PDT					
SK-ChA1	*percentage of population*				
	Control	**ZnPC-ITLs**	**ZnPCS4**	**AlPC-ITLs**	**AlPCS4**
AV-/PI-	93.2 ± 0.4	77.7 ± 1.1	95.0 ± 1.9	63.8 ± 1.3	92.7 ± 1.3
AV+/PI-	2.3 ± 0.2	2.4 ± 0.2	1.6 ± 0.2	9.6 ± 0.8	2.7 ± 0.9
AV+/PI+	4.2 ± 0.3	19.2 ± 0.8	3.3 ± 1.6	25.2 ± 2.2	4.4 ± 0.3
AV-/PI+	0.4 ± 0.1	0.7 ± 0.2	0.1 ± 0.0	1.4 ± 0.1	0.2 ± 0.1
HUVECs	*percentage of population*				
	Control	**ZnPC-ITLs**	**ZnPCS4**	**AlPC-ITLs**	**AlPCS4**
AV-/PI-	79.9 ± 5.4	31.9 ± 2.3	45.8 ± 8.0	17.5 ± 1.4	19.4 ± 4.2
AV+/PI-	14.0 ± 4.0	32.6 ± 1.4	29.8 ± 5.8	54.0 ± 9.6	34.2 ± 2.0
AV+/PI+	6.0 ± 1.4	31.0 ± 1.8	24.1 ± 6.2	27.9 ± 10.5	45.0 ± 3.9
AV-/PI+	0.1 ± 0.0	4.5 ± 0.3	0.3 ± 0.2	0.6 ± 0.5	1.4 ± 0.8
NIH-3T3	*percentage of population*				
	Control	**ZnPC-ITLs**	**ZnPCS4**	**AlPC-ITLs**	**AlPCS4**
AV-/PI-	90.9 ± 0.4	34.2 ± 4.9	87.6 ± 3.0	17.2 ± 3.1	61.4 ± 3.7
AV+/PI-	3.6 ± 0.2	5.3 ± 1.4	3.9 ± 0.6	12.7 ± 1.4	7.1 ± 5.4
AV+/PI+	4.4 ± 0.4	49.9 ± 1.8	7.9 ± 2.4	58.6 ± 5.0	28.5 ± 2.3
AV-/PI+	1.1 ± 0.1	10.5 ± 1.7	0.6 ± 0.1	11.5 ± 0.6	3.0 ± 0.3
RAW 264.7	*percentage of population*				
	Control	**ZnPC-ITLs**	**ZnPCS4**	**AlPC-ITLs**	**AlPCS4**
AV-/PI-	88.3 ± 1.0	3.4 ± 3.2	60.3 ± 5.9	25.8 ± 1.1	28.4 ± 3.4
AV+/PI-	6.4 ± 1.1	6.9 ± 1.3	6.9 ± 4.3	22.6 ± 2.1	8.6 ± 1.7
AV+/PI+	3.7 ± 1.2	81.9 ± 6.5	26.8 ± 9.6	35.6 ± 2.4	46.5 ± 0.8
AV-/PI+	1.6 ± 0.6	7.8 ± 7.5	6.0 ± 0.5	15.9 ± 1.5	16.5 ± 4.6
4 h after PDT					
SK-ChA1	*percentage of population*				
	Control	**ZnPC-ITLs**	**ZnPCS4**	**AlPC-ITLs**	**AlPCS4**
AV-/PI-	84.9 ± 3.8	66.1 ± 1.9	79.1 ± 0.2	63.5 ± 0.4	82.8 ± 0.5
AV+/PI-	3.6 ± 0.3	4.3 ± 0.3	2.8 ± 0.1	26.3 ± 0.4	3.7 ± 0.9
AV+/PI+	11.2 ± 4.0	24.3 ± 1.3	16.6 ± 0.2	8.9 ± 0.6	13.0 ± 0.6
AV-/PI+	0.4 ± 0.0	5.3 ± 1.0	1.6 ± 0.0	0.9 ± 0.1	0.4 ± 0.1
HUVECs	*percentage of population*				
	Control	**ZnPC-ITLs**	**ZnPCS4**	**AlPC-ITLs**	**AlPCS4**
AV-/PI-	74.3 ± 1.4	30.6 ± 2.9	52.7 ± 1.6	12.4 ± 5.8	17.2 ± 0.4
AV+/PI-	17.3 ± 0.5	45.4 ± 1.8	40.6 ± 0.8	39.2 ± 7.1	40.6 ± 0.2
AV+/PI+	8.1 ± 0.9	15.0 ± 2.2	6.3 ± 0.7	47.3 ± 1.2	41.4 ± 0.6
AV-/PI+	0.2 ± 0.1	9.0 ± 1.0	0.4 ± 0.1	1.2 ± 0.3	0.8 ± 0.1
NIH-3T3	*percentage of population*				
	Control	**ZnPC-ITLs**	**ZnPCS4**	**AlPC-ITLs**	**AlPCS4**
AV-/PI-	94.0 ± 2.3	8.8 ± 1.1	83.5 ± 1.5	6.5 ± 2.2	6.9 ± 2.1
AV+/PI-	2.9 ± 0.8	4.1 ± 0.5	7.2 ± 0.8	29.4 ± 2.3	7.5 ± 1.3
AV+/PI+	2.9 ± 1.5	80.3 ± 3.1	9.1 ± 0.9	62.3 ± 0.3	83.4 ± 4.1
AV-/PI+	0.2 ± 0.1	6.9 ± 1.9	0.3 ± 0.2	2.0 ± 0.1	2.3 ± 0.9
RAW 264.7	*percentage of population*				
	Control	**ZnPC-ITLs**	**ZnPCS4**	**AlPC-ITLs**	**AlPCS4**
AV-/PI-	76.4 ± 0.5	3.4 ± 0.3	74.8 ± 1.7	8.8 ± 0.4	15.7 ± 0.8
AV+/PI-	4.7 ± 1.2	9.6 ± 0.1	11.1 ± 1.7	4.4 ± 0.8	23.7 ± 0.1
AV+/PI+	12.4 ± 0.3	77.2 ± 0.8	11.3 ± 0.4	82.1 ± 0.4	43.6 ± 1.2
AV-/PI+	6.5 ± 1.0	9.8 ± 0.3	2.8 ± 0.5	4.7 ± 0.3	17.0 ± 0.6
8 h after PDT					
SK-ChA1	*percentage of population*				
	Control	**ZnPC-ITLs**	**ZnPCS4**	**AlPC-ITLs**	**AlPCS4**
AV-/PI-	89.8 ± 0.3	71.5 ± 3.6	87.2 ± 1.8	42.6 ± 0.2	90.4 ± 1.1
AV+/PI-	4.7 ± 0.3	6.4 ± 0.9	6.4 ± 0.8	25.6 ± 1.5	4.1 ± 0.4
AV+/PI+	4.9 ± 0.1	20.1 ± 2.7	5.8 ± 0.9	29.5 ± 1.2	5.1 ± 0.8

AV-/PI+	0.5 ± 0.1	2.0 ± 0.1	0.7 ± 0.3	2.2 ± 0.1	0.4 ± 0.0
HUVECs	*percentage of population*				
	Control	**ZnPC-ITLs**	**ZnPCS4**	**AlPC-ITLs**	**AlPCS4**
AV-/PI-	78.3 ± 3.6	6.7 ± 1.9	28.6 ± 4.5	3.2 ± 1.0	12.4 ± 0.5
AV+/PI-	17.2 ± 3.6	73.1 ± 2.1	54.4 ± 4.6	38.0 ± 1.7	8.7 ± 3.8
AV+/PI+	4.4 ± 0.1	20.2 ± 1.4	16.9 ± 1.3	58.8 ± 2.6	78.7 ± 3.6
AV-/PI+	0.1 ± 0.0	0.0 ± 0.0	0.1 ± 0.0	0.1 ± 0.0	0.2 ± 0.1
NIH-3T3	*percentage of population*				
	Control	**ZnPC-ITLs**	**ZnPCS4**	**AlPC-ITLs**	**AlPCS4**
AV-/PI-	90.8 ± 0.2	30.1 ± 15.6	89.0 ± 2.7	3.9 ± 1.8	30.3 ± 5.9
AV+/PI-	4.0 ± 0.1	17.7 ± 2.8	6.2 ± 1.5	10.2 ± 1.7	18.2 ± 0.6
AV+/PI+	3.8 ± 0.3	47.4 ± 13.8	4.4 ± 3.8	83.3 ± 0.2	48.4 ± 5.3
AV-/PI+	1.3 ± 0.2	4.9 ± 0.9	0.5 ± 0.5	2.6 ± 0.3	3.1 ± 0.2
RAW 264.7	*percentage of population*				
	Control	**ZnPC-ITLs**	**ZnPCS4**	**AlPC-ITLs**	**AlPCS4**
AV-/PI-	69.3 ± 3.6	2.4 ± 0.7	72.2 ± 4.5	6.4 ± 3.5	11.3 ± 5.8
AV+/PI-	4.5 ± 0.3	3.6 ± 0.1	4.4 ± 1.1	5.4 ± 1.5	7.0 ± 1.8
AV+/PI+	24.9 ± 3.2	93.4 ± 0.8	22.9 ± 4.0	88.0 ± 3.3	81.3 ± 7.3
AV-/PI+	1.2 ± 0.3	0.6 ± 0.2	0.6 ± 0.2	0.2 ± 0.1	0.4 ± 0.2

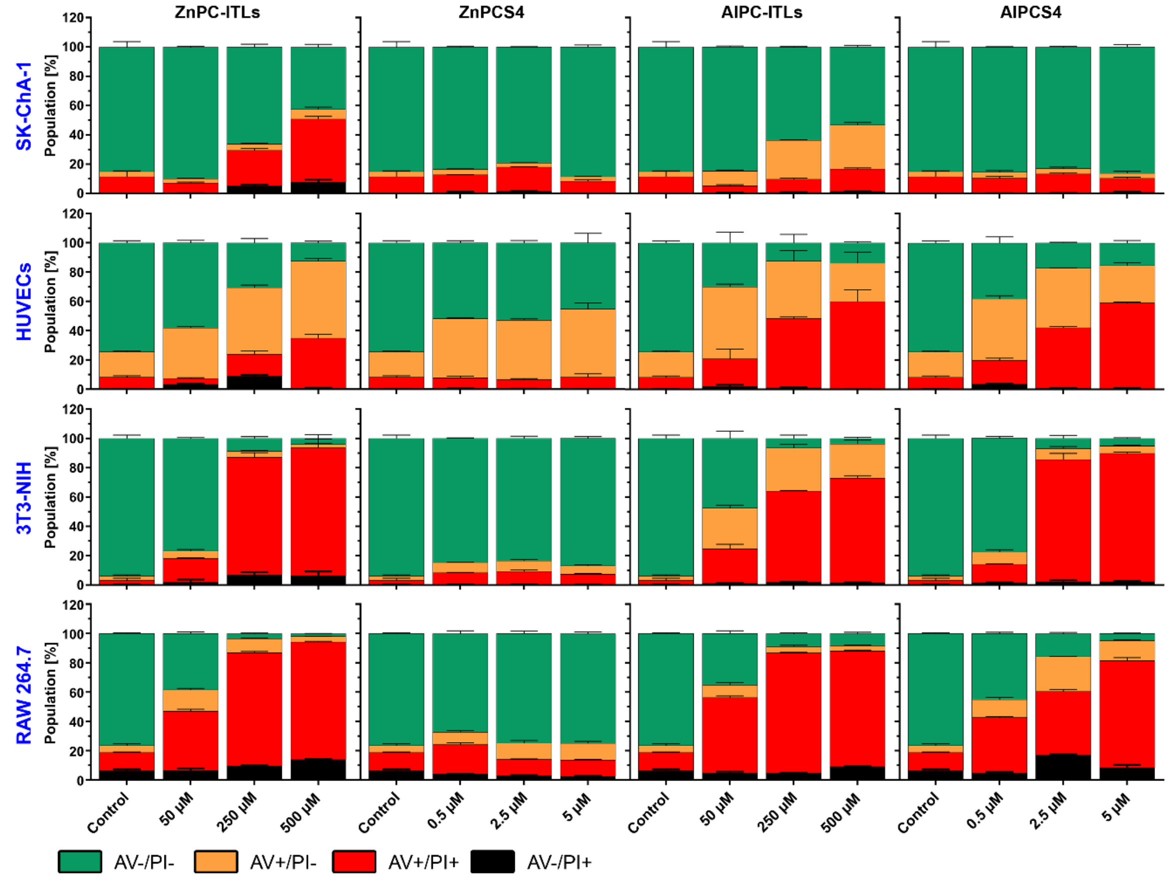

Figure S3.15 - Photosensitizer concentration-dependent PDT-induced mode of cell death in cultured cells. Cells were incubated with ZnPC-ITLs or AlPC-ITLs (50 µM, 250 µM, and 500 µM final phospholipid concentration; 0.15 µM, 0.75 µM, and 1.5 µM final PS concentration) and 0.5, 2.5 and 5 µM of ZnPCS4 or AlPCS4 for 60 min and subjected to PDT (cumulative radiant exposure of 15 J/cm²). Cells were analyzed 4 h post-PDT by flow cytometry following staining with Annexin-V (AV) and PI. Cell populations were stratified as: AV-/PI-, viable cells; AV+/PI-, early apoptosis; AV+/PI+ and AV-/PI+, cells in late apoptosis or necrosis. Data are presented as mean ± SD of N = 3 experimental replicates.

S3.7. References

1. Berridge MV, Herst PM, and Tan AS. Tetrazolium dyes as tools in cell biology: new insights into their cellular reduction. *Biotechnol Annu Rev.* 2005;11(127-52.
2. Dias LM, Sharifi F, de Keijzer MJ, Mesquita B, Desclos E, Kochan JA, de Klerk DJ, Ernst D, de Haan LR, Franchi LP, et al. Attritional evaluation of lipophilic and hydrophilic metallated phthalocyanines for oncological photodynamic therapy. *J Photochem Photobiol B.* 2021;216(112146.
3. Weijer R, Broekgaarden M, Kos M, van Vught R, Rauws EA, Breukink EJ, van Gulik TM, Storm G, and Heger M. Enhancing photodynamic therapy of refractory solid cancers: Combining second-generation photosensitizers with multi-targeted liposomal delivery. *J Photochem Photobiol C.* 2015;23(103-31.
4. Bock FJ, and Tait SWG. Mitochondria as multifaceted regulators of cell death. *Nat Rev Mol Cell Biol.* 2020;21(2):85-100.
5. Vichai V, and Kirtikara K. Sulforhodamine B colorimetric assay for cytotoxicity screening. *Nat Protoc.* 2006;1(3):1112-6.
6. Hermsen SA, van den Brandhof EJ, van der Ven LT, and Piersma AH. Relative embryotoxicity of two classes of chemicals in a modified zebrafish embryotoxicity test and comparison with their in vivo potencies. *Toxicol In Vitro.* 2011;25(3):745-53.

Chapter 4

General Conclusions and Future Perspectives

4. Chapter 4 - General Conclusions and Future Perspectives

4.1. General Conclusions

The treatment modality of PDT is still evolving through the years despite of its long history, and it continues evolving through the searching for higher safety and efficiency in curing oncological malignancies. Although, many PSs were approved for clinical application in a variety of cancers, the efficiency in treatment for solid tumors is still considered poor for the field, especially in tumors that reside in internal organs such as the pancreas and the biliary tree. The PS suboptimal properties together with the route of administration are often associated with unfavorable pharmacokinetics. Therefore, one of the main concerns when it comes to the administration of a PS is the adverse effect of skin phototoxicity, where often patients are asked to be shielded from any light exposure for weeks after treatment, compromising unethically their quality of life.

In order to participate in the progression of the PDT field, our team have decided to encapsulate second-generation of PSs into liposomal carriers that are targeted to the tumor interstitium after intravenous administration. Metallated phthalocyanines such as the lipophilic zinc phthalocyanine (ZnPC) and aluminum phthalocyanine (AlPC) as well as their hydrophilic tetrasulfonated derivatives ZnPCS4 and AlPCS4 meet the clinical requirements for PSs. Despite that the creation of such PS-liposomal formulation cannot be considerate a novelty at current times, up to date there has been no head-to-head comparison to determine which of these PSs is the most phototoxic to tumor cells, and hence deserves further preclinical and clinical development. These studies therefore, were conducted in a way that allows the selection of the most optimal PS for further development into third- and fourth-generation (*e.g.*, co-encapsulating inhibitors of tumor cell survival pathways with PSs of second-generation). In addition, with our studies we aimed to establish a minimalistic research framework for translational science colleagues who develop and test novel PSs and help them bring it at warp speed to clinical trials. Using our approach, novel photosensitizers can be quickly and facilely tested and benchmarked against clinically approved photosensitizers by following our attritional approach.

In our first study (chapter 2), we initiated our research through an attritional assessment performed *in vitro* using all four PSs in a single cell line. The analyses were performed in cultured A431 cells as a template for tumor cells with a dysfunctional P53 tumor suppressor gene and EGFR overexpression. Through our observations we concluded that Liposomal AlPC is the most potent PS for oncological PDT, whereas ZnPCS4 was photodynamically inert in A431 cells. AlPC did not induce dark toxicity at PS concentrations of up to 1.5 μM, which is approximately 37 times higher than its calculated LC_{50} value, and therefore highly in favor clinical applications. AlPC photosensitized multiple intracellular loci, which was associated with extensive, irreversible cell death signaling that is expected to benefit treatment efficacy and possibly immunological long-term tumor control, granted that sufficient AlPC will reach the tumor *in vivo*. Given the differential pharmacokinetics, intracellular distribution, and cell death dynamics, liposomal AlPC may be combined with AlPCS4 in a PS cocktail to further improve PDT efficacy.

With the goal of validating our previous research, we have move forward with our comparative model shown in chapter 3 by using the four metallated-phthalocyanines in a human cholangiocarcinoma cell line and tumor-comprising cells (endothelial cells, fibroblasts, and macrophages), as a representation of the tumor's microenvironment. In addition to all parameters assessed in the previous study, we went one step further and evaluated the systemic toxicity of each PS in zebrafish and chicken embryos. In addition, we have determined the risk for skin phototoxicity using BALB/c nude mice as our *in vivo* model. A pilot study on PDT efficacy was conducted as well in BALB/c nude mice bearing human triple-negative breast cancer (MDA-MB-231) xenografts. Through our findings we concluded that all photodynamically active PSs (except ZnPCS4) were able to effectively photosensitize cancer cells and non-cancerous cells. In addition, PSs in study did not induced any notable systemic toxicity in zebrafish and chicken embryos. However, ITL-delivered ZnPC and ZnPCS4 were associated with skin phototoxicity, while the aluminum containing PSs did not exert any detectable skin phototoxicity. Last but not least, ITL-delivered ZnPC and AlPC are equally effective in their tumor-killing capacity in human tumor breast cancer xenografts and superior to other non-phthalocyanine PSs when appraised on a per mole administered dose basis. Overall and considering both studies, our team have decided that all applications with ZnPCS4 for oncological PDT in our group will be discontinued, as ZnPCS4 failed the attrition step concerning efficiency and it showed alarming signs of cutaneous phototoxicity. It is therefore concluded that AlPC are the least toxic and the most effective PSs to employ with respect to ITLs as part of the comprehensive tumor targeting and PS delivery platform.

In conclusion, the present thesis demonstrated that:

1. Tumor-comprising cells take up ITLs in a concentration and incubation time-dependent manner, and are ubiquitously photosensitized by liposomal and tetrasulfonated metallated phthalocyanines;
2. Liposomal phthalocyanines are the least cytotoxic (up to 1.5 μM) while tetrasulfonated phthalocyanines can induce mild-to-moderate dark toxicity at concentrations of ≥ 2.5 μM;
3. All PSs except ZnPCS4 exhibit strong-to-potent toxicity in illuminated tumor-comprising cells, and aluminum-based phthalocyanines are more phototoxic than zinc-based phthalocyanines;
4. ITL-delivered metallated phthalocyanines are more potent inducers of cell cycle arrest, apoptosis, and necrosis;
5. Liposomal photosensitizers and AlPCS4 exhibit minimal dark toxicity in zebrafish and chicken embryos;
6. *In vivo* skin phototoxicity manifested in nude mice exposed to ZnPC and ZnPCS4 but not AlPC and AlPCS4;
7. ZnPC-ITLs and AlPC-ITLs extend the time to sacrifice in a mouse model of human triple negative breast cancer.

Therefore, through all the points above mentioned, we concluded that AlPCS4 and AlPC encapsulated in ITLs have shown the best outcome and performance either *in vitro* and *in vivo* comparatively to ZnPCS4 and ZnPC in ITLs, respectively.

4.2. Future Perspectives

In a near future our PDT group is planning a next round of attritional comparisons, where the formulations will be optimized and benchmarked against standard chemotherapy and clinically employed PSs. Testing will be performed in an in situ human cholangiocarcinoma model currently being developed in our laboratory. If, after formulation optimization, the ITLs underperform relative to the clinical standards in terms of skin phototoxicity and therapeutic efficacy, then the ITLs will be abandoned and focus will be placed on more effective photopharmaceuticals in comparison to clinical standards. The planned optimizations will therefore feature an increase in AlPC:lipid ratio as well as the co-encapsulation of AlPCS4 (in the liposomal aqueous core). Given the uptake of ITLs by target cells and subsequent PS dispersion, triplet state deactivation as a result of PS aggregation at PS:lipid ratios of > 0.003 should not constitute an obstacle. In addition to the optimization of this PDT strategy, future work should also include the co-encapsulation of PSs with drugs that interfere with the main survival pathways involved in tumor cells after PDT, and potentially increase the therapeutic efficiency against solid and recalcitrant tumors.